UNIVERSITY OF PRETORIA

DEPARTMENT OF CIVIL ENGINEERING

USE OF RAYLEIGH AND LOVE WAVES IN SEISMIC SURFACE WAVE TESTING

February 2022

USE OF RAYLEIGH AND LOVE WAVES IN SEISMIC SURFACE WAVE TESTING

MOHAMMED SHARIFUL ISLAM

A dissertation proposal submitted in partial fulfilment of the requirements for the degree of

MASTER OF ENGINEERING (GEOTECHNICAL ENGINEERING)

In the

FACULTY OF ENGINEERING

UNIVERSITY OF PRETORIA

Supervisor: Prof G. Heymann

DISSERTATION SUMMARY

USE OF RAYLEIGH AND LOVE WAVES IN SEISMIC SURFACE WAVE TESTING

MOHAMMED SHARIFUL ISLAM

Supervisor:	Prof G. Heymann
Department:	Civil Engineering
University:	University of Pretoria
Degree:	Master of Engineering (Geotechnical Engineering)

Seismic surface wave tests have made an impact in the Geotechnical Engineering industry due to their non-invasive and inexpensive procedures for attaining important soil parameters, such as the small strain shear modulus (G_0) by measuring the shear wave velocity (Vs) profile. Essentially, conventional surface wave tests incorporate Rayleigh waves alone due to the ease in their generation and detection in the fields. However, another type of surface wave, known as Love waves, is often neglected during testing due to the difficulties faced in integrating Love waves in the tests. The study explored the use of both Rayleigh and Love waves to obtain the Vs profile using synthetic data and experimental data, which was collected at two selected test sites. Two approaches were investigated for the generation of Love waves through the Continuous Surface Wave (CSW) tests and Spectral Analysis of Surface Wave (SASW) tests using standard test specifications. Surface wave signals from these tests were processed using Python based codes to determine and interpret the respective dispersion points. The dispersion data from both the synthetic and experimental data were used to conduct discrete and joint inversions, from which the spread in the Vs profiles was evaluated within misfit limits. The study demonstrated that by using both Rayleigh and Love waves in a joint inversion, the spread in the Vs can be reduced compared to using Rayleigh waves alone. However, this is only possible when the quality of the Rayleigh and Love wave signals are good. The generation of good quality Love wave signals remains a major problem when using joint inversions and it is recommended that newer and improved designs be tested and evaluated.

DECLARATION

I, the undersigned hereby declare that:

- I understand what plagiarism is and I am aware of the University's policy in this regard;

- The work contained in this dissertation is my own original work;

- I did not refer to work of current or previous students, lecture notes, handbooks or any other study material without proper referencing;

- Where other people's work has been used this has been properly acknowledged and referenced;

- I have not allowed anyone to copy any part of my dissertation;

- I have not previously in its entirety or in part submitted this dissertation at any university for a degree.

Signature:

Name: Mohammed Shariful Islam

Student number: 15246711

Date: 10/02/2022

ACKNOWLEDGEMENTS

This research was conducted and compiled during the COVID 19 pandemic and as a result, several unforeseen obstacles and closings were endured during this period. Through the support, guidance and kindness from several organisations and people, it was possible to breathe life into this dissertation. I wish to extend my sincere gratitude and appreciation to the following:

TABLE OF CONTENTS

APPENDIX A: LOVE WAVE IMPACT SOURCE DESIGN

APPENDIX B: SIGNAL PROCESSING CODE

LIST OF TABLES

LIST OF FIGURES

1   INTRODUCTION

Seismic testing methods have been used for the recognition of shallow subsurface stratigraphy and stiffness by obtaining the shear wave velocity (V_S) profile (Ganji *et al.*, 1998). The V_S profile is an important benchmark to geotechnical engineers and designers as certain building codes require the V_S profile for site classification in terms of seismic response (Foti *et al.*, 2018). Seismic tests characterize mediums under undisturbed states and serve as tools in identifying important soil parameters such as the small strain shear modulus, G_0, which is strongly influenced by disturbances in sampling and reconsolidation procedures. Thus, to obtain acceptable estimates of G_0, non-invasive and inexpensive, in-situ seismic testing methods are utilized (Foti *et al.*, 2009).

Seismic energy is composed of predominantly two types of seismic waves namely body waves (Compression and Shear waves) and surface waves (Rayleigh and Love). For a period, the characterization of soils was widely dependent on seismic tests that used the propagation of body waves. Such tests included seismic refraction and reflection, vertical profiling in up-hole tests, down-hole tests and cross hole tests. During this period, surface waves, previously known as 'ground roll', were excluded in the analysis stage as they were viewed as coherent noise burying practical signals. However, in the last decades, surface wave testing methods have received a great deal of attention in the geotechnical industry due to the intrinsic nature of these waves in stratified media and developments in surface wave approaches are still progressing (Strobbia, 2003).

Current industry surface wave test methods focus on attaining the velocity of the Rayleigh surface wave (V_r), which is subsequently used to attain the V_s profile. These methods provide reasonably good data in majority of the cases. Due to the ease in generating and detecting Rayleigh waves, a second type of surface wave known as Love waves is often ignored for seismic tests. This is on account of Love waves being limited in terms of generation and stratigraphy requirements. To the authors knowledge, a limited amount of research exists on the analysis of shallow profiles incorporating both Love waves and Rayleigh waves using conventional surface wave tests due to limitations that exist in integrating Love waves into seismic tests.

Inversion techniques which are used to deliver the V_s profiles are often mathematically ill posed (Foti *et al.*, 2018). Therefore, additional Love wave experimental data could complement the well-established analysis of Rayleigh waves (Guzina and Madyarov, 2005) . The author aims

to investigate the advantages of incorporating Love waves during the analysis stage for the recovery of soil stiffness profiles as well as evaluate any differences obtained. From these evaluations, a recommendation could be proposed on the way seismic tests are currently implemented for the practicing geotechnical engineer.

1.1 OBJECTIVES OF THE STUDY

The main objectives of the study were as follows:

- To design and develop equipment to conduct surface wave seismic tests using Love waves.
- To determine if there is an improvement in the parameter that governs the fit between experimental and theoretical dispersion curves when employing a joint inversion analysis.
- To investigate if there are significant differences in the velocity profiles generated using joint inversions compared to conventional Rayleigh wave inversions methods.
- To determine whether there is a need to incorporate Love waves together with Rayleigh waves during seismic tests for recovery of the stiffness profile.

1.2 SCOPE OF STUDY

The scope of the study was limited to the following:

- The experimental tests were field based with the goal of measuring Love and Rayleigh waves simultaneously.
- Experimental tests were considered for joint (Rayleigh wave and Love wave) and discrete Rayleigh wave approaches using the same test sites.
- Tests were carried out at two selected test sites for which test pit and borehole information were available.
- Theoretical analysis was conducted using synthetic dispersion data based on a theoretical model.
- The following inversion approaches were considered for the study:
  1) Shear wave profile analysis using conventional seismic testing methods using Rayleigh waves alone.
  2) Shear wave profile analysis using joint methods using Rayleigh and Love waves

1.3   METHODOLOGY

The methodology that was used to attain the listed objectives were as follows:

- A literature review, regarding the fundamentals of seismic surface waves tests and the current procedures used to obtain geotechnical parameters was conducted. Information attained from the literature was used to develop the experimental framework of the study.

- Two test site locations with available borehole logs were selected for the purpose of the study.

- Love wave sources and their respective experimental components were designed and developed for their applicable seismic tests.

- Continuous Surface Wave (CSW) tests and Spectral Analysis of Surface Waves (SASW) tests were conducted on the test site, accommodating both Rayleigh wave and Love wave experimental settings.

- Synthetic dispersion curves for Rayleigh and Love waves were generated from a theoretical model.

- Computer based programming algorithms were developed to facilitate the processing of the seismic data, which extracted the experimental dispersion curve profiles.

- An inversion analysis was conducted using the computing software, Dinver, to derive the shear wave velocity (V_S) profiles for each set of seismic tests for both experimental and synthetic dispersion curves.

1.4   ORGANIZATION OF THE REPORT

The dissertation report comprises of the following:

- Chapter 1 serves as an introduction to the dissertation providing a short background of the topic as well as the importance for conducting this research. The chapter profiles the objectives, scope and methodology of the study.

- Chapter 2 reviews relevant current literature, focusing on the fundamentals of waves, seismic surface wave tests and the analysis procedures currently implemented in surface wave testing.

- Chapter 3 describes the experimental design implemented to acquire the relevant seismic surface wave data and discusses the observations made from synthetic data.

- Chapter 4 discusses the observations and results from the acquired experimental data.

- Chapter 5 discusses the conclusions arrived at as well as provides recommendations for prospective further studies.
- Chapter 6 provides a list of the references used to support the research topic.
- Appendix A contains the parts list for the manufacture of the Love wave impact source.
- Appendix B presents the Python based codes used during the processing stages.

2   LITERATURE REVIEW

The purpose of this chapter was to gain insight into the current world of seismic tests using surface waves as the media of propagation. In this chapter, the different types of surface waves that could be incorporated during seismic tests along with their limitations are discussed. Furthermore, seismic tests currently considered as state of practice in the industry are discussed and critiqued in terms of their performance. The study focused on seismic techniques involving surface waves only and therefore body waves and their relevant testing techniques were not explored in detail. The literature review aims to guide the reader in understanding the problem the study addresses. Using the content presented in this chapter, a hypothesis was made, which guided the development of the experimental design.

2.1   SURFACE WAVES

Seismic techniques study the propagation phenomenon of seismic waves in the medium of interest (Strobbia, 2003). A wave is defined as localised disturbances travelling in a physical medium transmitting energy (Graff, 1975). The application of a force on a body generates stresses and strains which propagate through the body as waves. Based on the material and geometry of the body, different types of waves can be generated – body waves and surface waves. Body wave techniques build on the reflection and refraction of such waves whilst surface wave techniques focus on the dispersive property of surface waves.

2.1.1   Body Waves

Body waves propagate in the interior of the medium in all directions following a spherical geometric distribution (Strobbia, 2003). Their propagation velocities are solely dependent on the elastic stiffness of the medium resulting in two types of body waves namely compressional (primary) and shear (secondary) waves (Figure 2.1). According to Strobbia (2003), body waves attenuate in amplitude proportionally to the distance from the source.
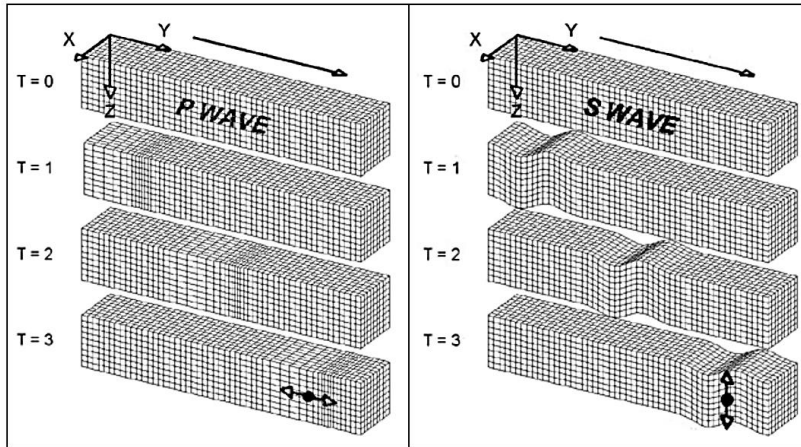
Figure 2.1: Propagation methods of body waves inside the medium (Strobbia, 2003).

Primary waves (P – waves), as they represent the first arrival in seismic records, induce a particle motion parallel to the direction of propagation. The seismic energy is transmitted by both the soil medium as well as the pore fluids (Heymann, 2007). In an elastic medium, the propagation velocity of P- waves (Vp) is given by Equation 2.1.

$$V_P = \sqrt{\frac{(K+4/3\mu)}{\rho}}$$ (Equation 2.1)

where: K = bulk modulus

μ = shear modulus

ρ = mass density

Secondary waves (S -waves) form the second arrival in seismic records and induces a transverse particle motion to the direction of propagation. Polarization of shear waves in a defined direction is possible implying that vertically and horizontally polarised shear waves can be generated individually: shear horizontal waves (SH) or shear vertical waves (SV) (Strobbia, 2003). Jackson and Anderson (1970) stated that through observation of earthquakes, the attenuation of shear waves was greater than compressional waves.

Shear wave velocities (Vs) in elastic mediums can be estimated using Equation 2.2.

$$V_S = \sqrt{\frac{\mu}{\rho}}$$ (Equation 2.2)

Foti (2000) stated that the ratio in the velocities of the P-wave and S-wave (γ) is dependent on the Poisson's ratio (ν) (Equation 2.3). Thus, it could be seen that for any real media, where $0 \leq \nu \leq 0.5$, the compressional wave always travelled faster than the shear wave.

$$\gamma = \frac{Vs}{Vp} = \sqrt{\frac{1-2\nu}{2(1-\nu)}}$$ (Equation 2.3)

Due to the relationships that exist between seismic wave velocities and the elastic geotechnical parameters (Equation 2.1 – Equation 2.3), seismic tests are considered attractive and becoming increasingly popular.

2.1.2 Surface Waves

Wave propagation in mediums bounded by a free surface result in a type of phenomenon where surface waves are generated and travel in shallow zones near the surface. Surface waves originate from a point source and propagate with a cylindrical wavefront distribution with most of their energy concentrated near the surface. Surface waves altogether are only developed in a 'halfspace', which is essentially a structure enclosed by a free boundary and extends infinitely below in all directions (McCaskill, 2014).

Their amplitude distribution is stationary along the horizontal axis and therefore, energy is only spread in the horizontal direction compared to body waves, where energy is spread both horizontally and vertically within the medium. This implies that surface waves experience a lower geometric spreading compared to body waves and do not spread energy into the medium. The energy in surface waves reduces linearly with distance as the cylindrical wavefront on the surface increases (Foti, 2000; Strobbia, 2003).

Essentially, there a two different kinds of surface waves namely Rayleigh waves and Love waves as shown in Figure 2.2.
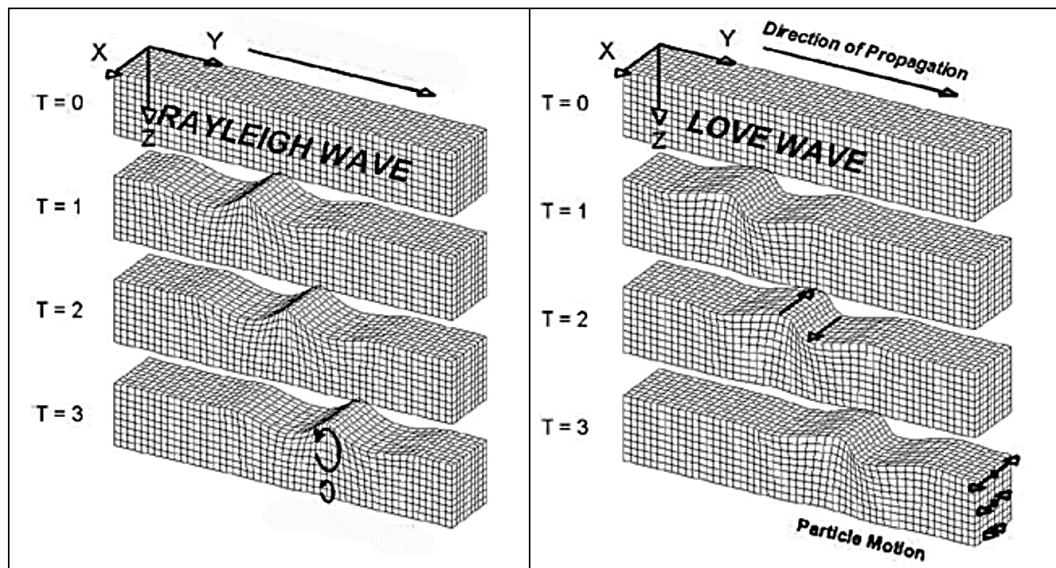
Figure 2.2: Surface waves propagate parallel to the surface of the medium (Strobbia, 2003)

2.1.2.1 Rayleigh Waves

Rayleigh waves generate particle motion in the vertical plane of the direction of propagation with a retrograde elliptical orbit as seen in Figure 2.2 (left). The interaction of combined compression waves and vertically polarized shear waves with the free surface boundary result in the generation of Rayleigh waves (Beaty *et al.*, 2002). Depending on the type of media – homogeneous or heterogeneous media, the decay of the Rayleigh wave amplitude varies. In a homogeneous media, the amplitude tends to decrease exponentially with depth experiencing different rates of decrease in the horizontal and vertical direction. This can be seen in Figure 2.3.
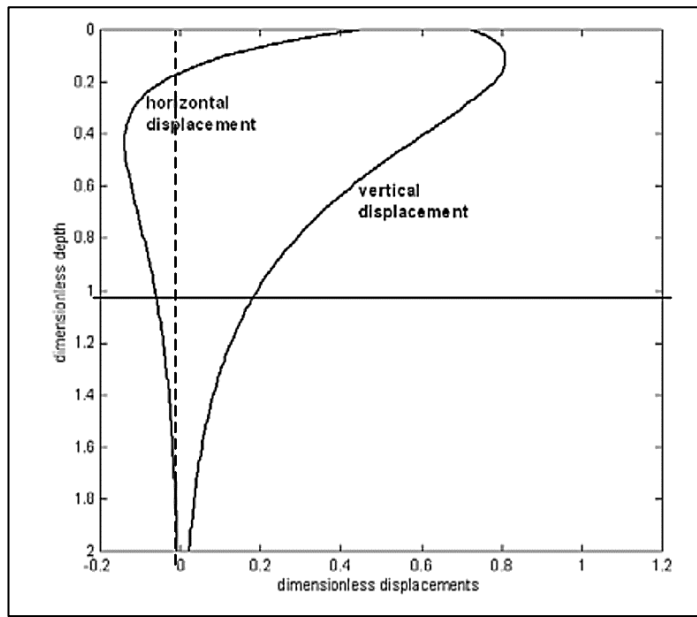
Figure 2.3: Displacements of Rayleigh waves with depth (Strobbia, 2003).

As the displacement components decrease with depth, the direction of the orbit of the Rayleigh wave changes (retrograde to prograde) and this usually occurs at a depth of $\frac{1}{2\pi} \times \lambda$ (wavelength). This depth also corresponds to the depth at which the displacement trajectory subsides into a vertical line. Thus, this implies that only the material properties of the shallow materials, roughly equivalent to one λ influence Rayleigh wave propagation.

The following power rules are used to express the proportion to which the amplitude of the wave decays, where *r* represents the distance from the source (Foti, 2000):

$$\frac{1}{r^n} \quad \text{where } n = \left\{ \begin{array}{ll} 1 & - \text{ for body waves into the medium} \\ 0.5 & - \text{ for Rayleigh waves} \\ 2 & - \text{ for compressional and shear waves located on the surface} \end{array} \right\}$$

From the above power rules, the amplitudes of both body waves and shear waves decay at a greater rate than that of Rayleigh waves. Thus, at a certain distance from the source, the majority of the energy detected by the receivers are that of the Rayleigh waves. Due to this property, many researchers have established surface wave testing based on Rayleigh waves alone (Lin, 2007; Chakraborty *et al.*, 2019).

The energy dissipation of these waves is primarily due to geometrical damping by the radiation of waves increasing with distance from the source (Richart *et al.*, 1970). In most engineering

applications, the soil is assumed to be a perfectly elastic medium, and thus a second mechanism of damping, known as material damping or internal damping, is often neglected completely. Material damping occurs within the skeletal structure of the soil through frictional losses incurred amongst the soil particles themselves as well as through fluid motion within the skeleton (Rix *et al.*, 2000). However, for shallow layers of soil, energy dissipation occurs predominantly through material damping (Ambrosini, 2006).

It should be noted that attenuation laws of the seismic waves are independent of frequency in homogeneous mediums and are frequency dependent in heterogeneous mediums (Rix *et al.*, 2000). The decay of the amplitude of the Rayleigh waves cannot be predicted for vertically heterogeneous media without any prior knowledge of the structure. This is mainly due to the superposition of the different modes of Rayleigh waves where each frequency may have different modes of vibration (Strobbia, 2003; Foti *et al.*, 2018). In homogeneous, isotropic mediums, Rayleigh waves are not dispersive, as their velocities are functions of the mechanical properties of the medium but not the frequency. According to Strobbia (2003), the Rayleigh wave velocity (V_R) is strongly dependent on the shear wave velocity (Vs) as well as the Poisson's ratio (ν).

Figure 2.4 shows the ratio between P-wave velocities and S-wave velocities as well as the ratio between V_R and Vs against the Poisson's ratio.
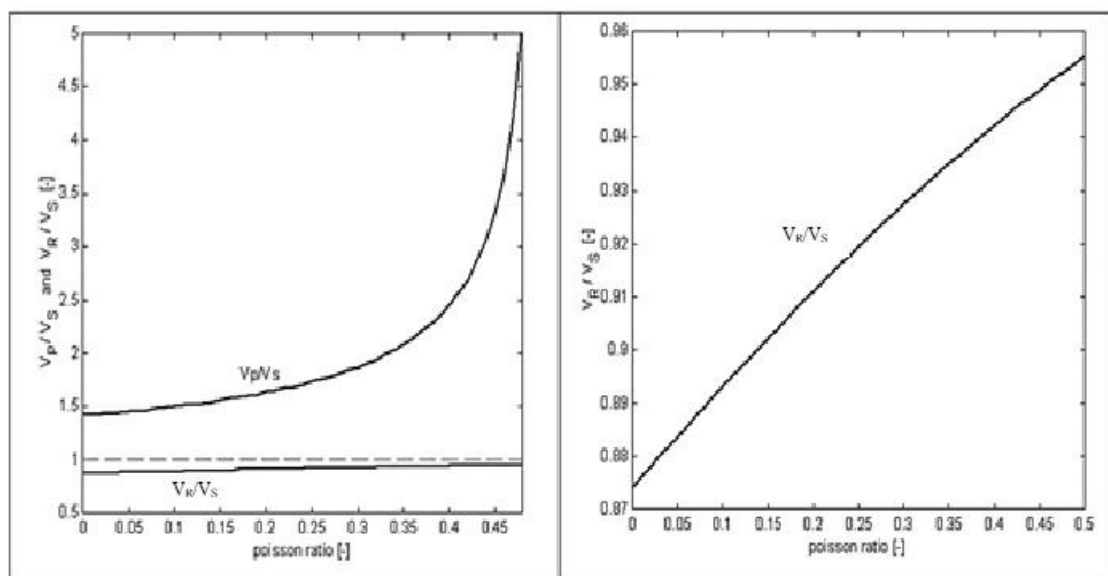
Figure 2.4: Ratio of Vp/Vs and V_R/Vs against the Poisson's ratio (ν) (Strobbia, 2003).

From Figure 2.4 (left), it could be seen that the minimum ratio between Vp and Vs is $\sqrt{2}$ and as ν approaches 0.5, this ratio tends to infinity implying that in such cases the Vs approaches zero. The ratio between V_R and Vs shows a small variation with increase in the ν, and this implied that the V_R could be used to estimate the shear wave velocity to a considerable degree of accuracy with a maximum error of 10 % due to a wrong assumption in the ν. According to Lin (2007), by reasonably estimating the ν (0.2 – 0.4), the error in the estimated Vs reduces to less than 5 %. The range given by Lin (2007) is:

$$0.874 < \frac{V_R}{V_S} < 0.955$$

Due to different segments of soil being sampled in heterogeneous mediums, different wavelengths sample each of the layers resulting in geometric dispersion (Figure 2.5). This dispersion is due to a variation in the elastic properties of each of the layers. This dispersive phenomenon only results in layered media and not in homogenous bodies where all frequencies produce the same velocity. Greater wavelengths, which are generated at low frequencies, are governed by deeper layers whilst shorter wavelengths are only affected by the shallower layers (Strobbia, 2003).
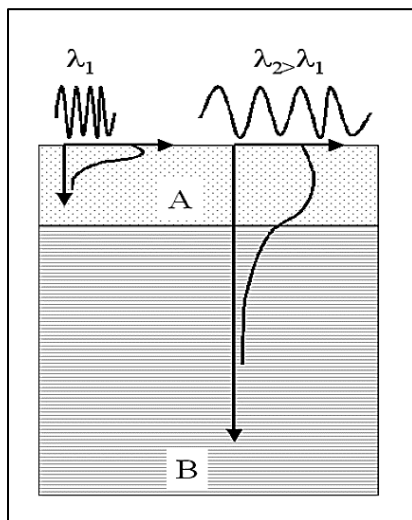
Figure 2.5: Geometric dispersion in a heterogeneous body (Strobbia, 2003).

2.1.2.2 Love Waves

Love waves induce polarized motion of particles perpendicular to the direction of propagation on planes parallel to the ground surface. They were first discovered through long distance

seismograms, which displayed two phases - the preliminary tremor and the main shock. It was thought at first that the main shock consisted of mainly Rayleigh waves, as the velocities of the higher amplitude waves were close to that of Rayleigh waves. However, the shear horizontal component of the earthquake vibrations was not explained by the definition of Rayleigh surface waves which consisted of shear vertical and longitudinal components. Thus, this led to the discovery of Love waves, which contained only one shear horizontal component of vibration (Kielczyński, 2018).

Love waves are only present in layered bodies (heterogeneous mediums), as such waves require a surface waveguide to propagate, which is composed of a surface layer fixed to an elastic substrate as shown in Figure 2.6.
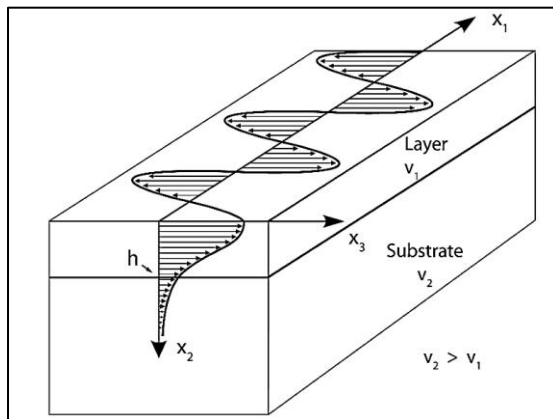
Figure 2.6: Fundamental waveguide structure required for Love wave propagation (Kiełczyński, 2018).

Along with the existence of the surface waveguide structure, the surface layer is required to hold the following condition:

$$v_1 < v_2$$

where v_1 and v_2 are defined as the bulk shear wave phase velocities in the surface layer and substrate, respectively. The above condition allows total reflection of the partial waves at the interface ($x_2 = h$) entrapping any partial waves in the surface layer. In the case where $v_1 > v_2$, the partial waves vanish in the direction of propagation (x_1) resulting in zero net power being transmitted along the surface (Kiełczyński, 2018).

Love surface waves are dispersive as their phase velocities are a function of the frequency. Their dispersive equation (Equation 2.4) contains a tangent function which is periodic (*tan(h) = tan (h + nπ) where n = 0,1,2, etc.*), implying that they exhibit multimodal nature. However, Love waves are less subjected to generate higher modes compared to Rayleigh waves in most geological environments (Safani *et al.*, 2005).

$$F[\omega, k(\omega)] = \mu_1 q_1 \tan(q_1 h) - \mu_2 q_2 = 0 \qquad \text{(Equation 2.4)}$$

where ω = angular frequency of wave

k = wavenumber of Love wave

μ_1, μ_2 = shear moduli of surface layer and substrate respectively

q_1, q_1 = functions of the wavenumber (k)

h = thickness of the surface layer

Kiełczyński (2018) investigated the decay of the amplitude of the fundamental Love wave mode (n = 0) using a copper-steel waveguide for different wave frequencies using a thickness of 100 μm for the surface layer. The results of his experiment are shown on a normalized plot in Figure 2.7.
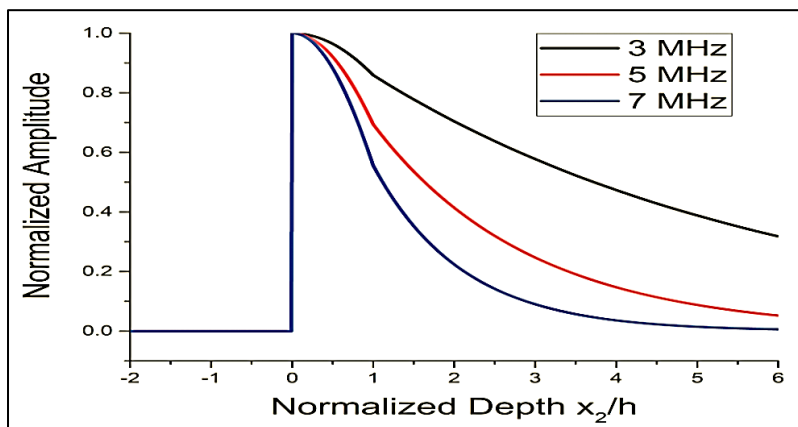
Figure 2.7: Amplitude decay of Love wave (n = 0) for different frequencies in a copper-steel waveguide (Kiełczyński, 2018).

From Figure 2.7, it was evident that higher frequency Love waves experienced a greater rate of decay in their amplitudes and therefore, more of the energy was concentrated in the locality of the surface. It was also shown that the maximum amplitude occurred at the free surface where $x_2 = 0$. Mitchell *et al.* (1976) compared the spectral amplitude plots of the fundamental and first higher mode surface waves to explore their attenuation over a period for an earthquake that occurred underneath the Pacific Ocean (Figure 2.8). The plots indicated larger amplitudes of Love waves compared to Rayleigh waves for both modes. Whilst the Rayleigh wave spectral amplitudes decayed in a similar pattern for both modes, the Love wave spectral amplitudes decayed at different rates for each mode. It was observed that the spectral amplitude of the fundamental mode Love wave was fairly constant at all periods.
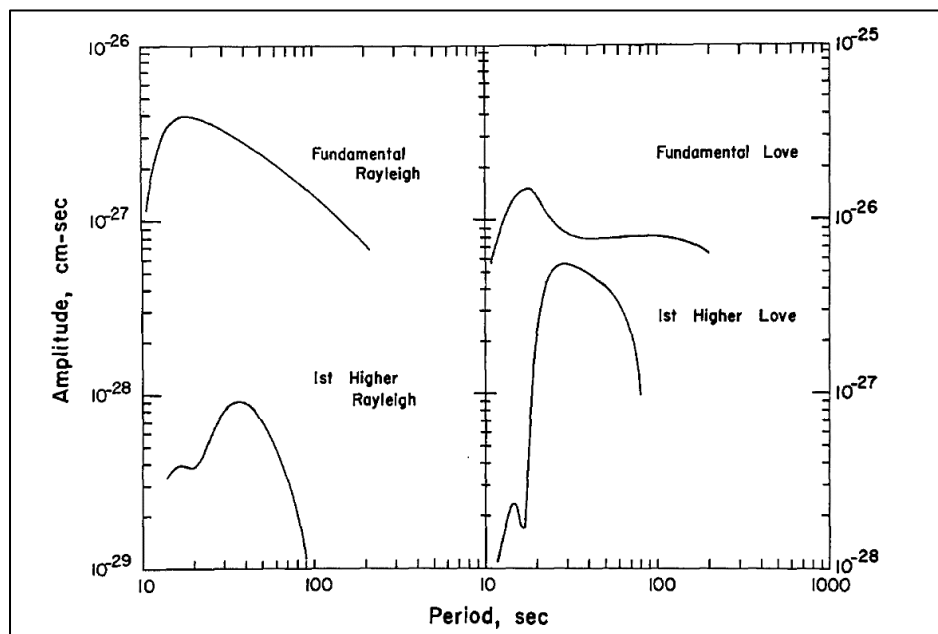
Figure 2.8: Spectral amplitude plots of fundamental and first higher mode Rayleigh and Love wave for earthquake on April 26, 1973 near Hilo, Hawaii (Mitchell *et al.*, 1976).

Love wave velocities have a variant property which is dependent on the frequency at which the surface wave propagates. Kiełczyński (2018) studied the behaviour of a range of phase velocities and group velocities of the fundamental mode Love wave (n = 0) of different frequencies in a copper-stainless steel waveguide as shown in Figure 2.9. The group velocity is defined as the velocity at which the surging impulse of the wave propagates (Kiełczyński, 2018). Only in non-dispersive mediums is the group velocity and phase velocity coincident with one another (Strobbia, 2003).
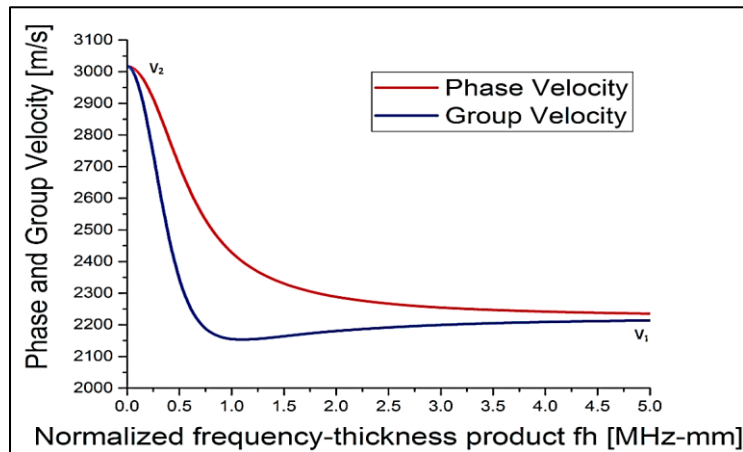
Figure 2.9: Phase and Group velocities of Love wave (n = 0) relationship at different normalized frequency thicknesses in a copper-stainless steel waveguide (Kiełczyński, 2018).

Figure 2.9 illustrates that at low frequencies both velocities approach asymptotically to the shear wave velocity of the substrate, that is $v_2 = 3017$ m/s. Contrarily, at higher frequencies, the phase and group velocities approached the shear wave velocity in the surface layer ($v_1 = 2224$ m/s).

It should be noted that a third class of surface waves exists at interfaces where a discontinuity occurs. Surface waves such as the Scholte waves (earth/water interface) and Stoneley waves fall under this class and were observed to attenuate rapidly as one moved away from the discontinuity (Foti *et al.*, 2018). Graff (1975) stated that these interface waves only existed at specific stiffness ratios between the two adjacent layers.

2.1.3 Geometric Dispersion

Surface waves show a dispersive phenomenon in stratified media which makes them useful for geotechnical characterization (Park *et al.*, 1998). Particle motions as well as deformations are produced at different depths below the surface, depending on the wavelengths (λ) of the surface waves. If the mechanical properties in each layer of the heterogenous body vary, different wavelengths propagate at different phase velocities depending on the combination of the density (ρ) and elastic properties of the layers in the body. This is known as geometric dispersion and the distribution plot of the phase velocities as functions of the frequencies is referred to as a dispersion curve (Foti *et al*., 2018). The dispersion curve can be plotted in three different domains as shown in Figure 2.10.
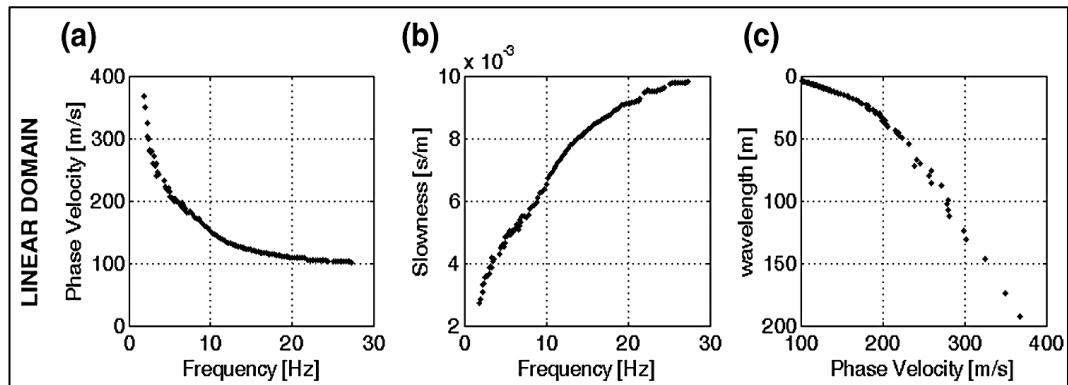
Figure 2.10: Dispersion curves in different linear domains: a) phase velocity-frequency domain b) slowness- frequency domain c) wavelength – phase velocity domain (Foti *et al*., 2018).

Through visual inspection of dispersion curves, it is possible to comment on the anticipated shear wave profile. For simple stratigraphic profiles where the ρ and Vs increases with depth, a smooth continuous decrease in the phase velocity with increasing frequency is typically observed (normally dispersive). Dispersion curves with kinks suggest the existence of inverse layers (a softer layer beneath a stiffer layer - inversely dispersive), which are typically found in pavement sites (Figure 2.11). Through observation, normally dispersive sites experience higher phase velocities for lower frequencies (long wavelengths) compared to higher frequencies (short wavelengths) and the opposite is true for an inversely dispersive site (Lin, 2007). Figure 2.12 shows the waveforms for two different dispersive geotechnical sites, illustrating the concept mentioned.
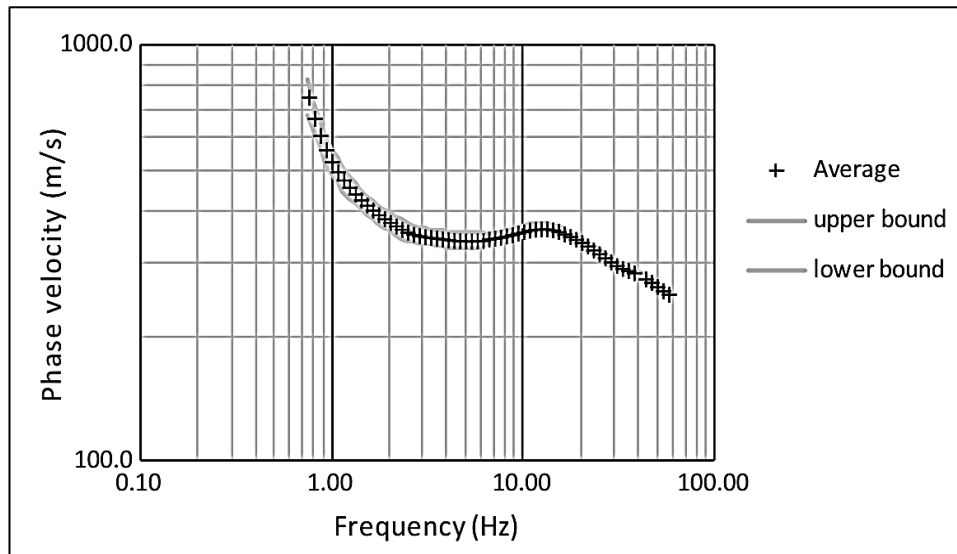
Figure 2.11: Dispersion curve for a profile with an inverse layer- a soft layer of clay in a stiffer deposit (Foti *et al*., 2018).
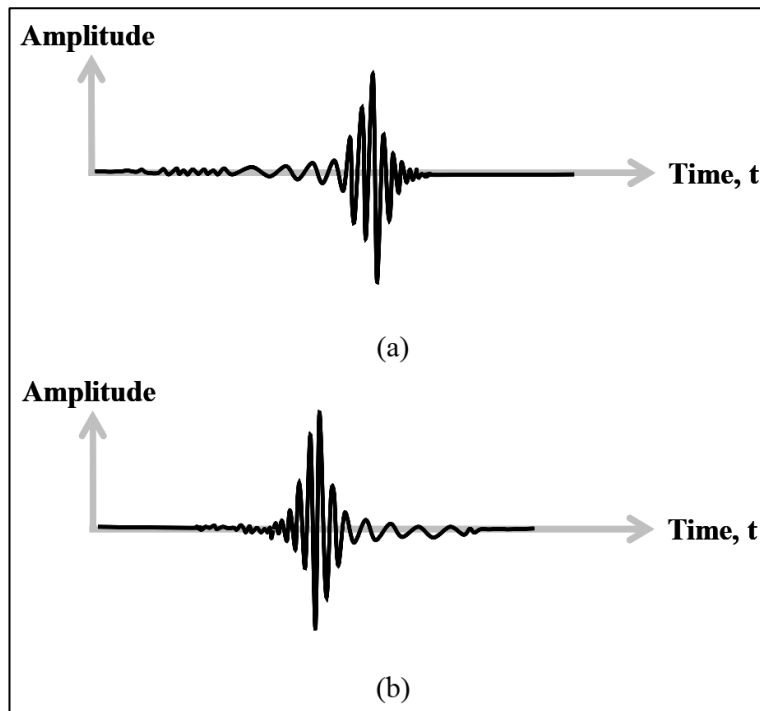
Figure 2.12: Comparison of arrival of different frequency waves for a) Normally Dispersive Site b) Inversely Dispersive Site (Lin, 2007).

2.1.4 Modes of Vibration

Multimodal waves occur due to a phenomenon that exists when surface waves propagate in stratified mediums: at frequencies past a cut off frequency, different modes of vibrations are experienced. The modes are differentiated from one another using their propagation velocities and are ranked from the fundamental mode to higher modes. Higher modes are also referred to as overtones (Foti *et al*., 2018).

In a stratified body, waves are reflected at each of the layer interfaces. These reflected waves undergo constructive interference which leads to the generation of higher modes of surface waves. The number of modes produced during each propagation as well as the exact value of the cut off frequency at which this phenomenon occurs is provided by the free vibration problem to each scenario. As each mode carries different amounts of energy, not all modes achieve an 'excited' level and therefore, these modes remain undetected. Specific frequency bands also exhibit the strong presence of certain modes within the band. This is due to the energy distribution of modes being dependent on the frequency of the modes (Foti *et al*., 2018).

For most seismic surface wave tests, the fundamental mode is utilized for characterizing the geotechnical body. However, this is not the actual case as surface wave seismic tests always generate higher modes and may possess considerable amounts of energy (Stokoe *et al.*, 1994). Higher modes of vibration tend to be more significant towards the higher frequency regions, which are often incurred in surface wave seismic tests (Tokimatsu *et al.*, 1992). According to De Nil (2005), ignoring higher modes leads to inaccurate dispersion curves for inversely dispersive profiles, often overestimating the Vs values at shallow depths. In such profiles, the layers display sharp variations in the Vs (300 % or greater) due to interfaces of low-velocity layers and bedrock or lower velocity layers sandwiched between two high velocity layers. However, for normally dispersive profiles, where there is an increase in the Vs with depth, the dispersion curve is dominated by the fundamental mode alone and therefore the higher modes are not considered during the inversion process (Tokimatsu *et al.*, 1992). During circumstances where higher modes are generated, there is an energy transfer between the different modes at specific frequencies, known as osculation frequencies, where successive modes have identical V_S allowing this interchange (Foti *et al*., 2018). To superimpose these modes, the different modes are firstly to be identified and separated as misinterpretation of the modes may lead to flawed conclusions and designs (Park *et al.*, 1998). With regards to resolution of the different modes of vibration, two cases were proposed by Tokimatsu *et al.* (1992):

1) The fundamental mode and its significant higher modes are identified separately and therefore the phase velocities from each mode could be determined individually.

2) A failure to identify and separate the fundamental mode and its significant higher modes, therefore only the apparent phase velocity from the superposition of all the different modes of vibration is extractable.

To achieve a Case 1 scenario, long array dimensions with many sensors are required. Based on this experimental approach, Gabriels *et al.* (1987) deployed 24 sensors over a long array, achieving a mode resolution of the fundamental mode and the first six higher modes within a frequency range of 5 Hz to 30 Hz. However, when a pair of sensors where placed a few meters apart from one another, a dispersion curve in the same frequency range was attainable, although any higher modes were not distinguishable from the fundamental mode due to superposition of the modes (Stokoe and Nazarian, 1985).

Rosenblad and Bertel (2008) presented an implicit approach to determine whether a Vs profile exhibited higher mode transitions or not. They observed that frequencies at which a mode transition was observed was significantly influenced by the thickness and the velocity of each respective layer and the transition frequency could be estimated from the shear wave resonant frequency (f_{rs}) of all the soft layers over the half space (Equation 2.5). A Vs ratio was initially calculated by Rosenblad and Bertel (2008), with a Vs ratio of less than 2.5 indicating no higher mode transitions present in the profile and vice versa. This ratio was obtained by dividing the velocity of the half space layer by the average Vs of all the surface layers calculated using Equation 2.6.

$$f_{rs} = \frac{\overline{V_S}}{4H} \qquad\qquad \text{(Equation 2.5)}$$

where: f_{rs} = resonant frequency of shear wave

$\overline{V_S}$ = average shear wave velocity

H = total thickness of soft layers above half space

$$\overline{V_S} = \sum_1^n d_i \,/\, \sum_1^n \frac{d_i}{V_{si}} \qquad\qquad \text{(Equation 2.6)}$$

where: $\overline{V_S}$ = average shear wave velocity

$d_i =$ thickness of surface layer i

$V_{Si} =$ shear wave velocity of surface layer i

2.1.5 Near field effects

The near field effects occur at distances less than a specific wavelength (λ) in the vicinity of the point source of the wave propagation. Depending on the soil profile, this distance varies from 1.5λ - 2λ (Sanchez-Salinero, 1987; Tokimatsu, 1997). Within the near field, the propagation theory of surface waves deviates resulting in biased phase velocities (underestimate the phase velocity) due to coupling of both spherical and cylindrical wave fronts in the near field. Any error in the seismic tests that results due the near field is known as the near field effect (Yoon and Rix, 2009; Foti *et al.*, 2018). Another definition of the near field area are regions close to the source where the surface wave fronts are not planar (Yoon and Rix, 2009). For this study, the former definition will be used. By observing vibrations at multiple offsets from the source during surface wave tests, the influence of the near field can be evaluated allowing the surveyor to estimate the near field region (Wood and Cox, 2012).

An extensive amount of research exists on the criteria employed for filtering out the near field effects during surface wave test. However, most of the recommended filtering criterion were solely based on SASW numerical simulations. A few were established from actual SASW experimental data such as that of Hiltunen and Woods (1990) as shown in Table 2.1, where x_1 was the source to first receiver offset, λ_R was the Rayleigh wavelength and Δx was the spacing between the two receivers.

Table 2.1: Synopsis of filtering criterion for Near Field effects using SASW Method (Yoon and Rix, 2009).

Reference	Filtering criterion	Receiver configuration	Method of study
Heisey *et al.* (1982)	$x_1/\lambda_R > 1/3$	$\Delta x/x_1 = 1$	Numerical
Sánchez-Salinero *et al.* (1987)	$x_1/\lambda_R > 2^a$	$\Delta x/x_1 = 1$	Numerical
Roesset *et al.* (1990)	$x_1/\lambda_R > 1/2$	$\Delta x/x_1 = 0.2\text{-}2$	Numerical
Hiltunen and Woods (1990)	$x_1/\lambda_R > 1/2$	$\Delta x/x_1 = 1$	Experimental
Gucunski and Woods (1992)	$x_1/\lambda_R > 1$	$\Delta x/x_1 = 1$	Numerical
Al-Hunaidi (1993)	N/A	$\Delta x/x_1 = 1$	Numerical

[a]It was also recommended that the criterion of $x_1/\lambda_R > 1$ could be used if more data were required in the low-frequency range.

Although various source offset distances have been proposed by different researchers, the extent to which the near field affects the dispersive properties tends to be site dependent (Wood and Cox, 2012). According to Yoon and Rix (2009), near field effects become more significant in profiles with intricate wave fields such as irregular soil profiles displaying both cases of underestimation and overestimation of the phase velocities. Profiles with homogeneous half spaces and regular structures do not suffer from the near field effects substantially (small degree of errors) when compared to irregular profiles.

Most commercial surface wave software's use a 'plane wave' model where the wave field consists of only planar surface wave components (far-field). This is the case for passive sources (microtremors) due to the distant sources. However, active sources are often positioned close to the receivers and these receivers may fall within the near field vicinity of the source. Within the near field, the wave fields tend to be relatively complex due to difficulty in separating the two wave fronts. However, as the train of waves propagate past the near field, the body wave components (spherical wave fronts) attenuate to negligible values (Foti *et al.*, 2014). A few studies have suggested that by increasing the number of receivers, the dispersion properties are less vulnerable to the effects of the near field (Tokimatsu, 1997; Hebeler and Rix, 2007).

2.2   SURFACE WAVE ANALYSIS

The aim of the surface wave analysis is to find the shear wave velocity (Vs) profile by using the experimental dispersion curve to find solutions to the inverse problem of parameters used

in the seismic model. Essentially, the analysis is conducted in three interconnected steps (Figure 2.13):

1) **Acquisition** of surface wave data
2) **Processing** of signals to generate experimental dispersion curve
3) **Inversion** of problem based on optimization of model parameters
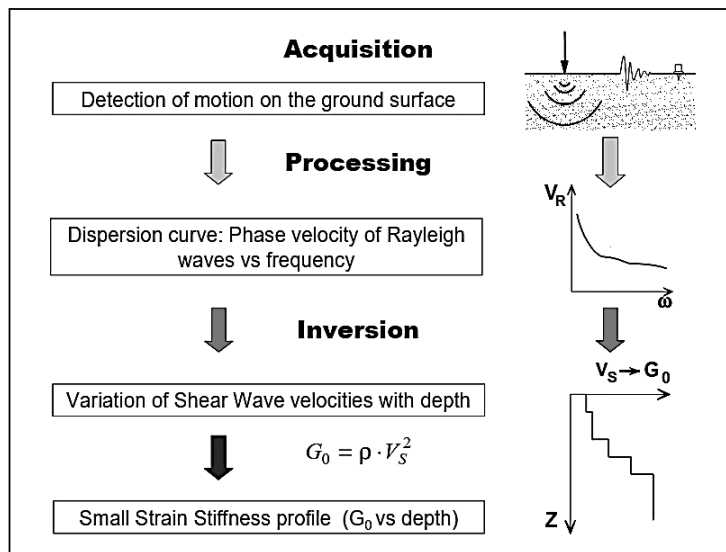
Figure 2.13: Conceptual flow of surface wave analysis procedures (Foti, 2005).

2.3   ACQUISITION

Before conducting tests, the surveyor must be acquainted with the depth of investigation as well as the objectives of the investigation. These objectives allow the selection of the equipment and testing strategies that are implemented to acquire the data. A typical situation consists of several receivers (minimum of two) that are arranged in varying configurations/arrays to detect and collect timed ground motion readings, which are generated from a source (Strobbia, 2003).

The acquisition process is considered as one on the most important aspects of surface wave testing as the quality of the acquisition directly influences the results. A difficulty that is often faced during this step is obtaining a recording with a high signal to noise ratio (SNR) over the whole frequency the analysis is conducted. During the generation of surface waves, external noise occurrences are often present and along with inherent observation margins; these two

often limit the acquisition process (Strobbia, 2003). The limitations are discussed in detail in the forthcoming sections.

Acquisition techniques can be split into two, namely active and passive techniques. Both techniques may be implemented together to assemble data, however each technique has its own limitations.

2.3.1 Active Measurements

This involves the generation of seismic waves externally using artificial means (active sources) which are then recorded by a number of receivers aligned in line with the source. Most commercial surface waves testing methods fall under this category; each differing in the source type, number of receivers and layout configuration. The following subsections will review these aspects which govern the active acquisition stage.

2.3.1.1 Testing Equipment

- **Seismic source** – the purpose of the seismic source is to administer seismic energy to generate surface waves in the medium at an acceptable signal to noise ratio over the targeted frequency range. The frequency range the source is to target is often estimated beforehand by considering the velocities expected at a site, as softer layers have lower velocities compared to stiffer layers. The depth at which a source is positioned also affects the energy distribution within the different modes and frequency bands. According to Strobbia (2003), a buried source was better at producing more information at lower frequencies compared to a source placed on the surface.

  Commercial surface wave tests usually implement either vertical impact sources or vertical shakers. Impact sources range from ordinary sledgehammers, which are either launched straight onto the ground or hit on a plate constructed of a certain material to increase the frequency, to heavy sources such as weight drops. Most impulsive sources are fitted with trigger systems which act as inertia switches which starts the recording of the signals (Strobbia, 2003). Depending on the weights of impact sources the investigation depths are restricted. Lighter sources are usually used to sample high frequency dispersion data (shallow characterization) whilst heavier sources sample lower frequency dispersion data. Impact sources lack control over the frequency bands at which energy is dispensed as well as difficulty in producing high signal-to-noise ratios over the required band leading to

dispersion uncertainty. Despite this they are popular due to being the cheapest options available and different energy sources could be superimposed to compensate the target depths that can be achieved by each source (Foti *et al*., 2018). Figure 2.14 compares the energy distribution for different impact sources with receivers 3 m away from the source.
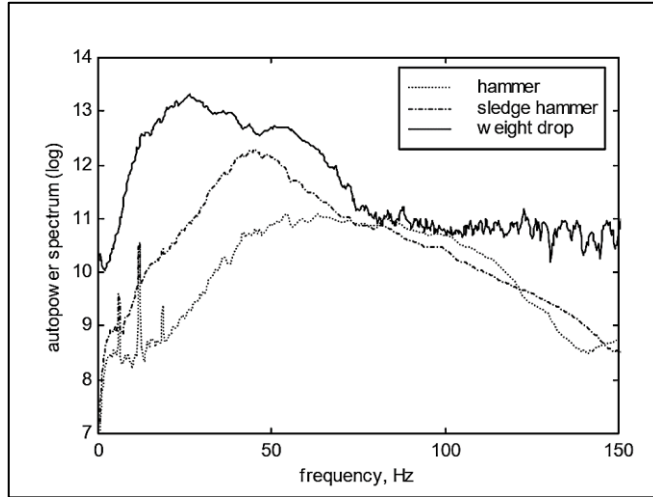
Figure 2.14: Energy distribution over frequency domain for different impact sources (Foti, 2000).

Shakers/vibrators proved to be beneficial in the seismic surface wave industry as they could accurately control the frequency bands of the vibrating impulse as well as provide high signal to noise ratios within the selected frequency band procured. These vertical shakers are propelled by signal generators which allow the generation of harmonic signals or transient signals, thereby producing higher quality signals. Controlled sources are available in different forms varying from electromagnetic shakers to truck mounted vibroseis.

1.1 Sweep signals (Transient signals)

Sweeps are used to produce and record wide ranges of frequencies over a short period of time. Transient signals are essentially non-stationary functions with the form shown in Equation 2.7:

$$A = A(t) * \sin(2\pi f + \varphi) \hspace{2cm} \text{(Equation 2.7)}$$

Different sweeps, such as linear sweeps, quadratic sweeps and logarithmic sweeps can be applied using a shaker. It is important to note that the amplitude observed over a swept

frequency could be different over a wide range of frequencies when represented in the time domain window. Due to this phenomenon, the signal to noise ratio in transient signals experience different amplitudes over the frequency bands as well. Thus, a difficulty that could be faced is that of experiencing low S/N ratios in certain frequencies. Figure 2.15 shows a time frequency analysis of a linear sweep that was conducted for 15 s for frequency ranges 5 Hz to 40 Hz.
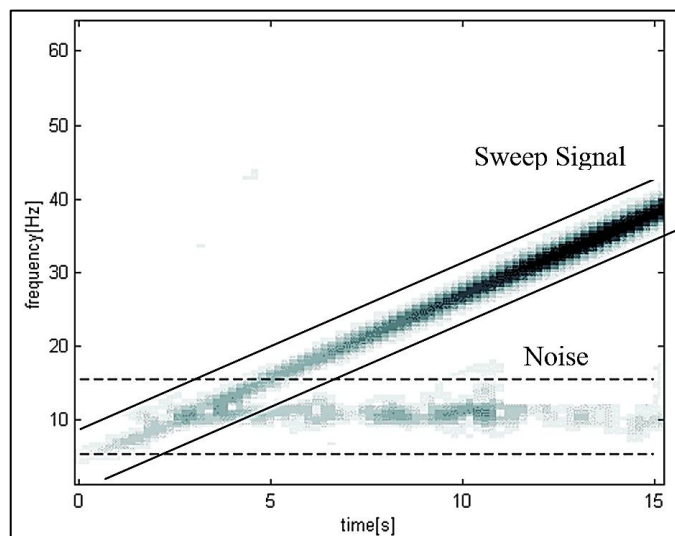
Figure 2.15: Analysis under time frequency domain for a linear sweep between 5 Hz and 40 Hz (Strobbia, 2003).

At low frequencies of 10 Hz and below 4 seconds, it could be observed that the noise levels were higher than the transient signal. Strobbia (2003) suggested that this was due to the duration of the signals being limited compared to the noise signals which acted over the entire interval. Thus, this implied that the S/N ratio was highly dependent on the durations of both signals and was greatly reduced when the durations differ, leading to the possibility of distorted information at low frequencies.

1.2 Steady State signals (Harmonic signals)

An alternative approach is the application of a set of harmonic signals (single frequency), with each signal having a constant amplitude over the entire interval. For the construction of the dispersion curve, only specific frequencies are considered at which the recorded signals are discretised. The different steady state signals from each individual record could then be stacked in the same file in the frequency amplitude domain, where the amplitude

represents the velocity at which the geophones (receivers) vibrate. This is shown in Figure 2.16.
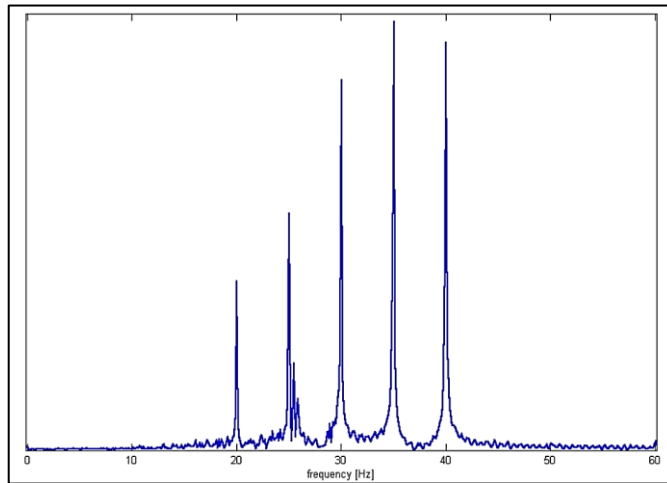
Figure 2.16: Stacking of 5 harmonic signals (20, 25, 30, 35 and 40 Hz) (Strobbia, 2003).

However, the stacking process often leads to deterioration of the S/N ratio for each individual record as the noise for a single record appears to affect the entire stacked record. To enhance the signals, Strobbia (2003) proposed that longer records be procured as the S/N ratio tends to increase with the record length. He further put forward the technique of internal stacking where a signal trace was divided into equal sections of an integer value of the period of frequency that was to be enhanced. This led to the generation of synchronised signals and allowed the selection of sections with reduced noise levels. Triggering systems, such as contact closures are typically employed during the acquisition stage, when stacking of the records is necessary (Foti *et al*., 2018).

- **Seismic sensors** –transducers that detect the generated vibrations, such as geophones are used for the acquisition of the surface wave data. The type of geophones to be used are selected based on the depth of investigation. Geophones are used to measure the particle velocity using a permanent magnet that is fixed firmly to its casing. Within the magnetic field of the magnet, a small electric coil system is contained along with a shunt resistor, that absorbs any undesirable source energy (Figure 2.17). On arrival of the vibrational energy, displacements are induced at the base of the geophones. Due to inertial forces of the suspended coil system, the coil moves relative to the permanent magnet, generating small voltages proportional to the velocity of motion (Strobbia, 2003).
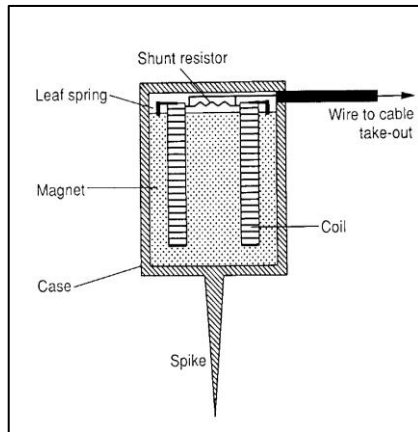
Figure 2.17: Construction layout of a typical geophone (Doyle, 1995).

Geophones are selected based on their natural frequency of vibration (resonance) as their response rates are dependent over the frequency range at which they operate. To maintain a flat response rate over the interested frequency range, it is necessary to acquire geophones, where the interested frequency range lies above the resonant frequency of the geophone. This is outlined in Figure 2.18, which shows a typical geophone response plot.
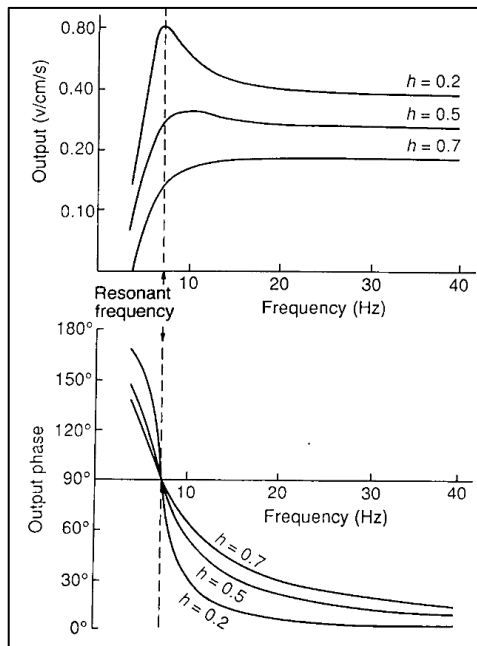
Figure 2.18: Geophone response plot (Doyle, 1995).

From Figure 2.18, it could be seen that the geophone displayed a non-linear response for frequencies below its resonant frequency and underwent a 180° phase shift at the resonant frequency. This leads to phase distortion errors for frequencies below the resonant frequency when the geophones are not ideally paired. However, this error could be mitigated by using several geophones in the array (Foti *et al*., 2018). According to Strobbia (2003), the maximum response occurred when the suspended coil aligned parallel to the direction of the vibration. Thus, both vertical and horizontal geophones are available.

Damping of the response curves to allow for flat response rates is usually facilitated by the shunt resistors installed across the terminals of the geophone. The shunt resistor influences the current flowing in the coils producing a magnetic field that counteracts the movement of the coil system, resulting in a damping effect. Damping factors between 0.6 and 0.7 are typically advised when selecting shunt resistors to conservatively flatten any amplitudes above the resonant frequency (Strobbia, 2003).

The natural frequency of vibration of the geophone (T_0) can be determined using Equation 2.8.

$$T_0 = 2\pi\sqrt{\frac{m}{k}}$$
(Equation 2.8)

where: m = mass of the suspended body

k = material spring constant

Low frequency geophones are often used for geotechnical surface wave testing. Equation 2.8 dictates that for low frequency geophones, a larger mass is a prerequisite, thereby requiring higher sensitivities and making such geophones expensive. Foti *et al*. (2018) suggested that 4.5 Hz resonant frequency geophones were usually suitable for 30 m explorations.

Before testing, the geophones are required to be coupled to the ground using spikes and by stripping off the uppermost layer from beneath the geophones. If the geophones are to be planted on hard pavements, a steel base plate may be utilised for coupling the geophones. Signals detected from geophones installed using spikes were very similar when compared to signals acquired using geophones laid on base plates. However, by introducing a connecting system (e.g. metal plate), an extra resonant frequency of the connecting system can be experienced, and this often appeared as a ringing in each signal (Strobbia, 2003).

- **Acquisition device** – the digitization of the analogous signal output from the seismic sensors is facilitated by such devices. These include seismographs, digital signal analysers and digital data loggers. Digital signal analysers allow real-time processing of the signals, thereby deeming attractive to surface wave testing as evaluation of the signal quality and preliminary checks can all be done on site. However, as they were designed to be utilized in laboratory conditions, they tend to suffer from lack of robustness on site and require additional setup efforts. For classical body wave seismic tests, seismographs are often used although they could be employed in surface wave testing provided their cut off frequency is selected correctly. As seismographs are designed for field use, they perform well with the only limitation being that of their acquisition software. The acquisition software for seismographs is often aimed at dealing with seismic refraction and reflection data, and therefore requiring visual inspections of the signals for a preliminary check. However, newer generation seismographs can process preliminary data though they tend to be expensive. Under budget constraints, digital data loggers, which have onboard acquisition boards can be used with the aid of PCs or laptops. An advantage of data loggers is that the acquisition software installed in these loggers can accommodate requirements for surface wave tests as well as provide onsite processing of the signals (Foti, 2005).

2.3.1.2 Testing Configuration

The sampling parameters which influence the acquisition process are dependent on both time and space. In the previous subsection, the testing equipment which affect the acquisition time were discussed. The spatial component in acquisition is influenced by the geometrical layout (Figure 2.19), which is based on the array length (L), the receiver spacing (ΔX) as well as the offset from the source. These parameters are discussed in the following subsections.
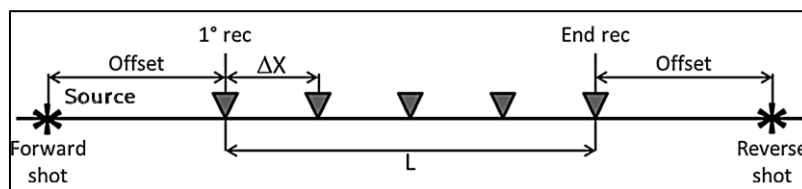
Figure 2.19: Active acquisition typical geometry layout and components (Foti *et al*., 2018).

- **Array Length (L)** – this is responsible for the sampling of adequately long wavelengths, which correspond to the lower frequency components of a propagation, as well as

influencing the resolution of the spectrum. However, this originates from a spectral analysis definition and implies that the maximum wavelength that can be analysed is fully dependent on the array length (longer array length required for deep characterization). Contrary to this, short array lengths are still implemented in surface wave tests, and this is because the maximum wavelength is strongly dependent on the site conditions and the frequencies at which propagation occurs (Strobbia, 2003).

The maximum wavelength can be calculated by considering the trace signals recorded by two receivers and computing the phase velocity using the time shift between the traces. Provided that the signals are harmonic, Equation 2.9 can be used to derive the maximum wavelength (λ_{max}) for a fixed frequency (Strobbia, 2003).

$$\lambda_{max} = \frac{\Delta X}{f \cdot \Delta t} \qquad \text{(Equation 2.9)}$$

where: ΔX = trace spacing

f = fixed frequency

Δt = sampling rate

Foti *et al*. (2018) suggested, as a rule of thumb, the array length should be at the very least be equal to twice the investigation depth (z) when using array-based processing techniques.

Therefore, this implies that the processing technique influences the effect the array length (L) has on λ_{max}. If the signals acquired are harmonic and phase differences are used to process the data, the array length does not limit the λ_{max}. According to Equation 2.9, λ_{max} can be increased by logging faster that is $\Delta t \to 0$. However, when using array-based processing techniques such as MASW, the λ_{max} is limited by the array length.

- **Receiver spacing (ΔX)** – for identifying the properties of the first layer, the minimum wavelength becomes crucial as it is associated with higher frequencies. The smallest wavelength that can be recorded is affected by the spacing of the receivers and ΔX should be adequate to accommodate such short wavelengths. Shannon-Nyquist sampling theorem suggested that for signals where the wavelength falls below $2\Delta X$, aliasing of the signals can occur, leading to incorrect interpretation of the dispersion curve especially when higher modes are involved. Foti *et al*. (2018) suggested a range of 0.5 m to 4 m for ΔX for near surface characterization purposes.

- **Receiver numbers** – the number of receivers is primarily chosen by the availability of equipment but is prescribed by the ratio between the array length and the spacing of the receivers. Furthermore, depending on the processing technique, the number of geophones used can vary. At the very least, only two receivers are required for surface wave test methods that incorporate phase difference processing techniques, such as that of SASW (Spectral analysis of Surface Waves) method. Foti *et al*. (2018) recommended a minimum number of 24 receivers to be employed when using array-based processing techniques, as done with Multichannel analysis of Surface Waves (MASW) method, to ensure an adequate sampling of both shallow structures as well as greater depths.

- **Source offset –** this dictates the distance between the first receiver and the source and is off importance in correcting 'near field effects which nullify the hypothesis of plane waves in the close vicinity of the source, as mentioned before. Thus, this requires a large offset but by doing so, higher frequency components are lost due to their attenuation in the far field. Foti *et al*. (2018) recommended a source offset value of three to five times that of the receiver spacing, provided that the source can meet the signal to noise ratio of the outmost receiver.

Strobbia (2003) suggested that to prevent the loss of higher frequency information, a considerably small offset should be used, and any signal affected by the near field effects should be screened and disregarded. He illustrated the importance of near field frequencies using Figure 2.20, where two data sets with the exact layout except for the source offsets were plotted in the frequency-wavenumber (f-k) spectra. A source offset of 2 m (Figure 2.20 left) and of 12 m (Figure 2.20 right) was used for the first and second cases respectively.
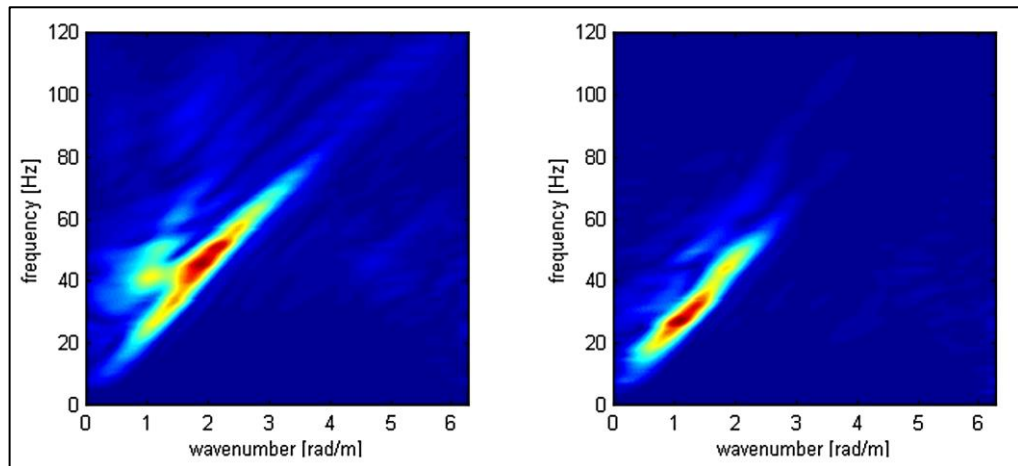
Figure 2.20: f-k spectra of two data sets at same site and layout but with different source offsets: left spectrum has a 2 m offset and right spectrum has a 12 m offset (Strobbia, 2003).

It can be seen from Figure 2.20 that a shorter offset sampled more higher frequencies than that sampled from a longer offset. The first mode could also be seen to follow higher frequencies in the Figure 2.20 (left) although a greater amount of noise was experienced in this high frequency zone.

To identify any lateral variations in the test medium, two end shots of either side of the array are conducted by simply moving the source on opposite sides of the array. According to Foti (2005), this should be made a common routine for every seismic test. The experimental dispersion curves obtained from the forward and reverse shots should be significantly similar (independent) when the stratified medium is subjected to surface wave energy. However, the existence of lateral variations causes the experimental dispersion curves to vary from either side due to their differences in the energy distributions as well as the weight of attenuation. Such a procedure could be used as a valuable guidance for the fundamental one-dimensional compliance of the site for seismic testing. Foti *et al*. (2018) suggested that multiple forward and reverse shots be conducted as this allowed more stacking, increasing the signal to noise ratio in the record and leading to better estimations of the dispersion curve.

2.3.1.3   Sampling Parameters

- **Sampling rate** – during the digitization of analogue signals, a constant time interval (δ) is applied between the data samples. The sampling rate (f_s) is defined as the reciprocal of the time interval. For any signal, there exists a sampling frequency known as the Nyquist critical frequency that can be determined by Equation 2.10.

$$f_c = 2f_h \qquad \qquad \text{(Equation 2.10)}$$

where: f_c = Nyquist critical frequency

f_h = maximum frequency of propagating signal

This critical frequency acts as a boundary for the information contained in a digital signal. Any sampling rate below the Nyquist critical frequency leads to an aliasing problem where the information in the signal content is undeveloped and distorted (Winter, 2009). The f_c is based on the Nyquist sampling theorem, which states that the sampled points dictate the signal completely when the sampling of the original sample is performed at least at a rate of twice the highest frequency in that signal (Hamill *et al.*, 1997).

At a geotechnical scale, frequencies above 100 Hz are rarely encountered but nonetheless, a sampling interval of 2 ms (f_s of 500 Hz) is recommended as this is satisfactory for most situations (Foti *et al*., 2018).

- **Time window** – this refers to the total length of time required to record the entire train of signals. Since surface wave analysis is conveyed in the frequency domain, this length of time is influenced by the frequency intervals of the digitized signal in the frequency domain. For most array setups, a 2 s time window (frequency resolution of 0.5 Hz) is advised although longer time windows should be employed for soft sediment tests (Foti *et al*., 2018). Additionally, a pre-trigger time is utilized to simplify the filtering techniques and avoid leakage when processing signals. This could be seen in Figure 2.21 where a pre-trigger of 1.9 s was applied.
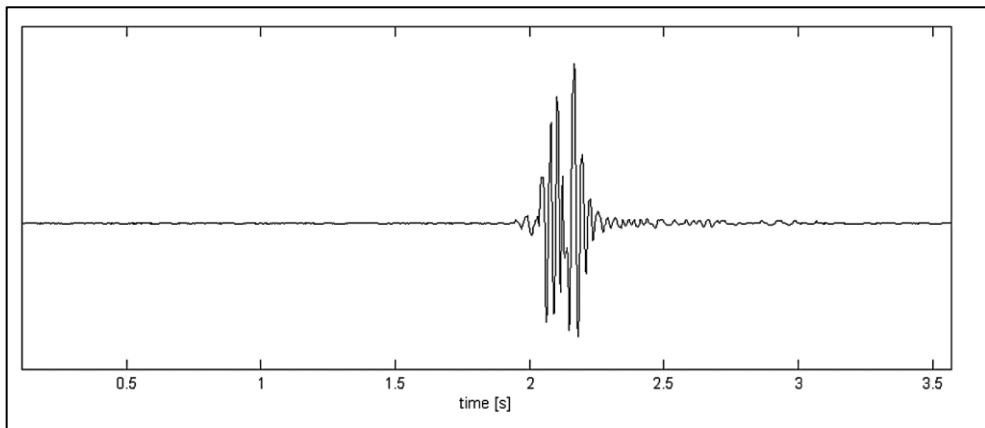
Figure 2.21: Single trace signal with a 1.9 s of pre-trigger time (Strobbia, 2003).

From Figure 2.21, it could be seen that the sampling of the trace only began at 1.9 s. Before this time, only noise was present, and the trace was silent before 1.9 s due to the pre-trig resulting in an overall good quality signal. Despite this, the actual noise levels vary depending on the frequency band as seen when plotted on a time amplitude domain – computed from the Fourier transformation of the signal (Figure 2.22). When noise levels are high, there is a possibility that the coherence in the signals vanish as could be seen for the low frequency zone (5 Hz) in Figure 2.22 (Strobbia, 2003).
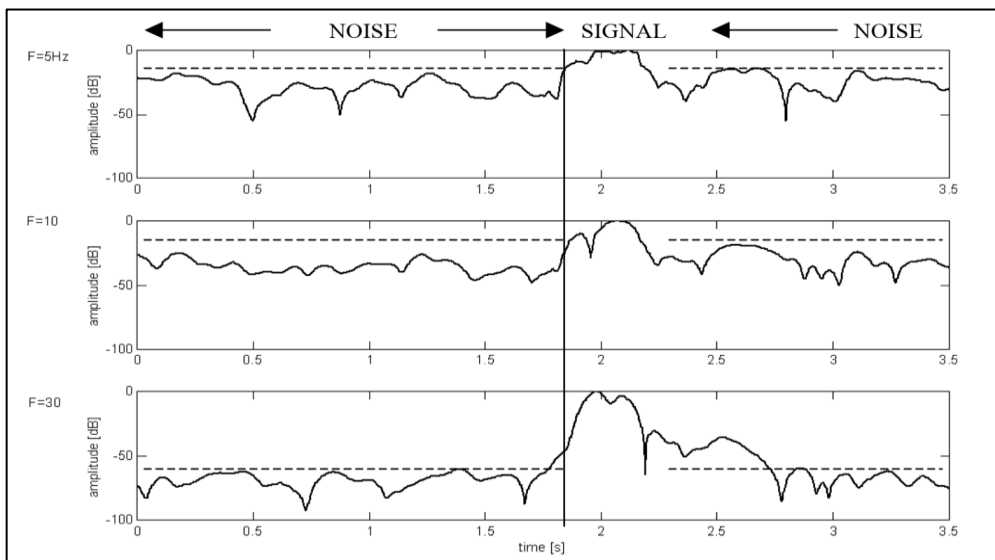
Figure 2.22: Analysis of signal in Figure 2.21 at three different frequencies (Strobbia, 2003).

2.3.1.4   Signal Quality Control

A field quality control check should be conducted beforehand, if possible, to assist the surveyor in tailoring the acquisition of the material results. The following could be performed regarding to quality control in the field.

- **Frequency content** – as the frequency band at which the seismic tests are conducted influence much of the sampling parameters, it is necessary to identify the limits of this band. The limits can be established by passing low pass and high pass filters to assess the energy contents of the signals. Low pass filters are used to obtain the lower limit by lowering the frequency threshold each time whilst high pass filters carry out the opposite. Figure 2.23 illustrates the use of low pass and high pass filters to formulate the frequency band for the Mirandola site, InterPACIFIC project.
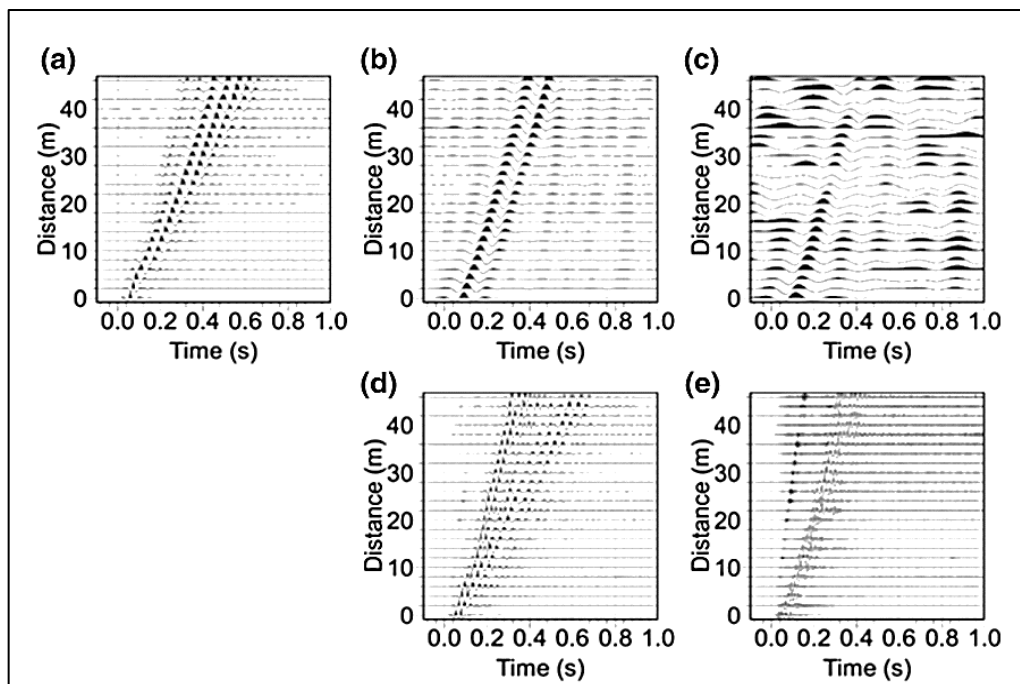
Figure 2.23: Frequency content check for the Mirandola site, InterPACIFIC project a) Raw data b) low pass filter data (10 Hz) c) low pass filter data (6 Hz) d) high pass filter data (27 Hz) e) high pass filter data (60 Hz) (Foti *et al*., 2018).

From Figure 2.23, it could be seen that a decreasing signal content was observed for the low pass filters starting at 10 Hz and ending at 6 Hz. At 10 Hz (Figure 2.23 b), the signal

displayed dominant characteristics, however as the frequency was decreased to 6 Hz (Figure 2.23c), the signal was seen to diminish. At a frequency of 27 Hz for the high pass filter, signals from both surface waves and air waves can still be observed although the waveform had significantly changed for the surface wave.

- **Signal to noise ratio** – noise is identified as any unwanted data that masks or interferes with the signal under consideration. The existence of noise can significantly deteriorate the quality of the signal procured in the recording, thereby setting limits in the successful interpretation of the signals. In the presence of noise, the quality of the signal is characterized by the signal to noise ratio (SNR) which is calculated using Equation 2.11 in decibels (db) (Johnson, 2006).

$$SNR = 10\log(\frac{P_{signal}}{P_{noise}}) \hspace{3cm} \text{(Equation 2.11)}$$

where: P_{signal} = signal power

P_{noise} = noise power

The difficulty in recovering the useful signal from the noise is dependent on the degree of the SNR. A lower SNR implies a greater interference of noise and thus burying the signal of interest during the signal processing. Thus, to improve the performance in the processing of the signals a higher SNR should always be targeted (Franco, 2015).

Foti *et al*. (2018) suggested that as good protocol, each receiver must adhere to a good signal to noise ratio of greater than 10 dBs and any evaluated traces with SNR values below this limit should be discarded. These noise levels could be detected based on measuring the background ambient vibrations, which utilizes the same test setup in the absence of the active source vibrations. Other alternatives include extracting portions of the records where active wavefield signals are not visible, although this is advised against due to the random nature of noise resulting in incorrect conclusions. Despite all this, surface waves tests tend to be more robust compared to other tests in terms of noise levels. According to Foti (2005), the success rate of surface wave tests in areas with high noise levels are significantly greater than other test methods.

2.3.2 Passive Measurements

In cases where it is difficult to generate the lower frequency components adequately, passive measurements methods are employed. This involves the use of ambient vibrations without the use of an artificial seismic source. These ambient vibrations are also referred to as microtremors and are as a result of natural phenomenon's such as wind blowing through trees, ocean waves crashing etc. as well as human activities including highway traffics, construction activities etc. Microtremors tend to be very useful in characterizing deep profiles due to their rich content in the lower frequency regions (0.2 Hz – 30 Hz) (Foti *et al*., 2018). It is often recommended that active and passive acquisitions be merged to optimally cover the dispersion curve over a large frequency band, although cross contamination of the wavefields from conducting active and passive seismic tests simultaneously must be avoided.

Passive acquisition techniques tend to be slightly more challenging as there are no set standards for the geometry or the number of sensors to be utilized. Often the largest issue lies in differentiating between the 'noise' and 'signal' constituents of the passive records. As signals from passive sources tend to be greatly variable, the steadiness of the results tends to be affected as well. Passive tests are usually convened using 2D layouts as it is assumed that the ambient vibrations can propagate in all directions.

As the study focused on active surface wave testing, only the primary affiliates of passive probing will be briefly discussed in the following.

- **Sensor setup –** As mentioned earlier, an important area is that of noise during passive acquisition owing to the weather, positioning of sensors, etc. Thus, the setup of the sensors is vital in the acquisition process to minimize the noise levels detected (Foti *et al*., 2018). Figure 2.24 illustrates the different possible setups available varying through levels of desirability from least desirable (a) to most desirable (d).
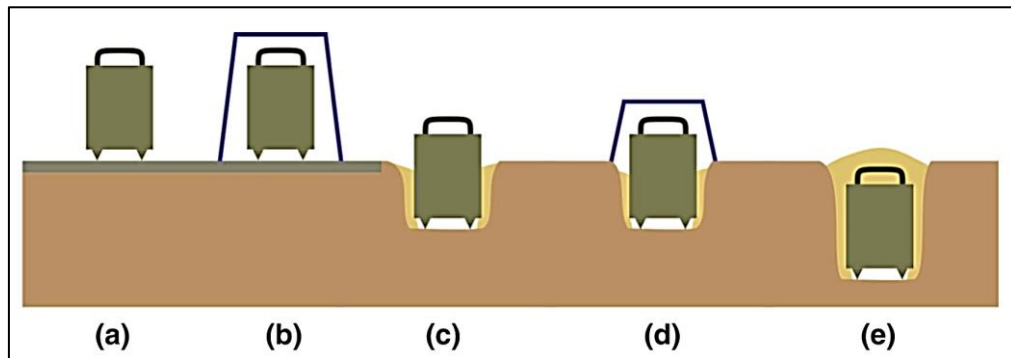
Figure 2.24: Possible setups when installing sensors for passive arrays, from (a) least desirable to (d) most desirable as well as setups for (e) best quality results (Foti *et al.*, 2018).

As seen from Figure 2.24, the optimum setup, which would produce the best results considering the noise, was when the sensors are buried in the ground half of their height. However, such a setup would require a considerably longer amount of time, especially when many sensors are used and as a coupling requirement, it is necessary to install the sensors firmly into the surrounding ground.

- **Array geometry** – for passive acquisition, linear arrays are disregarded as this demands the assumption that the distribution of the seismic energy is isotropic and homogeneous along the line of the array. Thus, 2D arrays are used to eliminate bias in the estimation of the V_S from a favoured sampling direction as the position of the source is unknown (Wood and Cox, 2012). It should be noted that in terms of the array length, the same principles are still applied to the geometries as before with array-based processing techniques. However, the number of sensors is dependent on the levels of the ambient vibrations present at the site, with more sensors being required for lower levels. Three dimensional sensors are often incorporated as well to assist in analysing both horizontal and vertical motions of the microtremors. Different array shapes can be implemented in the field (Figure 2.25), although the final decision depends on the following criteria:

  - availability of sensors as well as the type of sensors
  - availability of space for installation
  - time availability and difficulty in employing different arrays
  - processing technique capabilities and limitations
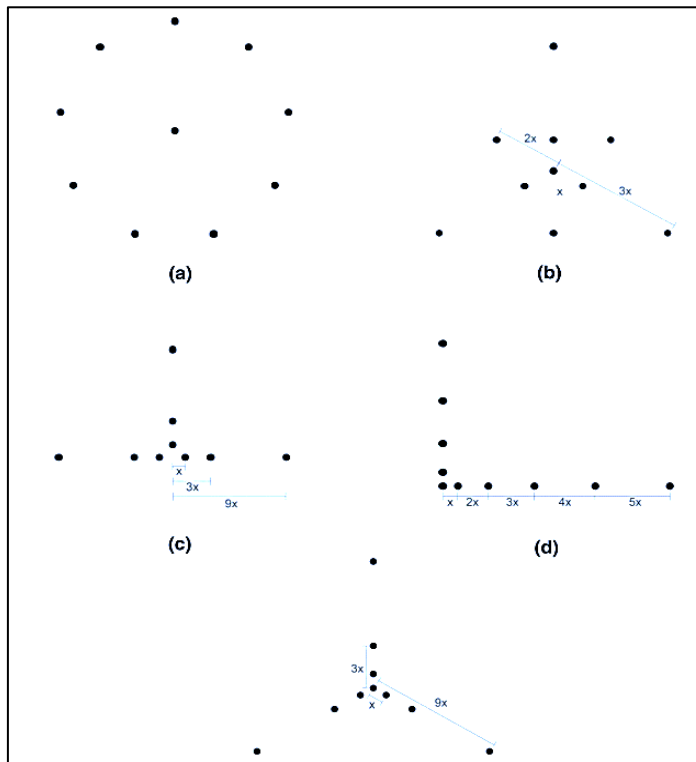
Figure 2.25: Passive acquisition geometries frequently used in passive seismic testing, (a) circular array b) nested triangle array c) T shaped array d) L shaped array e) sparse nested triangle array (Foti *et al*., 2018).

- **Sampling rate** - the sampling rate dictates the frequency band that can be occupied during the surface wave test. As passive analysis deals with data records with low frequencies, a lower sampling rate than that employed in active tests is commonly used. Foti *et al*. (2018) stated that for passive testing, frequencies between 100 and 200 Hz are generally sufficient.
- **Time window** – as there is no control over the signals from passive sources, the acquisition process demands longer durations of recorded data. Statistical handling is done on the passive recorded signals to obtain sound results of the wave propagation. Passive acquisitions often go for long periods of time (30 – 120 mins), from which the recorded data are split into smaller windows to assist in processing the signals (Foti *et al*., 2018).

2.4   PROCESSING

The processing step involves evaluating and interpreting the acquainted raw data from the field and using the results to extract the experimental dispersion curve - a plot of the phase velocity

against the corresponding frequency (Figure 2.26). Depending on the type of signal administered, different approaches can be initiated. As an example, when harmonic signals are administered during the surface wave test, each set generates a single phase-velocity respective to a certain frequency. Therefore, to generate the entire trace of the dispersion curve, multiple steady state surface wave tests are required.
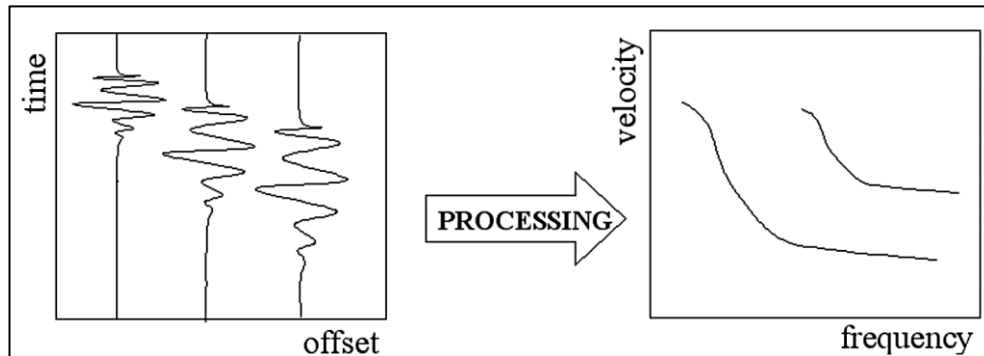
Figure 2.26: Overall objective of the processing step (Strobbia, 2003).

Essentially, the processing of the dispersion curve consists of two actions namely selecting the section of the recorded data to analyse - "masking" as well as identifying the dispersive properties. The phase velocity is usually obtained at a certain frequency by assessing the travel and distance times at sections in the record with energy high points. Most processing techniques are based on mapping the experimental data, which is acquired in the time-offset domain, as functions of processing parameters such as frequency, wavenumber (k) and slowness (Strobbia, 2003). By evaluating the coordinates in these new domains, the characteristics of the propagation can be interpreted.

Although the results are highly dependent on the acquisition step, the approach used to analyse the data also influences the results (Strobbia, 2003). When no noise is present, all approaches should typically generate the same results.

2.4.1 Approaches

2.4.1.1 Continuous Surface Waves (CSW)

This approach employs frequency-controlled shakers, which generate surface waves at a steady state along the ground and the vertical surface wave motion is detected by an array of vertical geophones - typically 6 geophones which are spaced equally and colinear with the vibrating

source (Menzies, 2001). To maximize the range of wavelengths covered, the shaker is stepped through a set of frequencies. Menzies and Matthews (1996) suggested frequency increments of 5 Hz to step through the range of frequencies. A steady state wave is generated at each frequency using a signal generator and an amplifier which is then captured by the geophones manifesting a sinusoidal output in the time domain. The approach is an indirect way of determining the shear velocity profile by the determining the fundamental Rayleigh wave velocity (V_R) first, as their velocities are correlated. However, this surface wave testing method is limited in terms of resolution, as the shakers fail to produce significantly high frequencies required for characterizing the upper most layers. Along with the surface waves being recorded, ambient noises are recorded too and could become problematic if generated at the same frequency as the source (Hunter and Crow, 2015).

The CSW analysis uses the frequency domain to assess the spectral amplitude at each geophone ensuring that a dominant spike is observed at the shaker frequency. A Fast Fourier transformation allows the conversion of the time domain into the frequency domain, which then allows the phase spectrum at each geophone to be obtained. The frequencies in the frequency domain can each be represented in the form of a vector z which comprises of an imaginary and real part. The spectral amplitude at this specific frequency can then be calculated by determining the magnitude of the vector, $|z|$. At the dominant frequency, the phase angle (ɸ) can be calculated at that specific geophone using Equation 2.12 (Heymann, 2007).

$$\varphi = \tan^{-1}\left(\frac{Im(z)}{Re(z)}\right)$$ (Equation 2.12)

By conducting a linear regression analysis of the plot of the phase angles at each geophone against the geophone distances from the source, the slope (dɸ/dx) can be determined (Figure 2.27). It should be noted that the slope represents the wavenumber (k) measured in rad/m (Joh *et al.*, 2011). The regression analysis is often used to quantify the quality of the data recorded at each frequency by judging the regression fit.
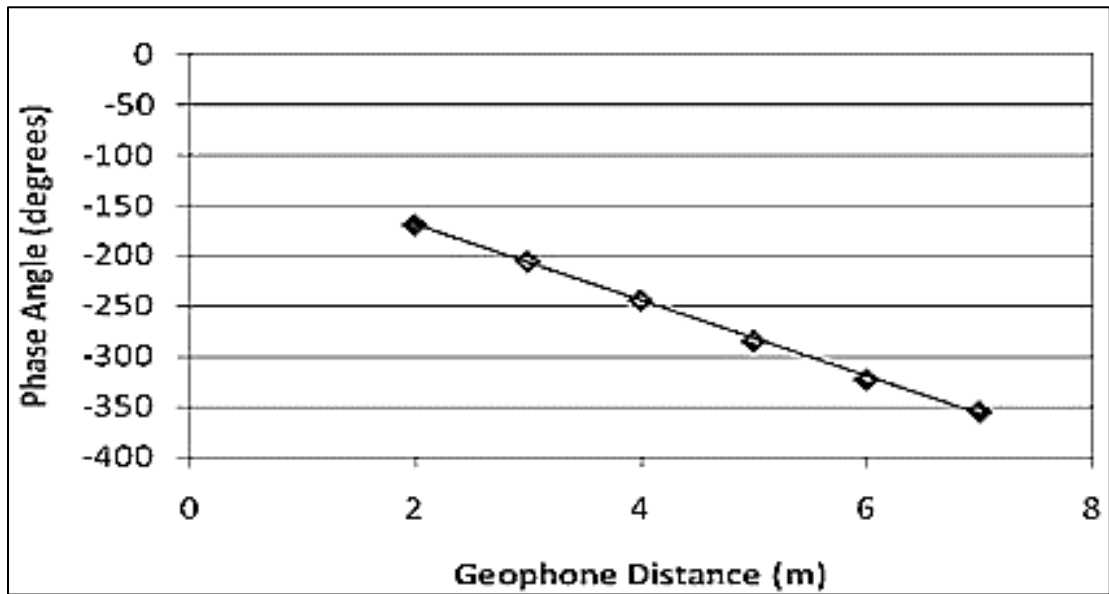
Figure 2.27: Linear regression analysis used to determine slope in Phase angle vs geophone distance plot (Hunter and Crow, 2015).

It can be seen in Figure 2.27, that the regression analysis complies to a linear relationship signifying the constant velocity of the surface wave along the array of geophones. Hereupon, the wavelength and the Rayleigh wave velocity are determined using Equation 2.13 and Equation 2.14 respectively, which are used to develop the experimental dispersion curve for the investigated site (Joh *et al.*, 2011). To close any gaps in the dispersion curve, further CSW tests could be conducted at other required frequencies.

$$\lambda = 2\pi \cdot \left(\frac{dx}{d\varphi}\right) = 2\pi \cdot \left(\frac{1}{k}\right)$$ (Equation 2.13)

$$V_R = f \cdot \lambda$$ (Equation 2.14)

According to Hunter and Crow (2015), the effective depth (z) to which the CSW test can survey for a specific λ is based on Equation 2.15. A scaling factor between 2 to 3 is frequently adopted. Menzies (2001) recommended scaling factor of 3 to be employed. The effective depth (z) is suggestive of the depth at which the Rayleigh wave components are fully decayed (Richart *et al.*, 1970).

$$z = \frac{\lambda}{scaling\ factor}$$ (Equation 2.15)

The shear wave velocity (Vs) can be approximated using the relationship (Equation 2.16) suggested by Stokoe *et al.* (2004) provided that the Poisson's ratio (v) is known for a homogeneous isotropic body. It should be noted that the Vs solutions recognised by Equation 2.16 are not rigorous, modelling the data using inversion techniques tends to yield more realistic results (Hunter and Crow, 2015). Early applications of the CSW approach assumed that only the fundamental mode of the Raleigh surface wave is sampled. However, the experimental dispersion curve developed by the CSW method might be a combination of the different modes inducing exaggerated values of the Vs. A brief outline of the CSW approach is illustrated in Figure 2.28.

$$V_S \approx \frac{1+\nu}{(0.874+1.117\nu)\cdot V_R}$$

(Equation 2.16)
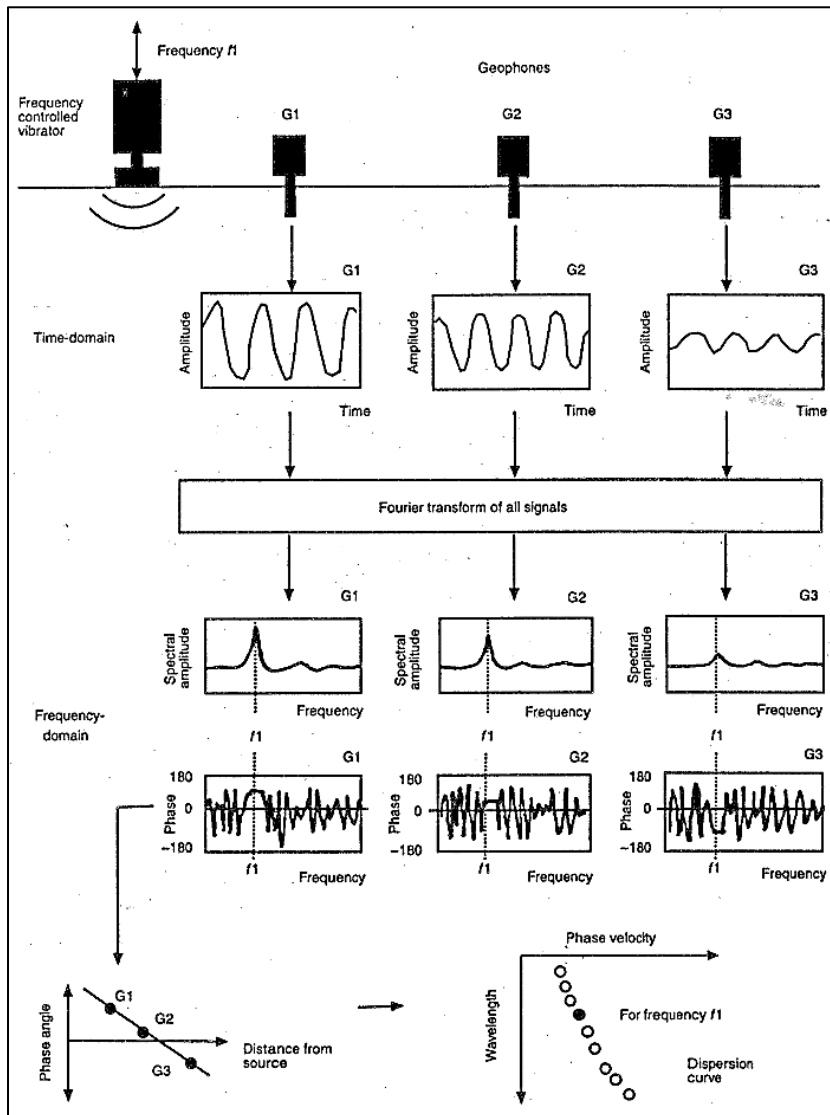
Figure 2.28: Schematic diagram of the CSW testing method (Menzies and Matthews, 1996).

When determining the wavenumber with phase angles more than π radians unwrapping is required. When a phase angle smaller than π radians is experienced, the phase angle is folded to a greater value than π radians (Figure 2.29). This jump indicates that the geophone is located more than one wavelength from the neighbouring geophone (Joh *et al.*, 2011). An unwrapping technique can be applied to recover a wrapped k which can then be used for determining the velocities. The unwrapping in the phase angle distance domain is administered by subtracting the phase angles in the jumped state by 2π radians.
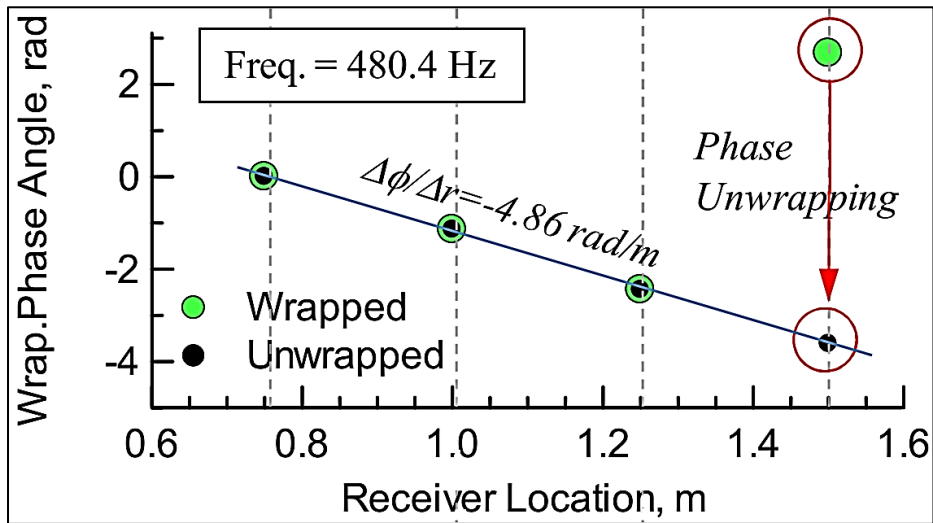
Figure 2.29: Phase angle unwrapping for determination of the slope dɸ/dx at a frequency of 480.4 Hz (Joh *et al.*, 2011).

2.4.1.2 Spectral Analysis of Surface Waves (SASW)

This approach incorporates a source along with a pair of receivers (2 or 3) at known distances from the source with these receivers spaced from one another at a distance (ΔX) equal to the source offset. According to Hunter and Crow (2015), this improves the accuracy of the phase difference determination. Sledgehammers of varying masses and drop weights are utilised in the SASW to accommodate the targeted frequency ranges (Menzies and Matthews, 1996). For shorter spacings (1 m to 8 m), sledgehammers are usually adequate to provide the required energy (Rosenblad *et al.*, 2002). However, with increasing spacings (16 m to 64 m), drop weights and walking bulldozers are implemented for generating low frequency energy to penetrate to deeper depths. Furthermore, during low frequency tests, the signal to noise (SNR) is highly influenced by the background noise. This influence can be minimized by applying larger amounts of energy from the source (Lin, 2007). The energy distribution of the various sources at each receiver can be considered using the spectral amplitude plot, which is discussed later in this section.

The SASW approach integrates geometrical array configurations to improve the signal to noise ratios through geometry and stacking. Customary, the two most common configurations used for SASW are the common receiver midpoint (CRMP) configuration and the common source (CS) configuration (Lin, 2007). The CRMP has a fixed centre line placed between the receivers for all test spacings (Figure 2.30). This implies that for each spacing both the source and the

receivers must be relocated. Despite the inconvenience, the CRMP layout ensures that the same position is profiled throughout the test when compared to the CS layout. The CS fixes the position of the source and displaces the receivers each time for each spacing (Figure 2.31). The challenge arises when lateral variation exists at the test site as the CS configuration probes different sections of the array (Lin, 2007). It should be noted that both forward and reverse shots are generally conducted for the CRMP configuration. Furthermore, Alexander (1992) stated that by averaging the forward and reverse shots for each spacing, the influence of internal phase shifts between the receivers is reduced. Nonetheless, in a study conducted by Lin (2007), forward and reverse shots were only conducted for shorter spacings ($\Delta X \leq 8$ m) and forward shots were only conducted for larger spacings ($\Delta X \geq 16$ m).
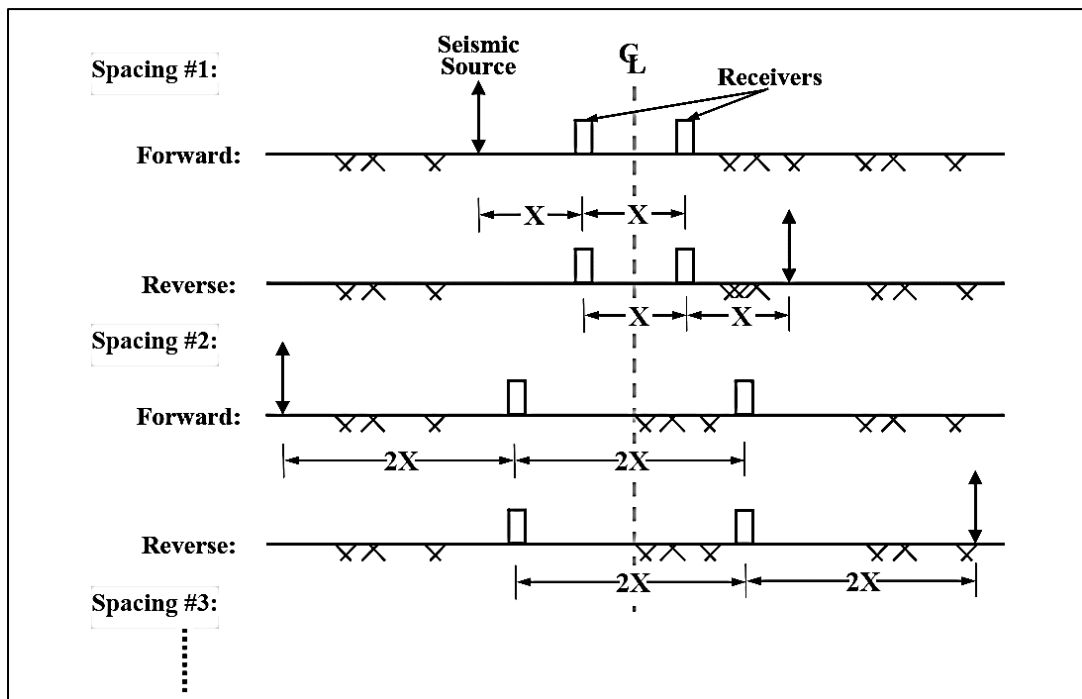
Figure 2.30: Common Receiver Midpoint (CRMP) configuration with two receivers (Lin, 2007).
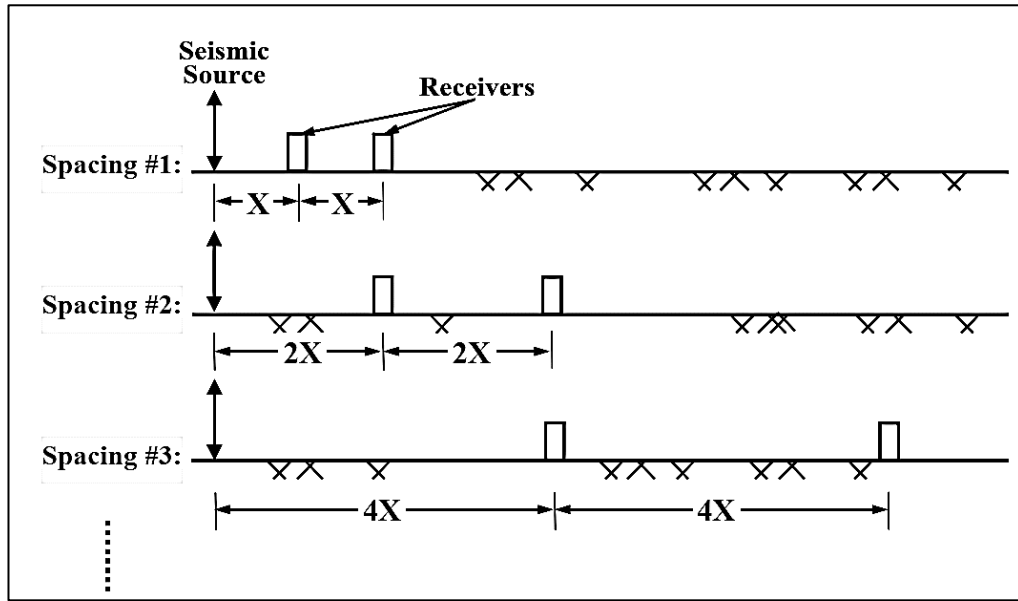
Figure 2.31: Common Source (CS) configuration with two receivers (Lin, 2007).

The data for SASW is analysed using the frequency domain where the frequency range is dependent on the type of source used. As the data captured by the seismogram is in the time domain, a Fast Fourier Transformation (FFT) is utilized to convert the data at each receiver to the frequency-based domain. Using the Fourier transformations, spectral amplitude (peak power amplitude), the phase difference and the coherence plots of the two signals are calculated (Equation 2.17 – Equation 2.19). The wavelengths of the signals are calculated using the phase difference (Δϕ) between the receiver points. The phase difference, which is obtained from the cross-power spectrum functions, represents the angle between sinusoidal waves having the same frequency. When harmonic signals are used for testing, the time shift between the two signals can be used to calculate the Δϕ as shown below in Figure 2.32.

$$A_{peak} = \sqrt{[Re(G_{YX})]^2 + [Im(G_{YX})]^2}$$ (Equation 2.17)

$$\Delta\phi_{wrap}\ (f) = \arctan\left(\frac{Im(G_{YX})}{Re(G_{YX})}\right) \cdot$$ (Equation 2.18)

$$\gamma^2(f) = \frac{|G_{YX}|^2}{G_{YY} \cdot G_{XX}}$$ (Equation 2.19)

where: A_{peak} = peak power amplitude of the two signals

$\Delta\phi_{wrap}$ = wrapped phase difference in radians

γ^2 = coherence function

G_{YX} = cross power spectrum of the receiver 1 and receiver 2

G_{YY} = auto power spectrum of the receiver 1

G_{XX} = auto power spectrum of the receiver 2
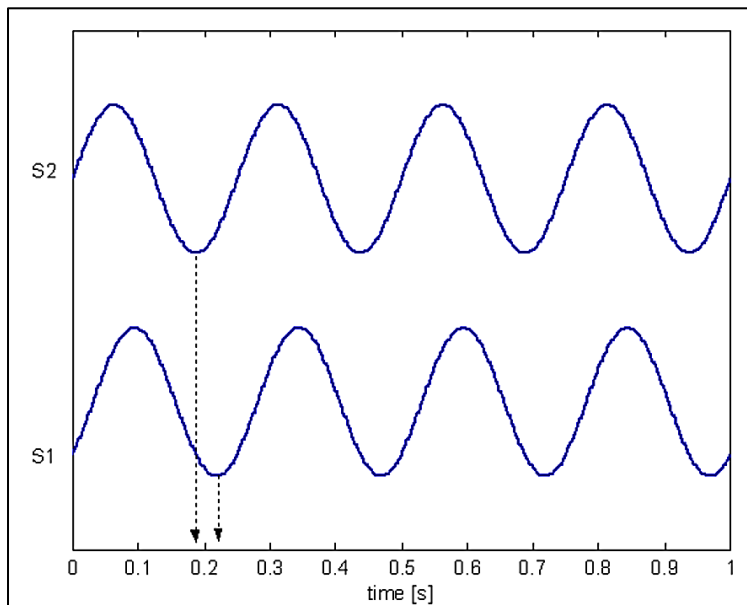
Figure 2.32: Phase difference computation between two harmonic signals (Strobbia, 2003).

If λ is greater than the receiver spacing (ΔX), the phase difference tends to be greater than 2π and therefore unwrapping is required. Every point at $n\lambda + \Delta X$ has equal phase differences as shown in Figure 2.33. Thus, this implies that a specific phase difference may be equivalent to ΔX or $n\lambda + \Delta X$. The phase difference plots collected initially are wrapped and therefore the phase differences are required to be unwrapped over the selected frequency range as shown in Figure 2.34.
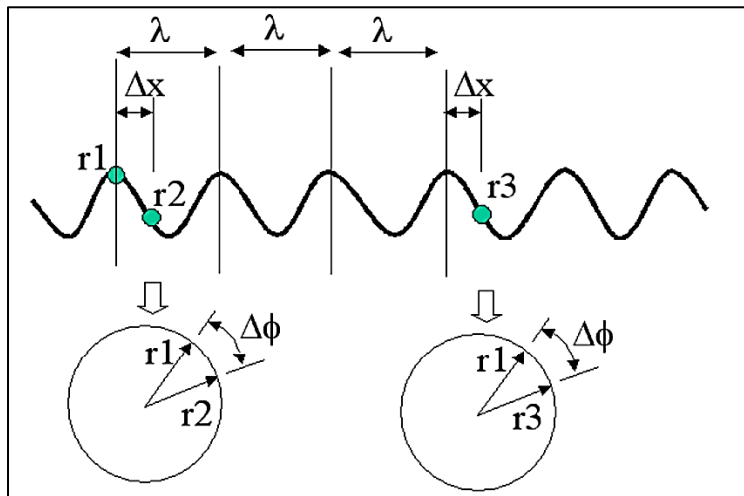
Figure 2.33: Phase difference implications (Strobbia, 2003).
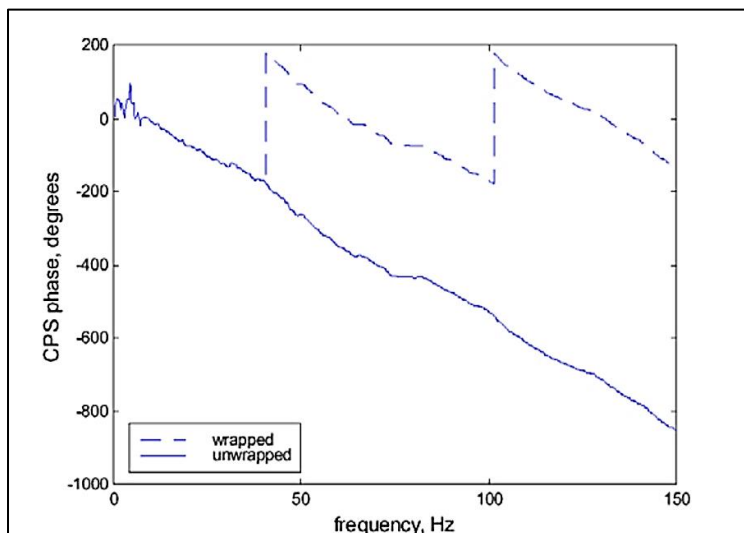
Figure 2.34: Unwrapping of phase differences (Strobbia, 2003).

Provided that the quality of the signal is good, and the signal shows a continuous phase difference behaviour, additional wavelengths ($\Delta\phi > 2\pi$) can be identified. Each jump in the wrapped phase difference ties to a wavelength. Wavelengths shorter than ΔX do not require unwrapping.

A key challenge found in SASW is that of gathering quality data, which is typically judged through the coherence function of the receivers along with the wrapped phase difference plots.

The coherence (γ^2) gives an indication of the signal to noise ratio (SNR), with a higher coherence indicating a higher SNR. Coherence function values range from zero to one and are determined over multiple input windows (Alexander, 1992). The process of selecting acceptable data is often referred to as 'masking' of the data, with values of $\gamma^2 > 0.9$ regarded as quality data (Nazarian and Stokoe II, 1986). A high coherence implies that output power of the signal received by both receivers was due to the same input signal, whereas a low coherence indicates failure to receive signals at both geophones from the same source (Chakraborty *et al.*, 2019). According to Heisey *et al.* (1982), low coherence values are typically due to insufficient frequency resolutions, background noise or weak excitations of waves over some frequency ranges. Furthermore, with increasing receiver spacings, coherence values drop significantly owing to the attenuation of high frequency waves, resulting in lower power signals at the far receiver. Studies have shown that by repeating the test four or five times for each spacing, the coherence of the data set can be improved (Heisey *et al.*, 1982; Kumar and Hazra, 2014). However, a study conducted by Chakraborty *et al.* (2019) showed a significant increase in the coherence by employing a constant impact energy during each repetition for each shot as opposed to the conventional SASW, which employs varying energies in each repetition. By maintaining a constant impact energy, the strength of the signal was stated to have improved as well as reduce any background noise influence, producing a high coherence value. The results of their study are shown below in Figure 2.35.
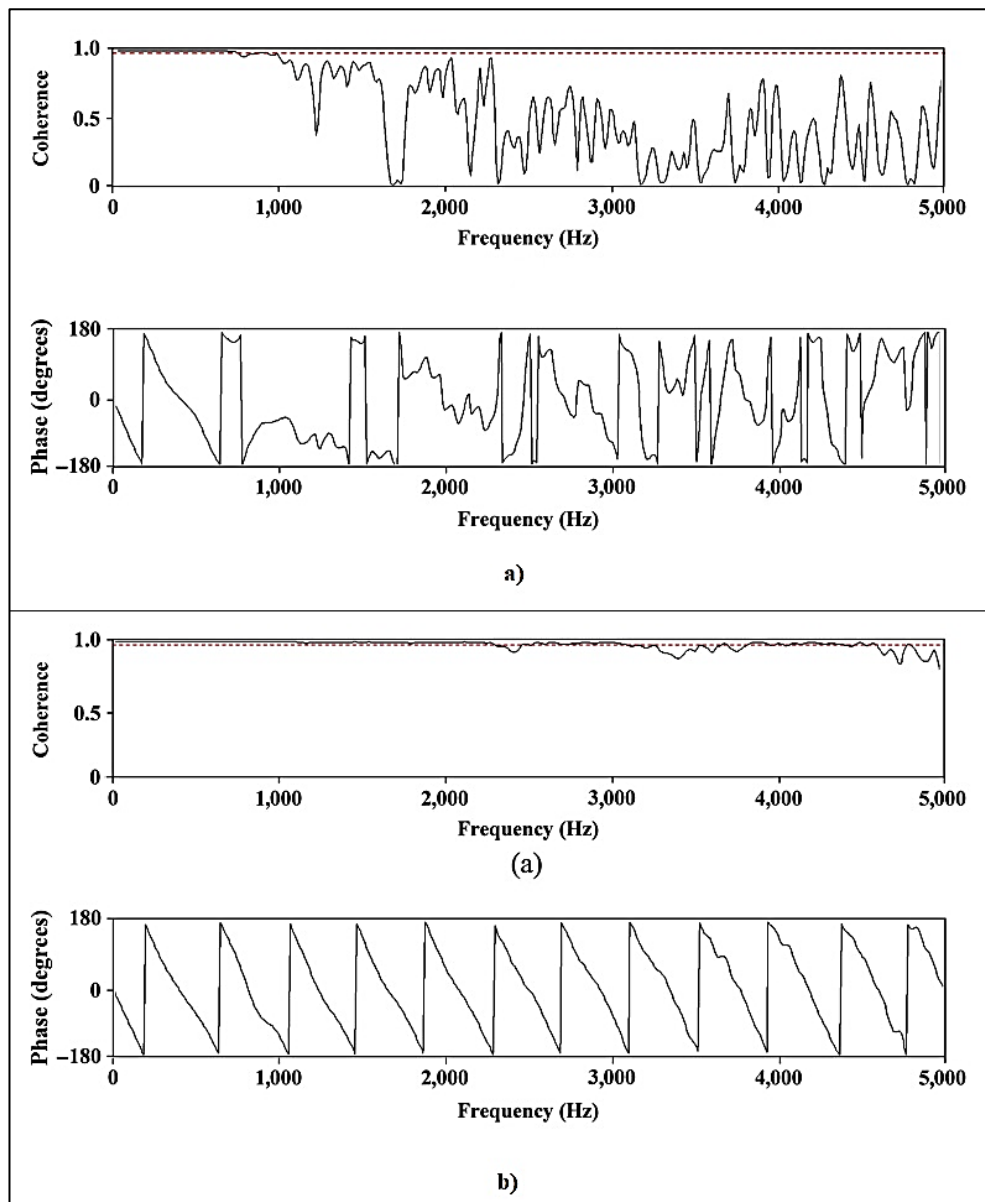
Figure 2.35: Field test coherence and wrapped phase difference plots for a) variable impact energy for four repetitions b) constant impact energy for four repetitions (Chakraborty *et al*., 2019).

Once the $\Delta\phi$ is known, the phase velocity and wavenumber can be determined using the principle of another approach known as the Steady State Rayleigh Method (SSRM). The principle essentially states that for any propagating wave, the phase difference equals 2π when the wavelength (λ) of the wave is equal to distance between the two receivers (ΔX). Thus, if the $\Delta\phi$ and ΔX are determined for the relevant signals then the λ and the Rayleigh wave velocity (V_R) can be determined using Equation 2.20 and Equation 2.21 respectively.

$$\lambda = \frac{\Delta X \cdot 2\pi}{|\Delta \phi|}$$ (Equation 2.20)

$$V_R = f \cdot \lambda$$ (Equation 2.21)

For each respective spacing, an individual dispersion curve is generated for a certain range of frequencies. By combining each of the respective individual dispersion curves, a composite dispersion curve is obtained for the inversion analysis. The quality of the SASW tests can then be assessed by observing the "overlap" of the individual dispersion curves (Lin, 2007). It should be realized that the composite dispersion curve generated using the SASW is an "apparent" dispersion curve which is the superposition all the different modes present (Yuan *et al.*, 2014; Hunter and Crow, 2015).

2.4.1.3 Multichannel Analysis of Surface Waves (MASW)

This approach was derived as an extension of the SASW method. The approach is essentially founded on the fundamental principles of SASW and CSW but varies in the number of geophones and equipment employed. The MASW at its core takes advantage of the present advanced technology available, such as modern seismographs, shortening the time to conduct these tests as well as improving accuracy in estimating the dispersion curves for different higher modes as well. Hunter and Crow (2015) suggested an array of 24 vertical geophones be used for recording seismic vibrations resulting from the seismic source. Due to the long array implemented in MASW, effects due to far offset need to be considered as well. The far offset effect signifies interference between low velocity surface waves and high velocity body waves far offset regions causing the linear coherency in the surface waves to diminish (Park *et al.*, 1999).

Depending on the depth of investigation, the seismic source implemented as well as the receiver spacing will vary. The seismic source may be active or passive (microtremor) (Figure 2.36). The MASW faces a limitation in the sense that the testing method assumes the body to be laterally homogeneous. In profiles where the topography varies substantially, a MASW approach is not recommended. Hunter and Crow (2015) further mentioned that sites with large quantities of soft material (Vs < 200 m/s) stationed near the surface as well as sites with shallow bedrocks are very demanding in site procedures when a MASW approach is implemented.
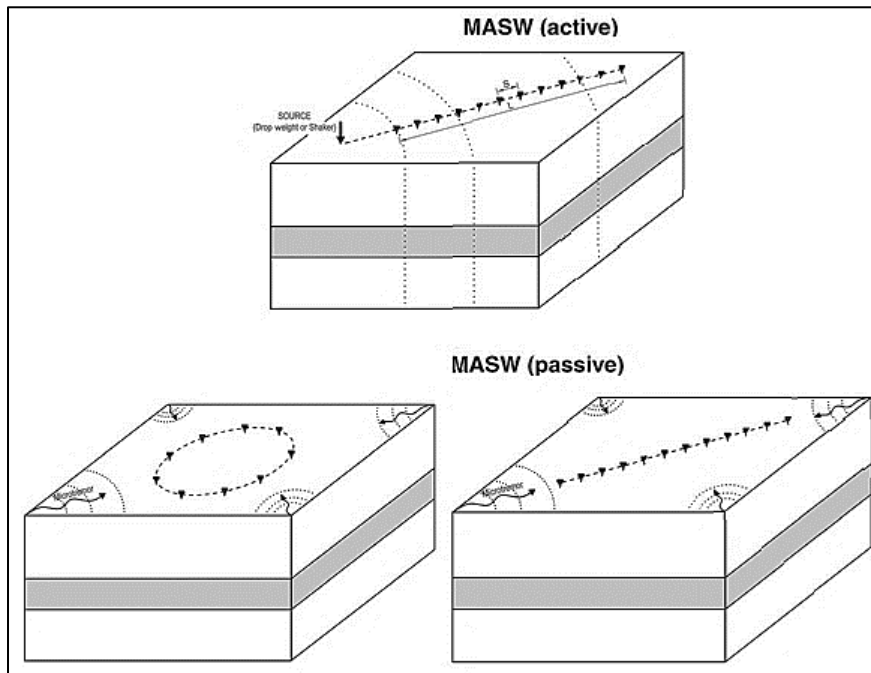
Figure 2.36: Conventional configurations used in MASW testing (Pelekis and Athanasopoulos, 2011).

The MASW produces dispersion images by determining the phase velocities through application of an integral transformation of the time domain data. Further transformation can be done processing the data to a different domain, such as the frequency-wavenumber (f-k) domain. The new domains present the spectra as energy levels and by interpreting patterns in these energies, not only can the different modes of the Rayleigh waves be identified but the dispersion curve can found as well (Pelekis and Athanasopoulos, 2011).

2.5   INVERSION

Geophysicists define the term 'inversion' as a process used to estimate the parameters of a given earth model determined from several observations (Lines and Treitel, 1984). The inversion forms the final stage in the surface wave test methods where the dispersive properties of the propagation are processed into properties of the investigated body (Figure 2.37). Amongst the three steps in surface wave testing, the inversion step is considered as the most challenging step as the problem is ill-posed and non-unique. An infinite number of solutions exists for the dispersion curve and therefore, an optimisation technique is required to find the

optimal solution (Pelekis and Athanasopoulos, 2011). Therefore, an inversion analysis not only characterizes an array of models but also maximizes/minimizes some objective function to acquire the best representative models.
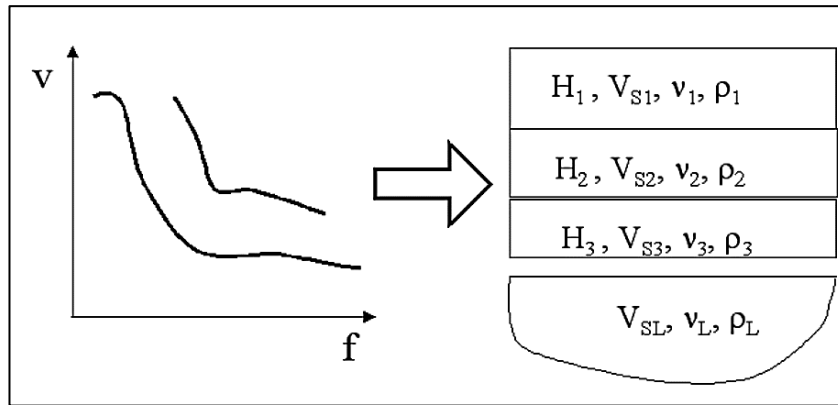
Figure 2.37: Basic outline of the inversion process for surface wave tests (Strobbia, 2003).

2.5.1   Inversion Background

Different approaches exist towards the inversion problem, with the simplest approach of Vs simply being 110 % of the Rayleigh wave velocity acting at a depth of one half or one third of the wavelength at that velocity (Abbiss, 1981). However, this approach produces errors when higher modes are involved and in most cases the inversion stage only considers the fundamental mode (Strobbia, 2003). Other common approaches involve conjuring linearization in selected models and applying linear inversion techniques. Such an approach fails to produce adequate results, especially when the inversion problem becomes severely nonlinear, often producing excessively optimistic estimates (Sambridge, 2001). A third approach involves searching the solution in the model space using an initial model computed from a set of model parameters. The development of the initial model (theoretical dispersion curve), from a set of model parameters for a specific soil profile to predict the experimental dispersion curve is termed as the forward problem and is based on solving the eigenvalue problem of the surface wave (Pelekis & Athanasopoulos, 2011). The forward problem is usually solved using the transform matrix method and its succeeding versions. The Thomson-Haskell algorithm, developed by Thomson (1950) and Haskell (1953), utilized the transform matrix method for modelling heterogeneous surface wave propagation. Likewise, Kausel and Roësset (1981) evolved their own techniques founded on the finite element dynamic stiffness matrix method. Other techniques include numerical integration (Takeuchi and Saito, 1972), the reflection and

transmission (R -T) coefficient method (Kennett, 1974) and the boundary element method (Manolis and Beskos, 1988).

Nazarian and Stokoe (1984) proposed a trial-and-error approach which was based on a global search algorithm where an initial theoretical dispersion curve was modified until a good fit was obtained with the experimental dispersion curve over the complete model space. Using different algorithms, an automated iterative inversion is conducted where a minimization criterion for the forward problem was updated throughout the inversion process until an acceptable model was found. An example is the Monte Carlo approach. The Monte Carlo approach randomly generates a set of models which are confined by the given parameter boundaries and the number of layers. These models are used to determine the corresponding theoretical dispersion curves, which are then displaced towards the experimental dispersion curve as closely as possible. The degree to which the two dispersion curves compare to one another (misfit) are then compared to obtain the best model (Foti *et al.*, 2009). Global search algorithms provide relatively stable results, although they are computationally expensive (Foti *et al.*, 2011).

Other approaches are founded on local search algorithms, which tend to move along the direction that results in the local reduction/minimization of the misfit whilst seeking for the solution in the vicinity of the initial theoretical dispersion curve. Local search algorithms are significantly faster than global search methods. However, due to their search field being limited to the vicinity of the initial model, there is a possibility of being trapped at a local minimum (Foti *et al.*, 2011).

The data fit measure, $\phi(m)$, also known as the misfit, is used as a data-acceptable model threshold and corresponds to a misfit function (χ^2). The $\phi(m)$ gets evaluated based on the differences between the theoretical and experimental dispersion curve models and must adhere to the following data fit criterion:

$$\phi(m) \leq \phi_t,$$

where ϕ_t represents a tolerance level. The ϕ_t is usually set at a value which deems all model curves generated within one standard deviation as data-acceptable models (Sambridge, 2001).

For instance, the stochastic direct search method known as the Neighbourhood Algorithm, initially proposed by (Sambridge, 1999a; Sambridge, 1999b) involves searching the whole parameter space using basic geometrical principles to locate suitable regions where the data misfit is below a certain tolerance level. In doing so, sampling of the data acceptable models is

condensed in prospective regions of the parameter space. The Neighbourhood algorithm calculates random parameters which are then used to calculate the misfit value using Equation 2.22.

$$misfit = \sqrt{\sum_{i=0}^{n_f} \frac{(x_{di}-x_{ci})^2}{\sigma_i^2 n_f}}$$ (Equation 2.22)

where: x_{di} = velocity of the experimental curve at frequency f_i

x_{ci} = velocity of the calculated theoretical curve at frequency f_i

σ_i = standard deviation of the frequency samples

n_f = number of frequency samples considered

Wathelet *et al.* (2004) states that if no uncertainty (σ_i) is given for the calculation of the misfit value, then σ_i is substituted by x_{di} in Equation 2.22.

It is important to understand the inversion step should not only focus on obtaining the best model but also study the uncertainties associated with the results. Duijndam (1988) stated that without examining the uncertainties in the findings, the inversion process remains unfinished. A major predicament of the inversion process is that of the equivalence problem, where various solutions to one inversion problem exists. The selected models are said to have equal probabilities of representing the experimental dispersion curve for the given data and confidence (Comina *et al.*, 2012). Foti *et al.* (2011) stated that by considering the uncertainties involved and having prior knowledge from borehole logs or other tests, the equivalence problem could be mitigated. By introducing priori information, such as borehole data, the inversion solution is constrained better and therefore provides improved results (Wathelet *et al.*, 2004) .

A finite set of model parameters is assumed to completely describe the unknown model and these parameters are used to provide a quantitative definition of the body under consideration. The model parameters define the subsoil in terms of geometrical and mechanical properties for each layer. The unknown model is defined by the following for each layer *i*:

$$m = [V_{si}, \nu_i, \rho_i, h_i; \dots ; V_{sl}, \nu_l, \rho_l]$$ (Equation 2.23)

where: V_{si} = shear velocity of layer *i*

v_i = Poisson's ratio of layer i

ρ_i = mass density of layer i

h_i = thickness of layer i

It should be noted that the final layer l, also known as the half space, is only defined by three parameters as seen in Equation 2.23. This is due to the half space assuming an infinite thickness.

The parameters listed in Equation 2.23 form the basis of the forward problem. The convergence of the forward problem varies in terms of sensitivity of the model parameters. The shear wave velocity and the thickness parameters are suggested to have a greater impact on the solution than the Poisson's ratio (ν) and mass density (ρ). Therefore, the ν and the ρ are often selected on a theoretical basis due to their small ranges (Park *et al.*, 1999; Strobbia, 2003). According to Wathelet *et al.* (2004), the ρ does not influence the dispersion curves significantly and thus it is generally fixed as a constant for each layer using geotechnical information. He also adds that the Vp and Vs are related to one another by the ν and thus a range between 0.2 to 0.5 should be considered. However, under conditions of saturation, both the P-wave velocity and Poisson's ratio are significantly affected. Thus, the position of the water table should be incorporated in the inversion analysis to avoid overestimates of the velocities (Foti and Strobbia, 2002).

2.5.2 Inversion Considerations

The inversion process primarily uses the parameters in the model space (m) to generate a dispersive function that maps into the data space (d), which consists of the experimental dispersive curve. The data space to be inverted is affected by certain aspects and these will be discussed in the following.

2.5.2.1 Group velocity or Phase velocity dispersion curve

Dispersion curves can be plotted in terms of the group velocity or the phase velocity. The group velocity, *U,* refers to the velocity at which a series of waves, consisting of different frequency signals propagates. On the contrary, the phase velocity, *V*, refers to the velocity at which a signal wave of a certain frequency propagates at. Equation 2.23 depicts the determination of the group velocity, *U* (Strobbia, 2003). It should be recalled that the *U* coincides with the *V* for homogeneous mediums (Sheriff and Geldart, 1995).

$$U = V + f \frac{dV}{df}$$
(Equation 2.23)

From Equation 2.23, it can be noticed that two scenarios could be depicted. If the phase velocity, *V*, increased with the frequency, then likewise the group velocity would increase too (*U > V)*. However, for sites which portray dispersive properties, where the *V* decreases with increasing frequency, the group velocity would be less than the phase velocity (*U < V).*

2.5.2.2 Modal dispersion curves

The generation of a dispersion curve depends largely on the sampling wavelength incorporated during the tests. According to Strobbia (2003), the information related to shallow layers is often available in surplus whilst a limited amount of information is available for the deeper layers. Strobbia (2003) stated that essentially shallow layers were examined by all wavelengths whilst deeper layers were only tested by long wavelengths. Figure 2.38 demonstrates this concept.
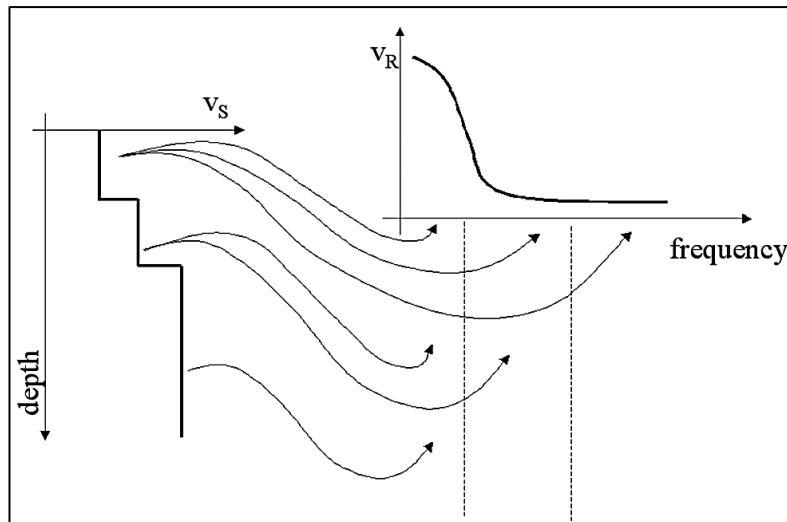
Figure 2.38: Domains of frequency information required for sampling different depths (Strobbia, 2003).

By investigating the partial derivatives of the first three modal phase velocities, Strobbia (2003) was able to explain which regions of frequencies held information with respect to the different modal curves. A model with three layers was considered with shear wave velocities of 100 m/s, 200 m/s and 400 m/s respectively. The results are shown in Figure 2.39.
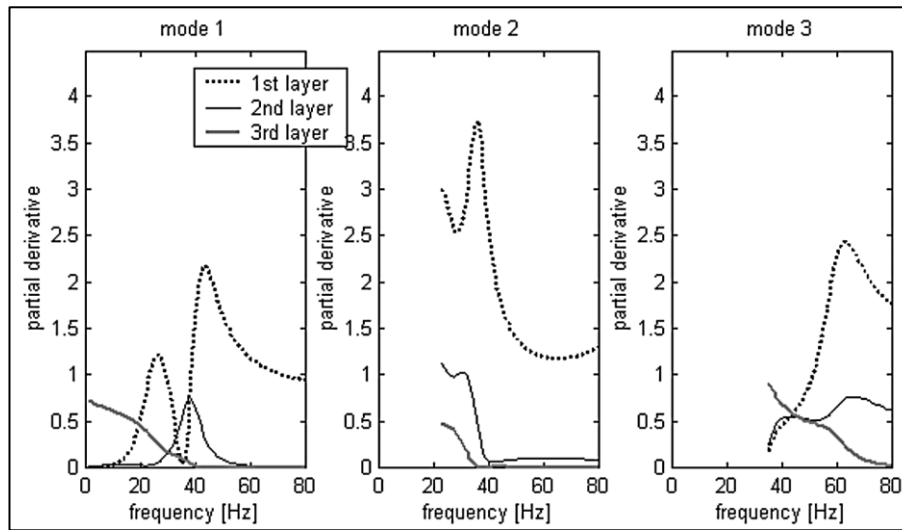
Figure 2.39: Relationship between partial derivative of phase velocities and frequency for the first three modes (Strobbia, 2003).

It could be seen from Figure 2.39 that for all three modes, the properties of the layers were influenced by the frequencies, with different modes exhibiting different sensitivities. For example, for the first mode the first layer displayed greater sensitivities at higher frequencies compared to the third layer for the same mode. Thus, Strobbia (2003) stated that different modes defined different regions, and this should be taken into consideration when designing experiments.

2.5.2.3 Apparent dispersion curves

Apparent dispersion curves arise due to modal superposition in the experimental data. Therefore, to consider the different modes during the inversion stage, multi-modal modelling is necessary (Strobbia, 2003). The inversion of a such a model poses difficulties due to jump discontinuities between the different modes, which are highly variable in nature. Strobbia (2003) suggested isolating the modes firstly and thereafter conducting a multi-modal inversion of each mode. However, mode identification tends to be challenging and may result in unstable results.

To overcome this problem, Leong and Aung (2013) proposed a forward modelling technique, known as the Weighted Average Velocity Method (Wave). Essentially the Wave method calculated the effective Rayleigh wave velocity (V_ϕ) in a layered profile for an assumed wavelength using weighting factors. The shear velocities in each layer down to a depth

corresponding to the assumed wavelength influenced the V_ϕ. The weighting factors fundamentally act as area ratios for the probed layer over the total layers contained in that wavelength domain. Using a β reduction factor incorporated in the weighting factors, it is possible to construct credible theoretical dispersion curves for soil profiles that 'excite' modes without having to identify modes.

2.5.2.4 Number of dispersion points

As mentioned previously, the quantity of information held in different frequency bands is not constant and therefore various sampling methods may need to be used. Strobbia (2003) stated that at low frequency bands, the points were independent and each point in the range provided more information. Nevertheless, points in the high frequency bands are dependent upon one another and reproduce duplicates of the same information. Therefore, more points in the lower frequency band compared to higher frequency bands would provide a more informative dispersion curve.

2.5.2.5 Number of layers

The number of layers incorporated in the inversion of the experimental dispersion curve influences the results. Strobbia (2003) compared the effects of inducing different number of layers during the inversion stage for a homogeneous site consisting of a sandy profile resting on gravel. Two inversion cases were considered. The first inversion consisted of implementing 6 layers with equal thicknesses, as shown in Figure 2.40.
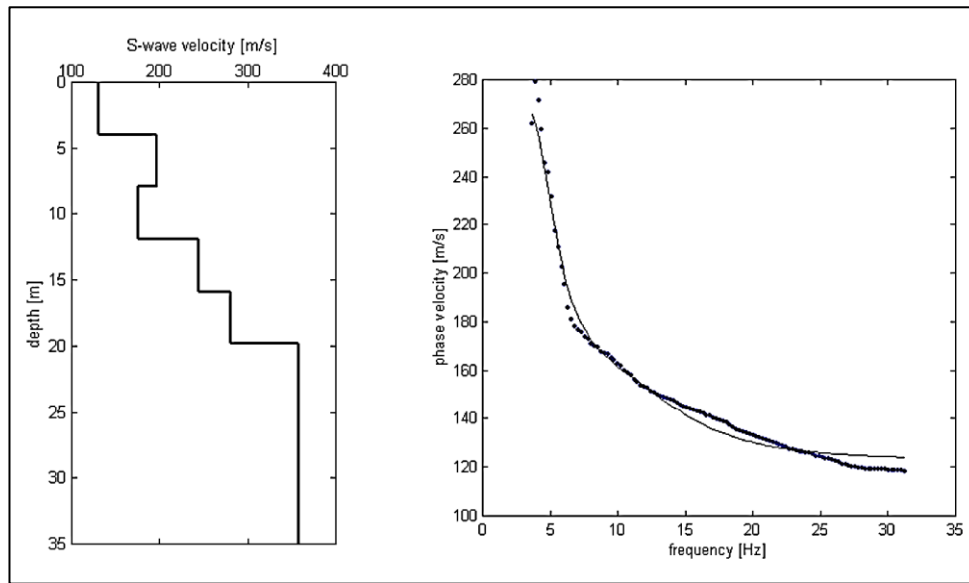
Figure 2.40: Resulting V$_S$ profile (left) and fitting of the dispersion curves for best model with 6 layers (Strobbia, 2003).

From Figure 2.40, it was evident that the fitting of the experimental dispersion curve suffered difficulties in the higher frequency regions due to the inadequate number of layers defining the shallower regions. Due to the insufficient number of layers in the shallow regions, the Vs profile depicted sharp variations (Figure 2.40, left), which was not the usual characteristic for that specific profile. Thus, a second inversion with 10 layers was conducted to rectify the error encountered in the higher frequency regions (Figure 2.41). The resulting fit improved significantly compared to before and the shear wave velocities displayed a gentle increase with depth as expected. Although, the thicknesses of each layer still needed to be tuned, the results were deemed acceptable. If one were to keep increasing the number of layers, the resulting model would begin to follow the shape pattern of the dispersion curve. However, as the number of layers increase, the deeper layers tend to lose resolution and remain unresolved (Strobbia, 2003).
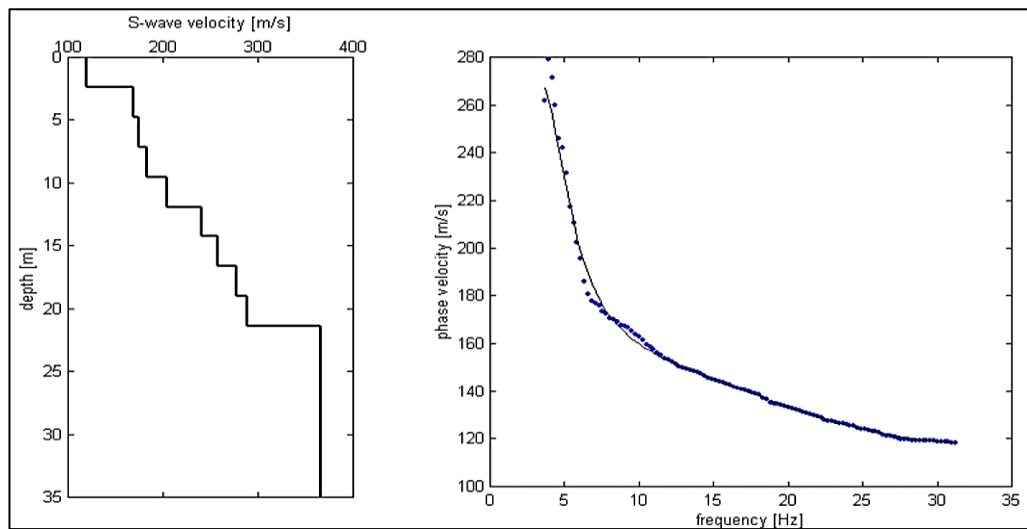
Figure 2.41: Best model for inversion with 10 layers along with the fitting of the dispersion curves (Strobbia, 2003).

2.6   USE OF LOVE WAVES FOR SITE CHARACTERIZATIONS

The research and development conducted on surface wave methods for geotechnical exploration utilizing Rayleigh waves is extensive. However, the application of Love waves in the field of geotechnical site investigations is reasonably new and only recently is it receiving attention (Martin *et al.*, 2014). Love wave surface tests were not considered primarily due to the two reasons: challenges faced in generating shear horizontal waves to a good degree as well as convenience of available equipment (Love wave detection require horizontal geophones which is typically not the standard equipment for seismic tests) (Foti *et al.*, 2018). However, over the last two decades a fairly wide literature pertaining to SAS_LW and MAS_LW using Love waves has brought some focus to these areas through publications by Strobbia (2005), Safani *et al.* (2005), Eslick *et al.* (2008), Xia *et al.* (2012) and Martin *et al.* (2014)

The generation of Love waves requires a source type that can achieve horizontal displacements parallel to the ground surface. An example of an impact source commonly used is the horizontal traction shear- beam, which essentially is a horizontal beam secured in place by a heavy vertical load and produces shear horizontal waves when struck by a hammer (Foti *et al.*, 2018). Other variants of the shear-beam exist, such as the hammer impact, aluminium, shear wave seismic source (Haines, 2007) and the "golf shoe" source (Hasbrouck, 1983). Harmonic sources, such as massive horizontal vibroseis can also be implemented to produce Love waves. Such sources allow the control of the frequency generated as well as the duration for which the signals are

applied, increasing the signal to noise ratio of the recordings. However, due to portability constraints and costs, harmonic sources are rarely pursued during tests (Foti *et al.*, 2018).

Martin *et al.* (2014) conducted MASW tests using both Love waves and Rayleigh waves at sites with different stratigraphy conditions. From his results, Martin *et al*. (2014) concluded that certain types of sites were better characterized using a Love wave approach than a Rayleigh wave approach: sites with a sudden increase in the Vs at shallow profile, such as a shallow rocky site, sites with steep Vs gradients and sites with thin low velocity layers positioned below stiffer sediment layers. All the above-mentioned sites resulted in generating higher modes for the Rayleigh wave but only the fundamental mode was generated for the Love wave as shown below in Figure 2.42.
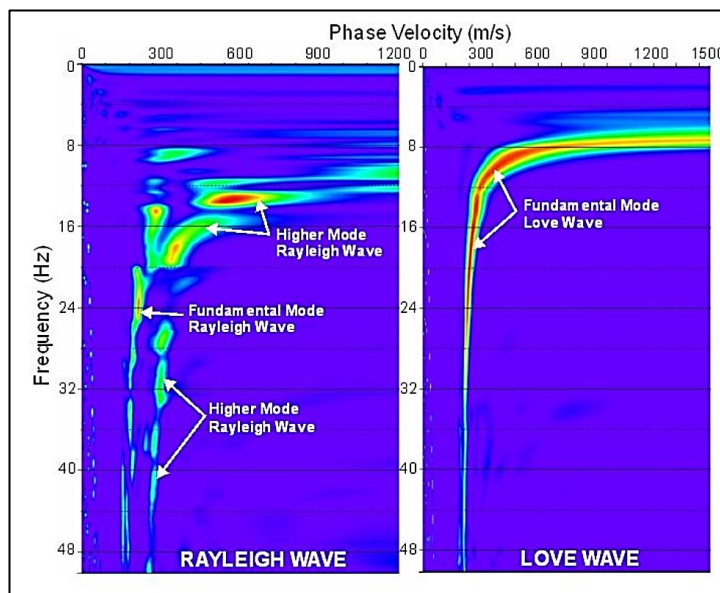
Figure 2.42: f-v spectrums of Rayleigh wave and Love waves for shallow rocky site (Martin *et al.* 2014).

From Figure 2.42, it could be seen that for the Rayleigh wave dispersion data only, the fundamental mode was dominant at frequencies greater than 17 Hz. In contrast, using the Love wave data, the fundamental mode was consistently dominant for the entire frequency range and thus, the Love wave data was used for the inversion stage. This agreed with the results obtained by both Safani *et al*. (2005) and Strobbia (2005) who both concluded that Love waves were less susceptible to higher mode generations.

The inversion of the Love wave dispersion data follows the same principles as that applied when conducting an inversion based on Rayleigh wave dispersion data. However, Foti *et al.* (2018) stated that the approach for the forward solution for Love waves was different to that of Rayleigh waves. Due to the ability to conduct discrete inversions with Love wave data, predicted best models computed using both Rayleigh and Love waves separately could be compared. This approach isolated Vs as the only parameter as Love waves were entirely dependent on the S-velocity distribution (Foti *et al.*, 2018). Thus, this introduced a secondary approach where Love and Rayleigh wave data are both inverted together at the same time, known as a joint inversion. A joint inversion approach intuitively lessens the non-uniqueness of the inversion problem as a boundary to the shear velocity can be effectively added due to the property of Love waves. However, Foti *et al.* (2018) stated that different portions of each respective dispersion curve contributed to varying extents and therefore, weights should be assigned for the dispersion curves during the joint inversion.

Although some researchers have investigated site characterization using Love waves, fundamental questions, such as near field effects and limitations due to source frequency are still yet to be explored (Foti *et al.*, 2018).

2.7   SUMMARY

A literature review on the different aspects of seismic surface wave testing was conducted in this chapter to acquire a deeper understanding of these techniques. These aspects include the different types of seismic waves and their respective wave characteristics, the three fundamental stages that structure every seismic surface wave test including an in-depth discussion of the various elements that forge each of the stages. A revision of the current utilization of Love waves for characterizing sites was also addressed in this chapter.

On account of the literature review, it could be concluded that a substantial amount of work and research had been conducted on the implementation and analysis of seismic surface wave tests involving Rayleigh waves specifically. Notwithstanding, Love wave techniques for site characterization have been explored to some extent. However, the majority of the approaches involving Love waves were based on MASW procedures, which implemented impulsive sources with little control over the frequency content. Therefore, this study will consider implementing an active Love wave harmonic source and in addition the effect of joint inversion of Rayleigh wave and love wave dispersion data to estimate the V_S profile will be investigated.

2-61

The study will also consider synthetic dispersion data to investigate the performance of the discrete and joint inversion runs. As stated by Foti *et al.* (2018), the inversion problem is ill posed due to the non-uniqueness leading to multiple solutions that provide similar fits to the experimental dispersion curves. Therefore, additional experimental data may be proven to be beneficial during the inversion process. To evaluate and compare the quality of the results, CSW tests implementing both Rayleigh and Love waves will be considered along with SASW tests incorporating both Rayleigh and Love surface waves. The experimental work for the study was adapted from the literature with a few modifications in the procedures. Joint and discrete inversions were addressed during the inversion stage.

Thus, the literature review formulated the hypothesis of this study, which is as follows:

"A joint inversion, which incorporates both Rayleigh and Love waves, depicts a better estimate of the Vs profile compared to a discrete inversion, which uses Rayleigh waves alone"

3   EXPERIMENTAL WORK

The purpose of this chapter is to present the experimental work that was adopted to attain the necessary data for the validation of the hypothesis. For this study, only CSW and SASW tests were conducted at two test sites in view of employing both Rayleigh and Love waves at each respective test site. The experimental work consisted of six principal parts namely identifying the test site location, developing the test specifications, the acquisition of the data, the processing of the data, the inversion of the data and lastly an analysis of the synthetic data. The first section provides an insight into the different locations where the tests for this research were conducted. Section 3.2 focuses on establishing the different parameters and configurations that were employed during each test. Test specifications were determined based on the literature reviewed. Section 3.3 discusses the different testing equipment's utilized for the tests. An insight on the processing of the acquired data through computer code to obtain the respective experimental dispersion curves is presented in Section 3.4. Subsequently, the approximation of the experimental dispersion data through the inversion process is outlined in Section 3.5. Lastly, Section 3.6 discusses the generation and the inversion of the synthetic dispersion data using discrete and joint inversions methods.

3.1   TEST SITES

TEST SITE 1: ENGINEERING 4.0

The grounds at Engineering 4.0 at the Hillcrest Campus, University of Pretoria, South Africa was selected as the first field test location (Figure 3.1). Test pit excavation logs up to a depth of 3 metres were available from Crossman, Pape and Associates at 21 test pit locations in and outside the perimeter of Engineering 4.0. 3 metres was the limit of the back actor used to excavate the test pits. As the surface wave tests were conducted near the existing dense bushes, the Test Pit 19 (TP19) and Test Pit 20 (TP20) profiles were used for assessment purposes during the analysis stage (Figure 3.2). The location of this site was selected such that the ambient noises were reasonably low, thereby increasing the signal to noise ratio (SNR) for the tests. This was beneficial, particularly for SASW tests, where a high SNR is required for quality data.
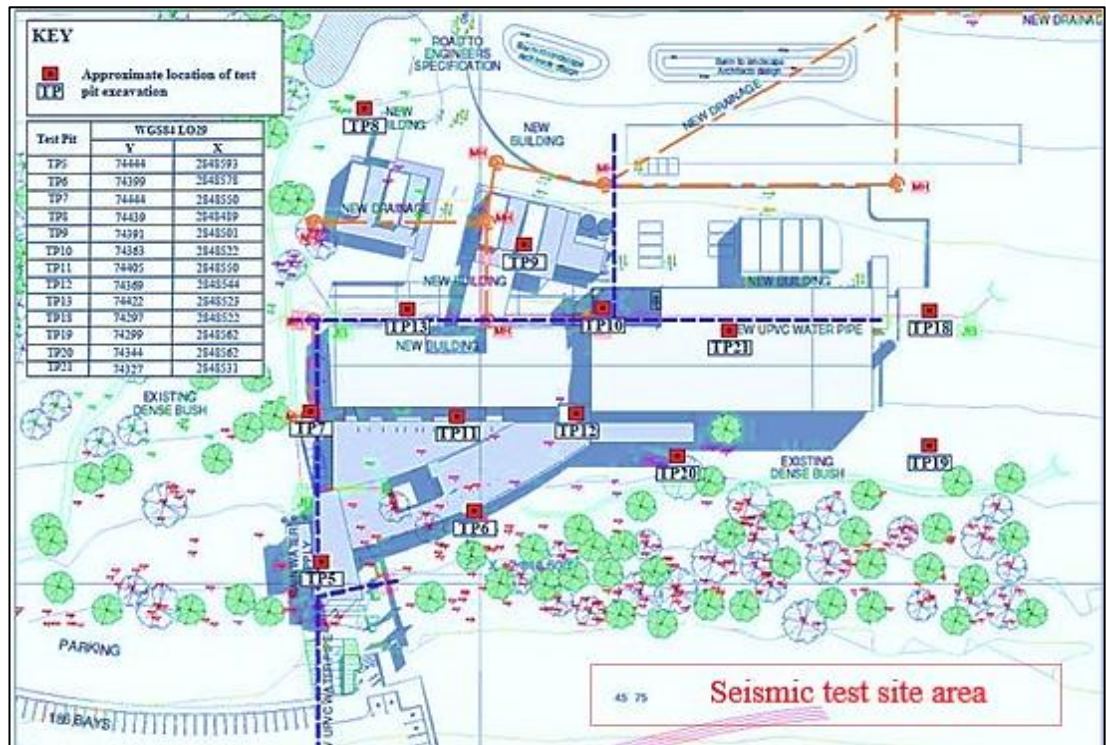
Figure 3.1: Site plan for Engineering 4.0 with respective test pit locations (Crossman, Pape and Associates).
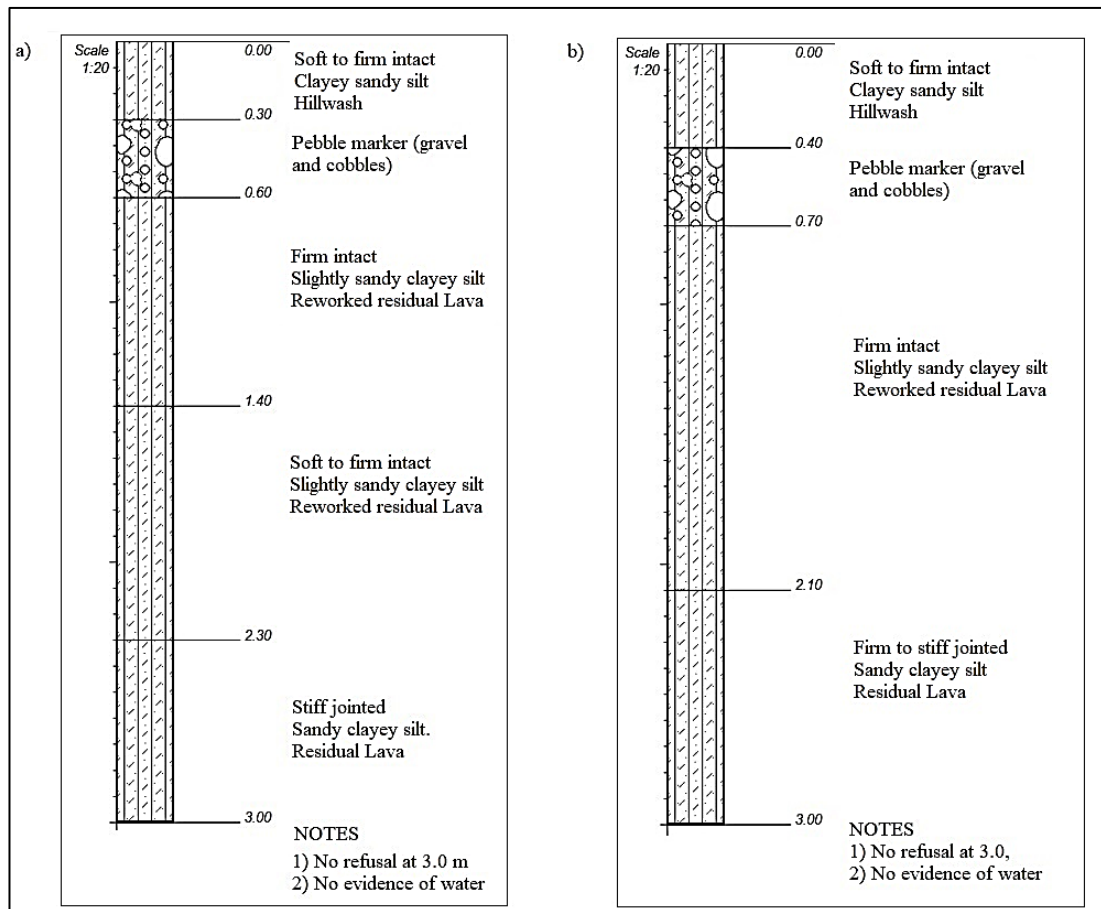
Figure 3.2: Engineering 4.0 lithologic results for test pit positions a) TP19 and b) TP20.

Existing geological maps indicated that the site area was underlain by residual andesite (lava) of the Hekpoort formation, Pretoria Group. This was reaffirmed through the test pits. According to the geotechnical investigation report by Crossman, Pape and Associates, the general soil profile at Engineering 4.0 comprised of:

- Upper soil layer of soft to firm intact clayey silty sand/ clayey sandy silt (0.3 m – 0.6 m)
- Transported pebble marker underlying the upper soil layer, consisting of soft to firm intact clayey silty sand with abundant quartz and quartzite gravel and cobbles (0.5 m – 0.9 m)
- Reworked residual lava (andesite) underlying the pebble marker layer, consisting of soft to firm/firm intact/ weakly ferruginised sandy clayey silt (2.1 m – 2.9 m)
- Residual lava (andesite) layer underlying reworked zone consisting of firm to stiff/ stiff jointed sandy clayey silt (3.0 m and below).

The description of the profile indicates that the origin of the material below the pebble marker is residual andesite lava. The description also indicates that the stiffness increases with depth as the level of weathering decreases. This implied that the test site exhibited a normally dispersive behaviour with regards to the dispersion of seismic waves. The existence of the andesitic layer was confirmed by Figure 3.3. It is known from geological maps that the residual andesite in the area is extensive, and it can therefore be assumed that the stiffness of the profile increases with depth as the degree of weathering decreases down the bedrock. Additionally, no perched water tables or seepage zones were confronted during the test pit excavations. The selected seismic test site was reasonably flat with vegetation on the either side comprising of grass and thick scrub vegetation as shown in Figure 3.4.
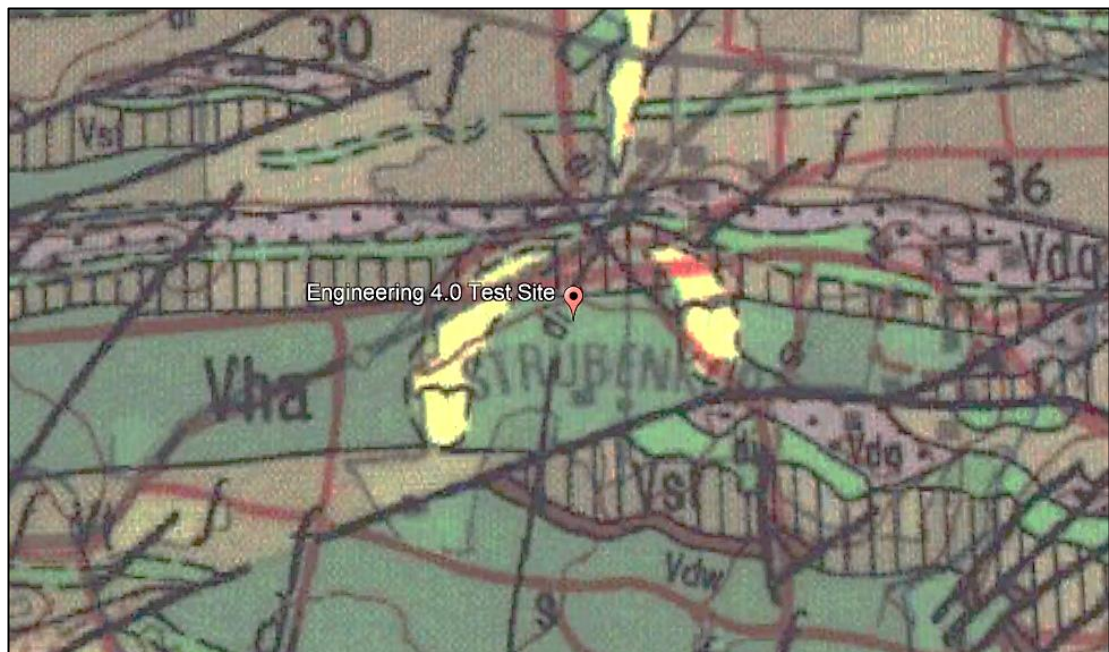
Figure 3.3: The geology underlying the Engineering 4.0 test site (Council for Geoscience, 2008).
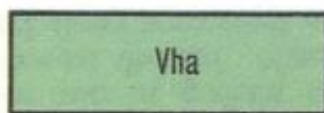
Andesitic lava, locally with interbedded agglomerate, shale and tuff.

a) View from east to west along centreline

b) View from west to east along centreline

Test site coordinates: 25°44'36.6"S 28°15'35.2"E

Figure 3.4: View of Engineering 4.0 testing site from test centreline.

TEST SITE 2: WIND AFRICA TEST SITE

The second test site was situated at the Freestate province in South Africa inside a bentonite mine currently operated by the Yellowstar Mining company. The test site primarily consists of stiff to very stiff weathered and expansive sandy silty clay owing to the high percentage of montmorillonite present in the soils. From the borehole logs, it was observed that the profile contained residual soils produced from intense weathering. The selected test area was reasonably flat with short vegetation on either side comprising of grass as shown in Figure 3.5. Additionally, two borehole excavation logs up to depths of 16.5 metres and 15 metres were available from the Davel & Van Huyssteen Consulting Engineering Geologists firm as shown in Figure 3.6.

a) View from east to west along centreline

b) View from west to east along centreline

Test site coordinates: 27°15'15.9"S 27°16'01.2"E

Figure 3.5: View of Wind Africa testing site from test centreline.
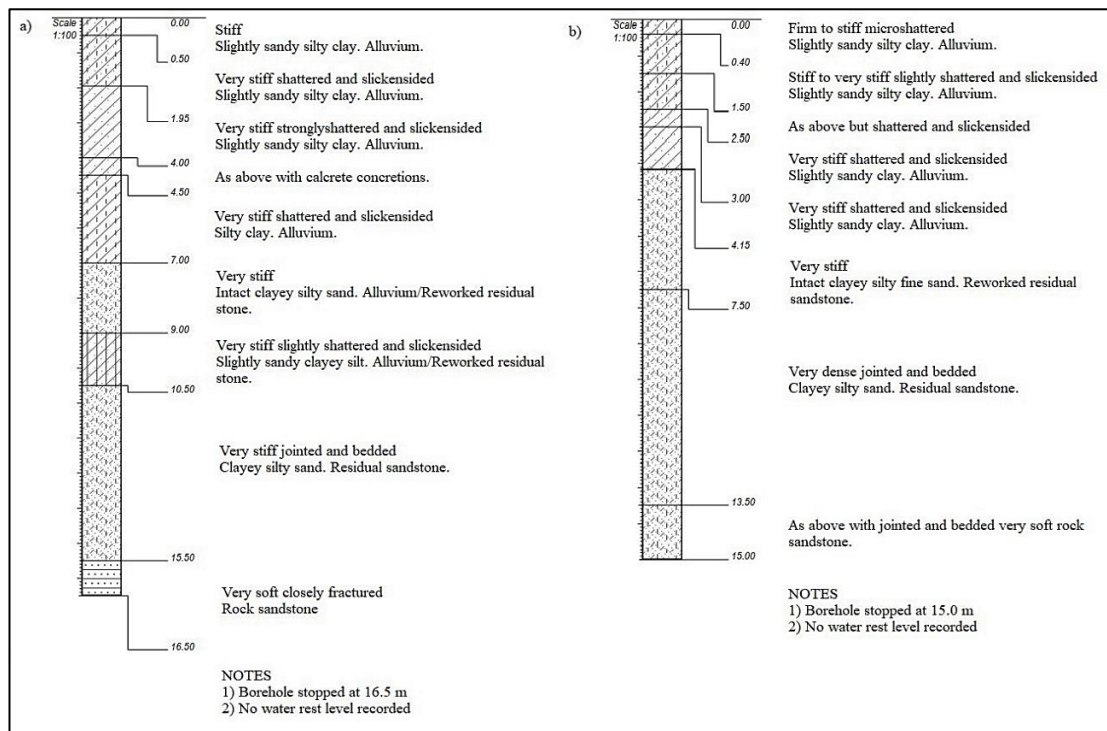
Figure 3.6: Wind Africa borehole lithologic results for boreholes a) BH1 and b) BH2.

SPT N values were available for both boreholes at the Wind Africa test site (Figure 3.7). Through examination of the SPT N data, it could be seen that in general the SPT N values increased with depth, indicating an increase in stiffness with depth. This suggested that the profile at the test site is normally dispersive in terms of the dispersion of seismic waves. Bulk and dry densities for the test site were available up to a depth of 6 metres from auger samples (Table 3.1). It was observed that both the bulk and dry densities were relatively consistent for the depth of investigation. On account of the remote location of the test site, the site was quiet resulting in a high signal to noise ratio (SNR). This was particularly useful for the SASW tests.
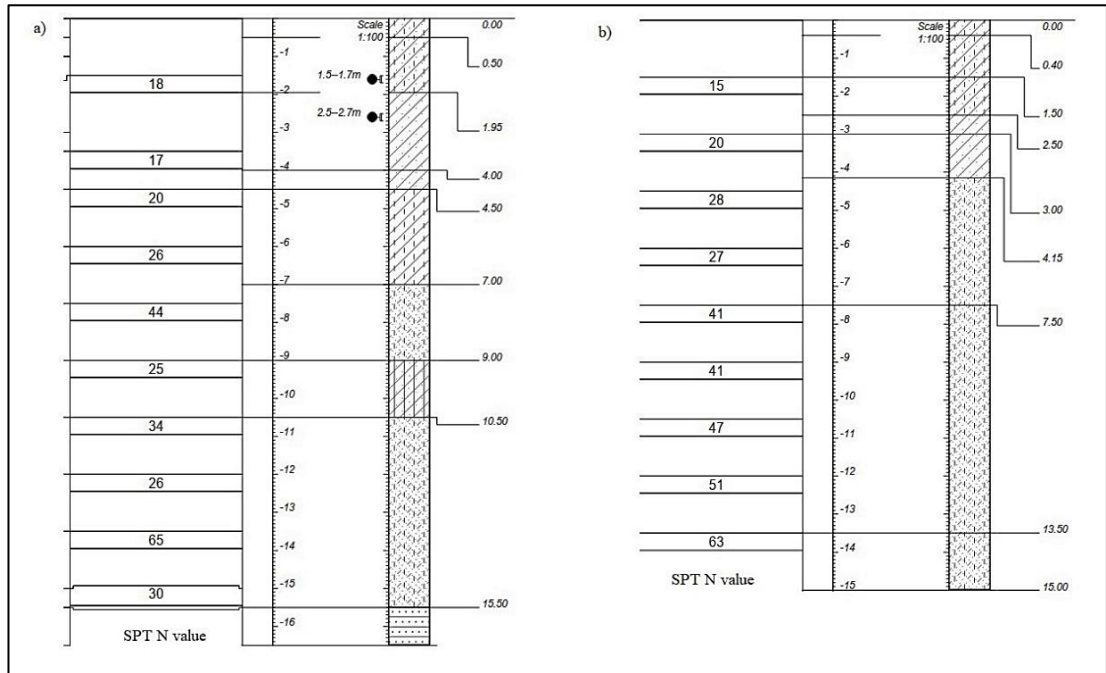
Figure 3.7: Wind Africa SPT N results for boreholes a) BH1 and b) BH2.

Table 3.1: Auger sample density results for Wind Africa test site.

Depth below surface(m)	Bulk Density (kg/m^3)	Dry Density (kg/m^3)
1	1689	1401
2	1823	1508
3	1699	1355
4	1780	1448
5	1805	1462
6	1777	1534
Average density (kg/m^3)	1762	1451
Average unit weight (kN/m^3)	17.29	14.24

A summary of the two test sites with respect to their locations is shown below in Figure 3.8.

Figure 3.8: Test site locations for the study.

3.2   TEST SPECIFICATIONS

3.2.1   Continuous Surface Wave (CSW)

- 5 vertical and 5 horizontal geophones were employed for the procurement of Rayleigh and Love wave data respectively as suggested by Heymann (2007) (Figure 3.9).

- According to Strobbia (2003), lower frequency ranges should incorporate more points compared to higher frequency ranges. Therefore, the following incremental steps were applied during the harmonic signal tests:
    - 0.5 Hz steps for 10 Hz to 20 Hz
    - 1.5 Hz steps for 20 Hz to 45 Hz
    - 2 Hz steps for 45 Hz to 70 Hz
    - 3 Hz steps for 70 Hz to 90 Hz

- For different frequency ranges, the sampling frequency and acquisition time were varied to allow clear acquisition of the seismic signals.

- Source offsets of 1 m, 2 m and 4 m were employed to keep consistent with SASW test specifications where the source offset was doubled each time.
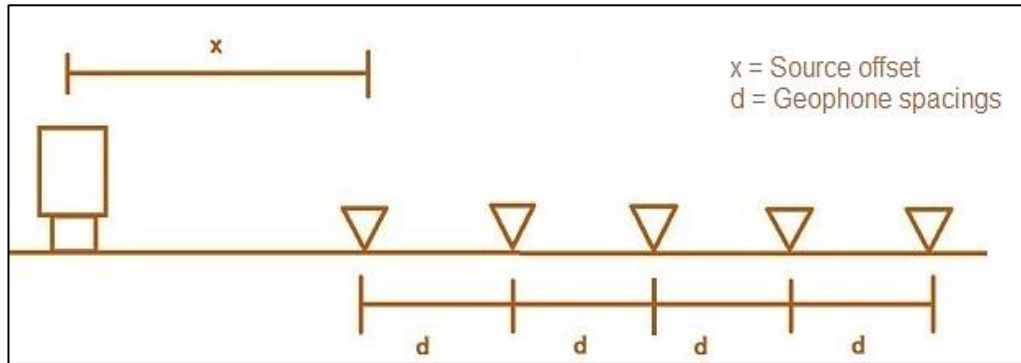
Figure 3.9: CSW test configuration.

Table 3.2 presents the different parameters that were exercised during the CSW tests.

Table 3.2: CSW Specifications.

Parameter	Value	
Geophone spacing, d	1 m (geophone array length of 4 m)	
Source offset, x	1*d, 2*d & 4*d	
Sampling frequency	< 22 Hz	500 Hz (2 ms)
	22 Hz - 50 Hz	1000 Hz (1 ms)
	50 Hz -90 Hz	2000 Hz (500 µs)
Acquisition time	< 22 Hz	10 s (steady state signal)
	22 Hz - 50 Hz	5 s (steady state signal)
	50 Hz -90 Hz	3 s (steady state signal)
	15 s (transient signal – linear sweep)	

3.2.2 Spectral Analysis of Surface Wave (SASW)

- 2 vertical and 2 horizontal geophones were used for the SASW test as suggested by (Svensson and Möller, 2001).
- A wide range of frequencies are generated through sledgehammers. Thus, to evaluate the characteristics of these sledgehammers, SASW tests were conducted up to spacings of 32 m using sledgehammers. Stokoe *et al.* (2004) mentions that for spacings greater than 8 m, impulse sources with masses of 100 kgs or more should be used. However due to availability of resources, SASW tests were only performed using sledgehammers.

- The common receiver midpoint layout was implemented for distances between the source and the geophones ranging from 1 m to 32 m as Svensson and Möller (2001) stated that this layout provided optimum results. During the test, an imaginary centreline was fixed between the two geophones, and this served as the reference line from which the geophone spacings, d was varied (Figure 3.10). The configuration displayed in Figure 3.10 was only for illustrative purposes, and the actual SASW tests were conducted up to spacings of 32 m.

- To evaluate any lateral variations in the soil medium, two shots (forward and reverse shots) were performed during the test for spacings up to 8 m. For larger spacings (> 8 m) a forward shot was conducted only, in accordance with the setup presented by Lin (2007). During each shot, a total number of 4 strikes was used to allow stacking of the data as a means reduce any influence of background noise.
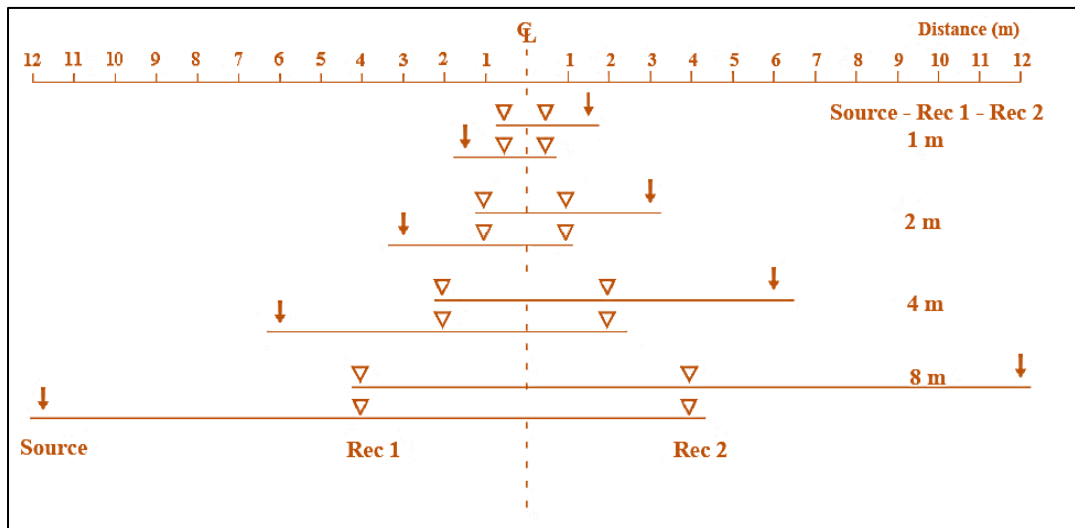
Figure 3.10: SASW test configuration up to 8 m.

The parameters that were applied for the SASW tests are shown in Table 3.3.

Table 3.3: SASW Specifications.

Parameter	Value
Geophone spacing, d	Common receiver midpoint layout
Source offset, x	$x = d$
Sampling frequency	2 ms (500 Hz)
Acquisition time	2 s

3.3 ACQUISITION OF DATA

3.3.1 Vibrating shakers

For the CSW tests, vibrating shakers were used to cover the different ranges of depth. A high frequency shaker (shallow depths) or a low frequency shaker (deep depths) was used for the test. Both shakers enabled the control of operating frequencies. Thus, this implied that different seismic energies could be applied either at once (steady state signal) or be varied over a set period (transient signal). To accommodate shallow depths during the investigation, a high frequency shaker comprised of a 14 kg electromagnetic actuator was used (Figure 3.11). Due to limitations in the deliverable energy of the shaker, the maximum frequency at which the shaker could operate was at 90 Hz: thereby, setting the upper frequency limit for the CSW tests. A lower frequency limit of 22 Hz was adopted for the CSW tests. Although the high frequency shaker could operate at frequencies less than 22 Hz, the quality of the energy delivered was inadequate and therefore, a lower limit of 22 Hz was used for the CSW tests.

Figure 3.11: High Frequency Shaker (Rayleigh Wave CSW test configuration).

Deeper depths of investigation were done using a low frequency shaker which incorporated a counter-balanced eccentric weight powered by a three-phase electric motor (1.5 kW), together with angular velocity control. The two eccentric weights had a total mass of 5.24 kgs with an eccentricity of 56 mm. In terms of frequency limitations, the shaker met a frequency bandwidth of 7 Hz to 22 Hz. For the CSW tests, a frequency range of 10 Hz to 22 Hz was adopted. All the system components of both shakers were embodied in a metal casing that was supported on an array of helix springs to improve the performance of the shakers. The metal casing was further painted to provide a protective coating for harsh environmental conditions. The low frequency shaker used for the CSW test is shown in Figure 3.12.
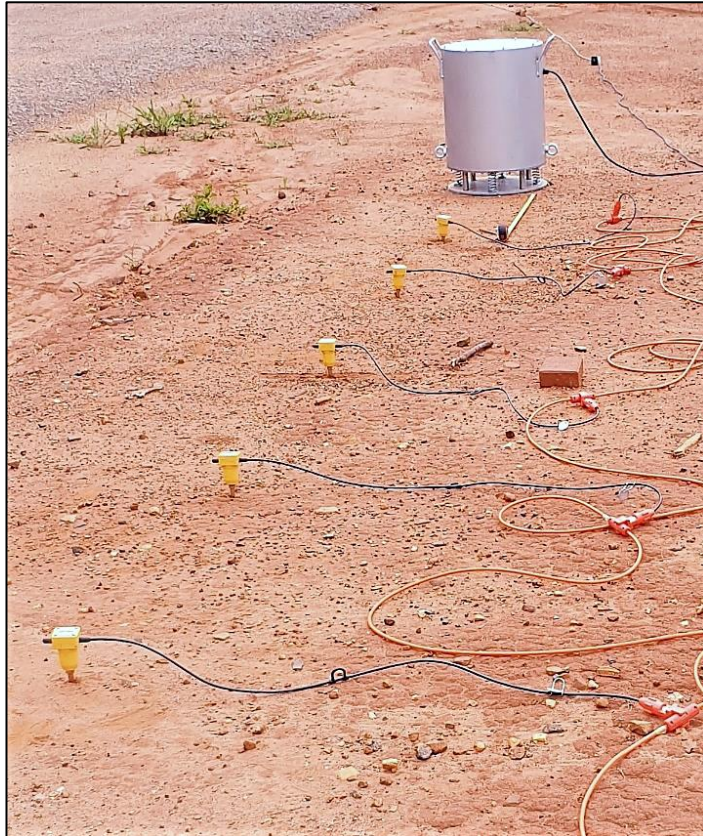
Figure 3.12: Low Frequency Shaker (Rayleigh Wave CSW test configuration).

A secondary device, known as the Variable Frequency Drive (VFD), was responsible for the conversion of the AC supply into the desirable frequency at which the shaker was to vibrate (Figure 3.13). The VFD controls a three-phase electrical motor, so the frequency displayed by the VFD is the frequency at which the motor is turning. The frequency at which the eccentric weights turned was governed by a turning belt, which was a fixed ratio relative to the frequency of the motor. As the VFD coordinated in a different frequency bandwidth (0 Hz to 50 Hz), a conversion factor had to be used when setting the frequencies on the VFD.

Figure 3.13: Variable Frequency Drive.

3.3.2   Love wave sources

For the generation of Love waves for seismic tests, two source variants were utilized to generate these surface waves. For the SASW tests, a steel impact source based on the design of the hammer impact, aluminium, shear wave seismic source by Haines (2007), was constructed for the generation of Love waves. The impact source comprised of 12 mm thick mild steel plates. Two impact plates and two longitudinal rails were welded to one baseplate, that contained shear spikes for coupling action. Two lengths of shear spikes were used with shorter shear spikes for firm ground conditions and longer shear spikes for soft ground conditions. Shear spikes were fabricated by grinding and machining the threaded ends of an 8 mm diameter (ø) bolt (Figure 3.14). To each impact plate, a 10 mm aluminium plate was bolted to act as a sacrificial plate during the tests (Figure 3.15). Furthermore, Haines (2007) states that by incorporating an aluminium plate in the design, the amount of noise delivered during each strike is reduced as well.

a) Shear spikes for coupling action

b) Short and long shear spikes for different ground conditions
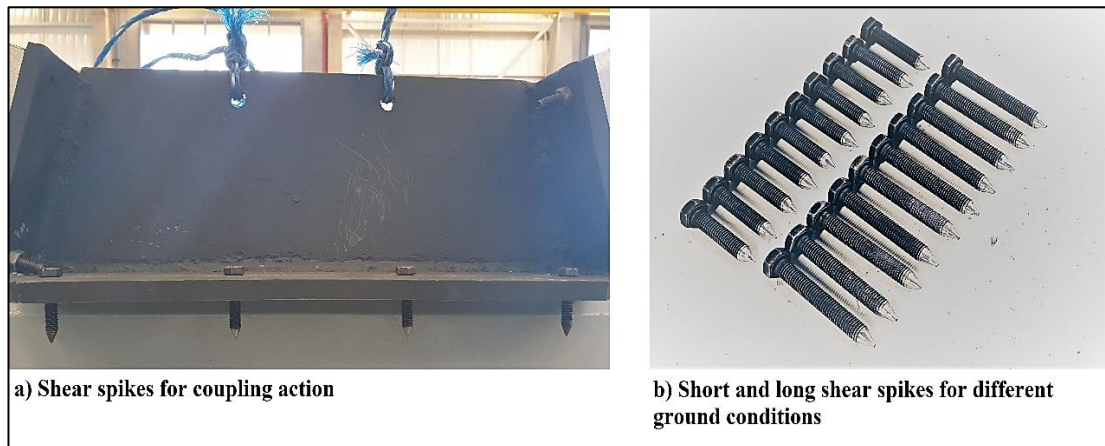
Figure 3.14: Use of shear spikes of varying lengths for coupling action.

Longitudinal Rail

Carrying rope

Aluminium impact plate

Base plate
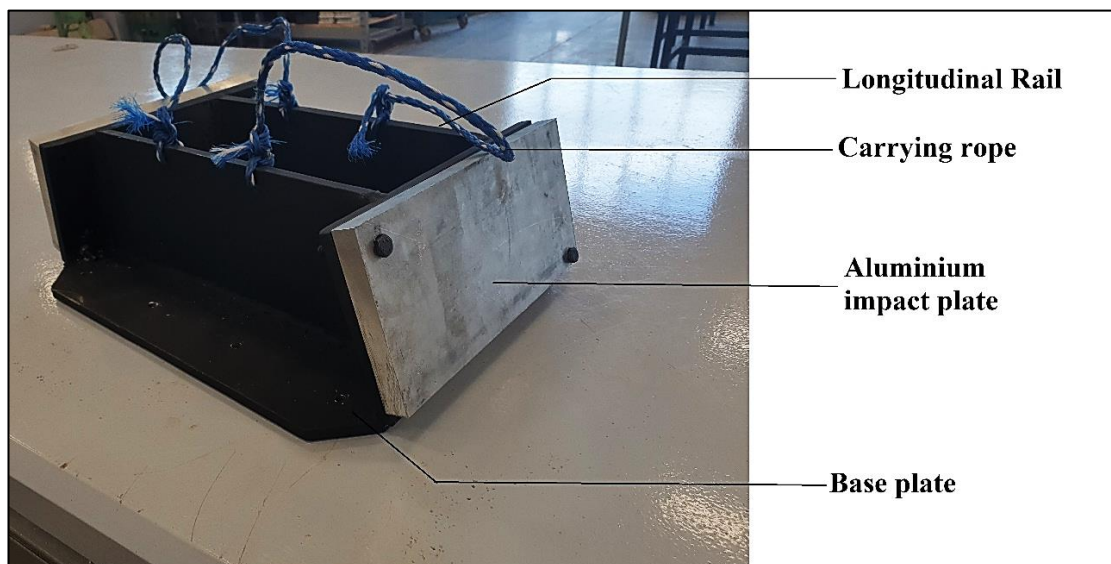
Figure 3.15: Love wave impact source (SASW tests).

The impact source weighed 34 kgs and contained drilled holes in each rail plate to insert ropes. This was done to assist with transporting the source. To effectively capture the swinging motion of the sledgehammer during each shot, the impact plates were angled at 74° on both sides. When conducting the SASW tests, the source was oriented with the direction of hitting parallel to the horizontal geophones to allow the shear horizontal movement to be recorded. Hence, the operator stood at right angles to the geophone array and hit the impact plates of the source in the same direction as the horizontal geophones as shown in Figure 3.16. A detailed description

of the fundamental parts used for constructing the steel impact source can be found in Appendix A.

a) Positioning of operator in relation to Love wave impact source

b) Layout of Love wave SASW tests
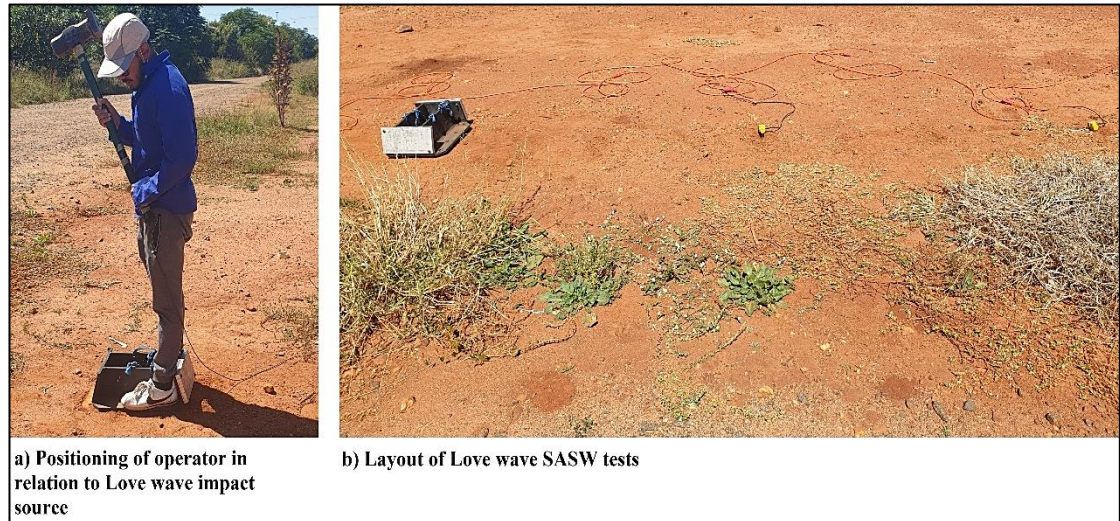
Figure 3.16: Positioning of Love wave impact source during SASW tests.

For CSW tests involving Love waves, the same high frequency and low frequency shakers mentioned in Section 3.2.1 were employed to deliver steady state and transient signals in the form of shear horizontal waves. A platform comprised of four wooden planks (1.22 m x 0.55 m), all held together through 11 steel screws, provided a supporting base for each of the shakers. Steel screws longer that the combined thickness of the platform was used, thereby protruding at the bottom of the wooden platform. The protruding steel screw tips provided shear coupling action. The shakers were then placed and strapped tight on the wooden platform at right angles to the horizontal geophone array and through the VFD, shear horizontal waves of different frequencies were generated. Figure 3.17 and Figure 3.18 shows the mechanism implemented for the generation of Love waves through the seismic shakers for CSW testing.

a) High frequency shaker strapped tight on to wooden platform

b) Right angle orientation to horizontal geophone array
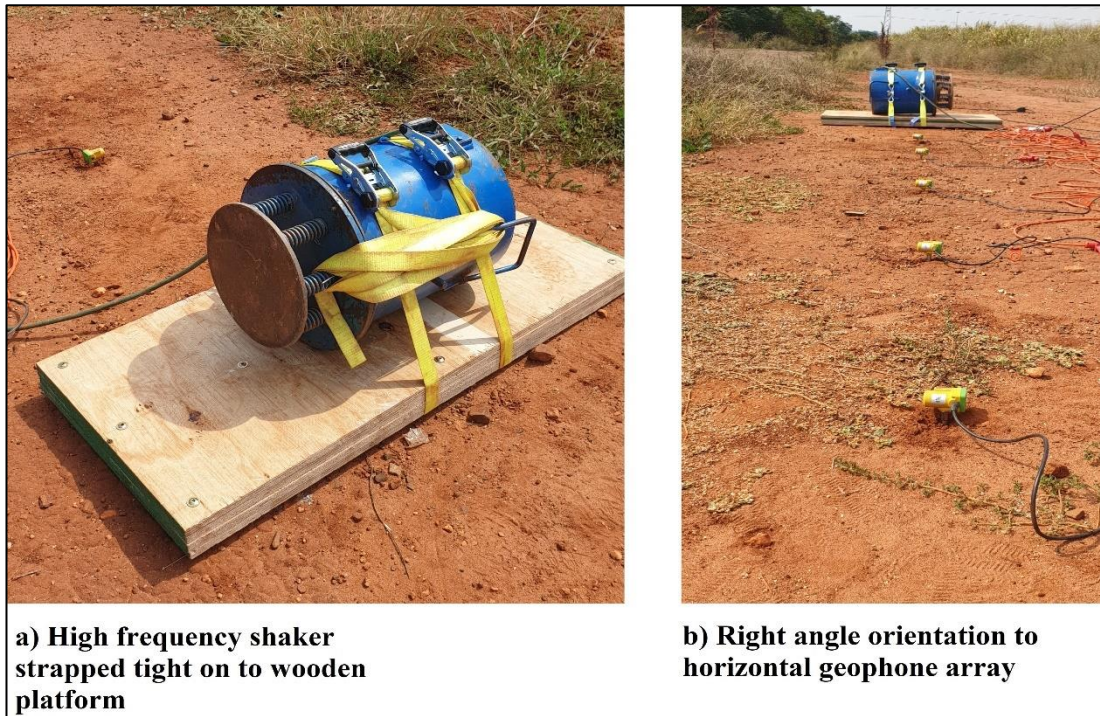
Figure 3.17: High frequency shaker setup for CSW using Love waves.

a) Low frequency shaker strapped tight on wooden platform

b) Right angle orientation to horizontal geophone array
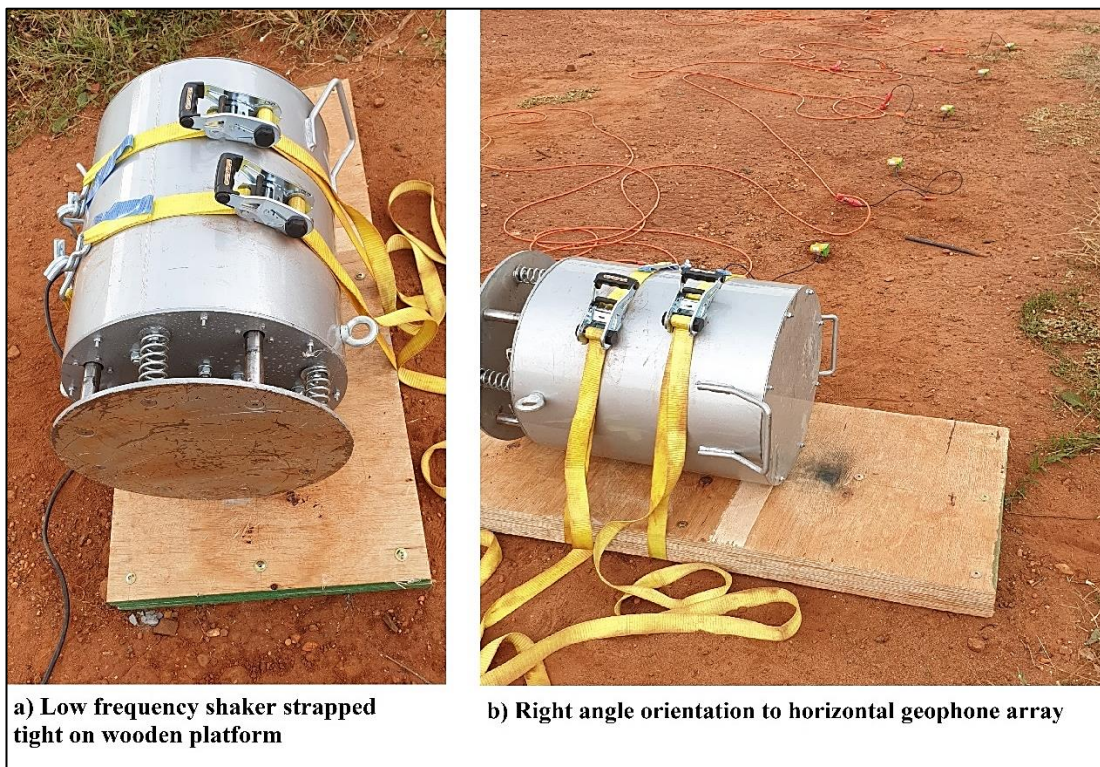
Figure 3.18: Low frequency shaker setup for CSW using Love waves.

3.3.3 Sledgehammers

In the study of the SASW tests, a number of sledgehammers was used to produce seismic energy over a range of frequencies. Literature states that different masses of impact sources generate different energy contents proportionally, consequently affecting the frequency range over which the energy is distributed. Lighter sources are recommended for higher frequency ranges – shorter arrays (shallow profile characterization) and heavier sources are to be employed for lower frequency ranges – longer arrays (deep profile characterization) (Rosenblad *et al.*, 2002).

The variants of sledgehammers used for the SASW tests in this study were as follows:

- 2 kg sledgehammer
- 6 kg sledgehammer
- 9 kg sledgehammer

To provide a fair comparison of the gathered data and consistency in terms of energy distribution and coherence of the sources, all three sledgehammers were employed for offsets of 1 m, 2 m, 4 m, 8 m, 16 m, and 32 m. At the same time, this allowed the characteristics of each sledgehammer to be evaluated and compared with one another.

For each individual sledgehammer, a trigger switch was taped to the head of the hammer. For Rayleigh wave SASW tests, each shot was registered by striking the sledgehammer on a 20 mm thick metal baseplate of 170 mm ⌀ (Figure 3.19). As the existing top surface at the Wind Africa test site was very stiff, the impact metal baseplate was buried 50 mm into the ground to improve the acquisition of the signals. For SASW tests involving Love waves, the sledgehammers were used to strike the aluminium impact plate of the seismic source as mentioned earlier in Section 3.3.2. The impact of the blow sent a signal to the trigger switch, which commenced the logging of the signals.

Figure 3.19: Characteristics of metal striking baseplate.

A 9 kg sledgehammer was not available, and it was necessary to construct the 9 kg sledgehammer at the workshops (Figure 3.20). This was achieved through welding an existing 6.4 kg hammer head to a 1.7 kg metal plate and reattaching it to the rubber handle. Figure 3.21 shows the three variants of sledgehammers used for the SASW tests.
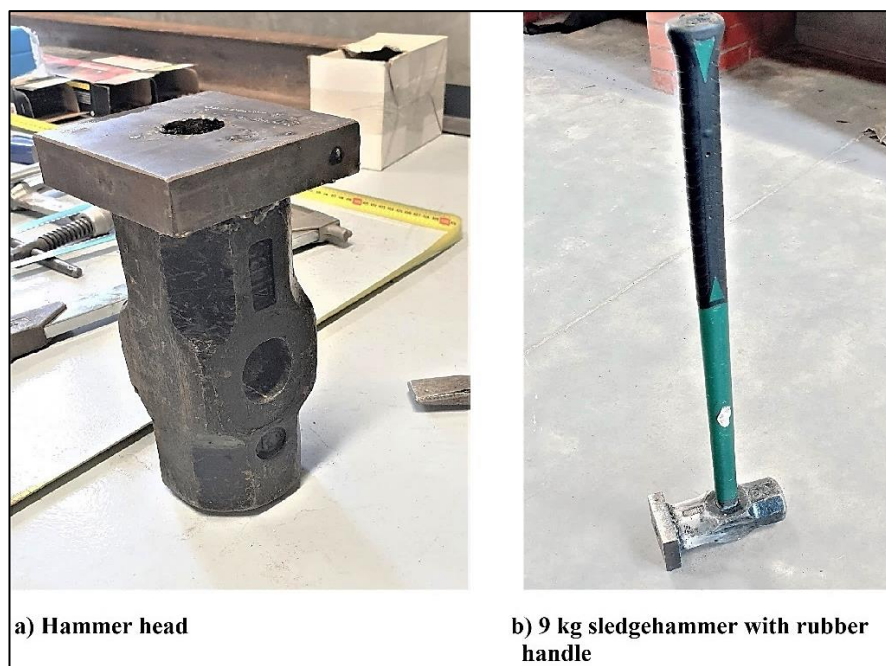
Figure 3.20: Design of 9 kg sledgehammer for SASW tests.

Figure 3.21: Sledgehammers used for conducting the SASW tests.

3.3.4   Geophones

The surface wave tests used two kinds of geophones- vertical geophones and horizontal geophones. The vertical geophones were applicable in tests where Rayleigh waves were measured, as is the case with most conventional surface wave tests (Figure 3.22). In contrast, horizontal geophones were used for detecting Love waves (Figure 3.23). Prior to the installation of the geophones, the top ground surface was prepared by removing any obstacles, to provide good coupling of the geophones. The horizontal geophones incorporated a horizontal level to assist the operator in inserting the geophones parallel to the ground surface. The study focused on frequencies between the range of 10 Hz and 120 Hz. It was therefore essential for the resonance frequency of the geophones to be below 10 Hz for a flat response over the test range. Therefore, vertical and horizontal geophones with a resonant frequency of 4.5 Hz were used.
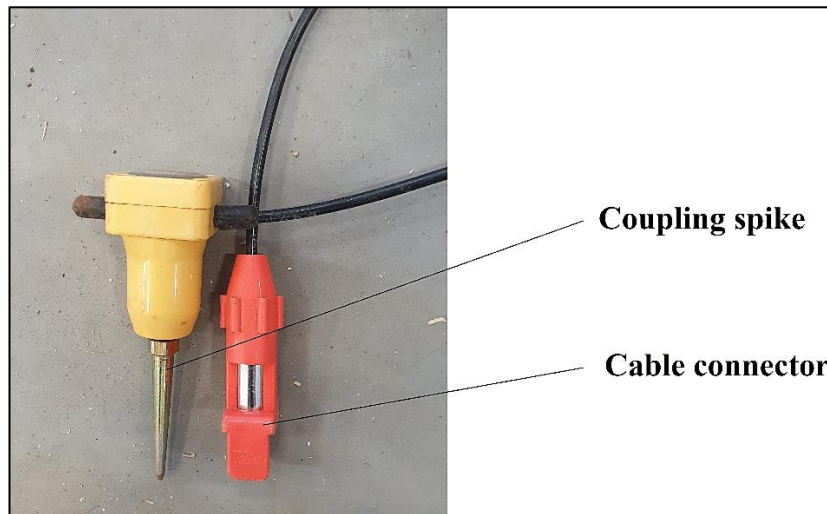
Figure 3.22: Vertical geophone 4.5 Hz for Rayleigh wave tests.

Figure 3.23: Horizontal geophone 4.5 Hz for Love wave tests.

3.3.5 Seismograph

The recording of the signals was accomplished with the use of a 24-channel seismograph developed by PASI. Acquisition parameters mentioned in Table 3.2 and Table 3.3 were entered manually before each respective test into the PASI Gea24 software, designed to be used together with the seismograph. Figure 3.24 shows a typical setup of the acquisition device components during a CSW test along with the various input channels found in the PASI Gea24 seismograph.

a) Typical setup of acquisition devices during a CSW Test

b) Input channels of PASI Gea24 seismograph
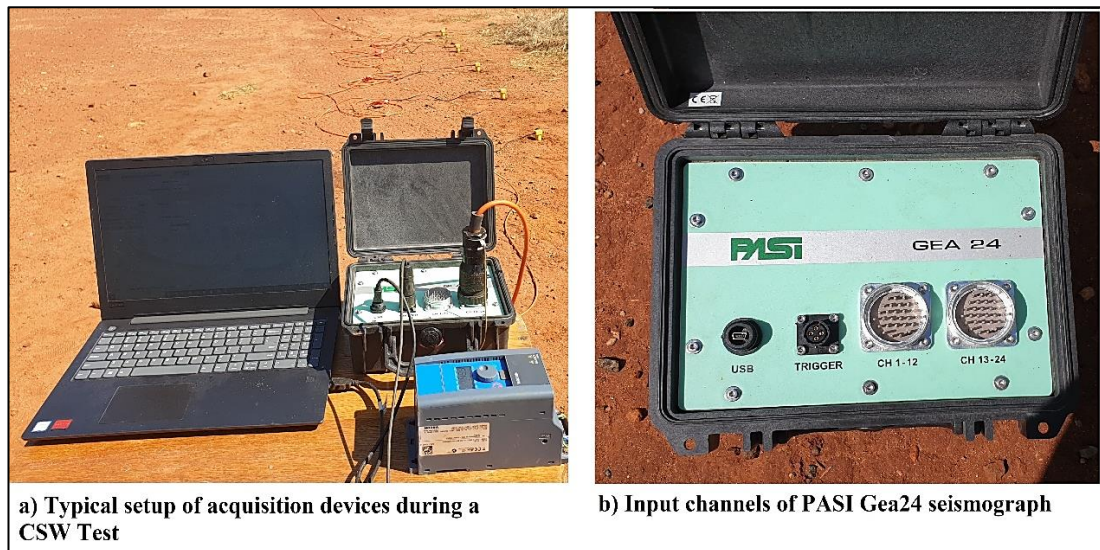
Figure 3.24: Typical setup involving the PASI Gea24 seismograph used for recording of the signals.

Along with the 24 channel inputs, the seismograph contained two other input parts namely the USB and the trigger. Power for the seismograph was supplied through the USB cable component which enabled the transfer of power into the seismograph from the laptop computer. The USB port also allowed data to be transferred from the seismograph to the laptop. On the immediate right of the USB input, the trigger was located which was responsible for initiating the recording of the signals. As SASW incorporates longer array lengths compared to CSW, extension cables for both the trigger and channels were required to be included in the experimental work, as shown in Figure 3.25. The channel extension cable was utilised for both tests as it served as connection points for the geophones.

a) Trigger extension cable   b) Channel extension cable
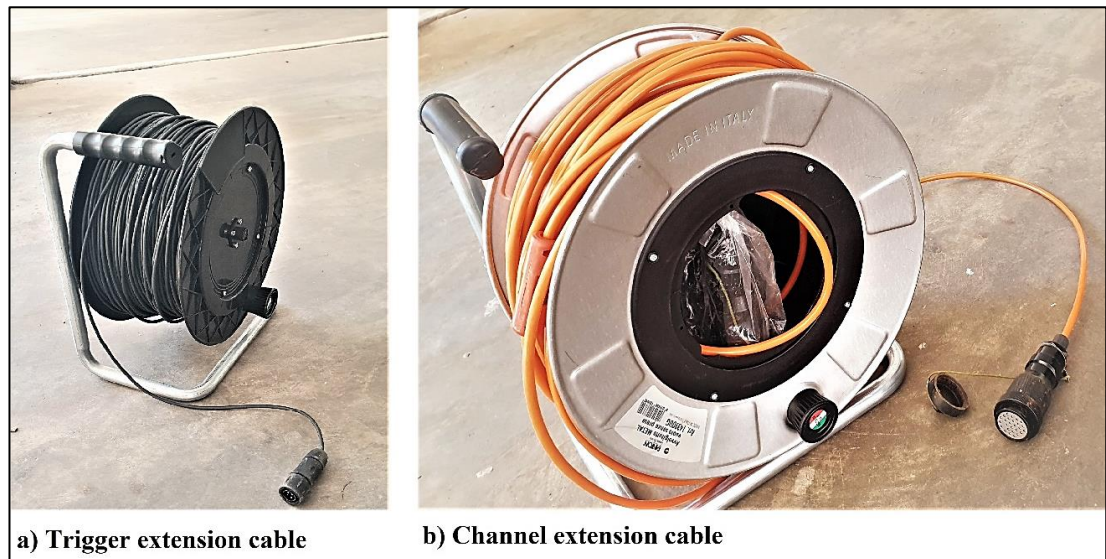
Figure 3.25: Cables used during signal recording.

3.4   PROCESSING OF DATA

3.4.1   CSW Python code

The signal processing of the CSW results was done using a Python based code developed by the author. The core component of the code ran on each individual file of a certain frequency and in its essence executed the following two functions:

1) identified the maximum Spectral Amplitude based on the frequency along with the respective index position; thus, establishing the shaker frequency
2) determined the phase angles at each geophone as well as unwrap any necessary phase angles in the Phase angle-distance plot to attain the phase velocity.

The CSW data files were each annotated with a frequency at which the shaker was assumed to produce active seismic energy. The files were individually opened and read, and the data was stored in a time variable (t) and geophone variables (g1 – g5).

As the signal data was stored in the time domain, it was necessary to implement a Fast Fourier transformation (FFT) to derive a frequency-based domain. By virtue of the FFT function (numpy.fft) of the Numpy module in Python, the domains of the signals were transformed. The magnitude squares of the Fourier values provided the spectral amplitudes at each frequency, enabling the researcher to pinpoint the dominant frequency of the seismic waves. As an extra

precaution against background noise, data within the proximity of the assumed shaker frequency was interpreted during inspection of the Spectral Amplitude plots. The maximum spectral amplitude and the associated frequency vector were identified and applied in Equation 3.1 to determine the phase angles at each geophone.

$$\varphi = \tan^{-1}\left(\frac{Im(z)}{Re(z)}\right)$$ (Equation 3.1)

where: φ = phase angle (rad)

   z = frequency vector at shaker frequency

Due to certain phase angles being wrapped at geophone locations, a second section of the code was responsible for unwrapping the angles. At each distinct jump, a multiple of 2π was subtracted, depending on the position of the jump in relation to the rest of the phase angles. Upon unwrapping the phase angles, a linear regression analysis was conducted on the phase angle against the distance of the geophones to determine the line of best fit together with the coefficient of determination (R^2) to evaluate the fit. The slope ($d\phi/dx$) of the best fit model was determined and used to estimate the phase velocity using Equation 3.2.

$$V = 2\pi \times f \times \frac{dx}{d\varphi}$$ (Equation 3.2)

where: V = velocity (m/s)

   f = shaker frequency (Hz)

   $\frac{dx}{d\varphi}$ = inverse of slope of phase angle distance regression line

Considering that the core component of the code only procured the phase velocities for each dominant frequency, it was necessary to automate the process for constructing the final dispersion curve. Thus, the core component of the code was embedded in a secondary code responsible for merging all the estimated phase velocities and their respective frequencies along with the R^2 values for each estimate. The estimated phase velocities were stored in the variable V, whilst the frequencies were stored in the variable f. In conjunction with the dispersion curve, a text file *(.txt)* containing the dispersion data was generated for any external application.

It should also be noted that the above Python code had been implemented in the analysis of CSW transient signals, with slight modifications in the code. The modified code involved

running through all the frequencies swept through during the 15 s acquisition time and determining the phase velocity at each of the frequencies upon unwrapping the respective phase angles. For analysing the transient signal data, the R^2 at each frequency was calculated together with the coherence of the signal between geophone 1 and geophone 5. This was necessary when it came to judging the quality of the data.

The full CSW code developed for the signal processing can be found in Appendix B.

3.4.2 SASW Python code

The data acquired for SASW was analysed using a Python based code, which facilitated the signal processing and included the spectral amplitude plot, the coherence plot, and the phase difference plot. Both forward and reverse shot data were inputted into the code, allowing each file to be opened and read. The time data was stored in the variable *t* and the averaged geophone data from the forward and reverse shots were stored in the variables *g1* and *g2*, with *g1* depicting the geophone closest to the source. It was noted that *g1* varied depending on the type of shot (forward or reverse) and this was accounted for in the code. By averaging the two shots, the influence of internal phase shifts between the two geophones was reduced (Alexander, 1992).

The NumPy library in Python enabled the domain transformations from time to frequency by utilizing the Fast Fourier transformation function, numpy.fft. This transformation allowed the Spectral Amplitude (magnitude squared of Fourier values) to be calculated for each geophone and plotted against each frequency. As the SASW test uses impact sources, the generated energy is distributed over a wide range of frequencies. Subsequently, the wrapped phase difference was derived using the cross-power spectrum of the two geophones. Equation 3.3 to Equation 3.5 were used to calculate the respective functions below.

$$A_{peak}(f) = +\sqrt{[Re(Y(f)]^2 + [Im(Y(f)]^2}$$ (Equation 3.3)

$$G_{YX}(f) = Y(f) \cdot X^*(f)$$ (Equation 3.4)

$$\Delta\phi_{wrap}(f) = \arctan\left(\frac{Im(G_{YX}(f))}{Re(G_{YX}(f))}\right) \cdot$$ (Equation 3.5)

where: $Y(f) = $ Fourier transformation at geophone 1

$X^*(f)$ = complex conjugation of Fourier transformation at geophone 2

$G_{YX}(f)$ = cross-power spectrum

A_{peak} = peak or spectral amplitude (volts)

$\Delta\phi_{wrap}$ (f) = wrapped phase difference (rads)

The coherence (γ^2) function was essential for the masking of the data in the phase difference plot. 'Masking' refers to the process of selecting acceptable data for the generation of the dispersion curve through evaluation of the coherence function. Therefore, the γ^2 between the two geophones were calculated using the signal module contained in the SciPy library and regions with γ^2 greater than 0.9 were inspected in the plot. When put in simple terms, the coherence measured the linearity of the relationship of the signals measured at the two geophones. These values ranged between 0 and 1, with 1 denoting a perfect linear relationship between the two geophones.

The Spectral Amplitude plot, the wrapped phase difference plot and the coherence formed the key components in selecting the frequency regions with quality data. Regions of high energies in the Spectral Amplitude plot were compared to regions with γ^2 greater than 0.9 to establish a match between the two regions from the plots. These regions were thereafter inspected in the wrapped phase difference plot to evaluate the quality of the signal data through inspection of the "sawtooth" pattern.

The end of the masking stage brought about the manual unwrapping of the phase differences. This segment of the code prompted the researcher to input index positions where the phase difference was required to be "unwrapped". Depending on the nature of the jump, a magnitude of 2π was either added or subtracted. Upon each unwrapping, a plot of the newly unwrapped phase was presented for visualising the phase differences over the masked frequency ranges.

Following the unwrapping stage, the surface wave velocity at each respective frequency was then calculated using Equation 3.6, upon which an individual dispersion curve for that geophone spacing was constructed. Additionally, the code compiled each dispersive data into a separate text file *(txt.)* for external use.

$$V = 2\pi \cdot f \cdot d \cdot \frac{1}{|\Delta\phi_{unwrap}|}$$ (Equation 3.6)

where: V = phase velocity (m/s)

f = frequency (Hz)

d = geophone spacing (m)

$\Delta\phi_{unwrap}$ = unwrapped phase difference (rads)

In accordance with the SASW literature, the final composite dispersion curve was assembled by merging each of the individual dispersion curves measured at each geophone spacing. The quality of the SASW tests was then inspected by observing how well the 'overlap' was between each of the individual dispersion curves.

Refer to Appendix B for a complete description of the SASW code.

3.5 INVERSION OF DATA

Following the generation of dispersion curves for Rayleigh and Love waves through the seismic surface wave tests, the experimental dispersion curve was used to estimate/recover the one-dimensional shear wave velocity profile of the chosen sites. This was achieved through the software, Dinver, which implemented Wathelets (2008) improved version of the Neighbourhood algorithm (NA). Version 3.3.6 of Dinver was used. Pseudo-random samples (each sample representing a set of parameters for one ground model) are generated by the NA in the parameter space from which the dispersion curves are approximated (forward model) for each model. A uniform probability density is set for the whole parameter space for which the limits are defined by priori ranges selected for the parameters. Computed results are compared to the experimental dispersion curves and a misfit value is calculated to indicate how far the computed model is from the actual solution. The parameter space is split into Voronoi cells and during each iteration a selected portion of Voronoi cells are resampled to locate models in promising areas of the parameter space. The software, Dinver (3.3.6) allows the tuning of the parameters which govern the NA such as adjusting the number of models generated by the NA (N_s) and the number of Voronoi cells holding data acceptable models (N_r) during each iteration.

Once the respective experimental dispersion data were input into the software, the phases of the dispersive curve (Rayleigh/Love) were selected providing the option of treating the inversion problem as a discrete or joint inversion scenario. A discrete inversion scenario utilizes only the Rayleigh wave dispersion curve during the inversion runs. On the contrary, a joint inversion scenario incorporates both the Rayleigh wave dispersion curve and Love wave dispersion curve for the inversion runs. Although discrete inversion runs employing Love waves alone are conducted occasionally, for this study two inversion scenarios were used:

1. Rayleigh wave discrete inversion
2. Rayleigh and Love wave joint inversion

Based on the experimental dispersion curves, the effective depth of investigation (z) was limited to $\lambda/2$ as stated in the literature (Hunter and Crow, 2015).

In the context of defining the inversion problem for the experimental dispersion data, a total number of ten layers and a half space was used with regards to both discrete and joint inversion cases. The Engineering 4.0 test site was assumed to have a fixed bulk density of 2000 kg/m^3 based on relevant literature. A fixed bulk density of 1800 kg/m^3 was chosen for the Wind Africa test site based on the auger sample data. From the literature, it was known that choice of density resulted in minor errors during the inversion (Park *et al.*, 1999; Strobbia, 2003). However, ranges for the primary wave velocity (Vp), the shear wave velocity (Vs), the Poisson's ratio (ν) and the bottom depth of each layer were inputted to narrow down the parameter space. As the Vp is linked to the Vs through the ν, emphasis was put on the choice of the Vs range. Wathelet *et al.* (2004) also states that the dispersion curves are more influenced by the Vs than the Vp, especially for the bottom half space layers where the Vp becomes negligible. It was assumed that the layers increased in thickness with depth. Table 3.4 and Table 3.5 show the search parameters that were used during the inversion runs for Engineering 4.0 and the Wind Africa test site respectively.

Table 3.4: Search inversion parameters for Engineering 4.0 test site.

Layer	Bulk density (kg/m^3)	Vp (m/s)	Vs (m/s)	Poisson's Ratio (ν)	Bottom Depth (m)
1	2000	100 - 1000	50 - 800	0.2 - 0.5	0.1 – 1.0
2	2000	100 - 1000	50 – 800	0.2 - 0.5	1.1 – 1.5
3	2000	100 - 1000	50 – 800	0.2 - 0.5	1.6 – 2.0
4	2000	100 - 2000	150 - 1500	0.2 - 0.5	2.1 – 2.5
5	2000	100 - 3000	150 - 3500	0.2 - 0.5	2.8 – 3.2
6	2000	100 - 4000	150 – 3500	0.2 - 0.5	3.5 – 4.5
7	2000	100 - 5000	150 – 3500	0.2 - 0.5	4.8 – 5.5
8	2000	100 - 5000	150 – 3500	0.2 - 0.5	5.8 – 6.5
9	2000	100 - 5000	150 – 3500	0.2 - 0.5	6.6 – 7.2
10	2000	100 - 5000	150 – 3500	0.2 - 0.5	7.4 - 8.0
Half Space	2000	100 - 5000	150 – 3500	0.2 - 0.5	Infinite

Table 3.5: Search inversion parameters at Wind Africa test site.

Layer	Bulk density (kg/m³)	Vp (m/s)	Vs (m/s)	Poisson's Ratio (ν)	Bottom depth (m)
1	1800	100 - 1000	50 - 800	0.2 - 0.5	0.1 – 1.0
2	1800	100 - 1000	50 – 800	0.2 - 0.5	1.1 – 1.5
3	1800	100 - 1000	50 – 800	0.2 - 0.5	1.6 – 2.0
4	1800	100 - 2000	150 - 1500	0.2 - 0.5	2.1 – 2.5
5	1800	100 - 3000	150 - 3500	0.2 - 0.5	2.8 – 3.2
6	1800	100 - 4000	150 – 3500	0.2 - 0.5	3.5 – 4.5
7	1800	100 - 5000	150 – 3500	0.2 - 0.5	4.8 – 5.5
8	1800	100 - 5000	150 – 3500	0.2 - 0.5	5.8 – 6.5
9	1800	100 - 5000	150 – 3500	0.2 - 0.5	6.6 – 7.2
10	1800	100 - 5000	150 – 3500	0.2 - 0.5	7.4 - 8.0
Half Space	1800	100 - 5000	150 – 3500	0.2 - 0.5	Infinite

Prior to the inversion runs, the ground and velocity parameters were adjusted accordingly to accommodate their dispersive characteristic - normally dispersive profiles vs inversely dispersive profiles. With regards to tuning the parameters, the following values were used for the inversion runs in the software:

- Ns = 20 000 (Total number of models generated by the NA)
- Ns0 = 50 (Number of initial models generated randomly by the NA)
- Nr = 50 (Number of best Voronoi cells to consider in each iteration)
- Nw = 2 (Number of random walks in the parameter space before generating models)

Upon conclusion of each inversion run, the software provided the minimum misfit value (M_m) computed for each run. The misfit value for each inversion run provided a numerical indicator of the fit between the experimental and theoretical dispersion curves and was calculated using Equation 3.7. The minimum misfit value was defined as the minimum of all the misfits calculated for the models generated before model *h* as shown below in Equation 3.8.

$$M_f = \sqrt{\sum_{i=0}^{n_f} \frac{(x_{di} - x_{ci})^2}{\sigma_i^2 n_f}}$$
(Equation 3.7)

where: x_{di} = velocity of the experimental curve at frequency f_i

x_{ci} = velocity of the calculated theoretical curve at frequency f_i

σ_i = standard deviation of the frequency samples

n_f = number of frequency samples considered

$$M_m(h) = min\{M_f(a = 1 \; to \; h)\} \hspace{3cm} \text{(Equation 3.8)}$$

where: M_m = minimum misfit value

$M_f(a)$ = misfit value associated to model a

The misfit value is influenced by parameterizations applied as well as by the number of models used and the standard deviation of the frequency samples as seen from Equation 3.7. However, detailed discussions on the choice of the parameterizations (parameters to invert and their ranges, number of layers, number of models to use) are often not discussed in literature. A range of methods have been considered by researchers often prioritizing the choice of Vs and using a large number of layers whilst some researchers choose to conduct a sensitivity analysis to guide them on the choice of parameters (Renalier *et al.*, 2010). Thus, the study only assumed the parameters given in Table 3.4 and Table 3.5 with a σ of 1.1 assumed for both the discrete and joint inversion runs. No sensitivity analysis tests were conducted with regards to parametrizations. As the M_f is influenced by various parameters, only profiles between the M_m (lower limit) computed and 10 % of the M_m above the M_m (upper limit) were considered to evaluate the spread in the Vs profiles for each inversion approach. The fit between the theoretical dispersion curve and experimental dispersion curve was also inspected between these limits.

3.6 SYNTHETIC DATA

A theoretical approach was considered using synthetic Rayleigh and Love wave dispersion data. A theoretical model with 2 layers and a half space layer with properties shown in Figure 3.26 was used to generate synthetic dispersion curves for both Rayleigh and Love waves. A Poisson's ratio (ν) of 0.25 was used for deriving the P-wave velocities (Vp). Synthetic dispersion curves were generated between 0 Hz and 100 Hz using an application known as gpdc, which is an extension of Dinver (3.3.6). Random noise of 10 % was added to the synthetic dispersion curves to investigate the effect of the quality of the dispersion data on the performance of the inversion runs. Figure 3.27 and Figure 3.28 displays the synthetic dispersion curves for Rayleigh and Love waves respectively.
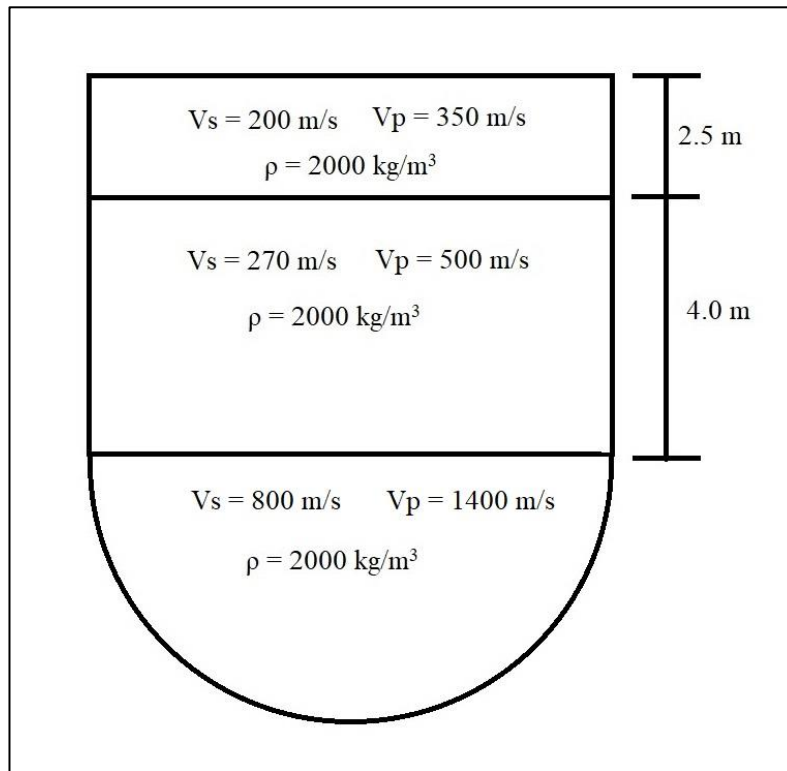
Figure 3.26: Theoretical model used for the generation of synthetic dispersion data.
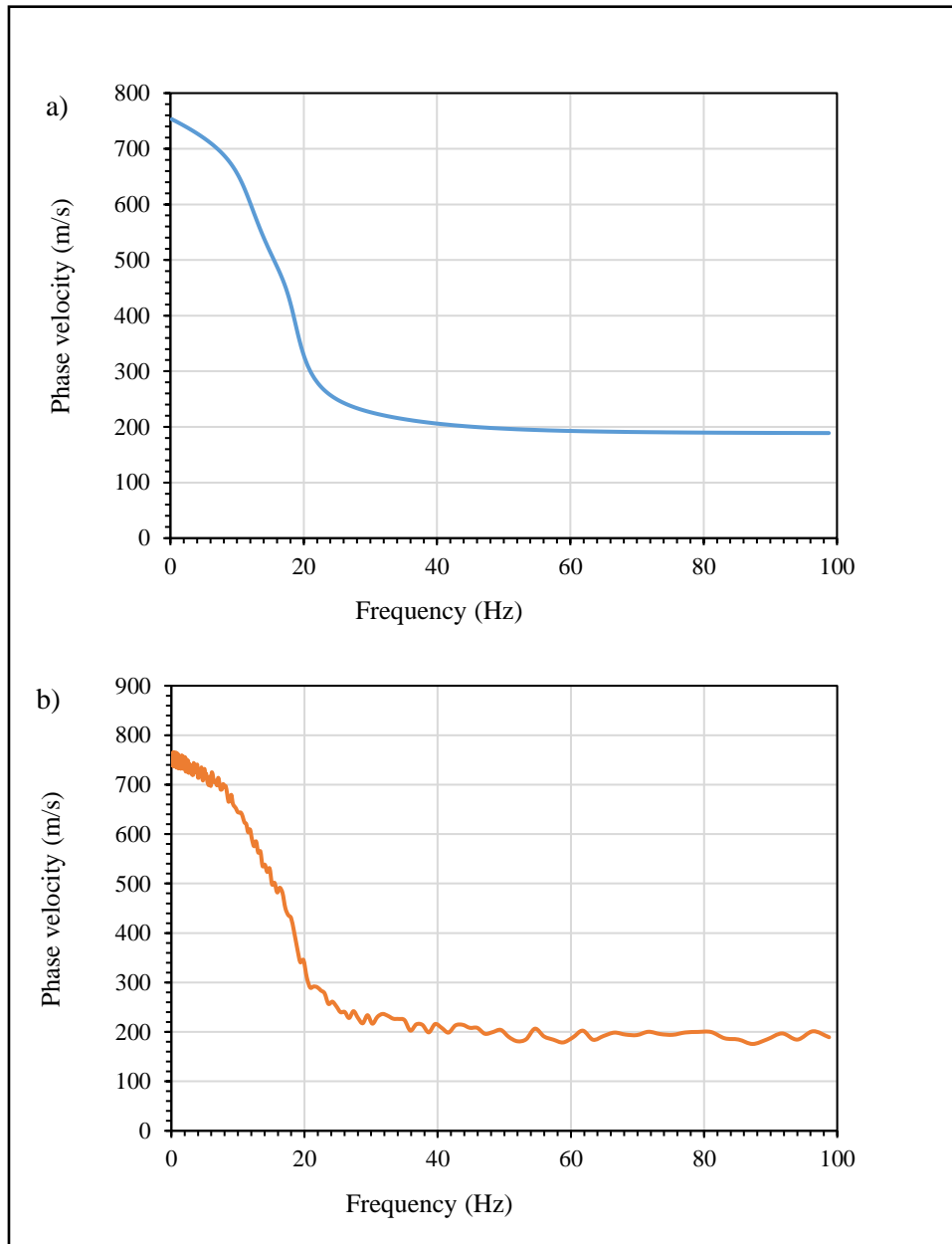
Figure 3.27: Synthetic Rayleigh wave dispersion curve with a) no noise b) 10 % random noise.
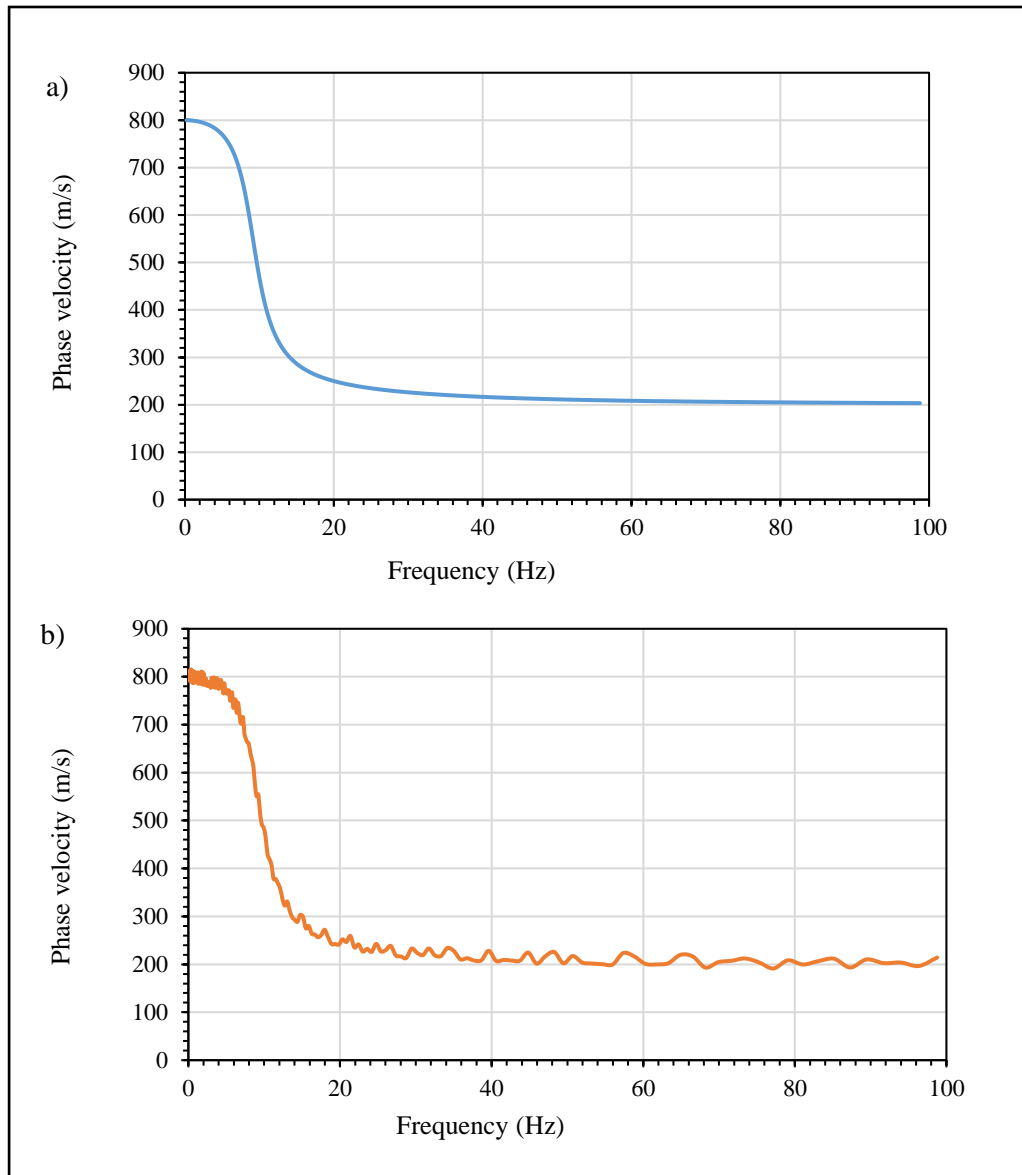
**Figure 3.28: Synthetic Love wave dispersion curve with a) no noise b) 10 %
random noise.**

For the inversion of the synthetic dispersion data, a total number of 6 layers and a half space
was considered. To be consistent with the scenarios used for the inversion of the acquired
experimental data, the following inversion scenarios were considered when using the synthetic
dispersion data:

1. Discrete inversion – Rayleigh waves (0 % noise) - A
2. Joint inversion - Rayleigh waves (0 % noise) and Love waves (0 % noise) - B
3. Joint inversion - Rayleigh waves (0 % noise) and Love waves (10 % noise) - C

4. Joint inversion - Rayleigh waves (10 % noise) and Love waves (0 % noise) – D

For the discussion below, the letters succeeding the above bullet points will be used to denote the respective inversion scenarios.

The inversion runs were conducted using the software, Dinver (3.3.6). The quality of the estimated Vs profiles were evaluated in terms of their spread in the Vs within the minimum misfit value (M_m) and 10 % of the M_m. Figure 3.29 to Figure 3.33 illustrates the Vs profiles obtained within the misfit limits for the inversion scenarios plotted along with the original Vs profile that was being approximated.
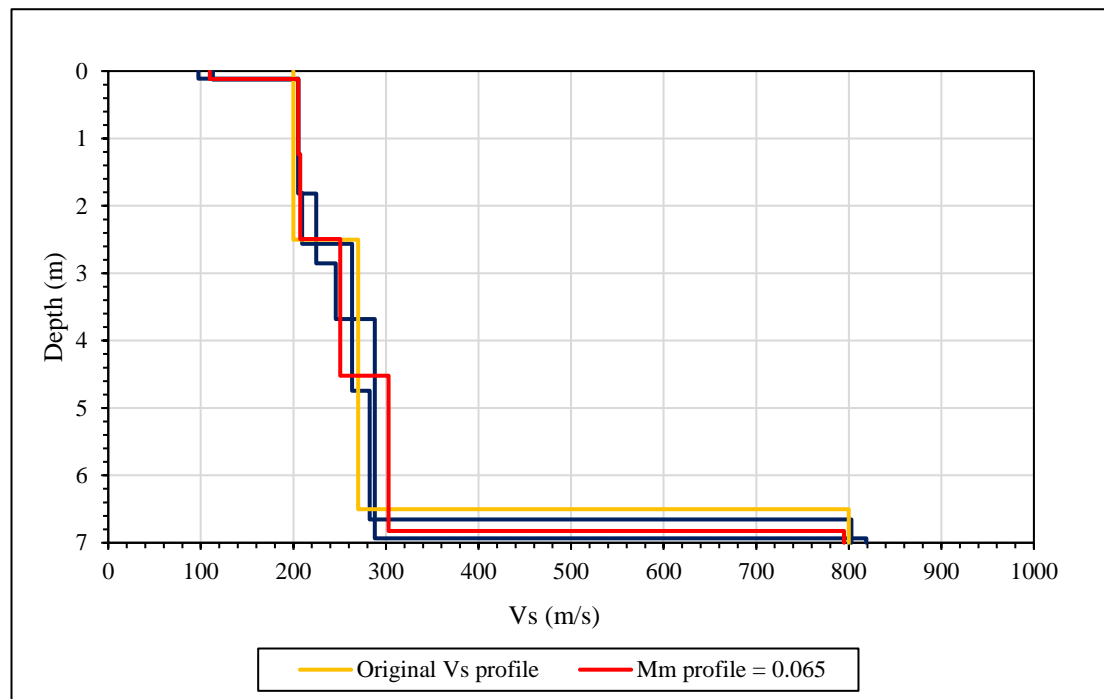
Figure 3.29: Vs profiles within misfit limits for inversion scenario A - Rayleigh waves (0 % noise).
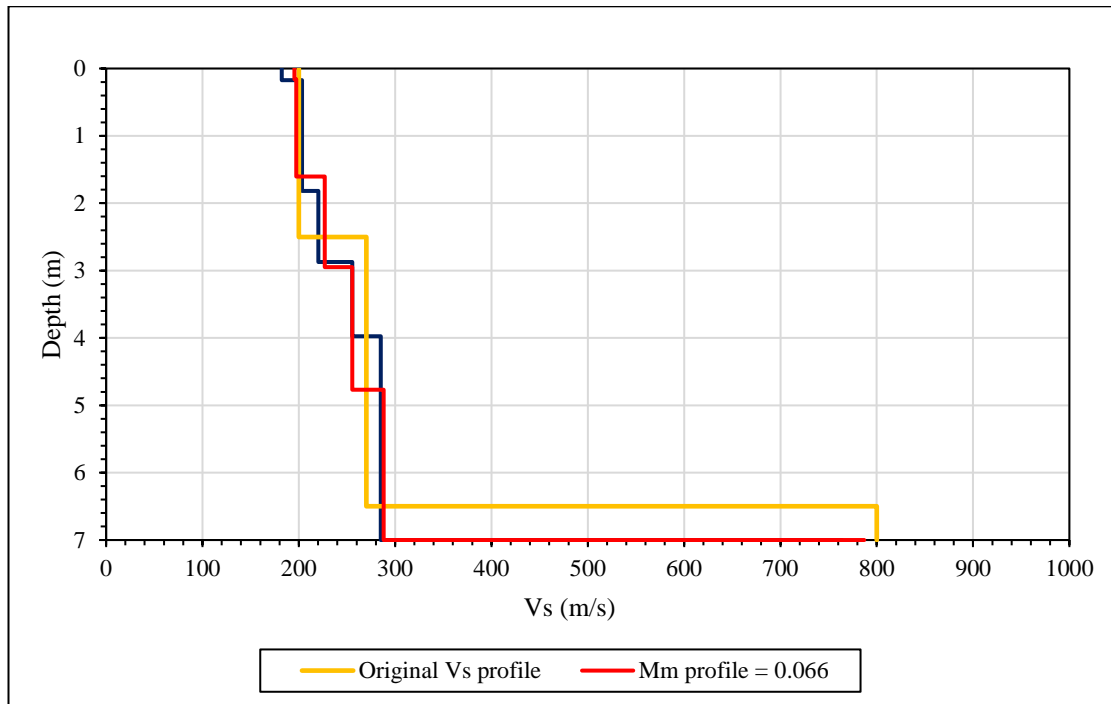
Figure 3.30: Vs profiles within misfit limits for inversion scenario B - Rayleigh waves (0 % noise) and Love waves (0 % noise).
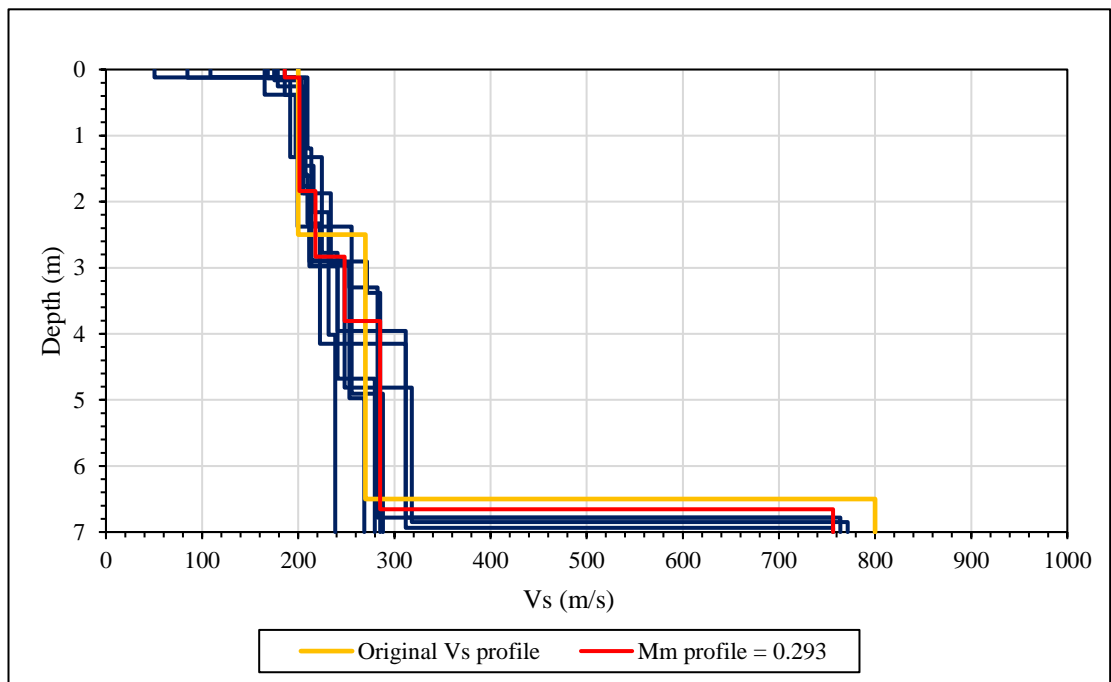
Figure 3.31: Vs profiles within misfit limits for inversion scenario C - Rayleigh waves (0 % noise) and Love waves (10 % noise).
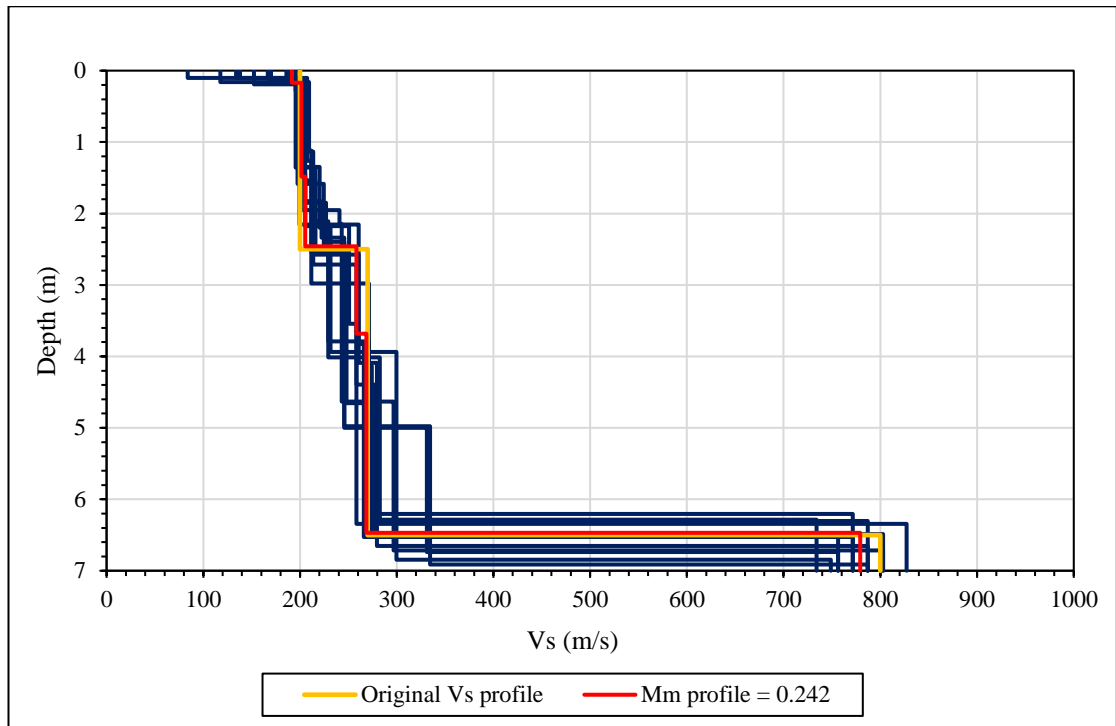
Figure 3.32: Vs profiles within misfit limits for inversion scenario D - Rayleigh waves (10 % noise) and Love waves (0 % noise).

From Figure 3.29 and Figure 3.30, it was firstly noticed that the number of Vs profiles approximated by scenarios A (discrete inversion Rayleigh waves with 0 % noise) and B (joint inversion Rayleigh waves and Love waves with 0 % noise) were significantly less than that approximated by Figure 3.31 (scenario C) and Figure 3.32 (scenario D) when noise was added. Both inversion scenarios A and B provided similar recoveries of the original Vs profile with reasonable estimates of the Vs profiles within the misfit limits. Upon addition of noise, the number of approximated Vs profiles increased (scenario C and D) and a greater spread was observed between the maximum and minimum Vs profiles as seen in Figure 3.31 and Figure 3.32. The spread in the Vs was used as an indicator to assess the performance of the different inversion scenarios in estimating and recovering the Vs profiles. The difference between the maximum and minimum estimated Vs profiles was determined until a depth of 7 m within the misfit limits. Figure 3.33 shows the spread in the Vs with regards to the above inversion scenarios.
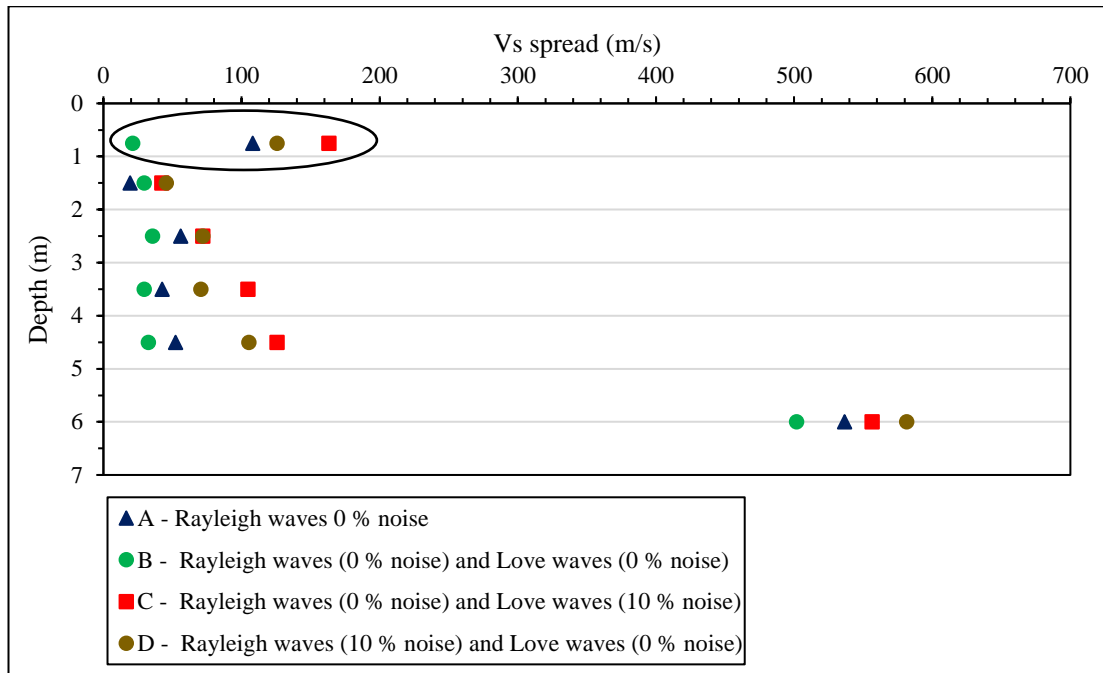
Figure 3.33: Spread in the Vs for different inversion scenarios using synthetic data.

It can be seen from Figure 3.33 that between depths of 1 m and 5 m, the spread in the Vs was below 200 m/s for all four inversion scenarios. A circle was enclosed around the Vs spread points for depths less than 1 m to indicate that these spread points were not considered when making an interpretation. This was because the minimum depth that could be resolved was 1 m based on the minimum wavelength measured by the theoretical dispersion points in Figure 3.27 and Figure 3.28. The spread in the Vs was greater when considering depths greater than 5 m. This implied that the ability to recover or estimate the original Vs profile decreased with depths greater than 5 m for this theoretical model. It was also noticed that when a joint inversion run incorporated good quality Rayleigh and Love wave dispersion data (B), the spread in the Vs was less than that observed when using a discrete inversion run alone with good quality Rayleigh wave dispersion data (A). This was observed for 4 out of the 5 cases. Thus, by supplementing Rayleigh wave dispersion data with Love wave dispersion data, the spread in the Vs is reduced. Upon addition of noise, the quality of the dispersion data deteriorated, and this affected the inversion process. From Figure 3.33, it was observed that at all depths, the spread in the Vs was greater for both C and D than that obtained from A and B. This implied that the quality of the dispersion data significantly affected the inversion process and possibly reduced the ability to accurately estimate the Vs profile.

4 RESULTS AND DATA ANALYSIS

This chapter presents the results obtained from the seismic tests in terms of dispersion curve plots and the Vs ground profiles for both Rayleigh and Love surface waves. Section 4.1 pertains to all the results and analysis conducted at the first test site (Engineering 4.0) and likewise Section 4.2 details the results and analysis from the second test site (Wind Africa). Within Section 4.1 and Section 4.2, the first subsection compares and discusses the experimental dispersion curves, in terms of Rayleigh and Love waves. Furthermore, the integrity of the two experimental methods (CSW and SASW) implemented to obtain Love waves are further discussed under this subsection. In the second subsection, the results obtained from the discrete and joint inversions are covered in detail for each respective test site. As mentioned before, two inversion scenarios were simulated - a discrete inversion and a joint inversion for each seismic test. The study involved comparing the fit qualitatively between the approximated theoretical experimental dispersion curves and the experimental dispersion curves and evaluating the spread in the Vs within the minimum misfit value (M_m) and 10 % of the M_m (upper limit). Moreover, the estimated Vs in the respective layers were compared with literature-based shear wave velocities for different types of materials.

4.1 ENGINEERING 4.0 TEST SITE

4.1.1 Dispersion Curve results

To obtain the experimental dispersion curves, two seismic tests were conducted namely, CSW and SASW, following the experimental procedures described in Section 3. Each seismic test was responsible for producing two experimental dispersion curves – Rayleigh wave dispersion curve and Love wave dispersion curve. Depending on the type of seismic test, the characteristics of the dispersion curves varied slightly in terms of frequency range and phase velocity jumps.

4.1.1.1 Rayleigh Wave Experimental Dispersion curves

i. CSW Rayleigh Wave dispersion curve

The CSW tests employed two methods to generate the experimental dispersion curves, by generating steady state signals and transient signals for source offsets of 1 m, 2 m, and 4 m. The analysis stage started with examining the Spectral Amplitudes for the three source offsets to assess the quality of the signals produced using the shakers. The Spectral Amplitude plots

were used to identify the frequency at which the signals were being produced. Figure 4.1 and Figure 4.2 shows the Spectral Amplitudes at geophone 1 and geophone 5 for the low frequency and high frequency shakers respectively.
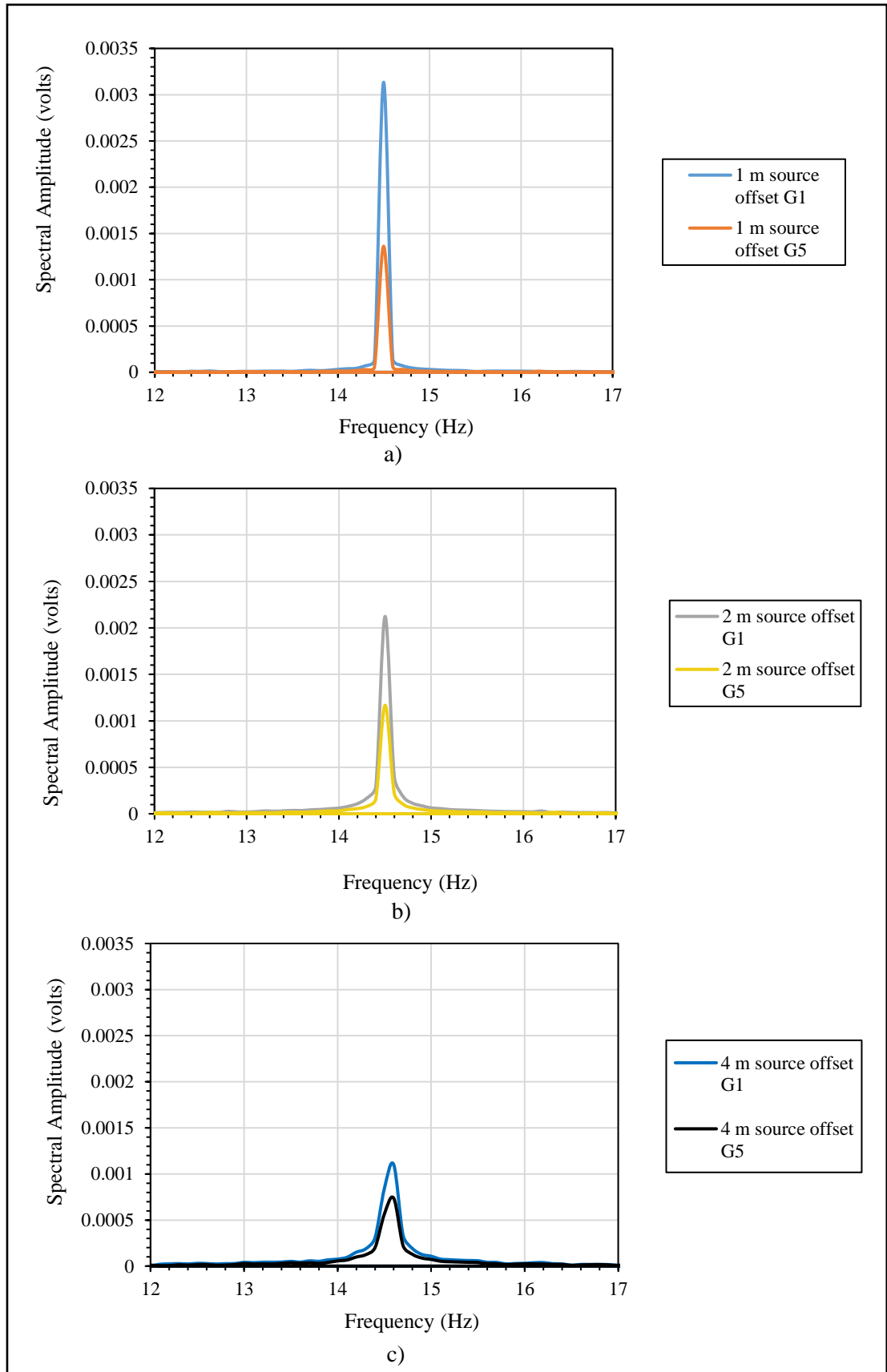
Figure 4.1: Spectral Amplitudes for CSW Rayleigh wave signals using Low frequency shaker at approximately 13 Hz at Engineering 4.0.
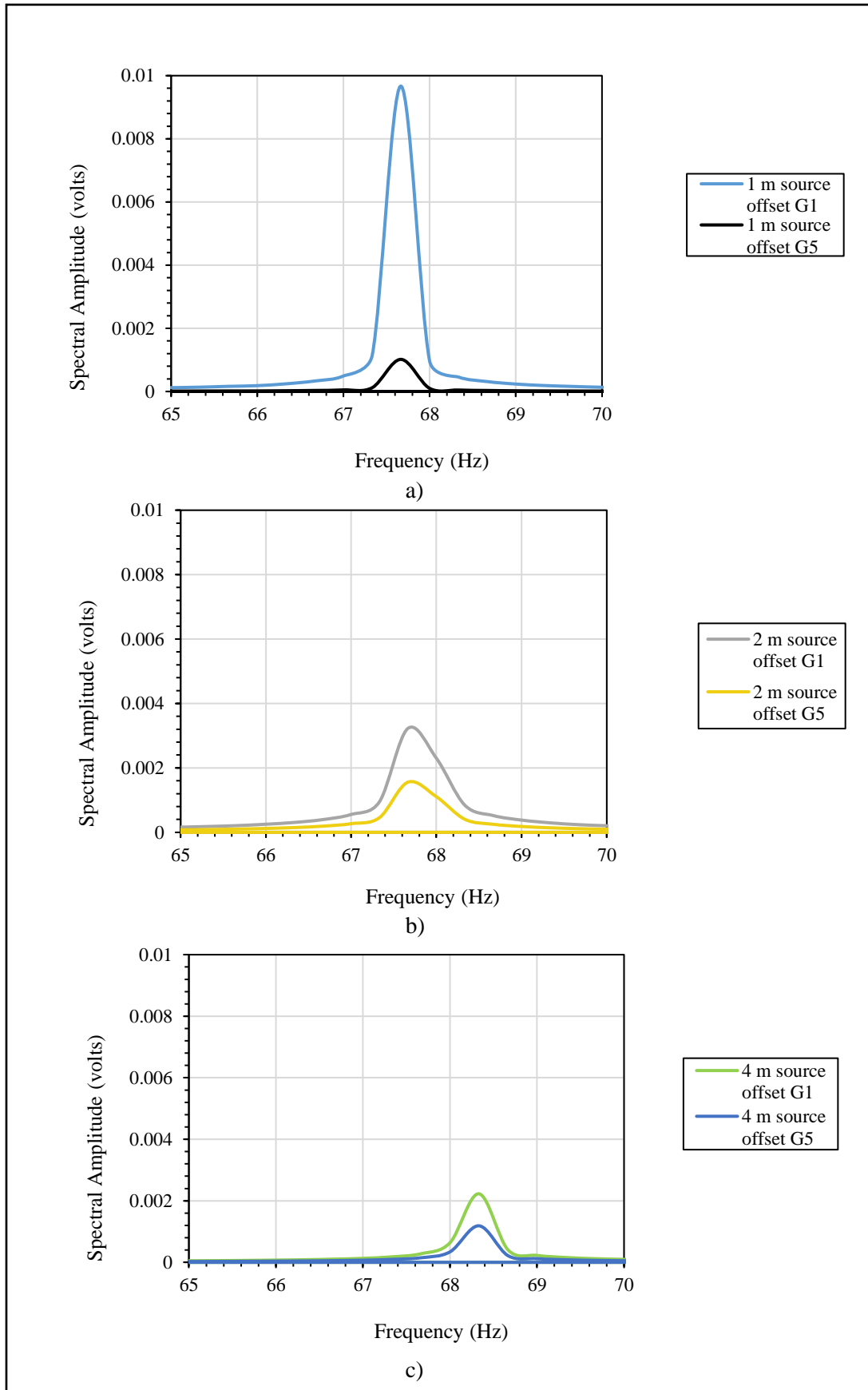
Figure 4.2: Spectral Amplitudes for CSW Rayleigh wave signals using High frequency shaker at approximately 66 Hz at Engineering 4.0.

From, Figure 4.1 and Figure 4.2 it could be seen that for each source offset, the spectral amplitudes peaked at the same frequencies for both geophone 1 and geophone 5. Thus, this implied that the performance of the two shakers was good. The low frequency shaker peaked at 14.5 Hz for both 1 m and 2 m source offsets while the 4 m source offset peaked at 14.6 Hz. The high frequency shaker also showed a similar behaviour of peaking at similar frequencies for the 1 m and 2 m source offsets (67.7 Hz) and peaking at a much higher frequency for the 4 m source offset (68.4 Hz). However, for this study, the spectral amplitude peaks were used to get the frequency at which the signals were produced and calculate the surface wave velocities. Therefore, differences in the peak amplitude frequency was not of concern.

During the steady state signal tests, the shakers were stepped through different frequencies depending on the type of the shaker used – high frequency shaker vs low frequency shaker. Therefore, different portions of the final dispersion curve were obtained from the two shakers as shown in Figure 4.3 and Figure 4.4. It should be noted that each shaker was constrained in terms of frequency due to their respective frequency limitations.
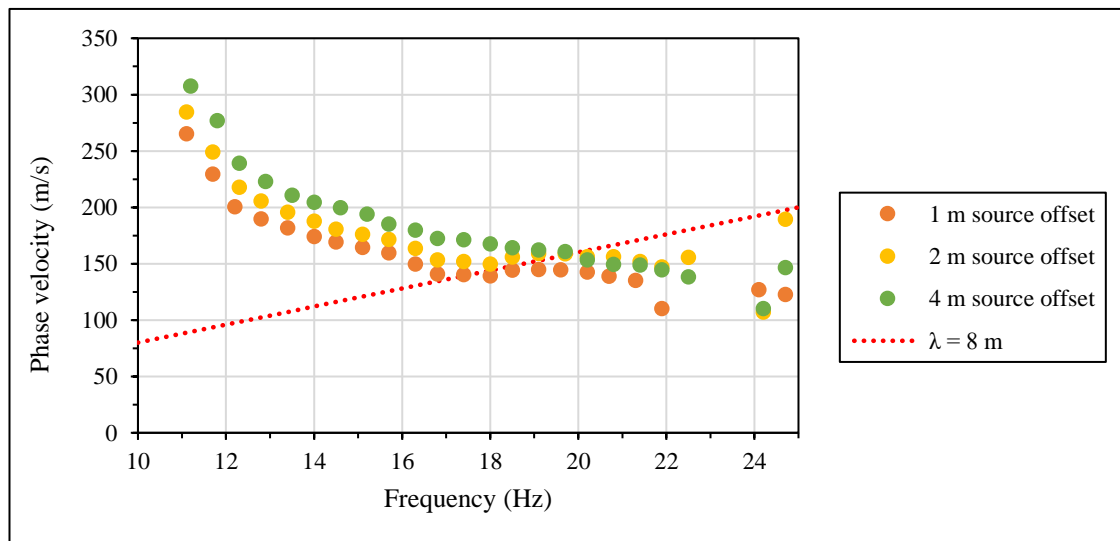
Figure 4.3: Rayleigh wave dispersion data before 'screening' for Low frequency shaker at Engineering 4.0 with Near field effect cut off line.
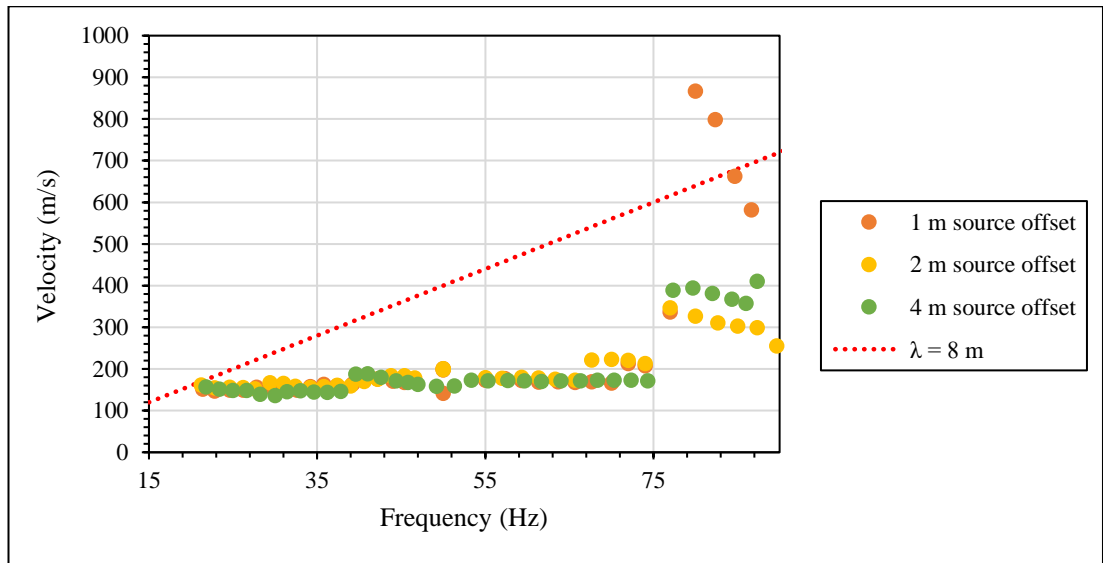
Figure 4.4: Rayleigh wave dispersion data before 'screening' for High frequency shaker at Engineering 4.0 with Near field effect cut off line.

From Figure 4.3, it was noticed that for frequencies below 20 Hz, the phase velocities approximated from source offsets of 1 m and 2 m fell below the velocities obtained from the 4 m source offset. A plausible explanation for this occurrence was that of near field effects. To investigate the near field effects, a cut off line for wavelength of 8 m was plotted in Figure 4.3. Hiltunen and Woods (1990) suggested the following near field effect criterion:

$$\frac{D_{min}}{\lambda} > \frac{1}{2}$$

where: D_{min} = minimum source offset required to avoid near field effects

λ = wavelength of surface waves

Figure 4.3 shows that for source offsets less than $\frac{\lambda}{4}$ (green and yellow points at 20 Hz) no near field effects are observed. However, for source offsets less than $\frac{\lambda}{8}$ (orange points below 18 Hz), near field effects are observed. This observation appears to suggest that the near field effect criterion of Hiltunen and Woods (1990) is conservative. For the purpose of this research, dispersion plots from the 4 m source offset alone were used in the final experimental dispersion curve with regards to the low frequency shaker data.

In context of the dispersion plots from the high frequency shaker, it was observed that for frequencies above 38 Hz, the velocities were constant, as seen in Figure 4.4. No near field effects were observed between the dispersion points of the three source offsets even at a source offset of $\frac{\lambda}{8}$. For frequencies above 40 Hz, the average velocity was noticed to increase from 150 m/s to 190 m/s, after which the dropped gradually to 180 m/s and attained this constant velocity below 66 Hz. At frequencies above 66 Hz, the dispersion points displayed velocity jumps for all three source offsets. At a frequency of 66 Hz, a jump was displayed by the 2 m source offset from 170 m/s to 220 m/s. Further jumps were observed by all three source offsets, with the velocities varying from 200 m/s to 900 m/s for higher frequencies. It should be noted that at this stage the authenticity of the observed data points had not yet been investigated and the dispersive data were in their raw unprocessed form. Therefore, no suggestions are made with regards to the jumps made at the higher frequencies.

During the processing stage of the steady state signals, the coefficient of determination (R^2) was calculated for each dispersion point to help eliminate any poor-quality fits. As discussed in Section 3.4.1, a regression line was calculated for the Phase angle - Distance plot at each frequency, from which the R^2 was determined (Figure 4.5). Dispersion plots with a R^2 value greater than 0.99 were selected and this was expressed as 'screening' of the data in the study. The 'screened' data points from the high frequency shaker and the low frequency shaker were integrated together to obtain the conceptual CSW experimental dispersion curve as shown in Figure 4.6.
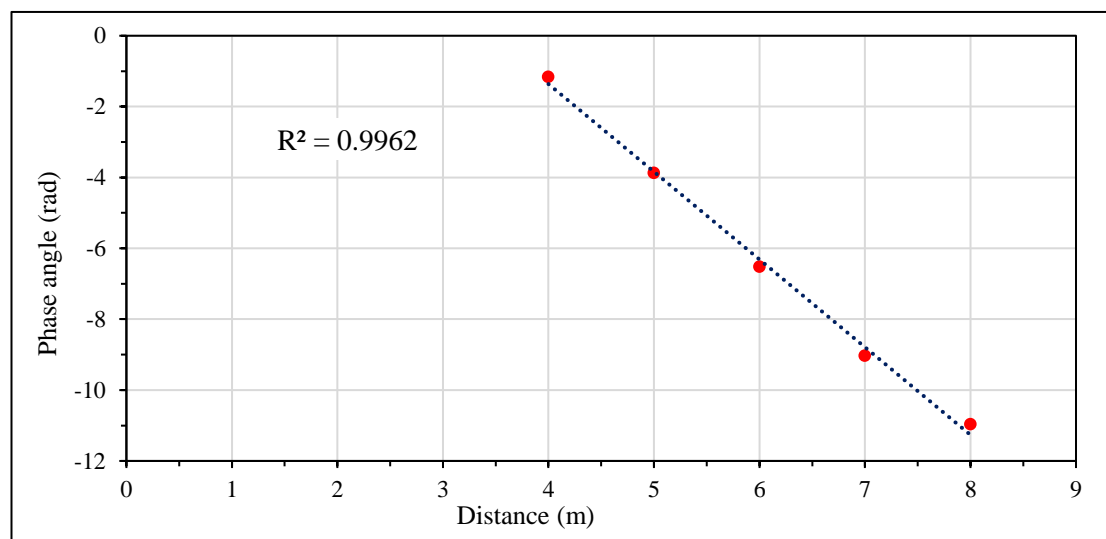
Figure 4.5: Regression analysis on Phase angle – Distance plot for 4 m source offset at 66 Hz.
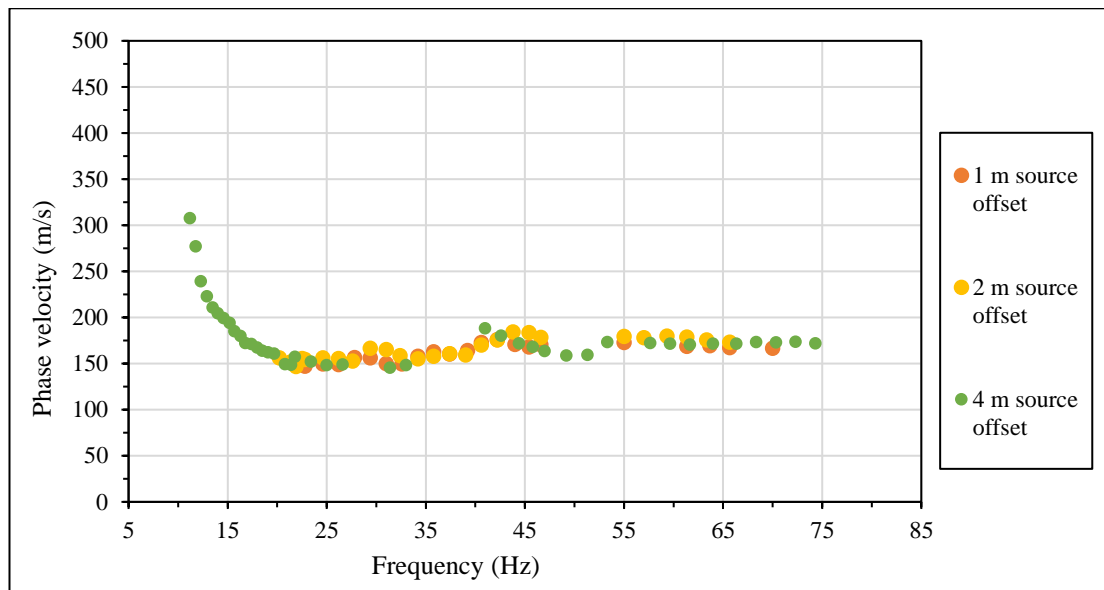
Figure 4.6: Combined Rayleigh Wave dispersion curve after 'screening' for Engineering 4.0.

From Figure 4.6, it could be seen that at frequencies between 35 Hz and 40 Hz, the dispersion points displayed a velocity jump from 150 m/s to 190 m/s for all three source offsets. The velocity gradually decreased for increasing frequencies to an average velocity of 175 m/s and maintained this velocity below 75 Hz. Two possible explanations may be suggested for the jumps. A higher mode of vibration could have existed at that frequency range, or a shallow layer of higher stiffness could exist above a layer with material of lower stiffness, causing an inversely dispersive profile. Due to the screening process of selecting quality data, the data points which portrayed large jumps at the higher frequencies initially, as seen earlier in Figure 4.4, were excluded in the final dispersion curve.

Additionally, a transient signal (Sweep) CSW test was conducted for the different source offsets. This provided an extra dataset and a quick verification process to compare the results to the steady state dispersion plots and establish the reliability of the steady state results. A fundamental step in the analysis of transient signals was to decide which dispersion data points are of suitable quality to include. Using the two criteria $R^2 > 0.99$ and a coherence ($\gamma^2 > 0.90$), dispersion points were identified and plotted, as shown below in Figure 4.7. For the frequency ranges where there are no data points, the data did not pass both criteria.
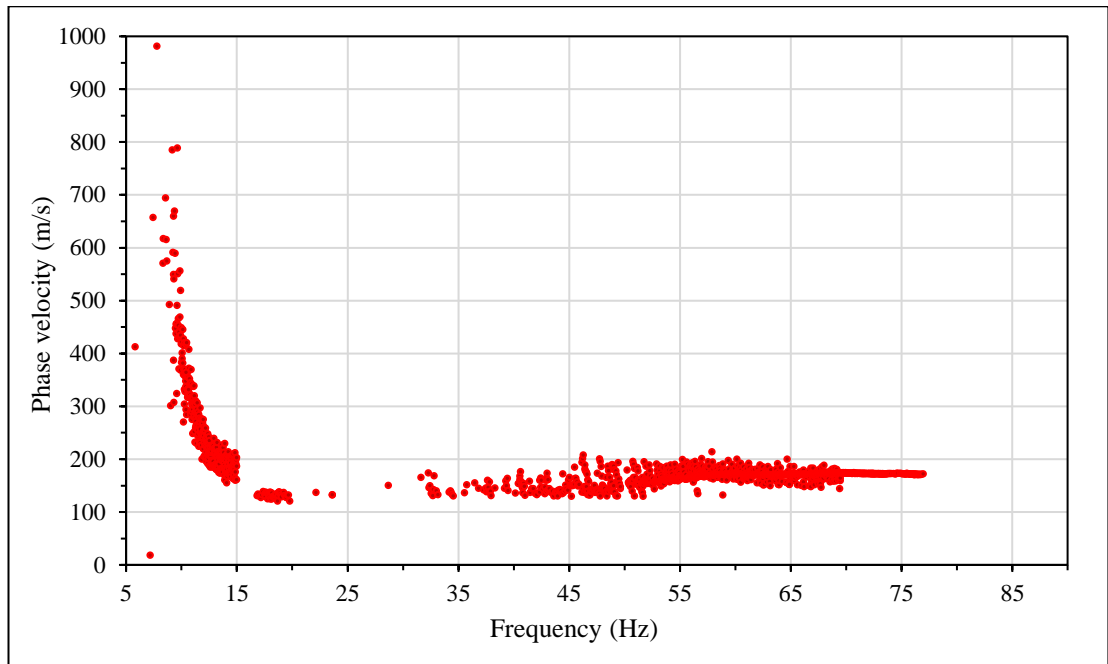
Figure 4.7: CSW combined Sweep dispersion curve for Rayleigh waves considering all three source offsets using both high frequency and low frequency shakers at Engineering 4.0.

As noticed in Figure 4.7, the average velocities made a gradual transition from 130 m/s to an average velocity of 175 m/s, commencing this transition at a frequency of 35 Hz. However, as the test pit profiles in Section 3.1 indicated the presence of stiffer materials with increasing depth at the Engineering 4.0 test site (normally dispersive), the only plausible explanation available was that of higher modes.

ii. SASW Rayleigh Wave dispersion curve

The SASW test targeted different frequency ranges of the dispersion curve by employing a range of sledgehammers, namely the 2 kg, 6 kg, and 9 kg sledgehammers, in both forward and reverse directions. Literature studies have suggested using lighter impact sources for shorter spacings (shallower depths) and likewise, heavier impact sources for longer offsets to measure deeper depths (Strobbia, 2003). However, for research purposes, all three sledgehammers were applied for all spacings, although in some instances, the dispersion data from one source alone was of adequate quality for a specific frequency bandwidth.

A key aspect that required attention during the SASW tests was that of the signal to noise ratio (SNR) of the signal produced by the impact source, considering that the energy of the signals from the sources deteriorate over increasing spacings. As the SNR is often affected by the background noise in the vicinity of the test site, the background noise was measured in advance in the form of its spectral amplitude. The spectral amplitude of the background noise was charted against the spectral amplitudes of the sledgehammers for each spacing to locate the frequency regions where an individual sledgehammer produced good energy as shown in Figure 4.8. This was essential during the processing stage to assist in masking of the signals.
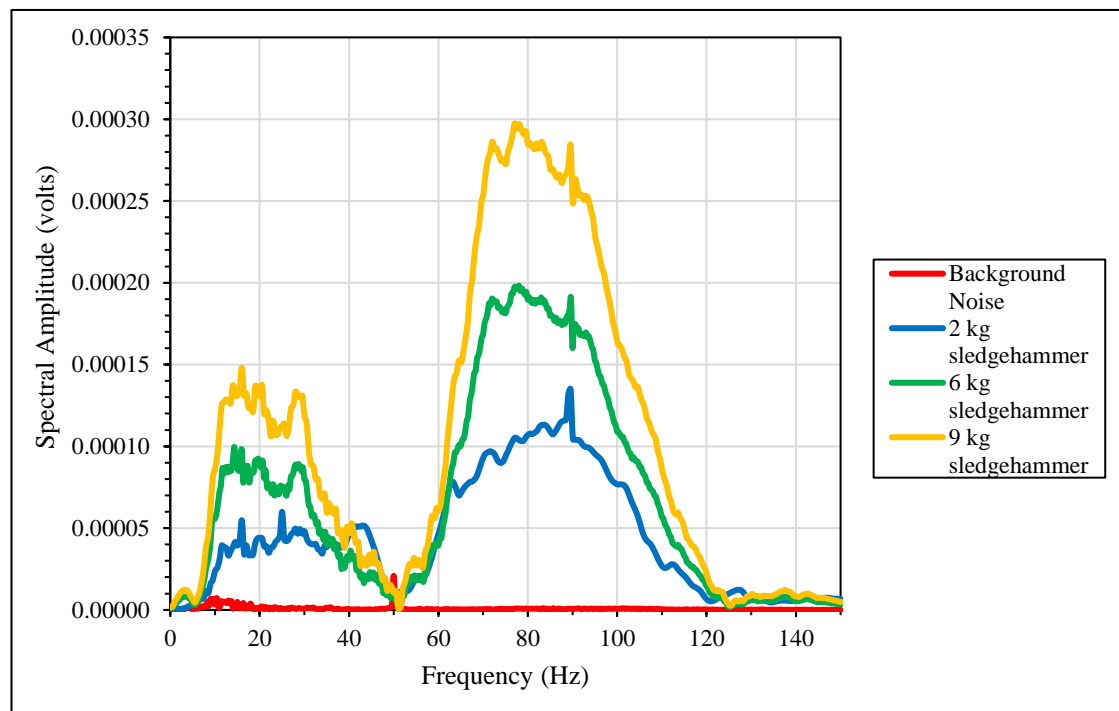
Figure 4.8: Spectral Amplitudes at Geophone 1 for 8 m spacing using SASW Rayleigh wave approach at Engineering 4.0.

For all three sledgehammers, the spectral amplitudes were significantly higher than that of the background noise, thus indicating a sufficiently high SNR during the SASW test. As expected, the magnitude of the spectral amplitudes decreased accordingly to their masses. In terms of energy distribution, it was noticed that the energy was contained up to 120 Hz for all three sledgehammers, after which the energy reduced to almost zero. An interesting observation made for the 8 m spacing was that all three sledgehammers displayed common behaviour of peaking at similar frequency ranges above and below 50 Hz. This might be due to the characteristics of the selected test site. The maximum Spectral Amplitude peak was observed

between 50 Hz and 100 Hz and the second lower peak occurring between frequencies of 10 Hz and 50 Hz. Thus, implying that the sledgehammers produced significantly more energy in the higher frequency ranges compared to the lower frequency ranges.

To assess the quality of the impact signals over the frequency ranges, the coherence (γ^2) between the two geophones was further estimated to determine to what extent were the input signals received at the output. Nazarian and Stokoe II (1986) stated that regions of frequencies displaying a $\gamma^2 > 0.9$ implied quality acceptable data and this concept was used to further supplement the analysis of the acceptable frequency ranges. Additionally, the wrapped phase difference plot was used to distinguish quality data by recognising the "sawtooth" pattern, which was used as a masking criterion. Upon masking of the data, the individual dispersion curves for each spacing and each sledgehammer were computed using the programming code outlined in Section 3.3.2. Figure 4.9 illustrates the significance of coherence and phase difference plots in the masking of the data with the pink shades representing data acceptable regions.
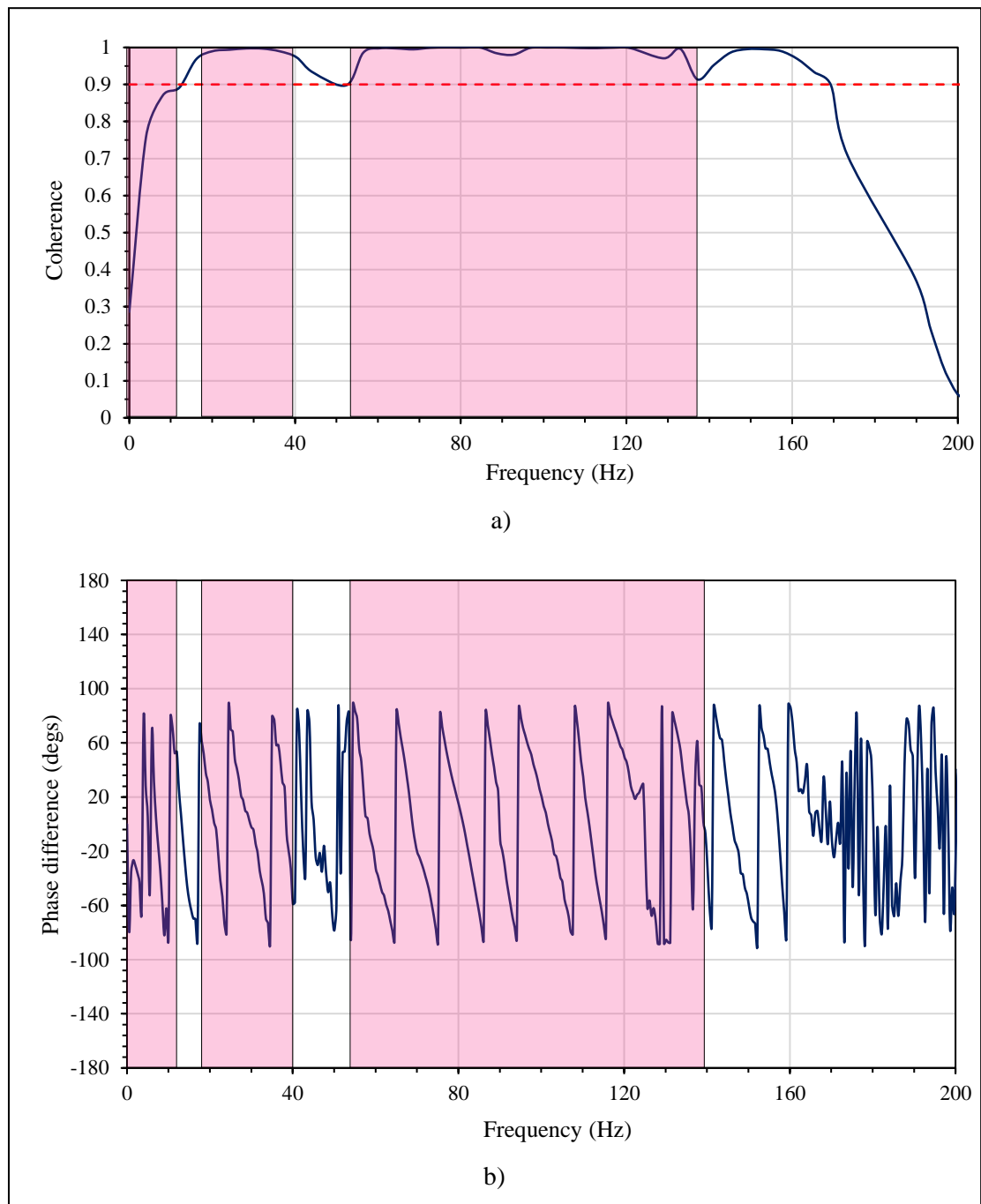
Figure 4.9: Coherence plot (a) and Phase difference plot (b) for 9 kg sledgehammer at 8 m spacing for SASW at Engineering 4.0.

Different portions of the composite experimental dispersion curve were sampled from the individual dispersion curves of the different spacings. Based on the quality of the signals and the overlap between these dispersion curves, certain dispersion curves were not used for approximating the composite dispersion curve, such as the 32 metre spacing data. Figure 4.10

shows the Rayleigh wave composite dispersion curve approximated by the different spacings whilst Figure 4.11 shows the comparison of the dispersion data points generated by the CSW and SASW approaches for Rayleigh waves at Engineering 4.0.
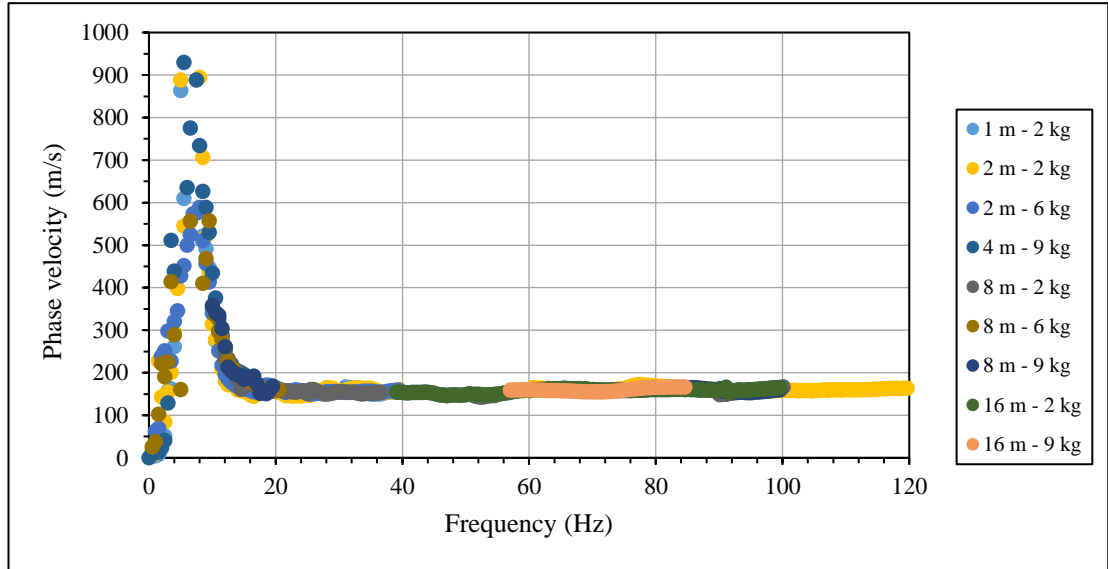
Figure 4.10: SASW Composite dispersion curve using Rayleigh waves at Engineering 4.0.
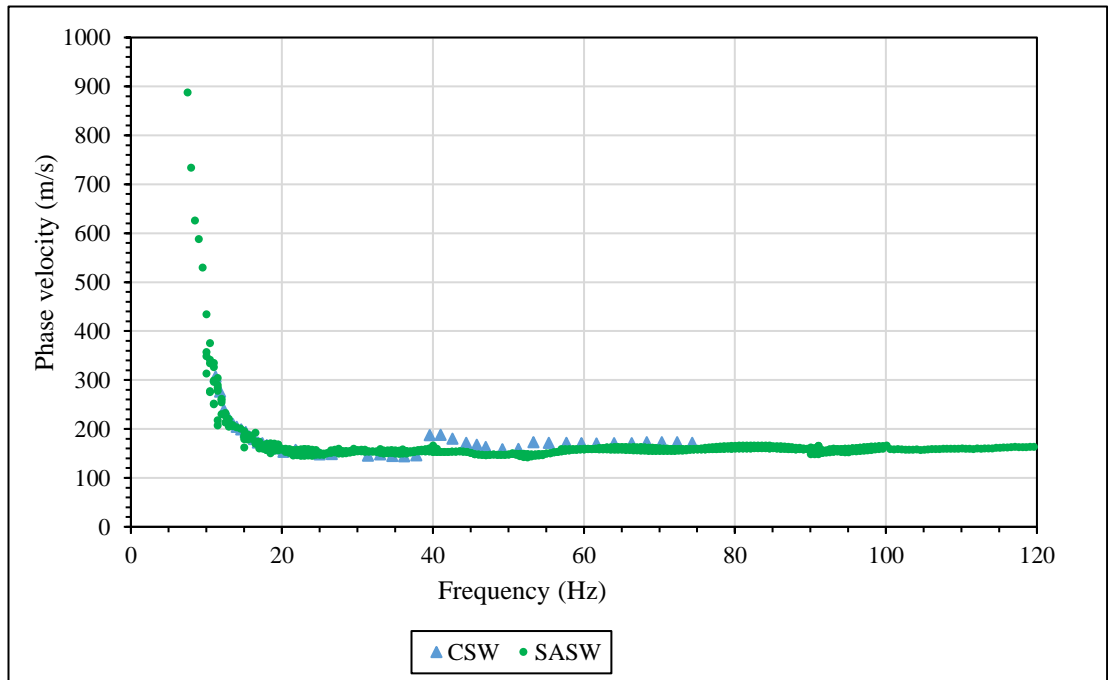
Figure 4.11: CSW and SASW Rayleigh wave dispersion points at Engineering 4.0.

Firstly, it could be noticed from Figure 4.10 that the range of frequencies observed using the SASW approach was considerably larger (5 Hz to 120 Hz) than that from the CSW approach. However, due to the quality of the overlapping of the individual dispersion curves, the smoothness of the dispersion curve varied in different regions of the dispersion curve. Figure 4.11 shows that the SASW dispersion points proved a close fit to the CSW dispersion points for Rayleigh waves, although a constant average velocity of 170 m/s was observed for the SASW dispersion points from 20 Hz to 120 Hz. A plausible explanation for this difference in the dispersion curves is based on the account of existence of higher modes which was encountered in CSW tests. Thus, Figure 4.10 illustrates the fundamental mode of vibration at the selected test site. For frequencies below 8 Hz in Figure 4.10, the dispersion points showed significantly low velocities which do not conform to the typical dispersion pattern. It is probably as result of insufficient energy to excite the ground at low frequencies. Therefore, these dispersion points were not included in the inversion analysis. Between frequencies of 8 Hz and 20 Hz, the velocities displayed significant drops to a final constant velocity of 170 m/s. Once more, this behaviour suggests a normally dispersive site profile.

4.1.1.2   Love Wave Experimental Dispersion curves

i. CSW Love Wave dispersion curve

The CSW Love wave test was conducted for both steady state signals and transient signals (Sweep) for the same source offsets used for Rayleigh waves, that is 1 m, 2 m, and 4 m offsets. However, the test configuration was slightly different to the conventional CSW setup, as horizontal geophones and a wooden platform with coupling spikes were used in conjunction with the high frequency and low frequency shakers. To begin with, the Spectral Amplitudes for the three source offsets were examined at the various frequencies to determine the quality of the signals produced using the chosen setup. Figure 4.12 and Figure 4.13 presents such a Spectral Amplitudes obtained at geophone 1 and geophone 5 for the low frequency and high frequency shakers for the different source offsets, respectively.
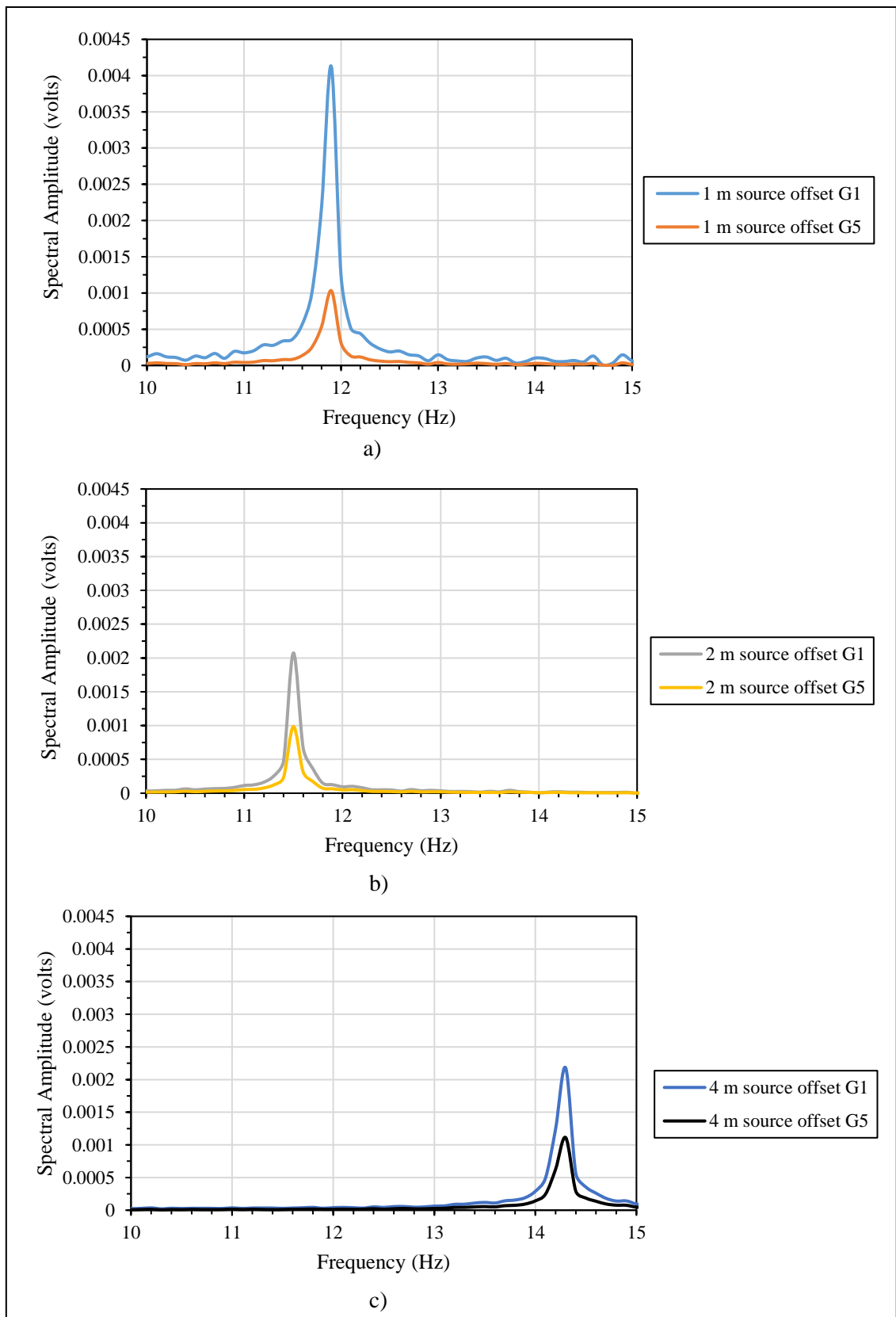
Figure 4.12: Analogy of Spectral Amplitudes for CSW Love wave signals using Low frequency shaker at approximately 13 Hz at Engineering 4.0.
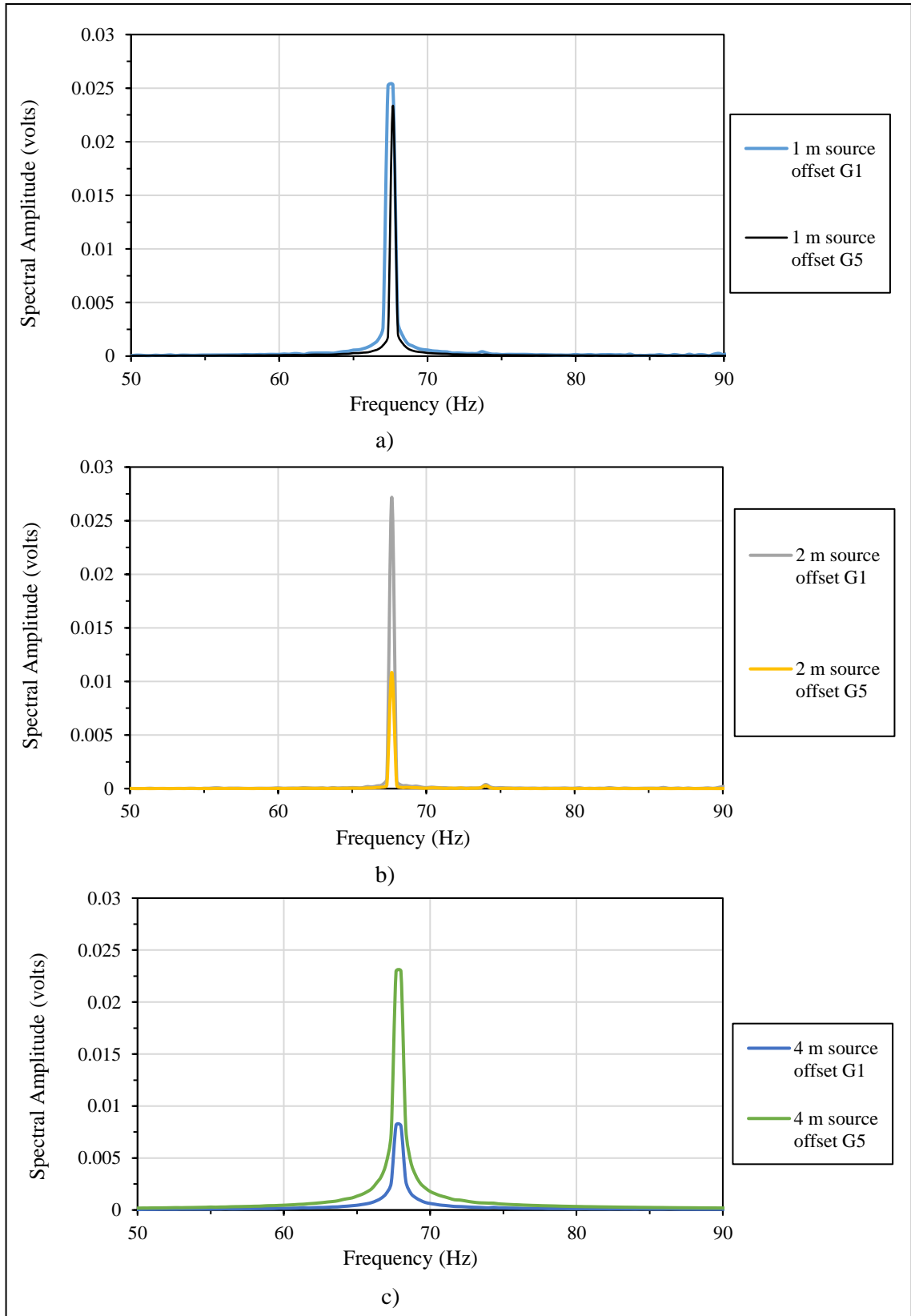
Figure 4.13: Analogy of Spectral Amplitudes for CSW Love wave signals using High frequency shaker at approximately 66 Hz at Engineering 4.0.

From Figure 4.12 and Figure 4.13, it was noticed that the performance in the Spectral Amplitudes for both shakers was good using the Love wave CSW approach as the peak frequencies obtained by both geophone 1 and geophone 5 aligned on top of one another. The low frequency shaker displayed peak amplitudes at different frequencies for different source offsets. For the 1 m and 2 m source offsets, the peak amplitudes for both geophones, were observed at 11.8 Hz and 11.5 Hz respectively However, the 4 m source offset displayed a peak amplitude at a frequency of 14.3 Hz. In contrast, the high frequency shaker produced similar peak amplitudes at 68.0 ± 0.5 Hz for all three source offsets as shown in Figure 4.13. The Spectral Amplitude plots were used to obtain the frequency for calculating the Love wave velocity, V_L.

Upon processing of the Love wave signals, raw dispersion plots were derived using the CSW code described in Section 3.3.1 for both the high frequency and low frequency shakers. These dispersion plots are shown below in Figure 4.14 and Figure 4.15, respectively.
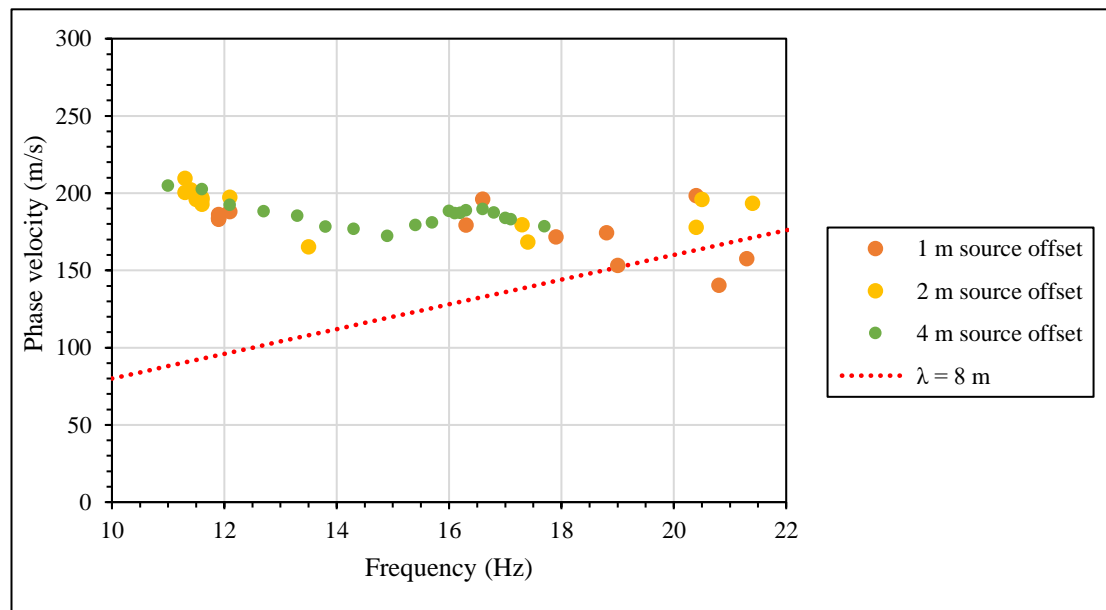
Figure 4.14: Dispersion data before 'screening' for Love wave data using Low frequency shaker with Near Field cut off line at Engineering 4.0.
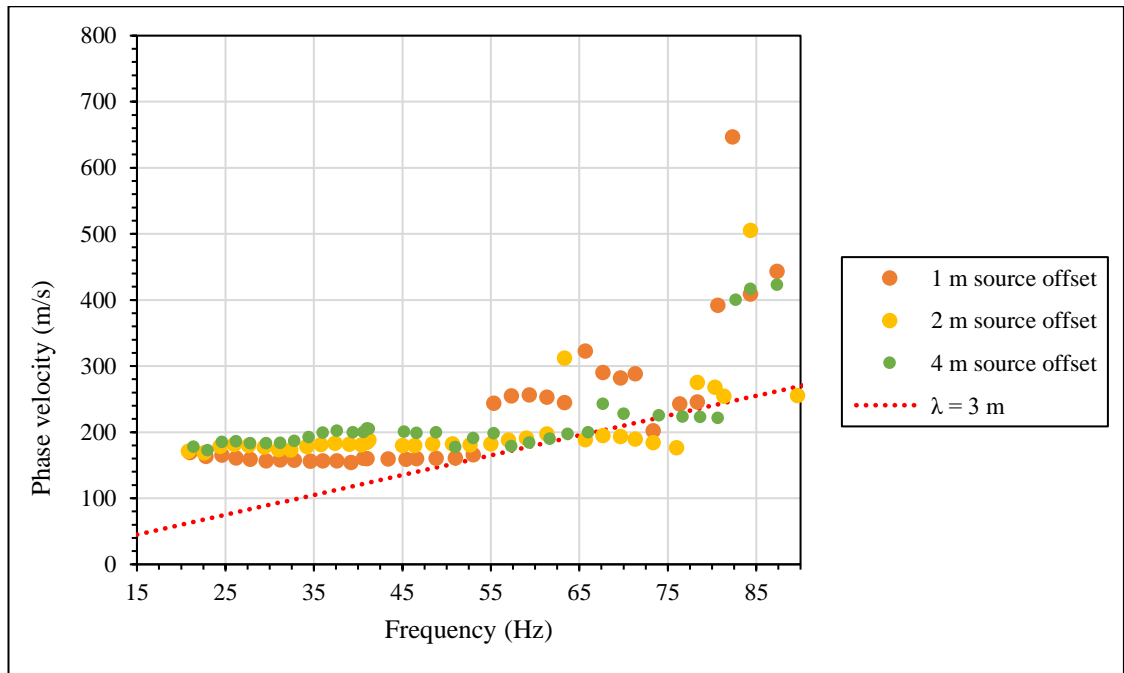
Figure 4.15: Dispersion data before 'screening' for Love wave data using High frequency shaker with Near field cut off line at Engineering 4.0.

From Figure 4.14, it could be seen that the dispersion plots acquired using the low frequency shaker varied between 140 m/s and 210 m/s for a considerably narrow frequency range of 10 Hz to 22 Hz. From visual analysis of Figure 4.14, no effects of near field were observed even at source offsets less than $\frac{\lambda}{8}$ as the dispersion points overlapped one another.

Although a considerable amount of scatter was observed in both cases, the dispersion data at the higher frequency regions was observed to follow a steadier pattern for all source offsets, as seen in Figure 4.15. It was noticed that the dispersion points acquired by the 1 m source had lower velocities than the 2 m and 4 m source offsets. This occurrence could be attributed to the effects of near field as for both 1 m and 2 m source offsets, the velocities were less in comparison to the 4 m source offset velocities. A near field cut off line with a wavelength of 3 m was also plotted in Figure 4.15 and it showed that for source offsets less than $\frac{\lambda}{3}$ (orange data points below 55 Hz), near field effects are observed. At a frequency of 55 Hz, the first dispersion point was seen to make a jump for the 2 m source offsets. Likewise, more jumps soon followed for all three source offsets at higher frequencies. These jumps could be ascribed to the existence of higher modes or a shallow inversely dispersive profile. However, based on the literature, Love waves require a normally dispersive profile to exist (Kiełczyński, 2018). It

may therefore be concluded that the jumps observed towards the higher frequencies were by virtue of higher modes of vibration in the profile.

It should be realized that the dispersion plots presented earlier in Figure 4.14 and Figure 4.15 were in their 'unscreened' state and this could be explained by the large scatter in the dispersion plots. Nonetheless, owing to the R^2 that was calculated for each selected frequency during the fitting of the regression line in the Phase difference – Distance plot, selected dispersion data was excluded from the final experimental dispersion curve (Figure 4.16). This was accomplished by selecting dispersion points with a R^2 values of greater than 0.99.
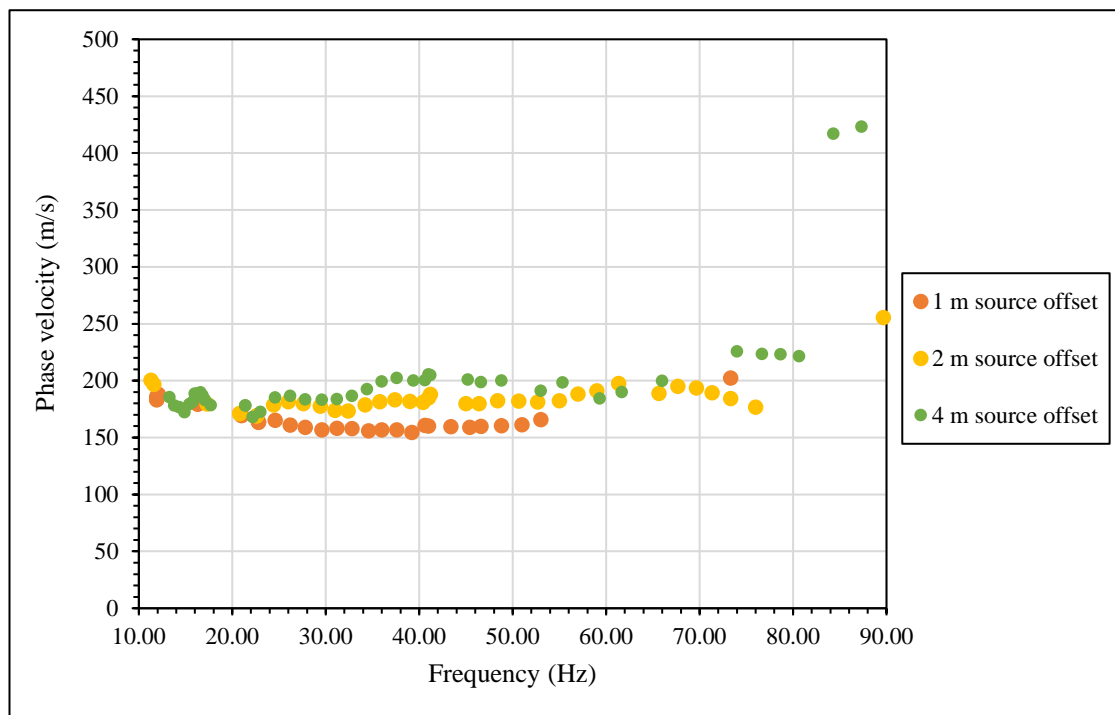
Figure 4.16: Experimental Love Wave dispersion curve after 'screening' at Engineering 4.0.

From Figure 4.16, it could firstly be seen that the 'screened' Love wave data points varied in terms of the velocities at different source offsets. For frequencies below 20 Hz, all three source offsets overlapped one another. The Love wave dispersion curve averaged at 175 m/s for frequencies below 55 Hz for the 2 m source offset. It could be noticed the dispersion points for the 2 m and 4 m source offset approached each another unlike the 1 m offset which underestimated the phase velocities when compared to them. For frequencies above 33 Hz, the phase velocities for both the 2 m and 4 m source offsets were seen to gradually increase. This

could be suggestive of the superposition of different modes of vibration, thus indicating the existence of a higher mode of vibration. For frequencies above 33 Hz, the dispersion points for the 2 m and 4m source offsets followed a similar trend until a frequency of 55 Hz, after which a further gradual increase in the phase velocity was observed once more. At frequencies greater than 70 Hz, a distinct higher mode jump was noticed by the 4 m source offset.

As an additional measure, a sweep CSW test was conducted to identify and compare any significant differences against the steady state Love wave dispersion curve. With the aid of the coherence estimated between geophone 1 and geophone 5 as well as the R^2 for every frequency, the transient signals from both shakers were 'screened' to preserve only acceptable data (Figure 4.17). The sweep dispersion curve provided a similar dispersion curve to that obtained in Figure 4.16, where a steady state signal was used. The sweep dispersion points had an average phase velocity of 175 m/s for majority of the investigated frequencies. Additionally, higher modal jumps were only observed at 67 Hz and 83 Hz which supported the presence of higher modes of vibration.
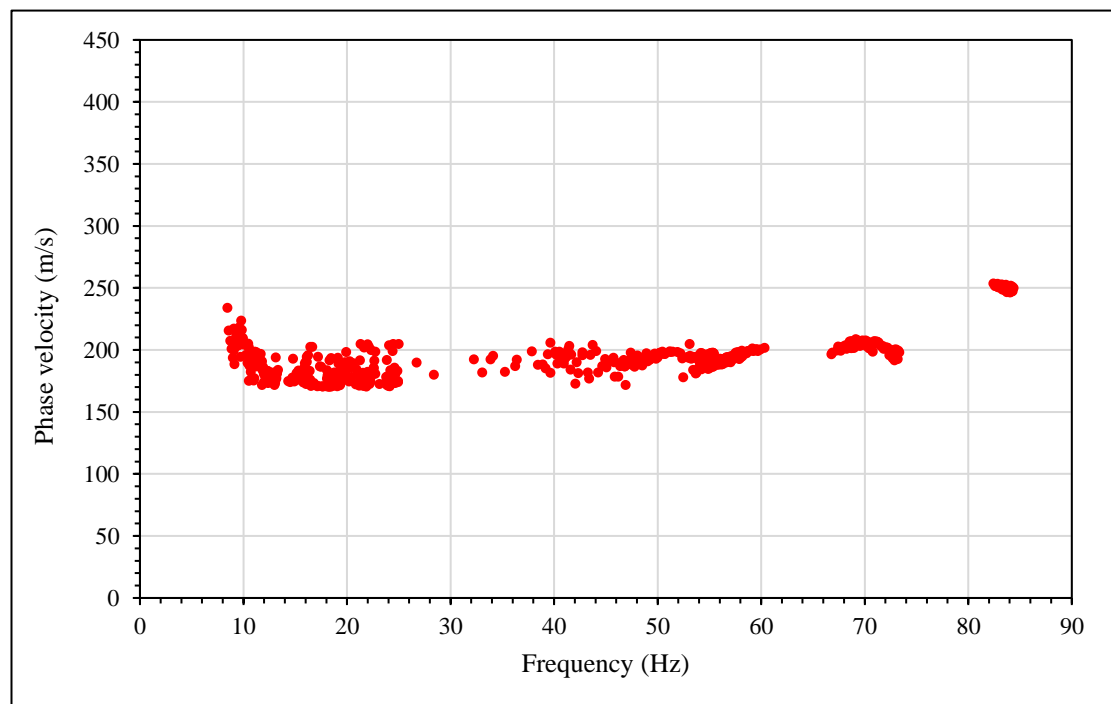
Figure 4.17: Love wave sweep dispersion curve considering all three source offsets at Engineering 4.0.

ii. SASW Love Wave dispersion curve

For the acquisition of Love wave signals through the SASW test, the same three sets of sledgehammers (2 kg, 6 kg & 9 kg) were employed together with a steel impact source (forward and reverse shots) for all spacings. In terms of the layout, the common receiver midpoint was once more used to accommodate fairness in the tests.

A difficulty with conducting seismic tests with Love waves is that of energy decay in the signals. This is one of the primary reasons why seismic tests are conventionally conducted using Rayleigh waves alone. Therefore, it was important to investigate how the Spectral Amplitudes of the Love wave signals delivered by each of the sledgehammers varied against one another as well as the site background noise. Figure 4.18 shows the Spectral Amplitudes of the different sledgehammers, when struck against the steel impact source at a spacing of 8 m.
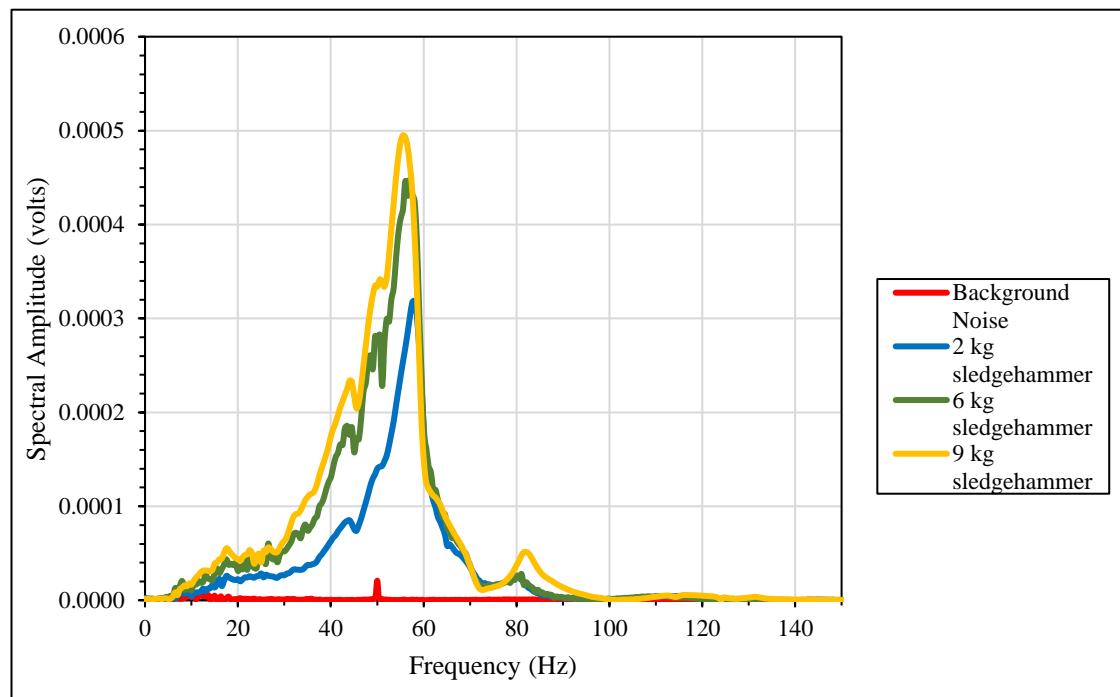
Figure 4.18: Spectral Amplitudes at Geophone 1 for 8 m spacing using the Love wave impact source at Engineering 4.0.

From Figure 4.18, it was noticed that all three sledgehammers peaked at a 57 ± 1 Hz, with the 9 kg sledgehammer exhibiting the greatest amplitude and the 2 kg showing the smallest amplitude. The background noise slight peaked at 50 Hz and this could possibly be due to the overhead electrical cables nearby. Furthermore, the shape of the Spectral Amplitude curves

resembled one another closely, with all three curves distributed over a frequency range of 0 Hz to 100 Hz. With regards to the signal to noise ratio (SNR), all three sledgehammers produced amplitudes that were significantly greater than the that of the background noise, suggesting a sufficient SNR. It was noticed that the Love wave SASW Spectral Amplitudes only produced one distinct peak, in contrast to what was observed in the Rayleigh wave SASW Spectral Amplitude plots.

Following the acquisition of the Love wave signals, the data was masked to identify quality data as well as frequency acceptable regions. For each respective spacing, the coherence between the two horizontal geophones were approximated to perceive how well the input signals were recovered between the two geophones. Once more, a coherence of 0.90 served as the margin to distinguish quality frequency regions. In conjunction to the coherence, the distinctive 'sawtooth' pattern in the wrapped phase difference plots was identified in the suggested frequency regions to evaluate the authenticity of the coherence plots. Figure 4.19 and Figure 4.20 presents the coherence and phase difference plots for 4 m and 8 m spacings respectively when employing the 9 kg sledgehammer.
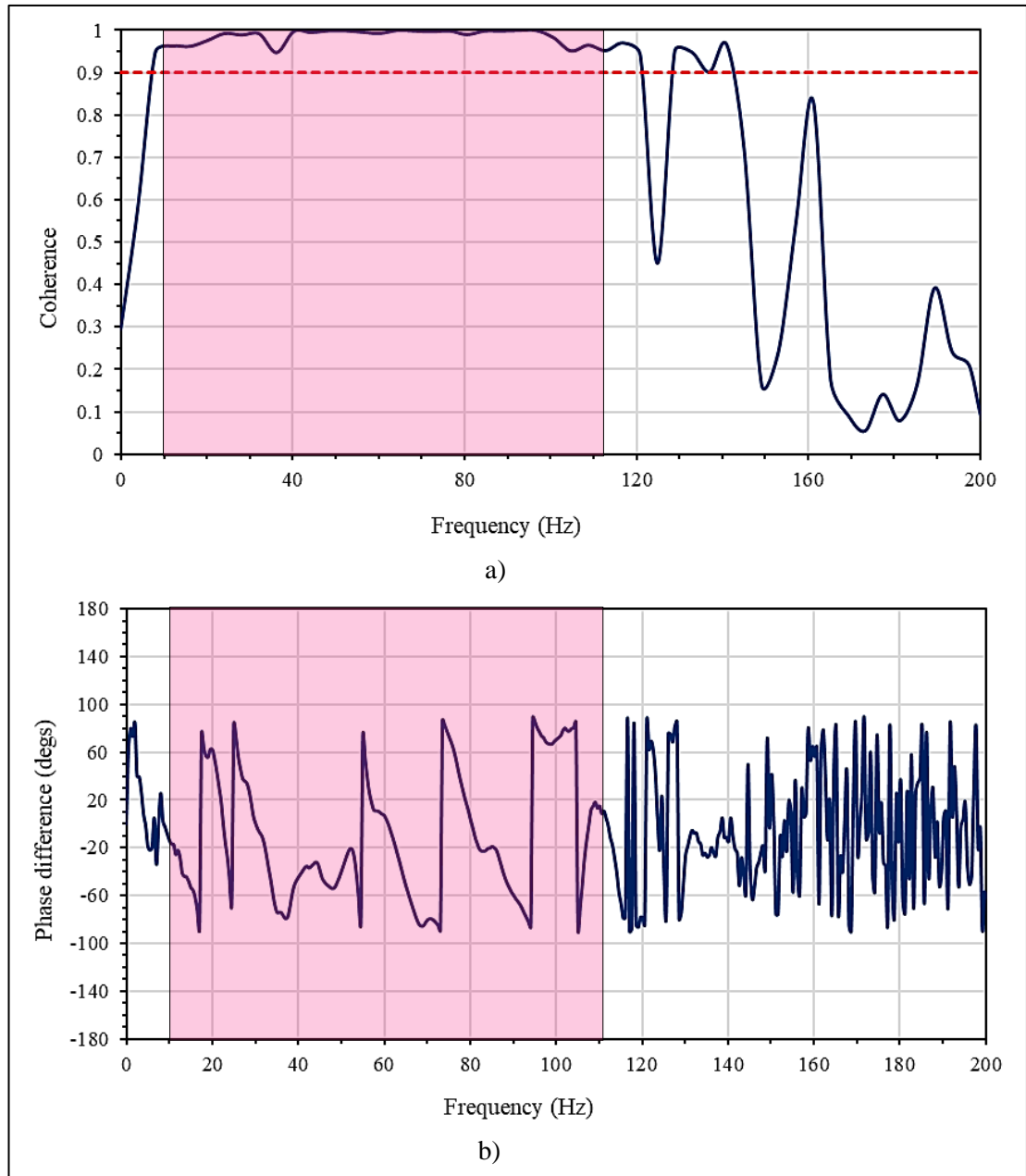
Figure 4.19: Coherence plot (a) and Phase difference plot (b) for 9 kg sledgehammer at 4 m spacing using the Love wave impact source at Engineering 4.0.
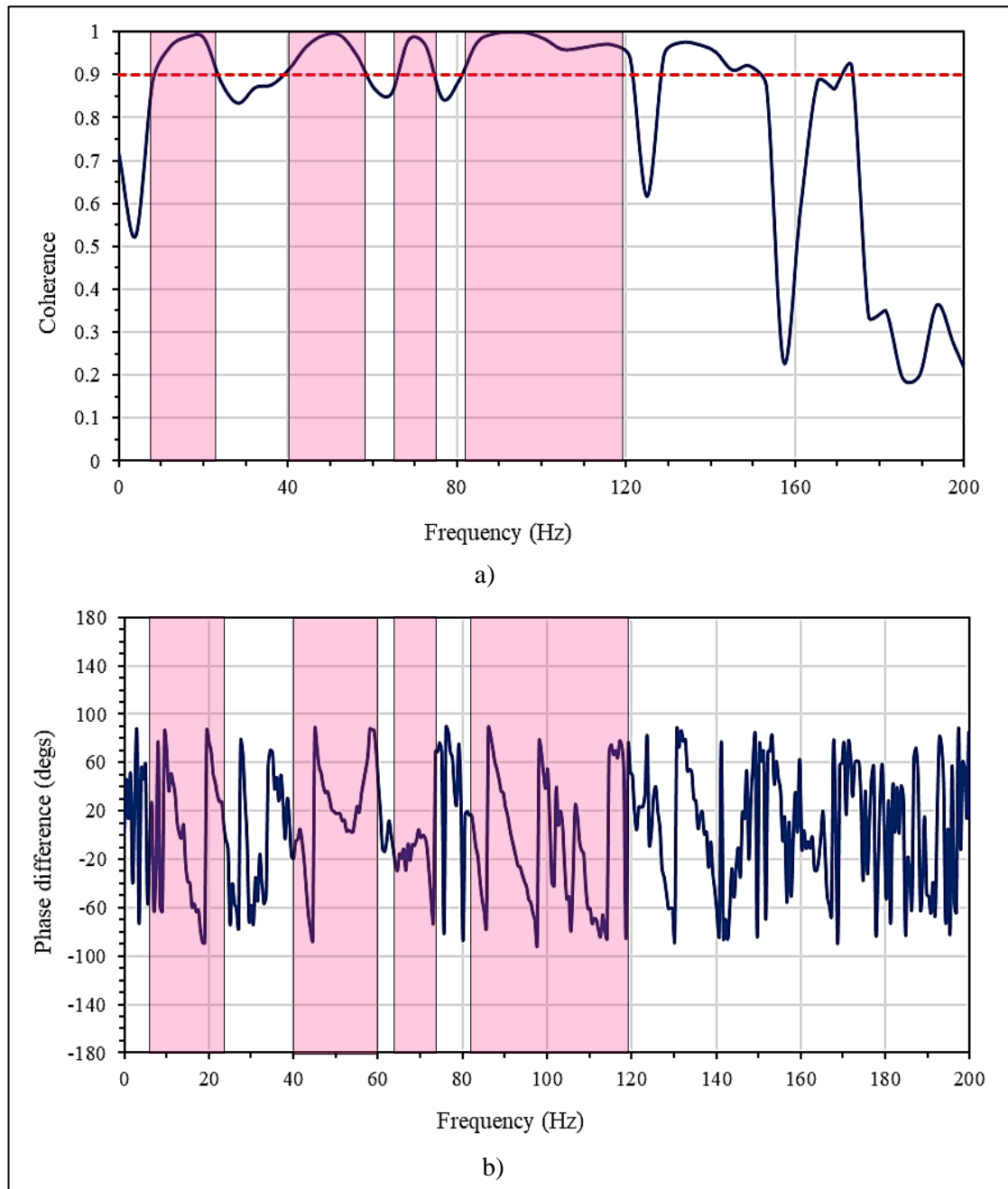
Figure 4.20: Coherence plot (a) and Phase difference plot (b) for 9 kg sledgehammer at 8 m spacing using the Love wave impact source at Engineering 4.0.

For both Figure 4.19 and Figure 4.20, unwrapping of the phase differences was done in selected frequency ranges, where the coherence criterion was met. However, it could be seen that with increasing spacing, the quality of the signal deteriorated for the same sledgehammer. This is evident in Figure 4.20 as the coherence values had dropped significantly compared to the

previous case in Figure 4.19. Consequentially, the phase differences were unwrapped for each spacing and were used to generate the experimental dispersion points in their selected frequency regions. As the SASW involved combining the various dispersion curves at different spacings into one composite dispersion curve, the data for certain spacings was completely discarded. An example of such a scenario was that for the spacings of 16 m and above. At a 16 m spacing, the coherence between the two geophones was below the 0.90 boundary line for all three sets of sledgehammers (Figure 4.21). Thus, this implied that the power of the signal arriving at the far receiver was low, owing to the attenuation of the Love waves.
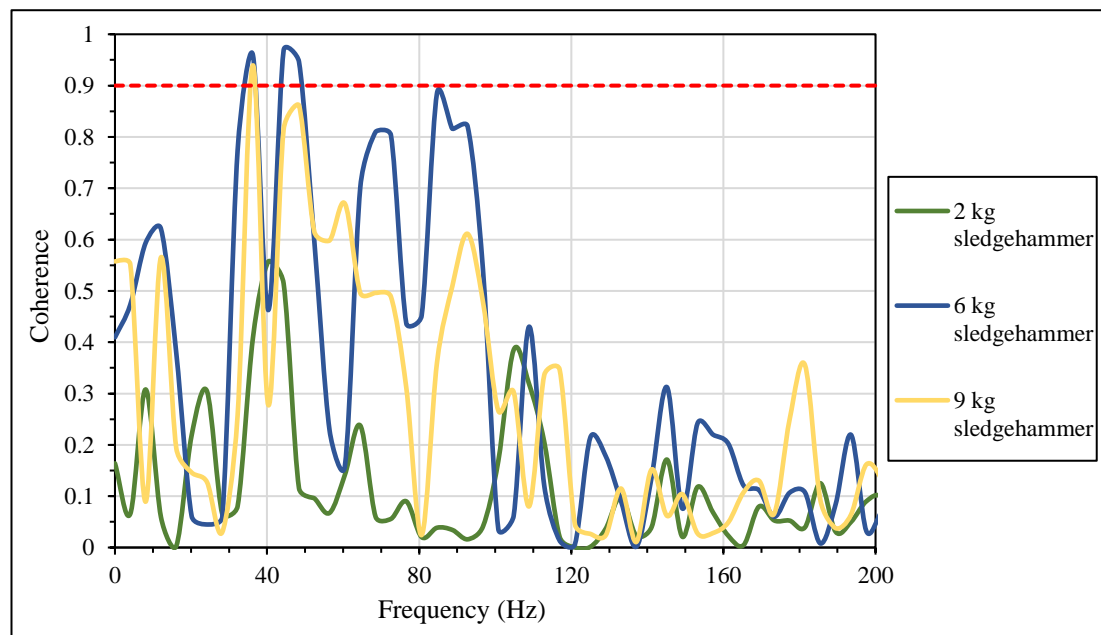
Figure 4.21: Coherence at 16 m spacing for Love wave impact source signals at Engineering 4.0.

Although the 16 m and 32 m spacings failed to appear on the composite dispersion curve, the rest of the spacings were incorporated and selected accordingly to their degree of 'overlap' between each of the individual dispersion curves. Figure 4.22 illustrates the Love wave composite experimental dispersion curve that was derived using the SASW approach implemented for this study.
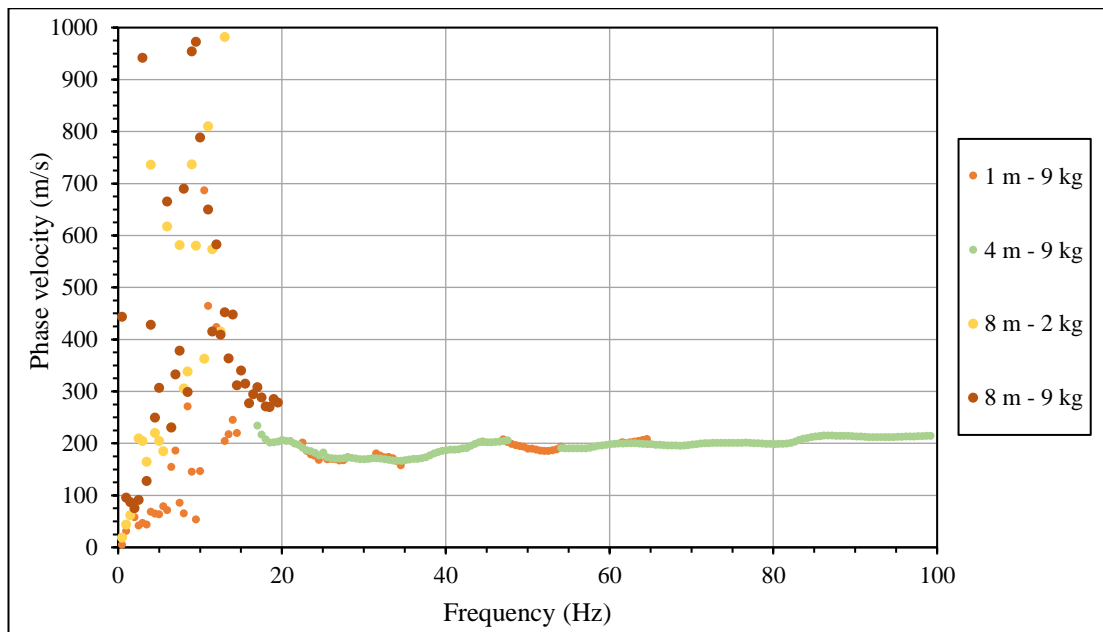
Figure 4.22: SASW Love wave composite dispersion curve for Engineering 4.0 test site.

From Figure 4.22, it could be seen that at low frequencies (< 20 Hz), a large amount of scatter was evident. A plausible cause for the large degree of scatter might be due to the signal being too weak to excite the ground at low frequencies. Regardless of the spacing and the sledgehammer used, the scatter prevailed for frequencies below 20 Hz. These dispersion points do not confirm to the typical dispersion pattern and therefore are not included in the inversion stage. For frequencies above 20 Hz, the phase velocity was observed to vary between 170 m/s and 215 m/s. This occurrence may be attributed to either the numerical effects contained in the processing of the signals or the superposition of higher modes as SASW tests generate apparent dispersion curves. For frequencies between 20 Hz and 36 Hz, it was observed that the phase velocities initially decreased from 205 m/s to 190 m/s. This was illustrative of the conclusion made earlier that the site was normally dispersive. Between frequencies of 36 Hz and 82 Hz, majority of the fluctuations occurred with regards to the phase velocities. Within this frequency bound, a higher mode of vibration possibly existed between frequencies of 48 Hz and 82 Hz, where the phase velocities dropped from 205 m/s and attained a constant 195 m/s phase velocity until the end. A final gradual increase of the phase velocities was noticed at a frequency of 82 Hz and this behaviour was thought to be on account of the superposition of different modes of vibration. Additionally, the dispersion data points generated through the CSW and SASW approaches were plotted on top of one another to evaluate the quality of the Love wave dispersion date points (Figure 4.23). Not only was it noticed that SASW approach provided a

close fit to the CSW approach, but similar frequency ranges were observed for the existence of higher modes of vibrations for both approaches.
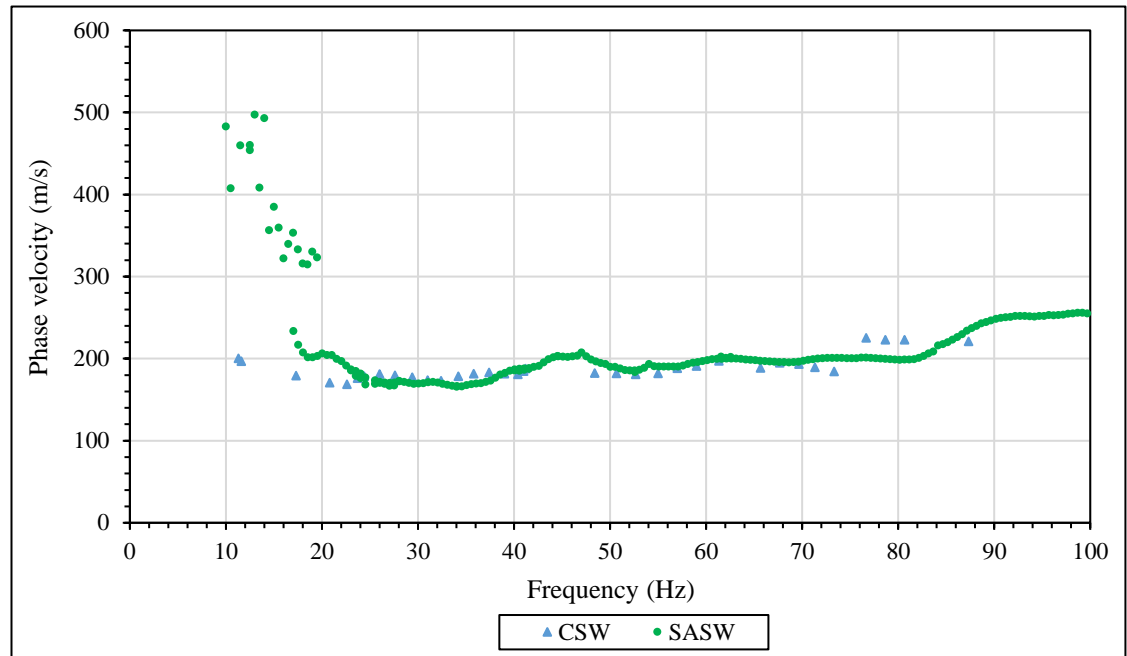
Figure 4.23: CSW and SASW Love wave dispersion points at Engineering 4.0.

4.1.2 Inversion Results

As the study conducted two variants of surface wave tests (CSW vs SASW) for the derivation of the dispersion curves, each approach of inversion analysis presented shear velocity estimates for the ground profile at the test site. Based on literature studies, the fundamental mode was sufficient alone for inversion runs incorporating normally dispersive profiles (Tokimatsu *et al.*, 1992). Thus, for all the inversion runs, the fundamental mode was adopted. For the CSW Rayleigh waves, dispersion points between 10 Hz and 40 Hz were considered and dispersion points between 10 Hz and 35 Hz were considered for the CSW Love waves. The fundamental mode for the SASW Rayleigh waves was between 0 Hz and 100 Hz and between 0 Hz and 40 Hz for the SASW Love waves. A multimode analysis was not conducted as it introduces additional uncertainties with regards to identifying the mode number or the possibility of superposed modes. By limiting the frequency ranges of the dispersion points, the minimum depth that could be resolved was 2 m. As the study was focused primarily on the Vs, results pertaining to the Vp are not discussed in this dissertation. During the analysis, only inversion results within the minimum misfit (M_m) and 10 % of the M_m (upper limit) were considered.

A discrete and joint inversion analysis was conducted to approximate the Vs profile using the parameters listed in Section 3.5. Each testing approach - CSW and SASW provided two sets of Vs profiles. Figure 4.24 and Figure 4.25 illustrates the V_S profiles approximated by the CSW testing approach. Figure 4.26 and Figure 4.27 shows the Vs profiles approximated by the SASW testing approach.
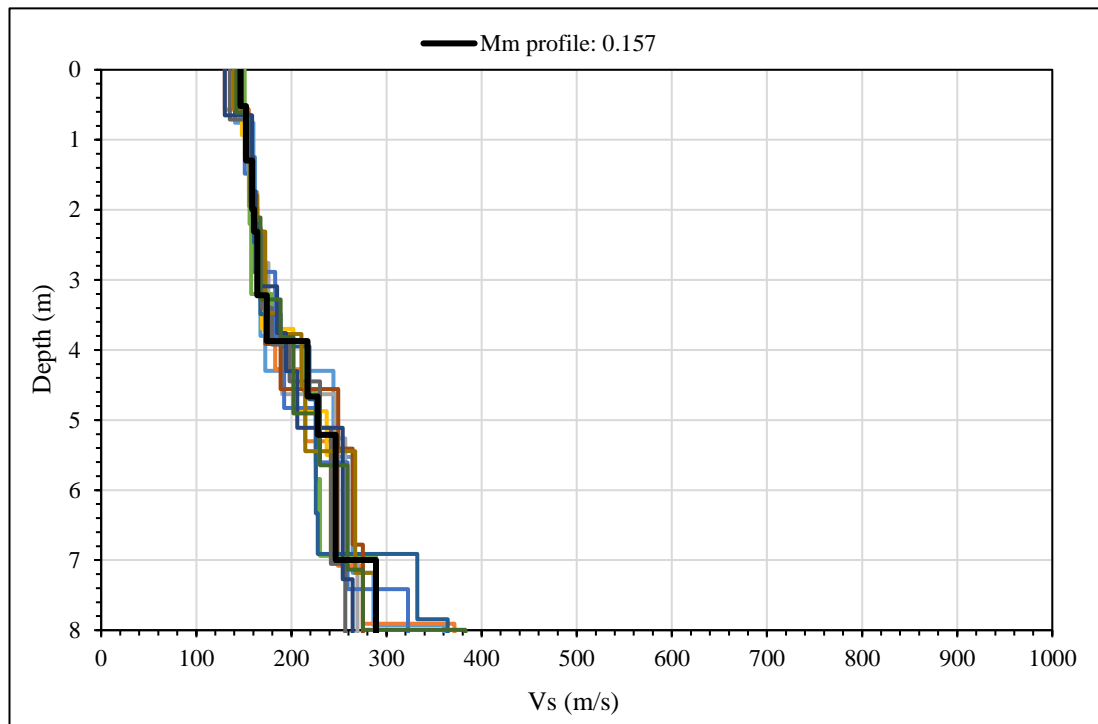
Figure 4.24: Vs profiles using discrete inversion - Rayleigh waves at Engineering 4.0 test site (CSW testing).
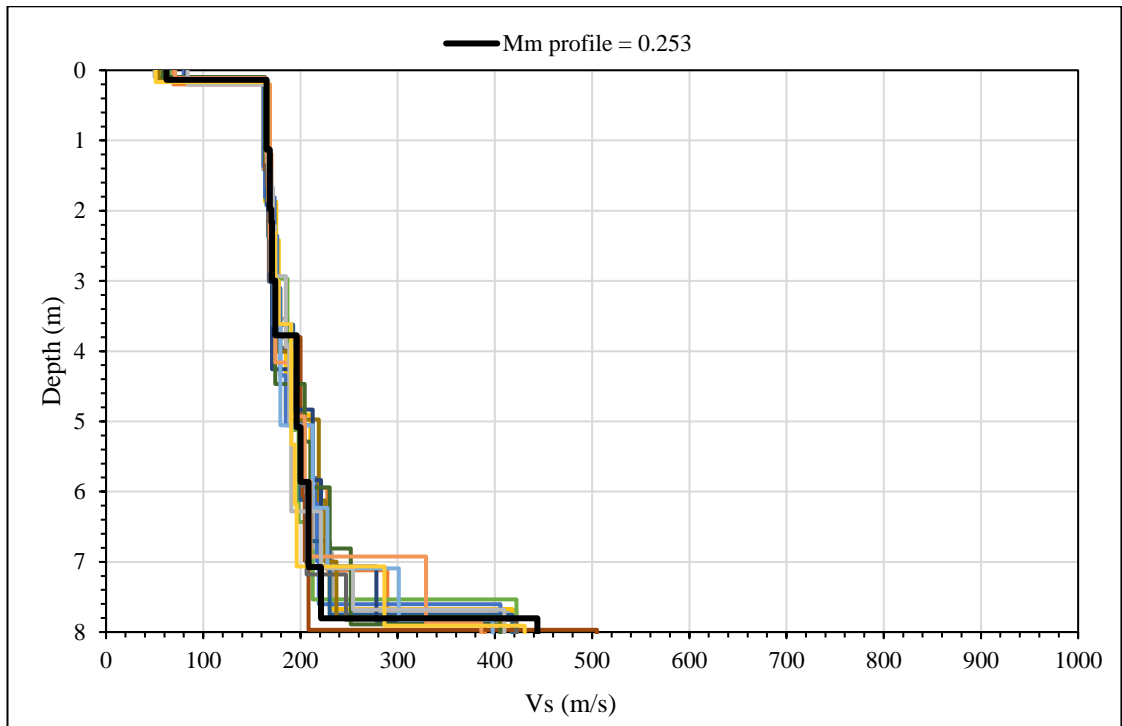
Figure 4.25: Vs profiles using joint inversion - Rayleigh and Love waves at Engineering 4.0 test site (CSW testing).
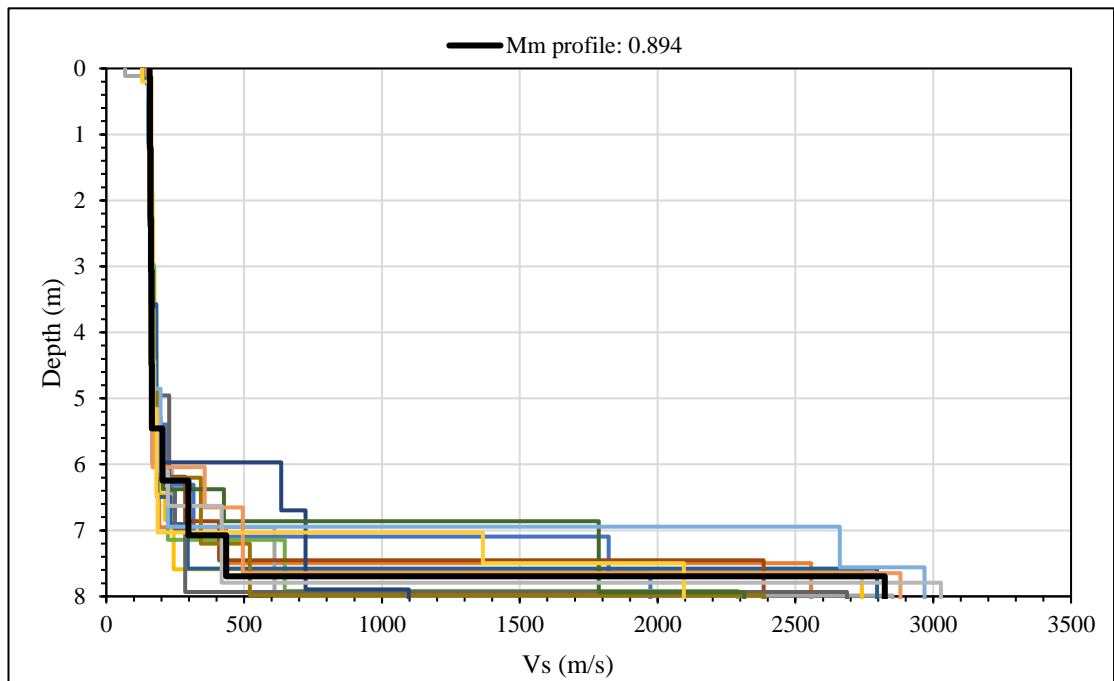
Figure 4.26: Vs profiles using discrete inversion - Rayleigh waves at Engineering 4.0 test site (SASW testing).
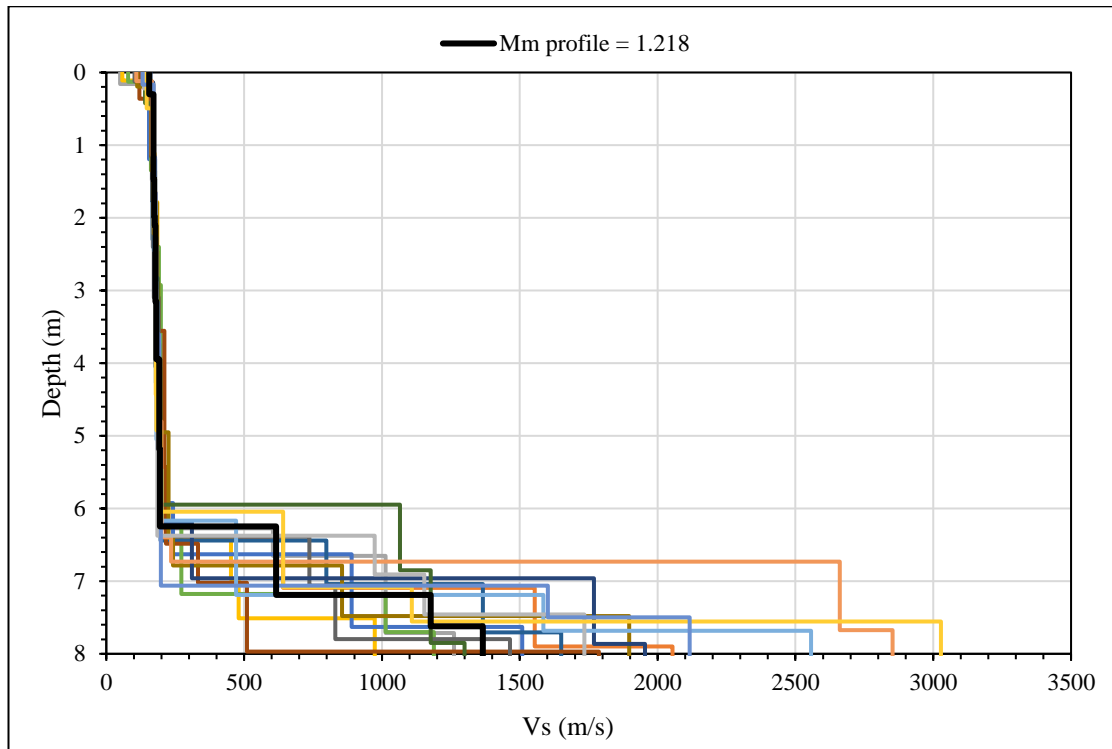
Figure 4.27: Vs profiles using discrete inversion – Rayleigh and Love waves at Engineering 4.0 test site (SASW testing).

At first glance, it was observed that upon conducting a joint inversion analysis, the minimum misfit value (M_m) increased for both CSW and SASW approach. This may imply that that there was a better fit between the experimental and theoretical dispersion data when conducting a discrete inversion analysis. However, a higher M_m could also be as a result of the joint inversion fitting both Rayleigh and Love wave dispersion data simultaneously. All four sets of Vs profiles exposed a normally dispersive profile, with the Vs increasing with depth. Test pit results for the Engineering 4.0 test site suggested an increase in stiffness of the materials as the materials transitioned from soft to firm clayey sandy silt to stiff jointed residual lava. For depths less than between 2 m and 3 m, both the CSW and SASW tests approached Vs within the range of 100 m/s and 200 m/s. According to Table 4.1 and Table 4.2, very soft to soft sandy soils/loose to dense sand/ soft to stiff clays are supportive of such V_s.

Table 4.1: Typical shear wave velocities for soils, (Borcherdt, 1994).

Very soft soils	50 m/s < Vs < 100 m/s
Soft soils	100 m/s < Vs < 200 m/s
Stiff clays and sandy soils	200 m/s < Vs < 375 m/s
Gravelly soils and soft rocks	375 m/s < Vs < 700 m/s
Firm to hard rocks	700 m/s < Vs < 1400 m/s
Hard rocks	Vs > 1400 m/s

Table 4.2: Typical shear wave velocities for clays, sands and rocks, Foti *et al.* (2018).

Soft clay	80 m/s < Vs < 200 m/s
Stiff clay	200 m/s < Vs < 600 m/s
Loose sand	80 m/s < Vs < 250 m/s
Dense sand	200 m/s < Vs < 500 m/s
Gravel	300 m/s < Vs < 900 m/s
Weathered rock	600 m/s < Vs < 1000 m/s
Competent rock	1200 m/s < Vs < 2500 m/s

To evaluate the quality in approximating the Vs profiles, the spread in the Vs was determined for each respective inversion scenario. The spread in the Vs was calculated by considering the maximum and minimum Vs profiles at every 1 m depth within the limits of M_m and 10 % of M_m. The spread in the Vs was used as an indicator to determine how well the Vs was estimated at every 1 m depth layer from each inversion scenario. Therefore, the smaller the spread in the Vs, the better the approximation of the Vs. Figure 4.28 and Figure 4.29 illustrates the spread in the Vs when using discrete and joint inversions for CSW and SASW approaches respectively.
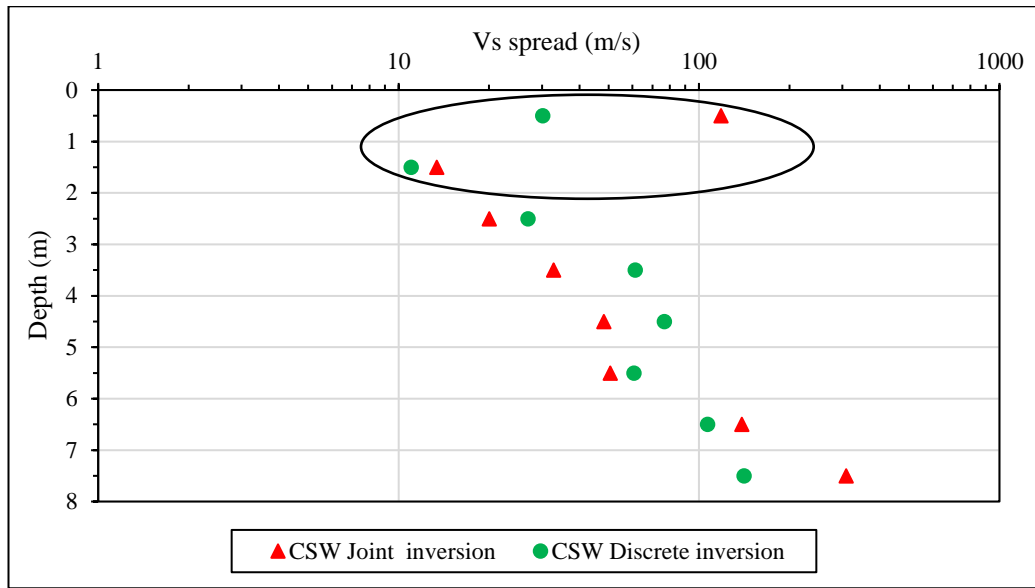
Figure 4.28: Comparison of the spread in Vs between discrete and joint inversions on CSW dispersion data.
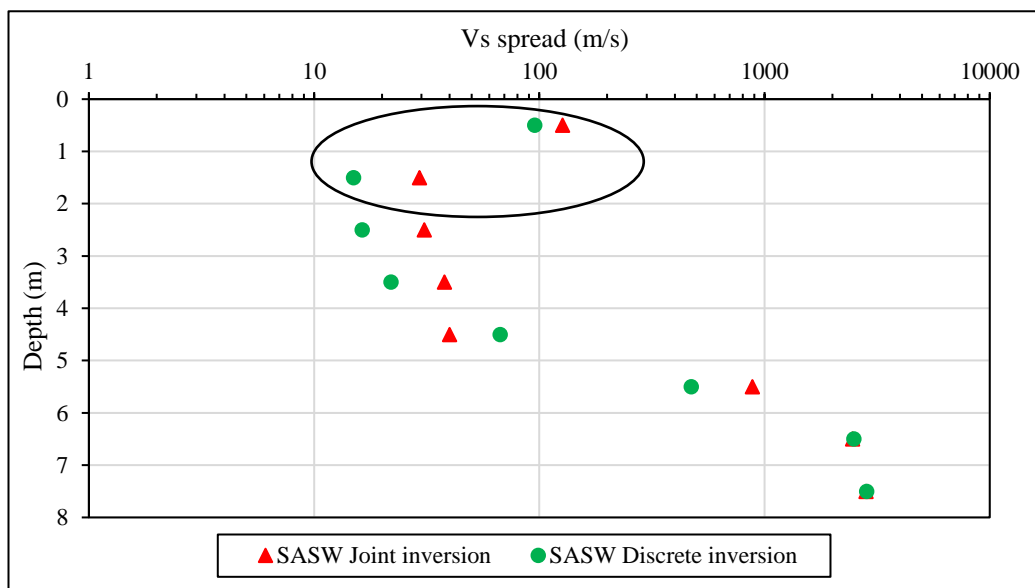
Figure 4.29: Comparison of the spread in Vs between discrete and joint inversions on SASW dispersion data.

In both Figure 4.28 and Figure 4.29, Vs spread points for depths below 2 m were circled and not considered during the analysis due to limitations in the minimum depth that could be

resolved by the Rayleigh and Love wave dispersion points. It was noticed from Figure 4.28, that between 2 m and 6 m, the joint inversion for the CSW approach produced a smaller spread in the Vs than that from the discrete inversion. This suggested that by incorporating CSW Love waves with CSW Rayleigh waves during the inversion process, a better approximation of the Vs profile could be obtained at these depths. For depths greater than 6 m, it was observed that the discrete inversion provided a better approximation of the Vs profiles due to a smaller spread in the Vs compared to the joint inversion. With regards to the SASW approach, it was observed from Figure 4.29 that the discrete inversion produced a smaller spread in the Vs than the joint inversion for depths between 2 m and 4 m and for depths between 5 m and 6 m. The joint inversion produced a smaller Vs spread than the discrete inversion between 4 m and 5 m. For depths greater than 6 m, both discrete and joint inversions produced similar spreads in the Vs. Based on Figure 4.28 and Figure 4.29, the CSW joint inversion appears to improve the results whereas for the SASW joint inversion it does not.

According to the inversion analysis conducted on the synthetic dispersion data in Section 3.6, a joint inversion could provide a better approximate of the Vs profile than a discrete inversion. However, for this to occur, it was necessary for both dispersion data (Rayleigh and Love waves) to be of good quality. A poor-quality signal results in a poor fit between the theoretical and experimental dispersion data during the inversion process. This was observed in Figure 4.30 and Figure 4.31, which illustrated the fit between the theoretical and experimental dispersion data for the CSW and SASW approaches respectively. From Figure 4.30 and Figure 4.31, it was visually noticed that there was a poor fit between the Love wave dispersion data compared to the Rayleigh wave dispersion data. One can clearly see that there was an issue with the Love wave dispersion data at low frequencies in Figure 4.31. Any form of joint inversion was therefore going to be difficult. It could be concluded that since the quality of the Love wave dispersion data was not as good as the quality of the Rayleigh wave dispersion data, the spread in the Vs was greater for the joint inversions than the discrete inversions.
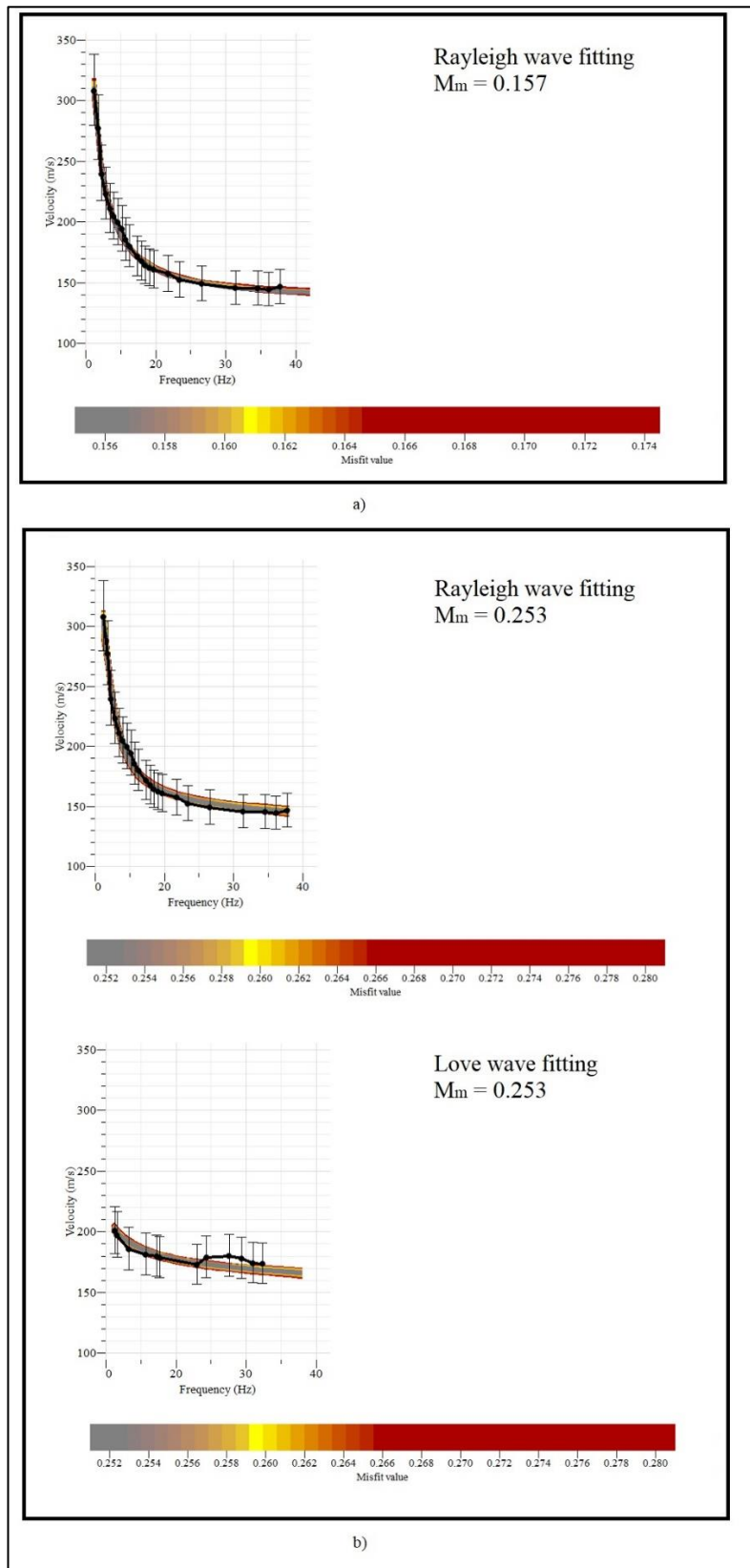
Figure 4.30: Fitting between theoretical and experimental dispersion data using a) discrete inversion b) joint inversion for CSW test at Engineering 4.0 test site.
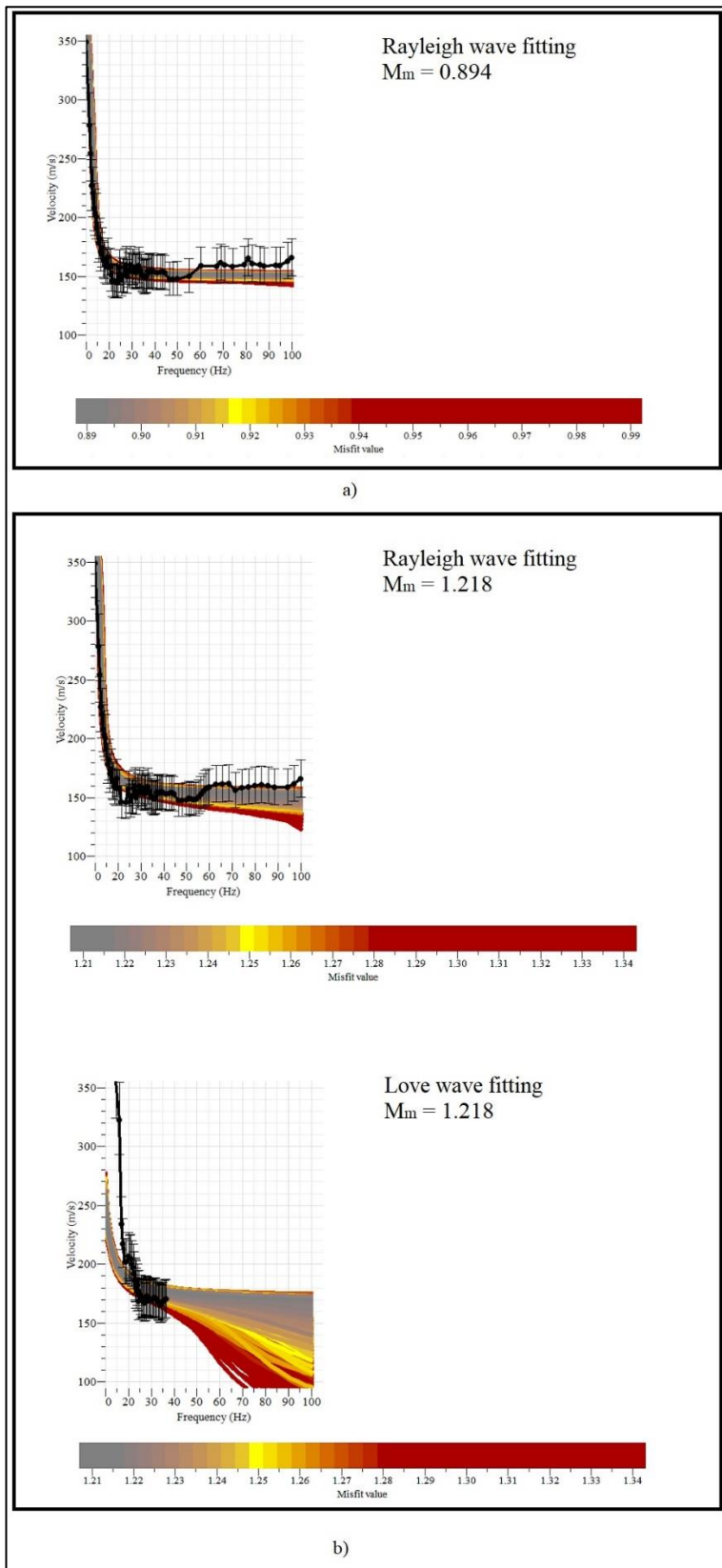
Figure 4.31: Fitting between theoretical and experimental dispersion data using a) discrete inversion b) joint inversion for SASW test at Engineering 4.0 test site.

4.2 WIND AFRICA TEST SITE

4.2.1 Dispersion Curve results

4.2.1.1 Rayleigh Wave Experimental Dispersion curves

i. CSW Rayleigh Wave dispersion curve

The CSW approach made use of the low frequency shaker and the high frequency shaker, each with its own limitations in the frequency ranges. Following the experimental design discussed in Section 3, the CSW tests were conducted for 1 m, 2 m and 4 m source offsets. Once more, the final dispersion curve was obtained by merging the dispersion results from the two shakers. Dispersion results acquired at the Wind Africa test site using the low frequency shaker and the high frequency shaker are shown in Figure 4.32 and Figure 4.33 respectively.
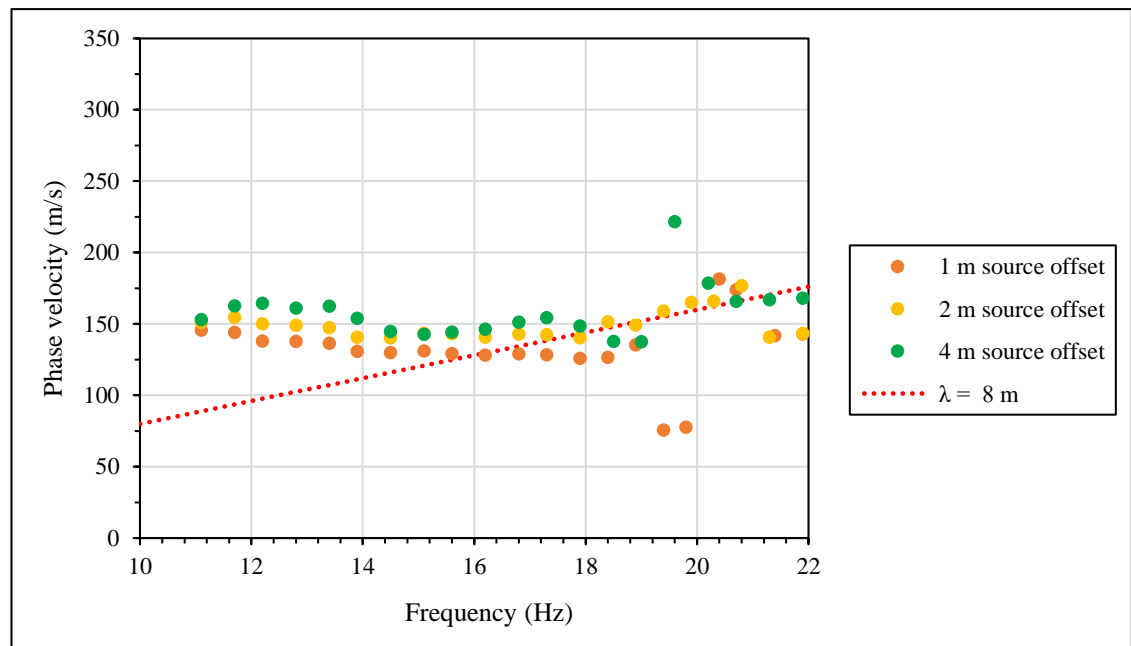
Figure 4.32: Rayleigh wave dispersion data before 'screening' for low frequency shaker at Wind Africa test site with Near Field effect cut off line.
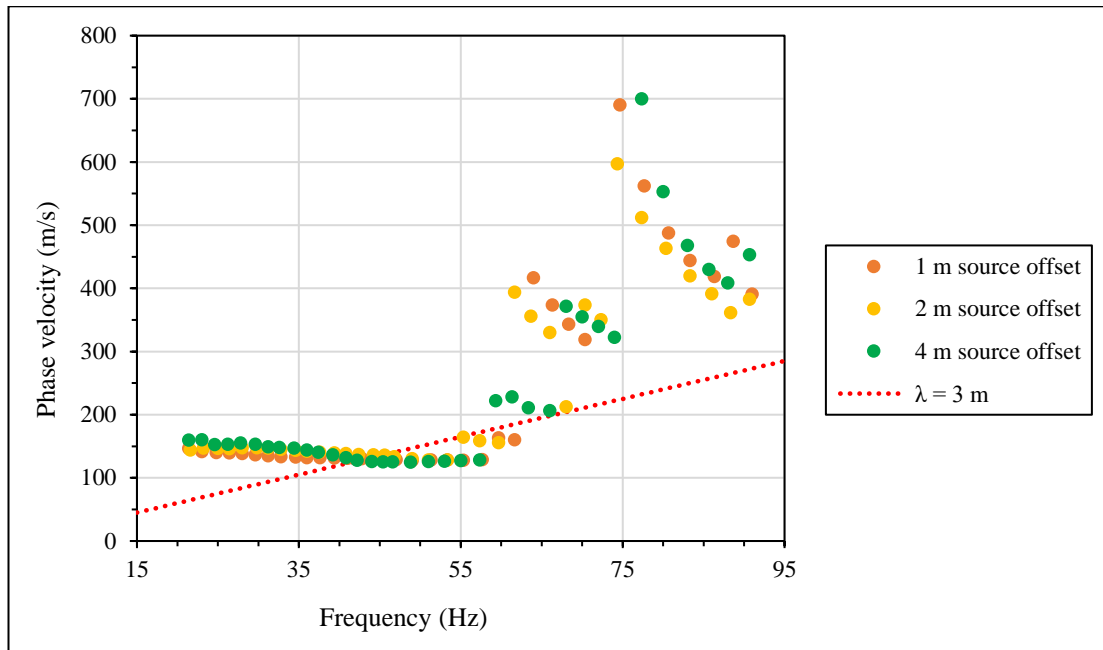
Figure 4.33: Rayleigh wave dispersion data before 'screening' for high frequency shaker at Wind Africa test site with Near field effect cut off line.

From Figure 4.32, it could be seen that majority of the dispersion points for all three source offsets using the low frequency shaker followed a constant pattern with phase velocities between 100 m/s and 150 m/s. Additionally, it was observed that below 19 Hz a flat pattern was evident, but the dispersion points plotted parallel to one other, with the lower source offsets producing lower phase velocities. Thus, the 1 m source offset generated the lowest phase velocity dispersion points when compared to the 2 m and 4 m source offsets. Such an occurrence may be explained by the near field effects. To evaluate the criterion set by Hiltunen and Woods (1990), a near field cut off line with a wavelength of 8 m was plotted in Figure 4.32. From Figure 4.32, it was observed that for source offsets less than $\frac{\lambda}{4}$ (green and yellow points at 18 Hz) no near field effects are observed. However, for source offsets less than $\frac{\lambda}{8}$ (orange points below 16 Hz), near field effects are evident. Therefore, the above observations suggests that the criterion set by Hiltunen and Woods (1990) deemed to be conservative. It should be realized that the scatter in the dispersion points after 19 Hz may be due to numerical effects and therefore required screening.

In context of the high frequency shaker dispersion points, it could be seen in Figure 4.33 that for frequencies below 60 Hz, a constant pattern was observed for all three source offsets and

the dispersion points overlapped one another. However, it was noticed that the phase velocities presented by 1 m and 2 m source offsets were slightly below that of the 4 m source offset for frequencies below 40 Hz and this was probably due to the near field effects. According to Figure 4.33, near field effects are observed only for source offsets less than $\frac{\lambda}{3}$ (orange points below 40 Hz). The flat pattern in phase velocities of the dispersion points was seen to gradually decrease. This implied that the test site exhibited decreasing phase velocities, with increasing frequencies. Towards the higher frequencies, it was observed that the source offsets produced phase velocity jumps for the dispersion points at three different frequency regions. These jumps could be indicative of different higher modes present in the test site. However, due to the coefficient of determination criterion ($R^2 > 0.99$), the clusters formed by the higher modes of vibrations were excluded and only the fundamental mode dispersion points were considered for the inversion analysis. Using the 'screened' data points from the high frequency shaker and the low frequency shaker, an experimental dispersion curve dispersion curve was constructed (Figure 4.34). Once again, it was observed that the dispersion points followed a decreasing pattern, with the phase velocities reducing from 160 m/s to 125 m/s over the range of 10 Hz to 60 Hz. Thus, according to Figure 4.34, the test site was normally dispersive. Furthermore, the 'screening' stage had reduced the dispersion points to only illustrate the fundamental mode of vibration, although from Figure 4.33, it was known that the site displayed higher modes towards the higher frequencies. It was known from literature that for sites with normally dispersive profiles, the fundamental mode alone was sufficient for the inversion analysis to be made (Tokimatsu *et. al*, 1992).

As a verification process of the steady state dispersion plots, a transient signal (Sweep) CSW test was conducted as well for the different source offsets (Figure 4.35). Sweep dispersion points were 'screened' before using the following criterion of $R^2 > 0.99$ and coherence ($\gamma^2 > 0.90$). Through visual inspections, the sweep signal generated dispersion plots with similar characteristics to that of steady state Rayleigh wave signals, including the higher modes of vibration witnessed at frequencies above 60 Hz.
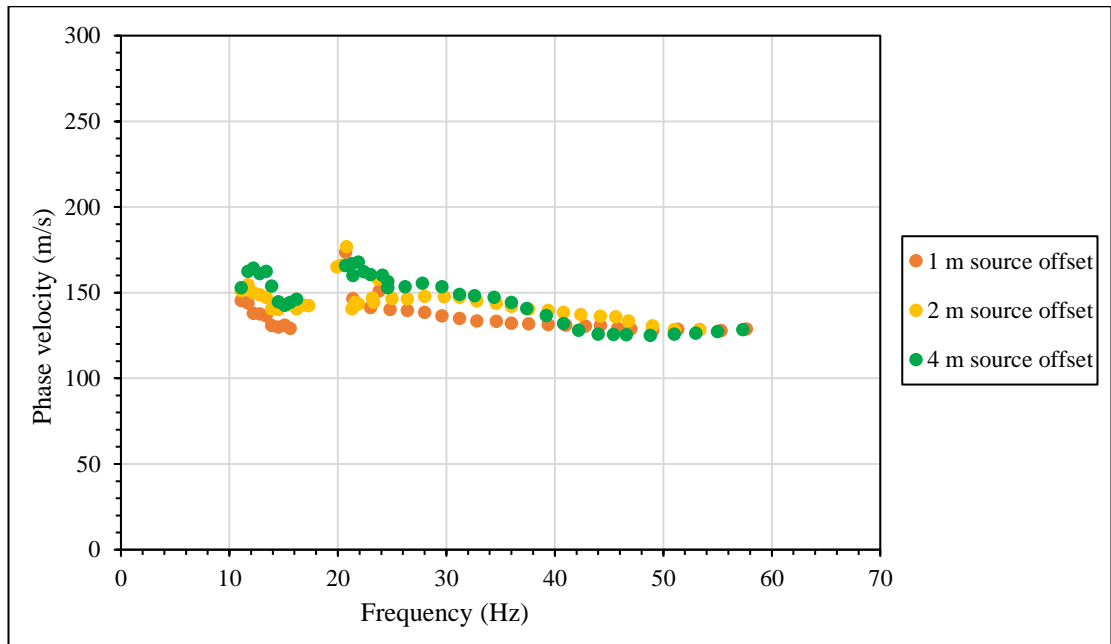
Figure 4.34: Experimental Rayleigh Wave dispersion curve after 'screening' at Wind Africa test site.
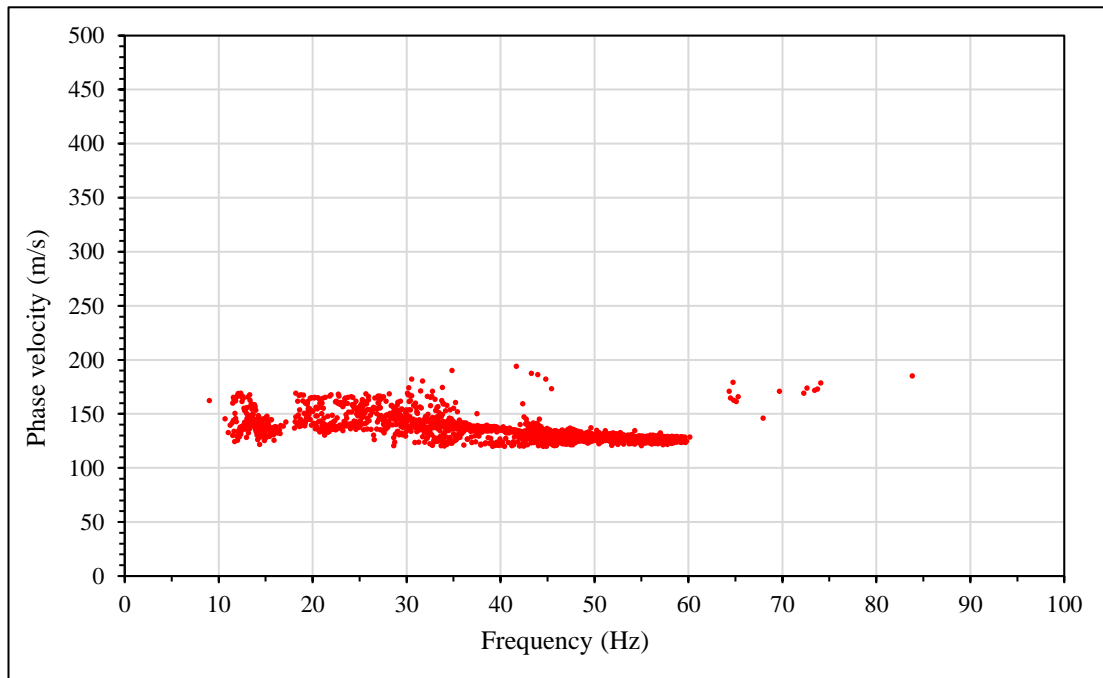
Figure 4.35: CSW combined Sweep dispersion curve for Rayleigh waves considering all three source offsets using both high frequency and low frequency shakers at Wind Africa test site.

ii. SASW Rayleigh Wave dispersion curve

At the Wind Africa test site, SASW Rayleigh wave tests were completed using three sets of sledgehammers, namely the 2 kg, 6 kg, and 9 kg sledgehammers for the range of spacings described in Section 3.2.2. As mentioned previously, a fundamental aspect of the SASW was the SNR of each individual impact source. To illustrate this aspect, the spectral amplitudes for each of the sledgehammers were measured and plotted adjacent to the spectral amplitude of the background noise experienced in the vicinity of the test site. The spectral amplitude plots were essential in identifying the frequency ranges over which the data was to be masked. Figure 4.36 illustrates the spectral amplitudes incurred by each sledgehammer for a spacing of 8 m.
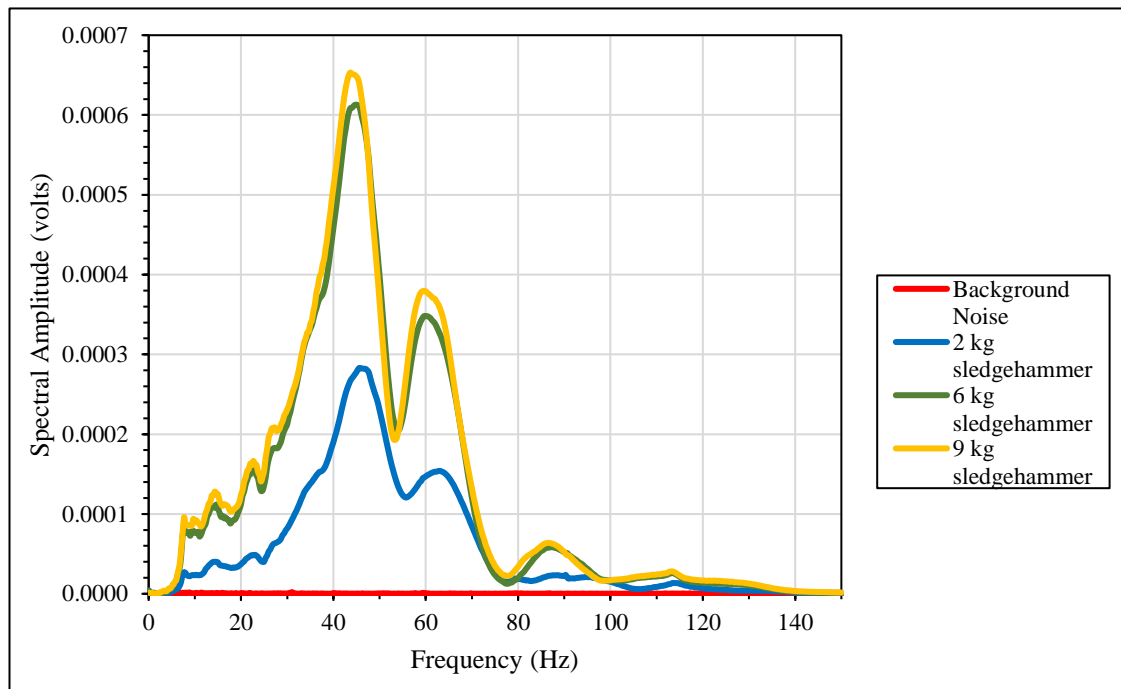
Figure 4.36: Spectral Amplitudes at Geophone 1 for 8 m spacing using SASW Rayleigh wave approach at Wind Africa test site.

With relevance to the SNR of the three sledghammers, all three sledgehammers produced sufficiently high SNR as the spectral amplitudes were significantly higher than that of the background noise as seen in Figure 4.36. In terms of the energy conveyed, the 9 kg sledgehammer delivered the greatest, although, the energy delivered by the 6 kg sledgehammer was substantially similar to that given by the 9 kg sledgehammer. This could possibly be due to the variation in the human input involved when swinging a sledghammer. Furthermore, it

was noticed that for all three sledgehammers experienced a drop in the spectral amplitudes towards the higher frequencies.

As SASW involved conducting tests at different spacings, the quality of the data delivered at each spacing varied significantly. The quality of the impact signals was evaluated using the coherence function (γ^2) together with the spectral amplitude plot to identify acceptable frequency ranges. By employing Nazarian and Stokoe II (1986) criterion of accepting frequency regions with a $\gamma^2 > 0.9$, acceptable frequency ranges were established. In addition to the above, the wrapped phase difference plot was examined for the distinctive "sawtooth" pattern at these frequency ranges; upon which the phase differences were unwrapped and utilized in the programming code to extract the individual dispersion curves. Figure 4.37 shows the coherence and phase difference plots used in masking the SASW data, with the pink shades depicting acceptable regions.
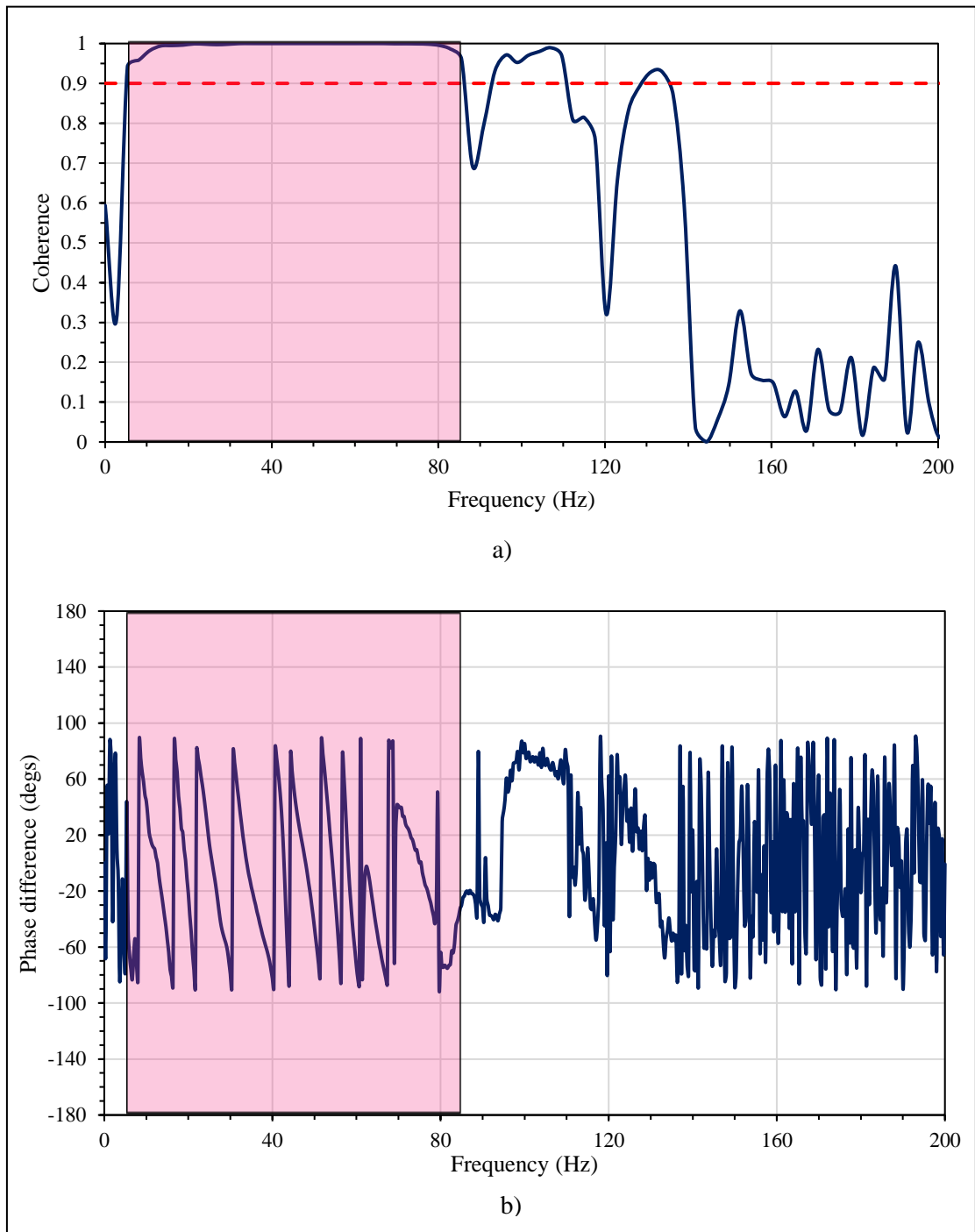
Figure 4.37: Coherence plot (a) and Phase difference plot (b) for 9 kg sledgehammer at 8 m spacing for SASW using Rayleigh waves at Wind Africa test site.

Upon extraction of the individual dispersion curves for different spacings, the composite experimental dispersion curve was generated by merging the respective individual dispersion curves (Figure 4.38). Depending on the degree of overlap between the individual dispersion

curves, some dispersion curves at different spacings were excluded. It could be seen from Figure 4.38, that the 1 m and 32 m spacings were not included in the composite experimental dispersion curve due to poor coherence and incompatibility in terms of overlapping with the rest of the individual dispersion curves. Furthermore, due to the coherence criterion mentioned previously, only specific portions of each individual dispersion were used to generate the composite dispersion curve. At frequencies below 7 Hz, a large degree of scatter was observed from the respective spacings. This could probably be due to insufficient energy to excite the ground at low frequencies. As the scattered dispersion points below 7 Hz do not confirm to the usual dispersion pattern, they were excluded during the inversion analysis. With regards to the phase velocities observed, a similar match to the CSW Rayleigh wave dispersion curve was obtained as shown in Figure 4.39. The phase velocities gradually decreased with increasing frequencies and maintained a constant phase velocity of 130 m/s towards the higher frequency ends. This behaviour suggested that the profile at Wind Africa was normally dispersive as suggested initially by the CSW Rayleigh wave tests.
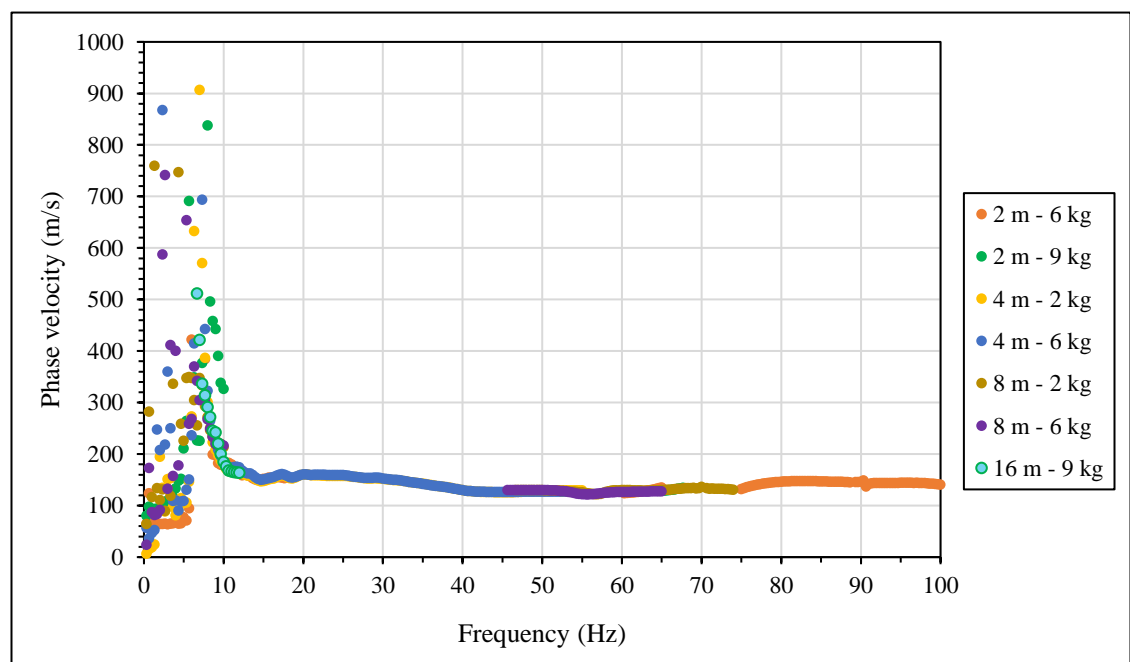
Figure 4.38: SASW Composite dispersion curve using Rayleigh waves at Wind Africa test site.
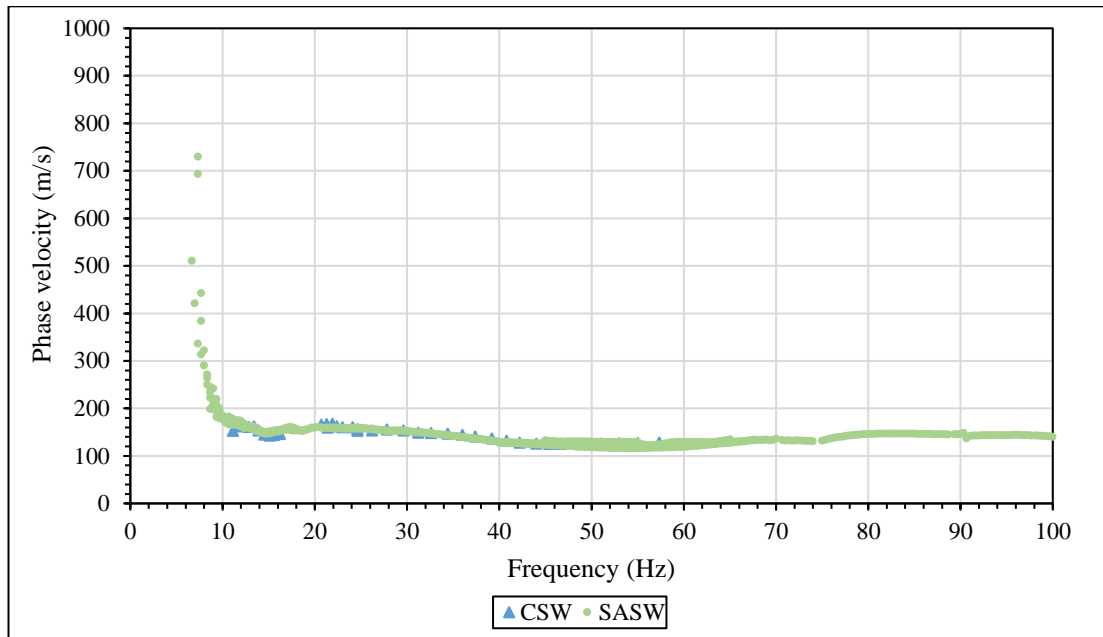
Figure 4.39: CSW and SASW Rayleigh wave dispersion points at Wind Africa test site.

4.2.1.2 Love Wave Experimental Dispersion curves

i. CSW Love Wave dispersion curve

The experimental setup described in Section 3.2 was employed at the Wind Africa test site for the generation of Love waves using the low frequency and high frequency shakers. The data from the two shakers was processed to obtain the dispersion points from which the inversion process was to be conducted. The raw dispersion points obtained from the low frequency and high frequency shaker are illustrated in Figure 4.40 and Figure 4.41 respectively.
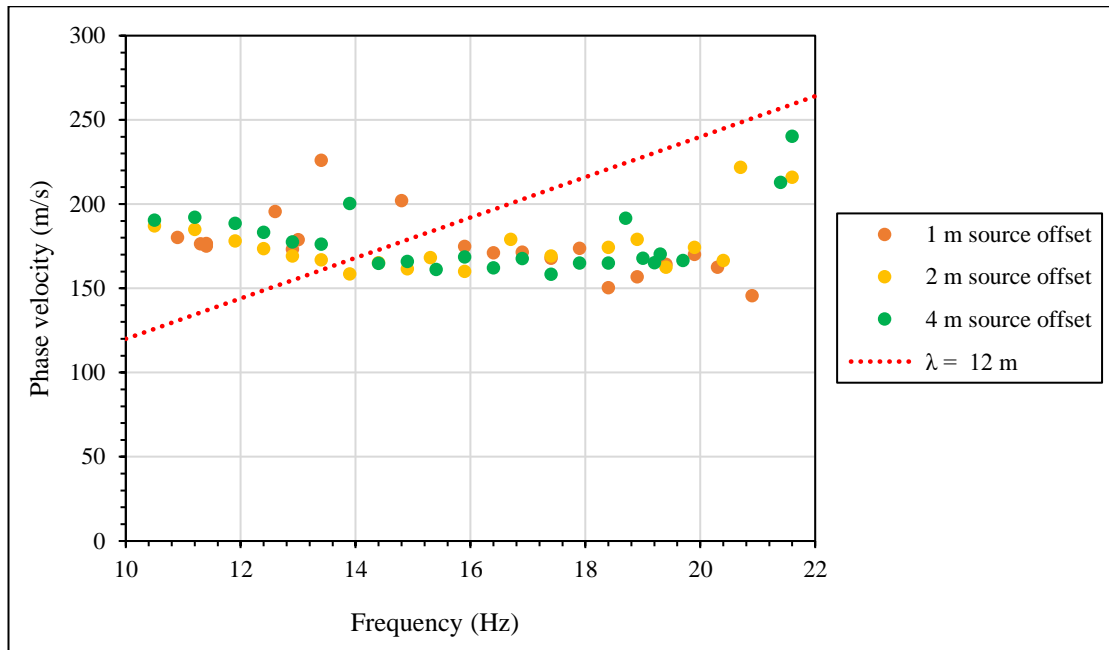
Figure 4.40: Love wave dispersion data before 'screening' for low frequency shaker at Wind Africa test site with Near Field effect cut off line.
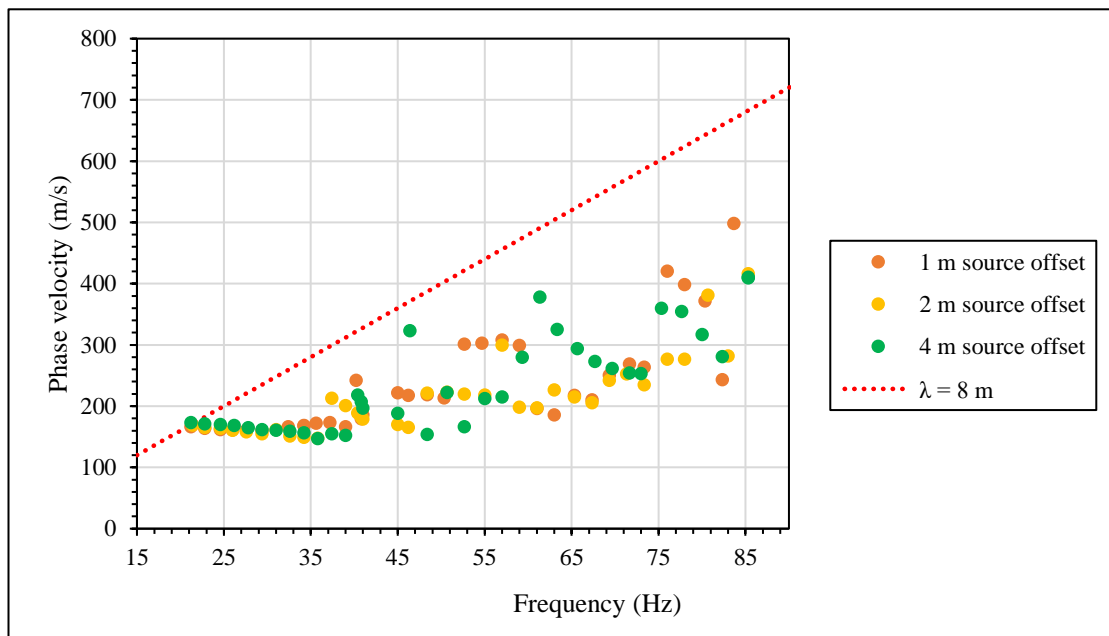
Figure 4.41: Love wave dispersion data before 'screening' for high frequency shaker at Wind Africa test site.

From Figure 4.40, it was observed that majority of the dispersion points were positioned close to one another for all three source offsets with close agreement for frequencies above 13.5 Hz. The effects of near field were observed at frequencies below 13.5 Hz for both the 1 m and 2 m source offsets. A near field cut off line with a wavelength of 12 m was also included in Figure 4.40 to assess at what wavelength near field effects no longer occurred. Based on Figure 4.40, it was observed that for source offsets less than $\frac{\lambda}{6}$ (yellow data points at 13.5 Hz), no near field effects are observed. However, from visual inspection it could be seen that all three source offsets produced dispersion points in similar phase velocity vicinities for frequencies above 13.5 Hz and therefore, dispersion points from all three source offsets were considered for the study.

In relation to the high frequency shaker dispersion points in Figure 4.41, a constant pattern was observed from all three source offsets for frequencies below 40 Hz. Between 20 Hz and 40 Hz, majority of the dispersion points were noticed to overlap for all three source offsets. No near field effects were observed for the three source offsets even at a source offset of $\frac{\lambda}{8}$. For frequencies greater than 40 Hz, all three source offsets displayed multiple phase velocity jumps. It is speculated that these are higher modes of vibrations. A possibility of an inversely dispersive profile was also brought into consideration. However, it is known from the profile description and SPT N values that the Wind Africa site is normally dispersive.

During the 'screening' process, the coefficient of determination was utilized to identify dispersion points with a good fit ($R^2 > 0.99$) in terms of the Phase angle - Distance plot (Figure 4.42). This allowed quality dispersion points to be extracted from both shakers. It was noticed that the dispersion points initially decreased from a phase velocity of 200 m/s to 175 m/s within the frequency range of 10 Hz to 15 Hz. For frequencies between 15 Hz and 30 Hz, a constant phase velocity of 175 m/s was observed after which the phase velocities decreased to 145 m/s between a frequency range of 30 Hz to 40 Hz. As majority of the overlap from all three source offsets occurred between 10 Hz and 40 Hz, this portion of the dispersion curve was considered as the fundamental mode. The phase velocity jumps above 40 Hz were speculated to be higher modes of vibration, and this was in accordance with the data presented by the CSW transient signal (sweep) test (Figure 4.43). According to the sweep dispersion curve, dispersion points for frequencies below 40 Hz were part of the fundamental mode of vibration.
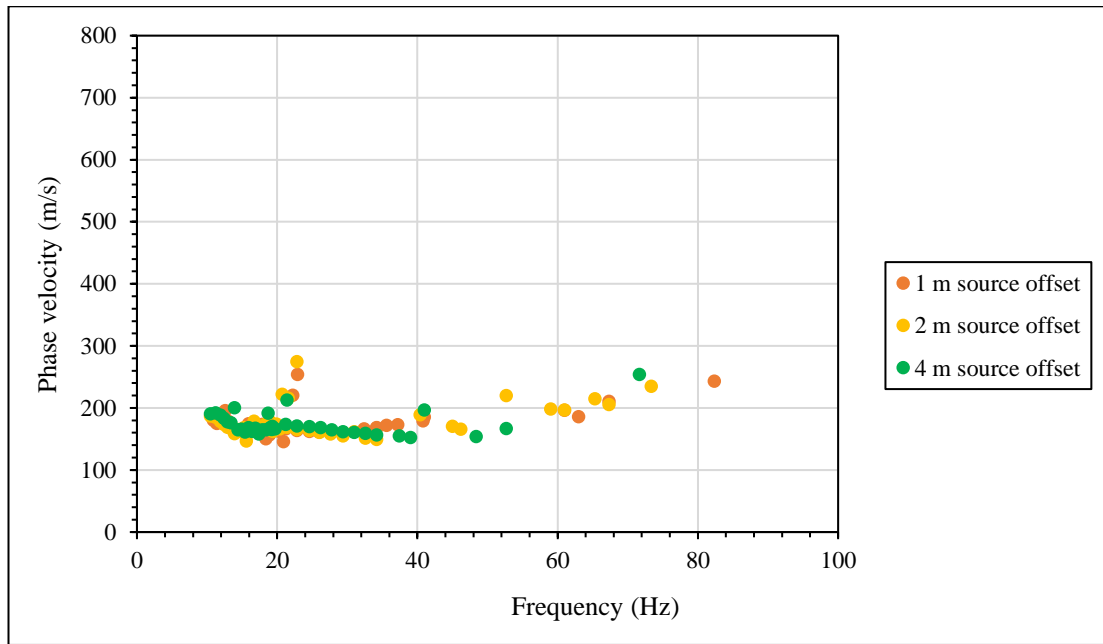
Figure 4.42: Experimental CSW Love Wave dispersion curve after 'screening' at Wind Africa test site.
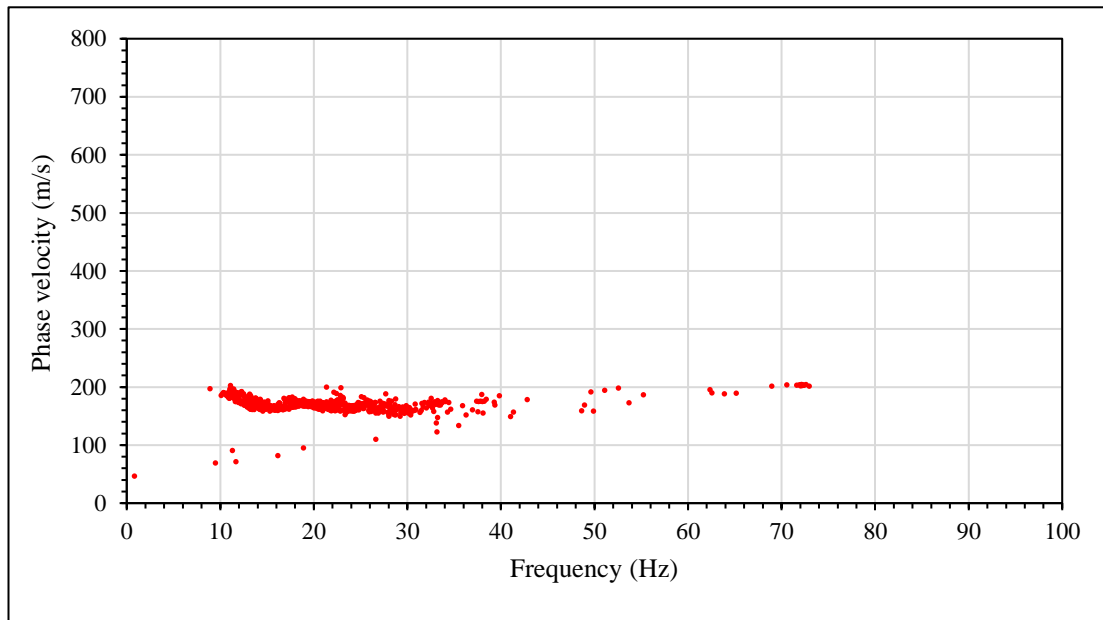
Figure 4.43: CSW combined sweep dispersion curve for Love waves at Wind Africa test site.

ii. SASW Love Wave dispersion curve

To investigate the performance of the SASW Love Wave impact source with regards to the energy provided, the spectral amplitude was measured at the second test site as well. Through evaluation of the spectral amplitudes generated by the three different sledgehammers against that of the background noise, the SNR at the Wind Africa test site was assessed. Figure 4.44 presents the spectral amplitude behaviour of the Love wave impact source at the Wind Africa test site.
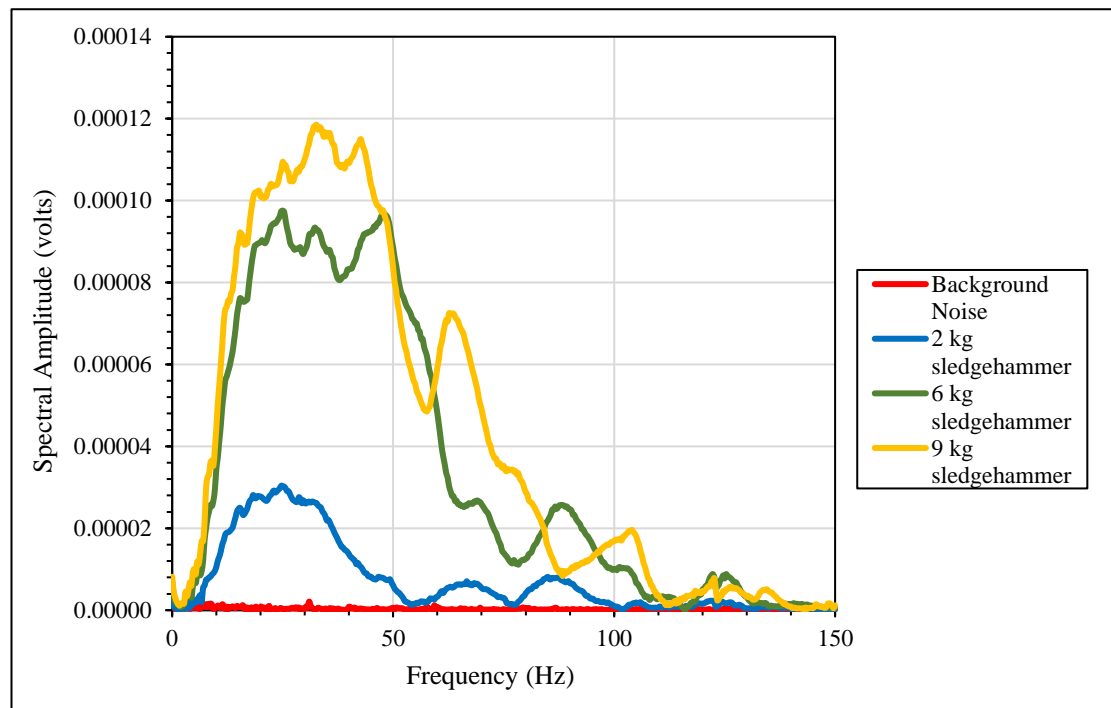
Figure 4.44: Spectral Amplitudes at Geophone 1 for 8 m spacing using SASW Love approach at Wind Africa test site.

From Figure 4.44, it was firstly observed that the test site location was quiet as the background noise was low. This indicated that the SNR was comparatively high for the sledgehammers used. In terms of the energy of the source, the spectral amplitudes varied according to mass, with the 9 kg sledgehammer delivering the highest amount of energy. An interesting observation was made with regards to the distribution of the energy. Irrespective of the mass of the sledgehammers, the energy was contained within a frequency range of 0 Hz to 150 Hz. Possible explanations for this observance include source behaviour or test site characteristics.

In conjunction with the spectral amplitude plots, the coherence function and the phase difference plots were used to process the data to generate the dispersion points for each spacing. The coherence criterion was applied ($\gamma^2 > 0.9$) (Nazarian and Stokoe II, 1986) to identify frequency regions where the signals had a constant phase difference, and these regions were used to 'unwrap' the phase differences as shown in Figure 4.45.
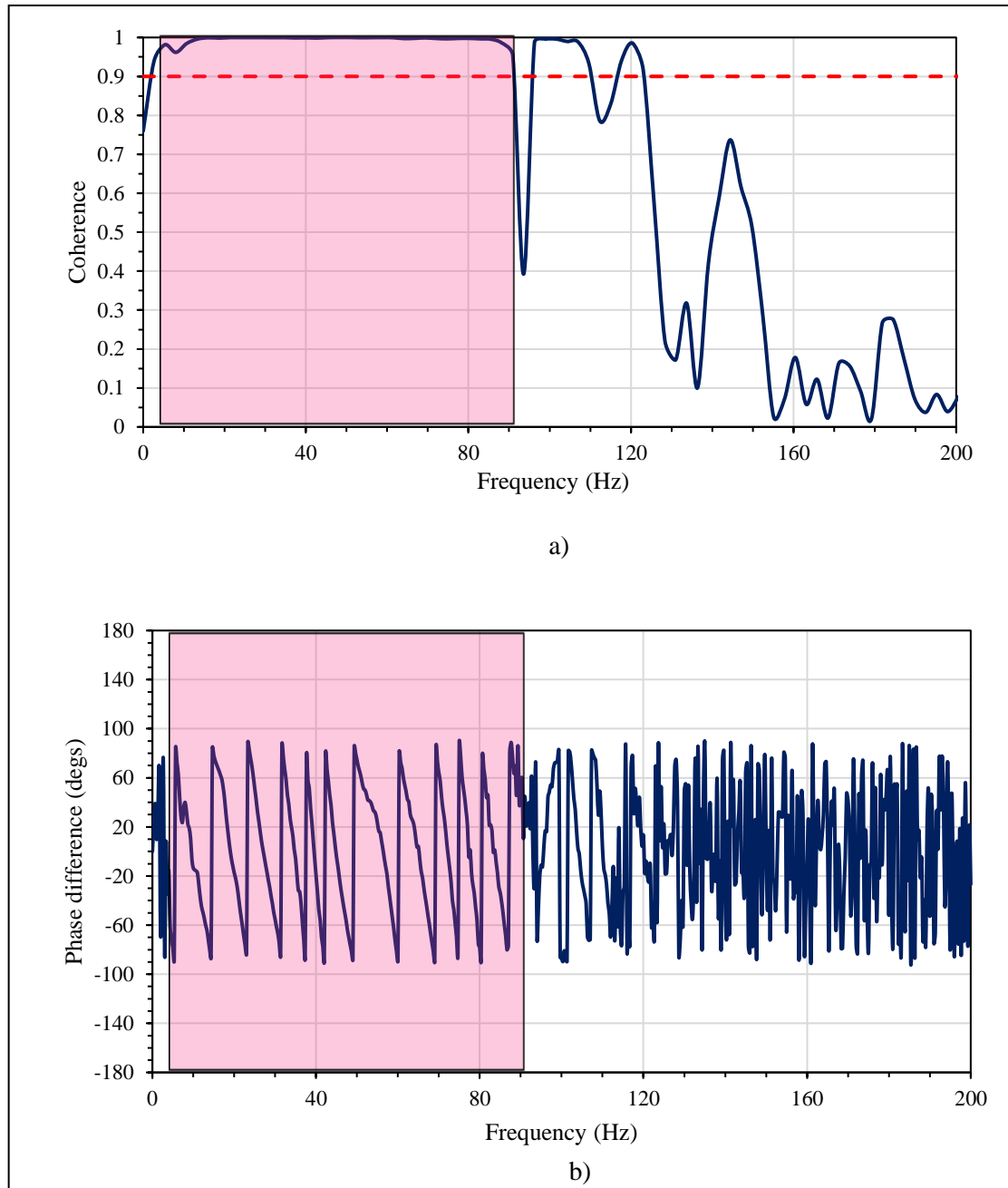
Figure 4.45: Coherence plot (a) and Phase difference plot (b) for 9 kg sledgehammer at 8 m spacing for SASW using Love waves at Wind Africa test site.

The masking process, which involved identifying the frequency ranges with high coherences and unwrapping the respective phase differences, was implemented for each spacing to obtain the individual dispersion points. Based on the overlap between the individual dispersion data, only a selected few were included in the composite experimental dispersion curve (Figure 4.46). It was firstly observed that for frequencies below 7 Hz, a large amount of scatter in the dispersion points was observed for the respective spacings. This observation was probably due to insufficient energy produced at the lower frequencies. For frequencies between 7 Hz and 10 Hz, phase velocities as high as 820 m/s was observed which eventually decreased rapidly to 175 m/s at a 10 Hz. A further decrease in the phase velocity to 165 m/s was observed between 10 Hz and 15 Hz. Following this decrease, a phase velocity of 165 m/s was maintained until a frequency of 45 Hz. For frequencies greater than 45 Hz, the phase velocities gradually increased to 225 m/s at 55 Hz. Between 55 Hz and 100 Hz, a constant phase velocity of 225 m/s was observed. Speculations for the occurrence of this behaviour included the superposition of different modes of vibration, with the fundamental mode contained in the frequency region of 7 Hz and 45 Hz and overlapping with the first higher mode contained in frequency regions greater than 45 Hz. This was due to the visual fact that at between 45 Hz and 50 Hz a gradual increase in the phase velocity was observed and it was known from literature that SASW tests measures apparent dispersion data. The observations made are consistent with the borehole results in Section 3.1 that clearly indicated the presence of a normally dispersive profile. The Love wave dispersion data for the Wind Africa test site was also compared for the two approaches as shown in Figure 4.47. It was noticed that both approaches produced similar dispersion data with identical frequency regions where a gradual increase in the phase velocity was observed.
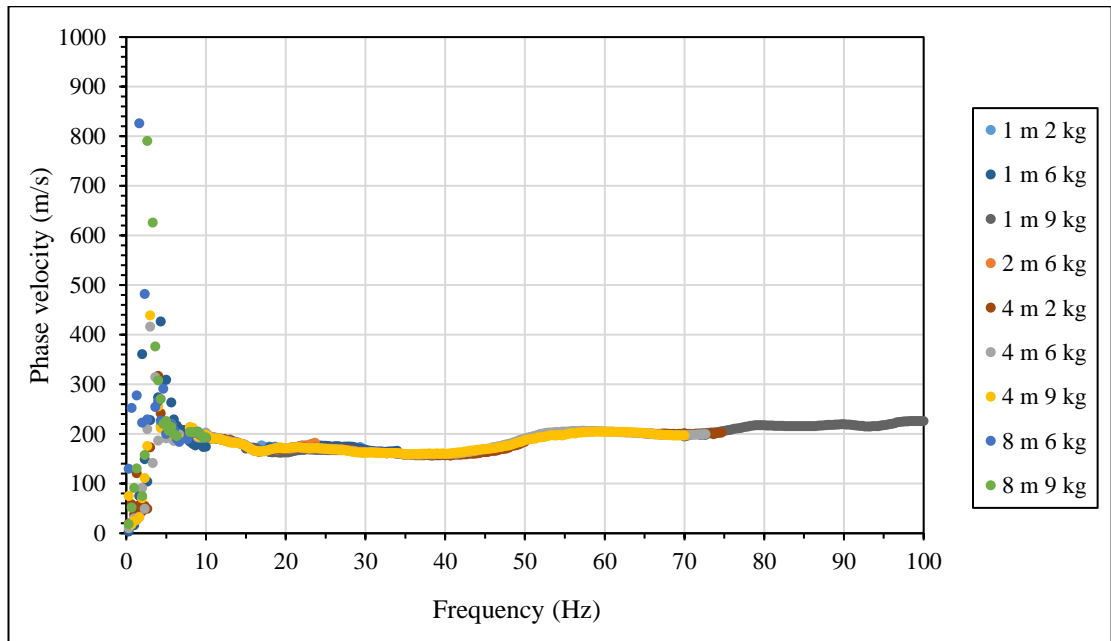
Figure 4.46: Love waves SASW composite dispersion curve at Wind Africa test site.
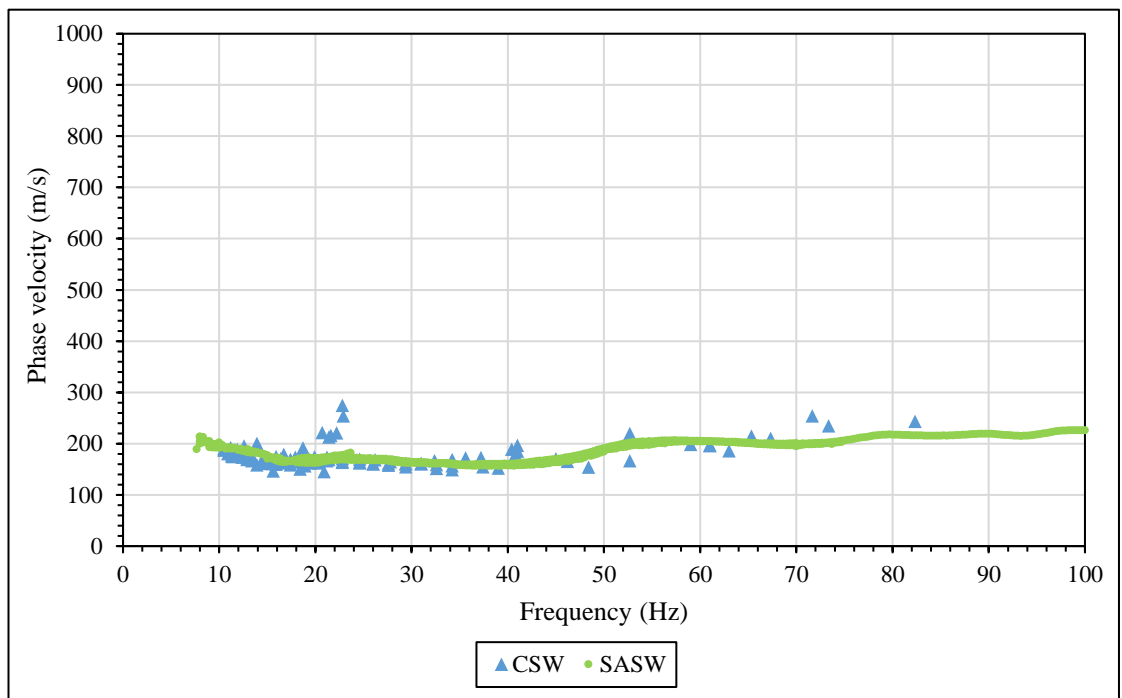
Figure 4.47: CSW and SASW Love wave dispersion points at Wind Africa test site.

4.2.2 Inversion Results

In a similar way to the inversion analysis conducted with the Engineering 4.0 data, discrete and joint inversions were conducted to generate Vs profiles for the Wind Africa test site. Dispersion data from both CSW and SASW tests were used to compute the Vs profiles. The inversion analysis was conducted using the parameters stated in Section 3.5. As mentioned before, the analysis only considered Vs profiles within the minimum misfit (M_m) and 10 % of the M_m (upper limit) due to the misfit value being dependent on several factors. Dispersion points between 10 Hz and 60 Hz were considered for the CSW Rayleigh wave and dispersion points between 10 Hz and 40 Hz were considered for the CSW Love waves. On the other hand, SASW Rayleigh waves between 0 Hz and 100 Hz and SASW Love waves between 0 Hz and 40 Hz were considered during the inversion process. No multimode analysis was conducted as it introduces additional uncertainties such as identifying the mode number or the possibility of superposed modes. However, based on the frequency ranges of the dispersion points, the minimum depth that could be resolved was limited to 2 m. The Vs profiles from the CSW tests are shown below in Figure 4.48 (discrete inversion) and Figure 4.49 (joint inversion). Figure 4.50 and Figure 4.51 shows the SASW Vs profiles using discrete and joint inversions respectively.
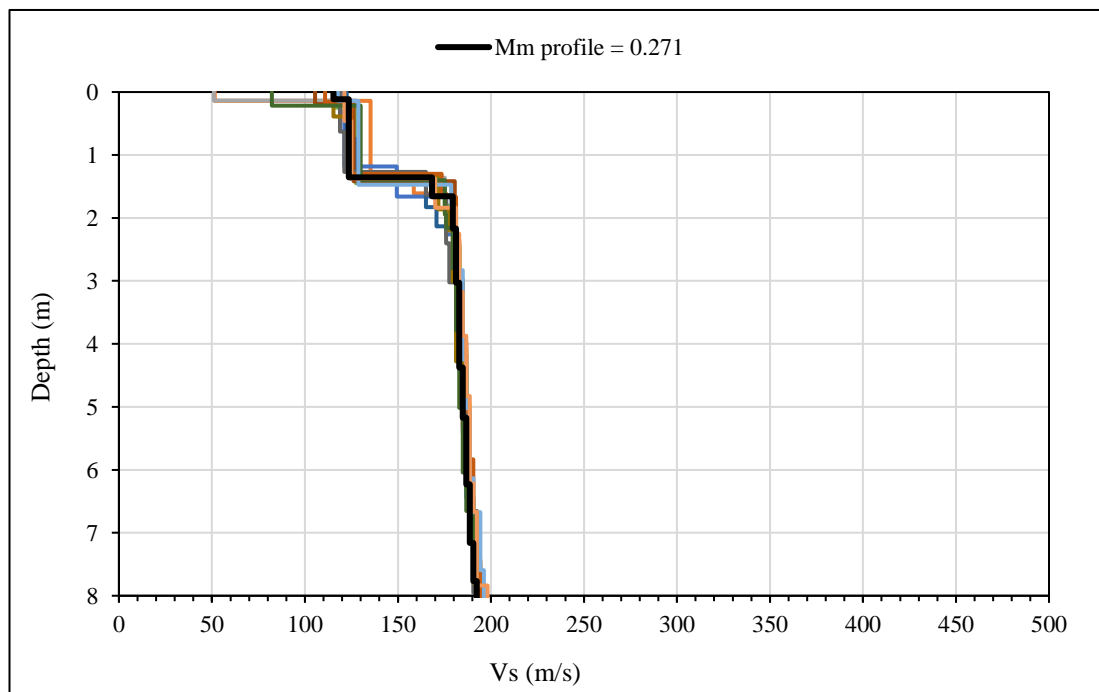
Figure 4.48: Vs profiles using discrete inversion - Rayleigh waves at Wind Africa test site (CSW testing).
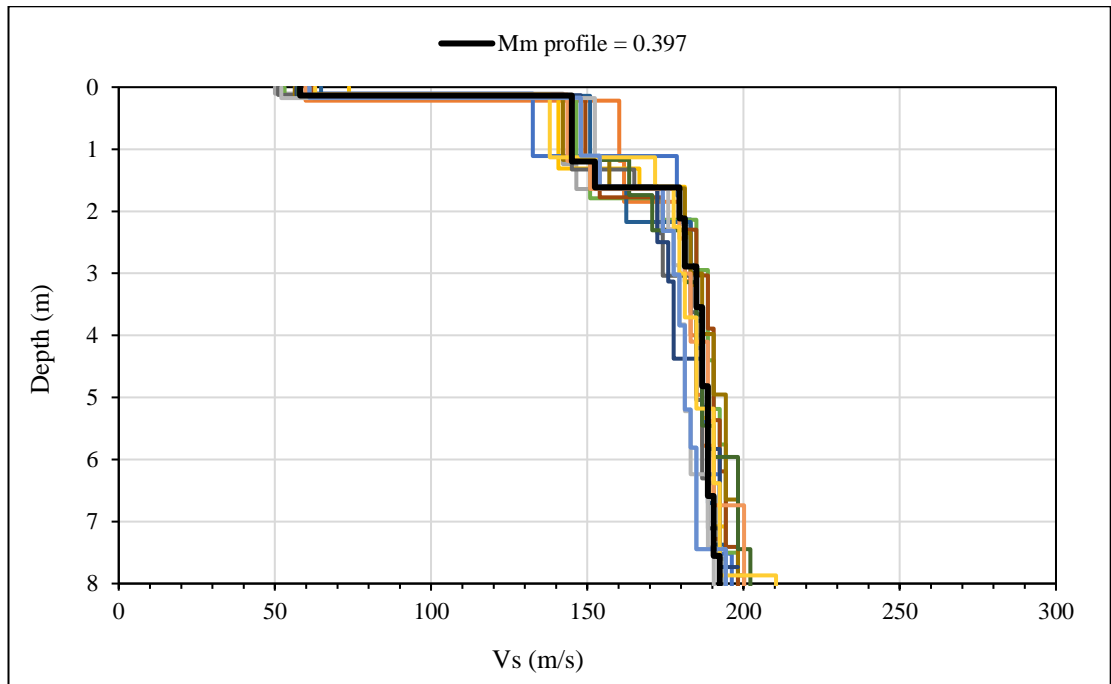
Figure 4.49: Vs profiles using joint inversion – Rayleigh and Love waves at Wind Africa test site (CSW testing).
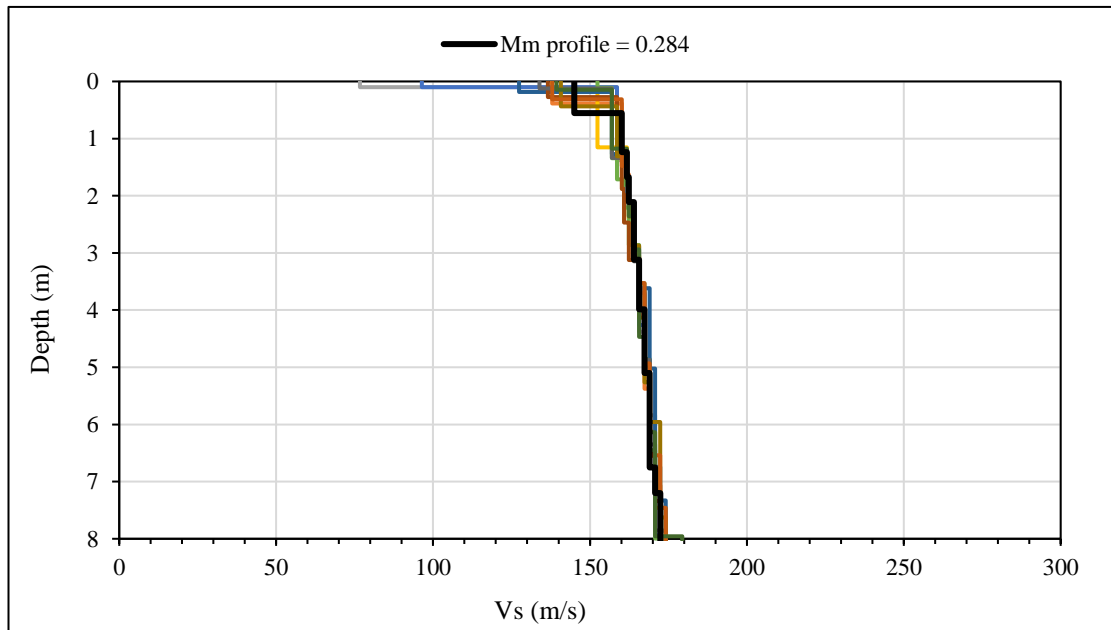
Figure 4.50: Vs profiles using discrete inversion - Rayleigh waves at Wind Africa test site (SASW testing).
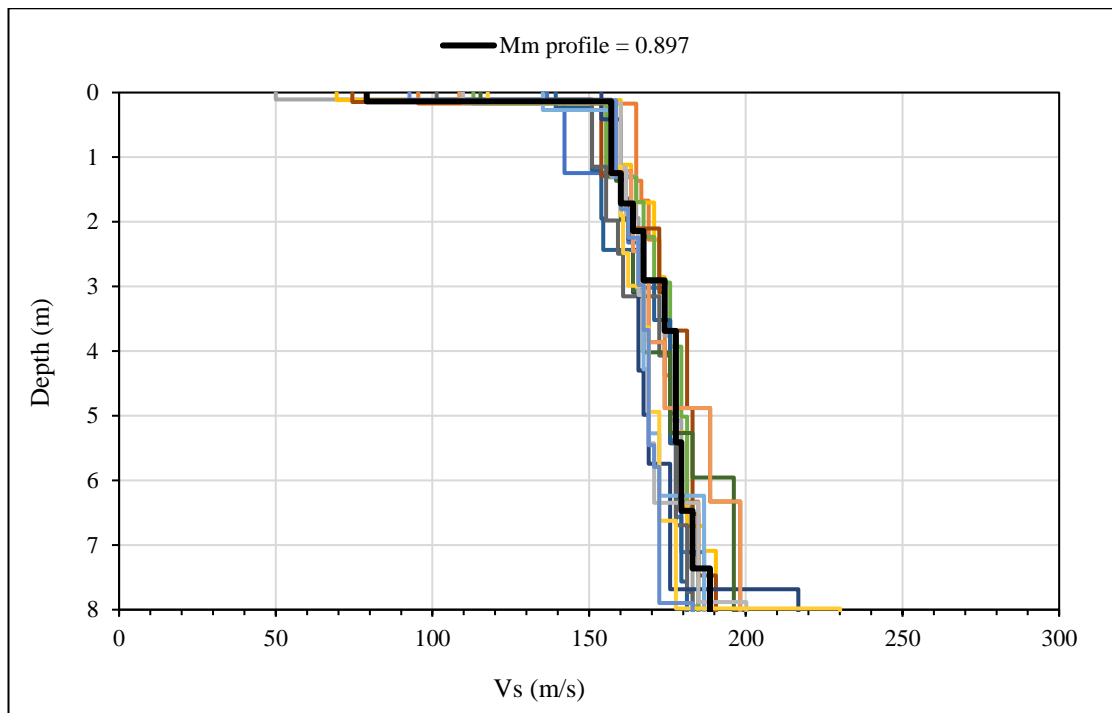
Figure 4.51: Vs profiles using joint inversion – Rayleigh and Love waves at Wind Africa test site (SASW testing).

Like the Engineering 4.0 test site, the M_m increased after conducting a joint inversion for each respective test. This could mean that there was a better fit between the experimental theoretical dispersion curves when conducting a discrete inversion. However, the increase in the M_m could possibly be due to the fitting of both Rayleigh and Love wave experimental data during the joint inversion. With regards to the generated V_S profiles, it could be seen that both discrete and joint inversion Vs profiles were comparable to one another for each respective testing approach.

As mentioned previously in Section 3.1, the Wind Africa test site exhibited a normally dispersive characteristic which was supported by the profile description and the SPT N values increasing with depth. This was evident in all four figures above, which displayed an increase in the Vs with depth. From Figure 4.48 to Figure 4.51, it was observed that the Vs varied between 100 m/s and 230 m/s for depths between than 0.2 m and 8.0 m. According to Table 4.1 and Table 4.2, such Vs were applicable to stiff clays and sandy soils/ stiff clays and dense sand. The borehole results for the Wind Africa test site suggested stiff/very stiff silty clays for these depths. Therefore, the Vs approximated by the surface wave tests were in agreement with the borehole results.

The quality of the different inversion scenarios were evaluated by comparing the spreads in the Vs profiles. At every 1 m depth, the spread in the Vs was calculated by considering the maximum and minimum Vs profiles within the limits of M_m and 10 % of M_m. Therefore, a smaller spread in the Vs implied a better approximation of the Vs. The spread in the Vs for the discrete and joint inversions using CSW and SASW tests are shown below in Figure 4.52 and Figure 4.53 respectively.
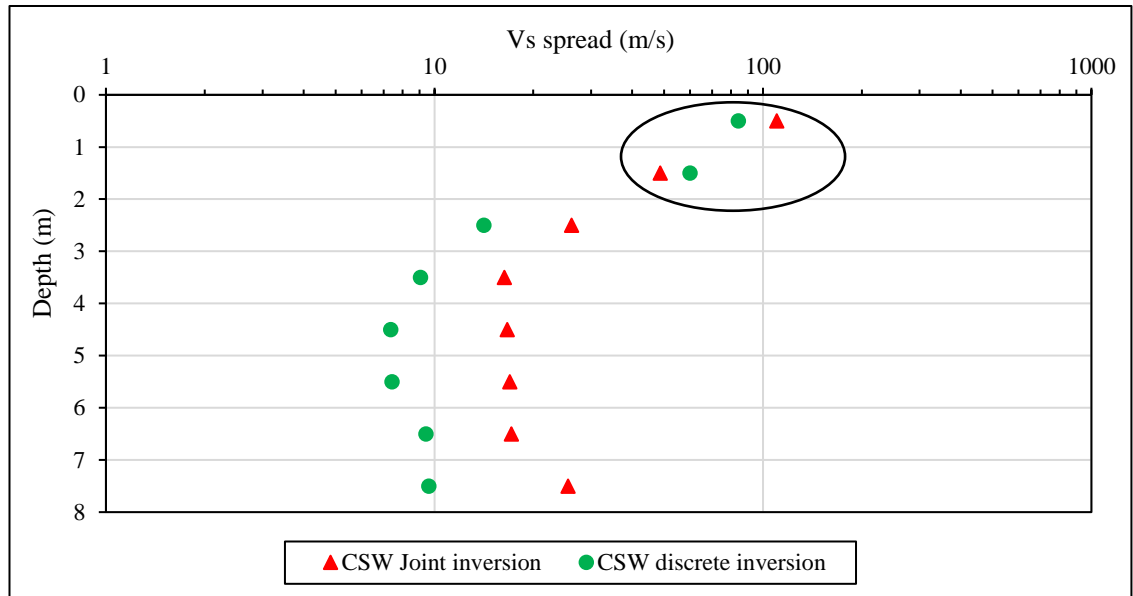
Figure 4.52: Vs spread between discrete and joint inversions for CSW dispersion data.
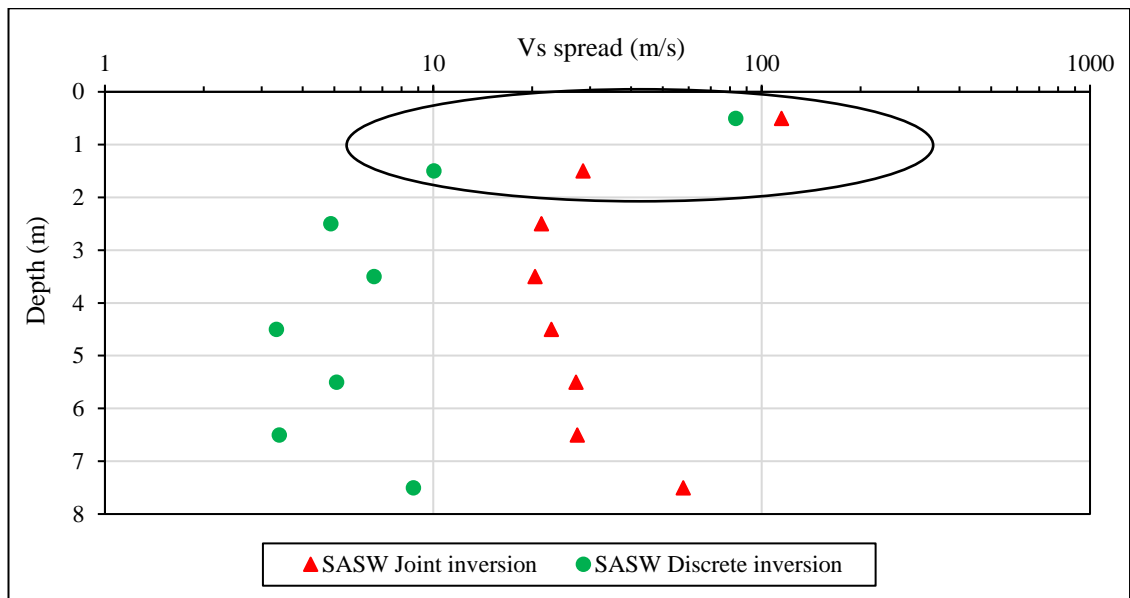
Figure 4.53: Vs spread between discrete and joint inversions for SASW dispersion data.

From Figure 4.52 and Figure 4.53, it could be seen that Vs spread points for depths below 2 m were circled due to limitations in the minimum depth that could be resolved by the dispersion points. Therefore, the Vs spread points below 2 m were not considered during the analysis. According to both Figure 4.52 and Figure 4.53, the discrete inversion provided a smaller spread in the Vs for all the depths considered when compared to the joint inversion spread. For both the CSW and SASW approach, there was not a single event where the joint inversion produced a smaller Vs spread. However, the observations made using the synthetic dispersion data suggested that a smaller Vs spread could be achieved when using joint inversion, provided that both the Rayleigh and Love dispersion data were of good quality. Upon conducting joint inversions with the addition of 10 % random noise to the synthetic dispersion data, it was observed that the spread in the Vs increased. Regardless of the surface wave to which the random noise was added to, the spread in the Vs increased when compared to the respective discrete inversion during the synthetic data analysis. Therefore, the observations made in Figure 4.52 and Figure 4.53 could possibly be due to the poor quality of the Love wave signals. As the quality of the Love wave data was not as good as the quality of the Rayleigh wave dispersion data, a larger Vs spread was observed during the joint inversion compared to the discrete inversion. This was further evident in Figure 4.54 and Figure 4.55, which showed the fit between the theoretical and experimental dispersion data for the CSW and SASW tests respectively. It is clearly evident in Figure 4.54 and Figure 4.55 that there was an issue with the

Love wave dispersion data at low frequencies and any form of joint inversion was going to be difficult compared to a discrete inversion.
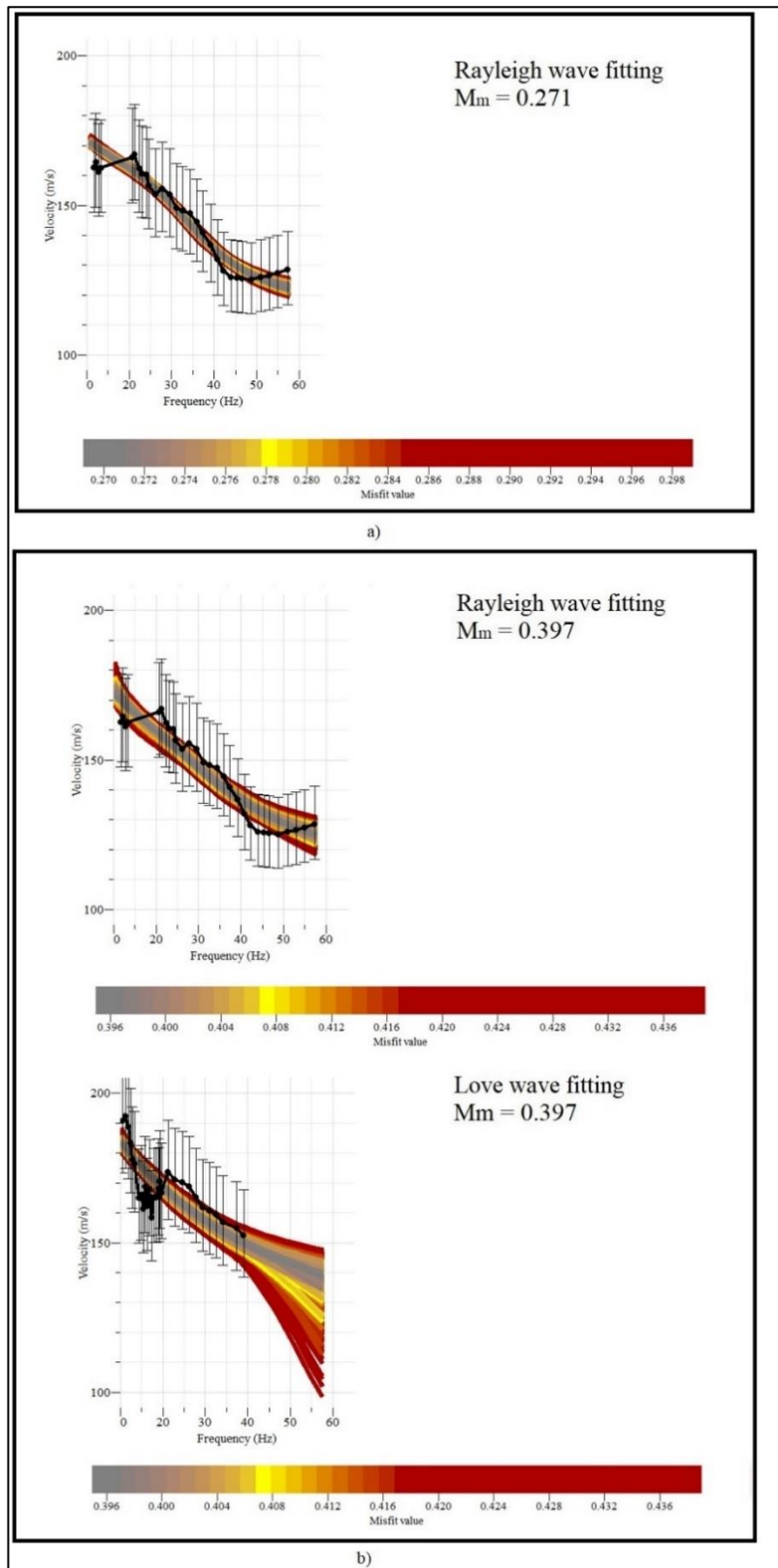
Figure 4.54: Theoretical and experimental dispersion data fitting using a) discrete inversion b) joint inversion for CSW test at Wind Africa test site.
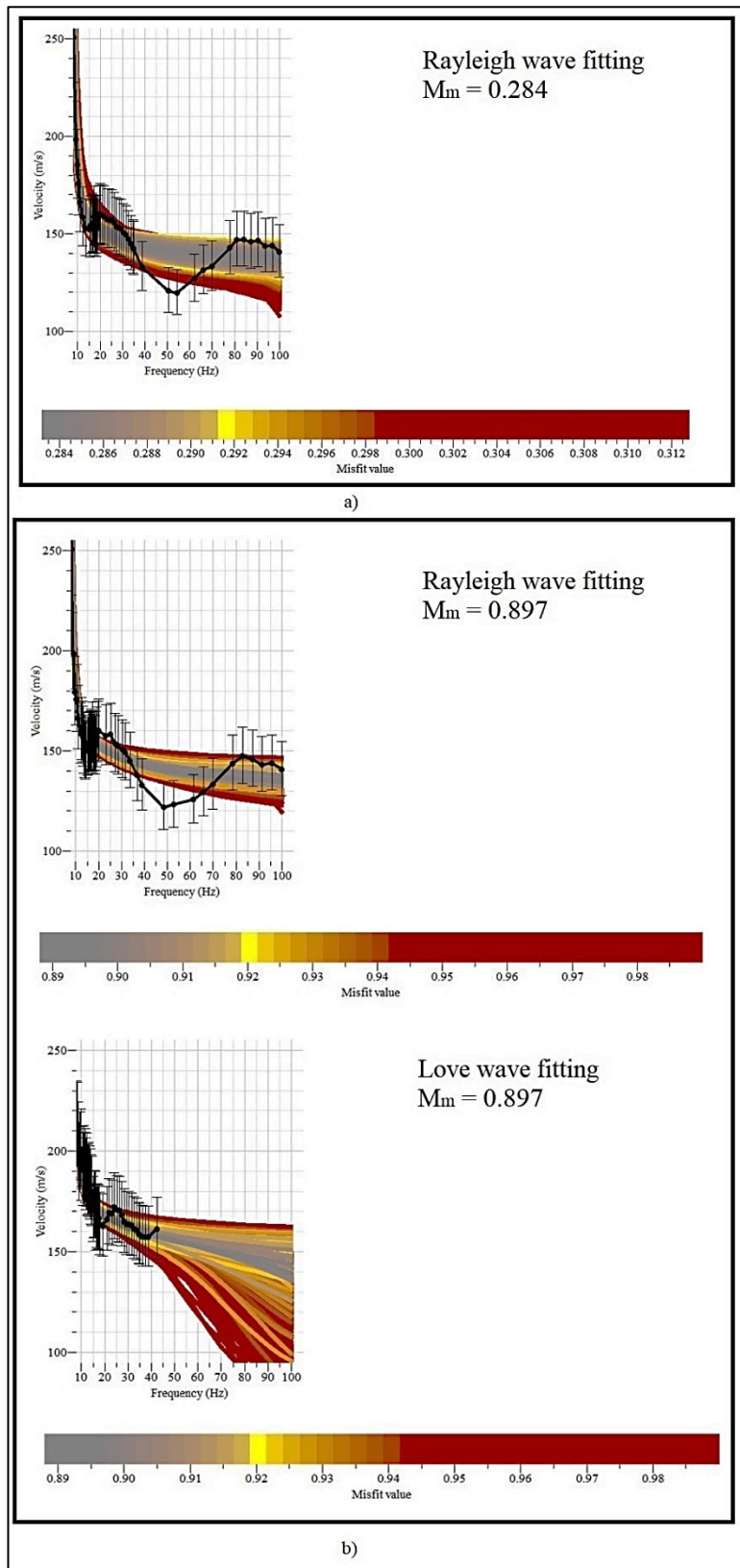
Figure 4.55: Theoretical and experimental dispersion data fitting using a) discrete inversion b) joint inversion for SASW test at Wind Africa test site.

5 CONCLUSIONS AND RECOMMENDATIONS

Current industry practices predominantly uses surface wave tests which use Rayleigh waves only and process the acquired signals to determine dispersion data and Vs profiles. The research conducted in this dissertation addressed the effects on the performance of obtaining the Vs profile when a second set of surface waves, known as Love waves, was measured in conjunction with the Rayleigh waves during seismic surface wave tests. The author built a Love wave SASW source which was based on the design published by Haines (2007). In addition, the author developed the Python code to calculate the dispersion data for both CSW and SASW tests.

Two inversion runs were explored during the analysis stage, namely the discrete and joint inversion runs using CSW and SASW tests. Theses surface wave tests were conducted at two independent test sites with different site profiles. Using literature studies, an experimental plan was developed with the required test specifications as well as the various steps used to generate, acquire and process the two types of surface waves. Conventional procedures were used for the generation of Rayleigh waves, whilst alternative methods were employed in the generation of Love waves.

Love waves were generated for both CSW and SASW tests using different techniques. The CSW test essentially used conventional mechanical shakers that were strapped on a wooden platform whilst the SASW test utilized a steel impact source with shear spikes bolted at the bottom. Both sources generated Love wave signals which were easily detected by the horizontal geophones and allowed similar processing to that of Rayleigh waves. The Love waves did not require any additional processing. Although the selected test sites were predominantly quiet, it was concluded that the sources consistently produced Love wave signals with high signal to noise ratios, which were evident in the Spectral Amplitude plots. With regards to practicality, both the CSW and SASW Love wave approaches proved to be cumbersome. The CSW approach required moving over the test site with an additional wooden platform with shear spikes and straps to attach the shakers firmly. When used at low frequencies with the low frequency shaker ($< 20\,\mathrm{Hz}$), the CSW approach was observed to produce significant dust, which can cause respiratory problems. Although the SASW impact source did not cause such conditions, it was not easily moved on site due to its weight. Nonetheless, both sources were able to perform well in generating Love waves for the purpose of this research.

An observation made during the acquisition of the Love waves dispersion data was that of the existence of higher modes when using both CSW and SASW sources described in this dissertation. Safani *et al.* (2005) mentioned that Love waves were less probable in generating higher modes than Rayleigh waves in certain geological environments. However, based on the data collected, it was observed that for both test sites, higher modes of vibration were present irrespective of the type of surface wave being produced.

During the dispersion analysis of the Rayleigh and Love waves using the CSW testing method, near field effects were observed in the dispersion data. Near field cut off lines were plotted to evaluate the D_{min}, which was the minimum source offset required to avoid near field effects. Based on the experimental observations, it was concluded that the near field effect criterion of Hiltunen and Woods (1990) is conservative. From the experimental observations, filtering criteria were suggested for each type of shaker at each test site, as shown in Table 5.1. It was firstly noticed that each test site had different filtering criteria for Rayleigh and Love waves. This implied that the near field effect was dependent on the test site conditions and the type of surface wave used. Although the study of the near field effects was not part of the objectives in this dissertation, a filtering criterion of $\frac{D_{min}}{\lambda} > \frac{1}{3}$ is suggested based on the experimental data, for avoiding near field effects when using Rayleigh or Love waves.

Table 5.1: Near field observations.

Test Site	Filtering criterion from observations	Surface wave	Testing method
Engineering 4.0	$\frac{D_{min}}{\lambda} > \frac{1}{8}$	Rayleigh	CSW (Low Frequency Shaker)
	–		CSW (High Frequency Shaker)
	–	Love	CSW (Low Frequency Shaker)
	$\frac{D_{min}}{\lambda} > \frac{1}{3}$		CSW (High Frequency Shaker)
Wind Africa	$\frac{D_{min}}{\lambda} > \frac{1}{8}$	Rayleigh	CSW (Low Frequency Shaker)
	$\frac{D_{min}}{\lambda} > \frac{1}{3}$		CSW (High Frequency Shaker)
	$\frac{D_{min}}{\lambda} > \frac{1}{6}$	Love	CSW (Low Frequency Shaker)
	–		CSW (High Frequency Shaker)

Joint inversion runs were conducted using Rayleigh and Love waves to approximate the Vs profiles using synthetic and experimental dispersion data. Both the joint and discrete inversion runs approached similar Vs profiles. After conducting a joint inversion using the synthetic dispersion data, it was observed that the spread in the Vs profiles were less than that from the discrete inversion runs. However, this was only true when no noise had been introduced into the dispersion data for either surface waves. It was noticed that upon adding noise to the dispersion data for either the Rayleigh or Love wave data, the spread in the Vs profiles for the increased for the joint inversion. This suggested that the performance of the joint inversion was dependent on the quality of the dispersion data acquired. From the inversion analysis of the experimental data at the two test sites, it was noticed that the joint inversion produced a larger spread in the Vs profiles when compared to the discrete inversion. Based on the fit between the theoretical and experimental dispersion data of the Love waves, it was concluded that the quality of the Love wave signals was not sufficiently good to reduce the spread of the Vs profile during the joint inversion.

The inversion problem ill posed, meaning that multiple solutions may exist for the same experimental dispersion data, and it is therefore favourable to include additional experimental data to help constrain the inversion problem. In conclusion, it was found that the application of both wave forms may result in a more precise determination of the shear wave velocity profile compared to only the application of Rayleigh wave. However, the quality of the joint inversion process was very much dependent on the quality of the Love waves generated. This aspect was found somewhat problematic in the present study.

It is advised that prospective researchers explore newer designs, which can be based on the approaches described in this study. Also, it should be kept in mind that Love waves require a normally dispersive profile, where the velocity of the layers increase with depth (Kiełczyński, 2018). This implies that inversely dispersive profiles may not necessarily be suitable for joint inversion analysis. The aspect of inversely dispersive profiles has not been addressed in this dissertation. Foti *et. al* (2018) states that material anisotropies present in the profiles could lead to inconsistencies and incompatibilities between Rayleigh and Love waves. Therefore, it is recommended that future studies be carried out to evaluate the effects of anisotropy on joint inversion analysis as well.

6 REFERENCES

Abbiss, C.P. 1981. Shear wave measurements of the elasticity of the ground. *Geotechnique*, Vol 31, No 1, pp. 91–104.

Alexander, D.R. 1992. *In situ material characterization for pavement evaluation by the spectral-analysis-of-surface-waves (SASW) method*. Technical Report-GL-92-10, US Army Corps of Engineers.

Ambrosini, R.D. 2006. Material damping vs. radiation damping in soil–structure interaction analysis. *Computers and Geotechnics*, Vol 33, No 2, pp. 86–92.

Beaty, K.S. Schmitt, D.R. and Sacchi, M. 2002. Simulated annealing inversion of multimode Rayleigh wave dispersion curves for geological structure. *Geophysical Journal International*, Vol 151, No 2, pp. 622–631.

Borcherdt, R.D. 1994. Estimates of site-dependent response spectra for design (methodology and justification). *Earthquake spectra*, Vol 10, No 4, pp. 617–653.

Chakraborty, S. Bheemasetti, T.V. Puppala, A.J. and Verreault, L. 2019. Use of Constant Energy Source in SASW Test and Its Influence on Seismic Response Analysis. *Geotechnical Testing Journal*, Vol 41, No 6, pp. 1102–1116.

Comina, C. Foti, S. and Socco, L.V. 2012. Inversion uncertainty in surface wave analysis. In: *GeoCongress 2012: State of the Art and Practice in Geotechnical Engineering*, pp. 2736–2745.

De Nil, D. 2005. Characteristics of surface waves in media with significant vertical variations in elasto-dynamic properties. *Journal of Environmental and Engineering Geophysics*, Vol 10, No 3, pp. 263–274.

Doyle, H. 1995. *Seismology*. John Wiley & Sons, Chichester.

Duijndam, A.J.W. 1988. BAYESIAN ESTIMATION IN SEISMIC INVERSION. PART I: PRINCIPLES 1. *Geophysical Prospecting*, Vol 36, No 8, pp. 878–898.

Eslick, R. Tsoflias, G. and Steeples, D. 2008. Field investigation of Love waves in near-surface seismology. *Geophysics*, Vol 73, No 3, pp. G1–G6.

Foti, S. 2000. *Multistation methods for geotechnical characterization using surface waves*. PhD Thesis. Politecnico di Torino.

Foti, S. 2005. Surface wave testing for geotechnical characterization. In: *Surface Waves in Geomechanics: Direct and Inverse Modelling for Soils and Rocks*. Springer, pp. 47–71.

Foti, S. Comina, C. Boiero, D. and Socco, L.V. 2009. Non-uniqueness in surface-wave inversion and consequences on seismic site response analyses. *Soil Dynamics and Earthquake Engineering*, Vol 29, No 6, pp. 982–993.

Foti, S. Hollender, F. Garofalo, F. Albarello, D. Asten, M. Bard, P.Y. Comina, C. Cornou, C. Cox, B. Di Giulio, G. and Forbriger, T. 2018. Guidelines for the good practice of surface wave analysis: a product of the InterPACIFIC project. *Bulletin of Earthquake Engineering*, Vol 16, No 6, pp. 2367–2420.

Foti, S. Lai, C. Rix, G.J. and Strobbia, C. 2014. *Surface wave methods for near-surface site characterization*, CRC press.

Foti, S. Parolai, S. Albarello, D. and Picozzi, M. 2011. Application of Surface-Wave Methods for Seismic Site Characterization. *Surveys in Geophysics*, Vol 32, No 6, pp. 777–825.

Foti, S. and Strobbia, C. 2002. Some notes on model parameters for surface wave data inversion. *15th EEGS Symposium on the Application of Geophysics to Engineering and Environmental Problems*. 2002 European Association of Geoscientists & Engineers, p. cp-191.

Franco, S. 2015. *Design with Operational Amplifiers and Analog Integrated Circuits*. 2nd ed. McGraw-Hill Education, New York.

Gabriels, P. Snieder, R. and Nolet, G. 1987. In situ measurements of shear-wave velocity in sediments with higher-mode Rayleigh waves. *Geophysical prospecting*, Vol 35, No 2, pp. 187–196.

Ganji, V. Gucunski, N. and Nazarian, S. 1998. Automated inversion procedure for spectral analysis of surface waves. *Journal of geotechnical and geoenvironmental engineering*, Vol 124, No 8, pp. 757–770.

Graff, K.F. 1975. *Experimental Studies in Longitudinal Waves: Wave motion in elastic solids*. Dover Publications INC., New York.

Guzina, B.B. and Madyarov, A.I. 2005. On the spectral analysis of Love waves. *Bulletin of the Seismological Society of America*, Vol 95, No 3, pp. 1150–1169.

Haines, S.S. 2007. *A hammer-impact, aluminium, shear-wave seismic source*. Technical Report OF 07-1406, United States Geological Survey.

Hamill, J. Caldwell, G.E. and Derrick, T.R. 1997. Reconstructing digital signals using Shannon's sampling theorem. *Journal of Applied Biomechanics*, Vol 13, No 2, pp. 226–238.

Hasbrouck, W.P. 1983. *Sketches of a hammer-impact, spiked-base, shear-wave source*. Open-File Report 83-917, United States Geological Survey.

Haskell, N.A. 1953. The dispersion of surface waves on multilayered media. *Bulletin of the seismological Society of America*, Vol 43, No 1, pp. 17–34.

Hebeler, G.L. and Rix, G.J. 2007. Site characterization in Shelby County, Tennessee using advanced surface wave methods. *MAE Center CD Release 06-02*.

Heisey, J.S. Stokoe, K.H. and Meyer, A.H. 1982. Moduli of pavement systems from spectral analysis of surface waves. *Transportation research record*, Vol 852, No 22–31, p.147.

Heymann, G. 2007. Ground stiffness measurement by the continuous surface wave test. *Journal of the South African Institution of Civil Engineering*, Vol 49, No 1, pp. 25–31.

Hiltunen, D.R. and Woods, R.D. 1990. Variables affecting the testing of pavements by the surface wave method. *Transportation research record*, Vol 1260, pp. 42–52.

Hunter, J.A.M. and Crow, H.L. 2015. *Shear wave velocity measurement guidelines for Canadian seismic site characterization in soil and rock*, Open-File Report 7078, Geological Survey of Canada.

Jackson, D.D. and Anderson, D.L. 1970. Physical mechanisms of seismic-wave attenuation. *Reviews of Geophysics*, Vol 8, No 1, pp. 1–63.

Joh, S.-H. Hwang, S.K. and Nayan, K.A.M. 2011. Real-time spatial profiling of subgrade stiffness for quality assurance of field compaction. *The 90th Annual Meeting of the Transportation Research Board*, Washington, DC, pp. 1–20.

Johnson, D.H. 2006. *Signal-to-noise ratio*. Scholarpedia, Vol 1, No 12, p. 2088.

Kausel, E. and Roësset, J.M. 1981. Stiffness matrices for layered soils. *Bulletin of the seismological Society of America*, Vol 71, No 6, pp. 1743–1761.

Kennett, B.L.N. 1974. Reflections, rays, and reverberations. *Bulletin of the Seismological Society of America*, Vol 64, No 6, pp. 1685–1696.

Kielczyński, P. 2018. Properties and Applications of Love Surface Waves in Seismology and Biosensors. *Surface Waves: New Trends and Developments*, p.17.

Kumar, J. and Hazra, S. 2014. Effect of input source energy on SASW evaluation of cement concrete pavement. *Journal of Materials in Civil Engineering*, Vol 26, No 6, pp. 1–7.

Leong, E.C. and Aung, A.M.W. 2013. Global inversion of surface wave dispersion curves based on improved weighted average velocity method. *Journal of geotechnical and geoenvironmental engineering*, Vol 139, No 12, pp. 2156–2169.

Lin, Y.-C. 2007. *Characterizing Vs profiles by the SASW method and comparison with other seismic methods*. PhD Thesis. The University of Texas at Austin.

Lines, L.R. and Treitel, S. 1984. A review of least-squares inversion and its application to geophysical problems. *Geophysical prospecting*, Vol 32, No 2, pp. 159–186.

Manolis, G.D. and Beskos, D.E. 1988. *Boundary element methods in elastodynamics*, Taylor & Francis.

Mari, J.L. 1984. Estimation of static corrections for shear-wave profiling using the dispersion properties of Love waves. *Geophysics*, Vol 49, No 8, pp. 1169–1179.

Martin, A. Yong, A.K. and Salomone, L.A. 2014. Advantages of active love wave techniques in geophysical characterizations of seismographic station-Case studies in California and the central and eastern United States. *The Tenth U.S. National Conference on Earthquake Engineering,* p. 11.

McCaskill, A. 2014. *A Study on the benefits of including near-field effects in active-source surface wave data collection and interpretation*. PhD Thesis. University of Missouri.

Menzies, B. and Matthews, M. 1996. The continuous surface-wave system: a modern technique for site investigation. *Special Lecture: Indian Geotechnical Conference, Madras*, pp. 11–14.

Menzies, B.K. 2001. Near-surface site characterisation by ground stiffness profiling using surface wave geophysics. Instrumentation in Geotechnical Engineering. *Oxford & IBH Publishing Co. Pvt. Ltd., New Delhi, Calcutta*, pp. 43–71.

Mitchell, B.J. Leite, L.W.B. Yu, Y.K. and Herrmann, R.B. 1976. Attenuation of Love and Rayleigh waves across the Pacific at periods between 15 and 110 seconds. *Bulletin of the Seismological Society of America*, Vol 66, No 4, pp. 1189–1202.

Nazarian, S. and Stokoe II, K.H. 1986. Use of surface waves in pavement evaluation. *Transportation Research Record*, Vol 1070, pp. 132–144.

Nazarian, S. and Stokoe, K.H. 1984. Nondestructive testing of pavements using surface waves. *Transportation Research Record*, Vol 993, pp. 67–79.

Park, C.B. Miller, R.D. and Xia, J. 1998. Imaging dispersion curves of surface waves on multi-channel record. In: *SEG Technical Program Expanded Abstracts 1998*. Society of Exploration Geophysicists, pp. 1377–1380.

Park, C.B. Miller, R.D. and Xia, J. 1999. Multichannel analysis of surface waves. *Geophysics*, Vol 64, No 3, pp. 800–808.

Pelekis, P.C. and Athanasopoulos, G.A. 2011. An overview of surface wave methods and a reliability study of a simplified inversion technique. *Soil Dynamics and Earthquake Engineering*, Vol 31, No 12, pp. 1654–1668.

Renalier, F. Jongmans, D. Savvaidis, A. Wathelet, M. Endrun, B. and Cornou, C. 2010. Influence of parameterization on inversion of surface wave dispersion curves and definition of an inversion strategy for sites with a strong Vs contrast. *Geophysics*, Vol 75, No 6, pp. B197–B209.

Richart, F.E. Woods, R.E. and Hall Jr, J.R. 1970. *Vibrations of Soils and Foundations*. Prentice–Hall, Englewood Cliffs.

Rix, G.J. Lai, C.G. and Spang Jr, A.W. 2000. In situ measurement of damping ratio using surface waves. *Journal of Geotechnical and Geoenvironmental engineering*, Vol 126, No 5, pp. 472–480.

Rosenblad, B. Rathje, E.M. and Stokoe, K.H. 2002. *Shear Wave Velocity Profiling by the SASW Method at Selected Strong-Motion Stations in Turkey*. Site response Report 2A02a, Pacific Earthquake Engineering Research Centre, Berkeley.

Rosenblad, B.L. and Bertel, J.D. 2008. Potential phase unwrapping errors associated with SASW measurements at soft-over-stiff sites. *Geotechnical Testing Journal*, Vol 31, No 5, pp. 433–441.

Safani, J. O'Neill, A. Matsuoka, T. and Sanada, Y. 2005. Applications of Love wave dispersion for improved shear-wave velocity imaging. *Environmental and Engineering Geophysics*, Vol 10, No 2, pp. 135–150.

Sambridge, M. 2001. Finding acceptable models in nonlinear inverse problems using a neighbourhood algorithm. *Inverse Problems*, Vol 17, No 3, p. 387.

Sambridge, M. 1999a. Geophysical inversion with a neighbourhood algorithm—I. Searching a parameter space. *Geophysical journal international*, Vol 138, No 2, pp. 479–494.

Sambridge, M. 1999b. Geophysical inversion with a neighbourhood algorithm—II. Appraising the ensemble. *Geophysical Journal International*, Vol 138, No 3, pp. 727–746.

Sanchez-Salinero, I. 1987. *Analytical investigation of seismic methods used for engineering applications*. PhD Thesis, University of Texas at Austin.

Sheriff, R.E. and Geldart, L.P. 1995. *Exploration seismology*, Cambridge University Press.

Stokoe, K.H. Joh, S.-H. and Woods, R.D. 2004. Some contributions of in situ geophysical measurements to solving geotechnical engineering problems. *The 2nd International Conference on Site Characterization,* pp. 97–132.

Stokoe, K.H. and Nazarian, S. 1985. Use of Rayleigh waves in liquefaction studies. *Measurement and use of shear wave velocity for evaluating dynamic soil properties*. ASCE, pp. 1–17.

Stokoe, K.H. Wright, S.G. Bay, J.A. and Roesset, J.M. 1994. Characterization of geotechnical sites by SASW method. *Geophysical characterization of sites*, pp. 15–25.

Strobbia, C. 2005. Love wave analysis for the dynamic characterisation of sites. *Bollettino di Geofisica Teorica ed Applicata*, Vol 46, No 2–3, pp.135–152.

Strobbia, C. 2003. *Surface wave methods. Acquisition, processing and inversion*. PhD Thesis. Politecnico di Torino.

Yoon, S. and Rix, G.J. 2009. Near-Field Effects on Array-Based Surface Wave Methods with Active Sources. *Journal of Geotechnical & Geoenvironmental Engineering*, Vol 135, No 3, pp. 399–406.

Svensson, M. and Möller, B. 2001. *Geophysics in soil mechanics-in situ shear moduli determined by SASW-technique and more traditional geotechnical methods*. Report 508, Swedish Geotechnical Institute.

Takeuchi, H. and Saito, M. 1972. Seismic surface waves. *Methods in computational physics*, Vol 11, pp. 217–295.

Thomson, W.T. 1950. Transmission of elastic waves through a stratified solid medium. *Journal of applied Physics*, Vol 21, No 2, pp. 89–93.

Tokimatsu, K. 1997. Geotechnical site characterization using surface waves. *First International Conference on Earthquake Geotechnical Engineering*, Vol 3, pp. 1333–1368.

Tokimatsu, K. Tamura, S. and Kojima, H. 1992. Effects of multiple modes on Rayleigh wave dispersion characteristics. *Journal of geotechnical engineering*, Vol 118, No 10, pp. 1529–1543.

Wathelet, M. 2008. An improved neighborhood algorithm: parameter conditions and dynamic scaling. *Geophysical Research Letters*, Vol 35, No 9, pp. 1–15.

Wathelet, M. Jongmans, D. and Ohrnberger, M. 2004. Surface-wave inversion using a direct search algorithm and its application to ambient vibration measurements. *Near surface geophysics*, Vol 2, No 4, pp. 211–221.

Winter, D.A. 2009. *Biomechanics and motor control of human movement*. John Wiley & Sons, New York.

Wood, C.M. and Cox, B.R. 2012. A comparison of MASW dispersion uncertainty and bias for impact and harmonic sources. In: *GeoCongress 2012: State of the Art and Practice in Geotechnical Engineering*, pp. 2756–2765.

Xia, J. Xu, Y. Luo, Y. Miller, R.D. Cakir, R. and Zeng, C. 2012. Advantages of using multichannel analysis of Love waves (MALW) to estimate near-surface shear-wave velocity. *Surveys in Geophysics*, Vol 33, No 5, pp. 841–860.

Yuan, J. Zhu, J. and Kim, C. 2014. Comparison of SASW and MASW methods using MSOR approach–a case study. *International Journal of Geotechnical Engineering*, Vol 8, No 2, pp. 233–238.

APPENDIX A

LOVE WAVE IMPACT SOURCE DESIGN

INTRODUCTION

The Love wave impact source was designed for the generation of Love waves during the SASW testing. It was constructed from mild steel with numerous design parts assembled and mounted together using arc welding. Figure A1 shows the design parts list along with their respective dimensions.
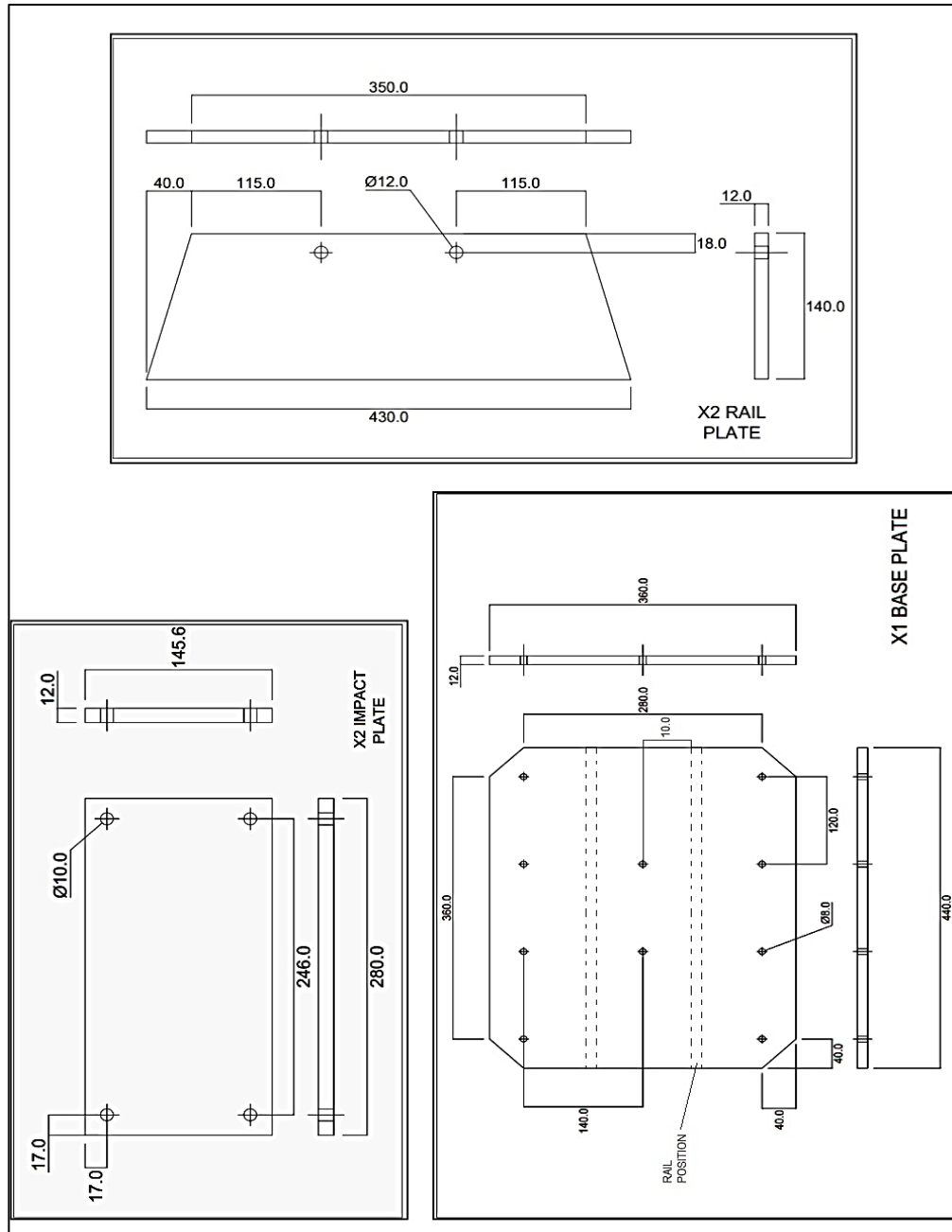
Figure A1: Love wave impact source design parts list.

APPENDIX B

SIGNAL PROCESSING CODE

INTRODUCTION

The processing stage of the experimental data used Python based code to interpret the signals acquired. The approaches used in the codes varied accordingly to the surface wave test being employed. The following subsections presents the Python based codes written by the author and used for the signal processing.

CSW PYTHON CODE

```python
"""

CSW Python Code

Mohammed Shariful Islam

"""

import os

from matplotlib import pyplot as plt

import numpy as np



path = (r"folderpath") # Directory of folder

folder = os.listdir(path)   # List of files in folder

f = [] # Frequency list

v = [] # Velocity list

r = [] # R squared list

for fl in folder:

    fp = os.path.join(path,fl)    # Joins list of file directory to folder directory
```

```python
# Reading data:

data = open(fp, "r") # Opens file

fhead,fname = os.path.split(fp) # Splits path into file head and file name as
string

if data.mode == "r":  # Checks if file is open

    lines = data.readlines()[1:]  # Starts reading all lines after first row

data.close()  # Closes file

ind = 0

for i in fname:       # Finds index positions of m(metres) and H(Hz) in
filename

    if i == "m":

        cst = ind # cst is the start of the index with m

    if i == "H" or i == "h":

        ced = ind # ced is the end of the index with H

    ind = ind + 1

ef = fname[cst+1]

for i in range((len(fname))):

    if i > cst+1 and i < ced:

        ef = ef + fname[i]

ef = float(ef)
```

```python
# Parameters

s_o = 1 # Source offset in m

g_s = 1 # Geophone spacing assuming equal spacing in m

ng = 5 # Number of geophones


# Geophones

g1 = []

g2 = []

g3 = []

g4 = []

g5 = []

t = []

for i in lines:

    t.append(float(i.split()[0]))

    g1.append(float(i.split()[1]))

    g2.append(float(i.split()[2]))

    g3.append(float(i.split()[3]))

    g4.append(float(i.split()[4]))

    g5.append(float(i.split()[5]))

N = len(g1)

fs = np.ceil(1/(t[1]-t[0]))  # Sampling frequency in Hz rounded up
```

```python
x = np.fft.fftfreq(N, d=1 / fs)  # Generating frequencies

fft1 = np.fft.fft(np.array(g1))  # fft.computation

fft2 = np.fft.fft(np.array(g2))

fft3 = np.fft.fft(np.array(g3))

fft4 = np.fft.fft(np.array(g4))

fft5 = np.fft.fft(np.array(g5))



# Maximum index location

fft_m = np.abs(fft1) # Calculates amplitude magnitudes

m1 = [] # Maximum list of amplitudes in that region

il = [] # Index list of maximum amplitudes

ind = 0

for i in x:

    if i > (ef-1) and i < (ef+1): # Expected frequencies ± 1Hz

        m1.append(fft_m[ind])

        il.append(ind)

    ind = ind + 1

# Finds maximum amplitude in the list

ma = max(m1)

cnt = 0

for i in m1:
```

```python
    if i == ma:

        i_ma = cnt

    cnt = cnt + 1

i_max = il[i_ma] # Index position of maximum amplitude



# Results

Ny = fs/2 # Nyquist frequency (symmetry line)

f_t1 = x[i_max]  # Frequency of geophones

    if f_t1 < 0: # if frequency is negative

    f_t1 = f_t1 * -1



# Phase angle determination

p_a = [] # Phase angle of each geophone

flist = [fft1, fft2, fft3, fft4, fft5]

g_d = np.linspace(s_o, s_o + g_s * ng, ng, endpoint=False) #Geophone
distances

for a in flist:  # Calculating phase angle

    ans = a[i_max].imag/a[i_max].real

    phase = np.arctan(ans)

    p_a.append(phase)
```

```python
# Phase unwrapping

uphase = [] # Empty unwrapped list

uphase.append(p_a[0]) # Adds first item

cnt = 0 # Counter

for k in range(0,len(p_a)-1):

    if p_a[k+1]< p_a[k] and cnt == 0: # if no wrapping has been done yet

        uphase.append(p_a[k+1])

    elif p_a[k+1] <= p_a[k] and cnt != 0: # if second element is less than first

        uphase.append(p_a[k+1]- cnt*np.pi) # Uses the same counter

    elif p_a[k+1] >= p_a[k]: # if second element is less than first, increase counter by 1

        cnt = cnt + 1 #

        uphase.append(p_a[k+1] - cnt*np.pi)


# Best fit line determination

xb = g_d

yb = np.array(uphase)

m, c = np.polyfit(xb, yb, 1)

yp = []  # Predicted y values

for d in xb:
```

```python
        ans = m*d + c

        yp.append(ans)


    # R² value

    cr_matrix = np.corrcoef(yb, yp)

    corr = cr_matrix[0,1]

    r_sq = corr**2


    # Velocity

    drdi = 1 / m  # dr/dphi

    vel = 2 * np.pi * f_t1 * drdi * -1

    f.append(f_t1)

    v.append(vel)

    r.append(r_sq) # Adds r squared to list


# Writing data into txt file

dp = open("FileName.txt","w+")  # Creates a text file, + means it will create it
a new file if it doesn't exist

for i in range(len(f)):

    dp.write(str(f[i])+" "+ str(v[i]) +" "+ str(r[i]) + "\n")   # Writes into columns

dp.close()
```

```
# Dispersion Curve plotting

x = np.array(f)

y = np.array(v)

plt.plot(x,y,'or')

plt.title ('Dispersion Curve')

plt.xlabel('Frequency (Hz)')

plt.ylabel('Velocity (m/s)')

plt.xlim(0.,100.)

plt.ylim(0.,1000.)

plt.grid(True)

plt.show()
```

SASW PYTHON CODE

```python
"""

SASW Python Code

Mohammed Shariful Islam

"""

import numpy as np

import easygui

import statistics as st

from matplotlib import pyplot as plt

from scipy import signal as sg



# Reading data

F = r"Forwardfile.txt" #Forward file path

R = r"Reversefile.txt" #Reverse file path

dataF = open(F, "r")



if dataF.mode =="r" :  # Checks if file is open

    linesF = dataF.readlines()[1:]  # Starts reading all lines after first row

dataF.close() # Closes forward file

dataR = open(R, "r")

if dataR.mode == "r":  # Checks if file is open

    linesR = dataR.readlines()[1:]  # Starts reading all lines after first row
```

```python
dataR.close() # Closes reverse file


# Geophones and time

t_i = [] # Time list initial

gF1 = [] #Geophone 1 Forward list

gF2 = [] # Geophone 2 Forward list

gR1 = [] # Geophone 1 Reverse list

gR2 = [] # Geophone 2 Reverse list

for i in linesF:

    t_i.append(float(i.split()[0]))

    gF1.append(float(i.split()[2]))

    gF2.append(float(i.split()[1]))

for i in linesR:

    gR1.append(float(i.split()[1]))

    gR2.append(float(i.split()[2]))


ga1 = [] #Averaged geophone 1 list

ga2 = [] #Averaged geophone 2 list

ga1 = [st.mean(k1) for k1 in zip(gF1,gR1)]

ga2 = [st.mean(k2) for k2 in zip(gF2, gR2)]
```

```python
tsp = 3   #Sampling window interval in seconds

t = [] #Time list

g1 = [] #Geophone 1 list for set time

g2 = [] #Geophone 2 list for set time


cnt = 0 #Index counter

for i in t_i:

    if i <= tsp:

        t.append(i)

        g1.append(ga1[cnt])

        g2.append(ga2[cnt])

    cnt = cnt + 1


# Parameters

gd = float(easygui.enterbox("Please enter geophone spacing", "Geophone Spacing")) #
Geophone spacing assuming equal spacing


N = len(g1)

dt = t[1]-t[0] #Sampling interval

fs = np.ceil(1/(dt)) # Sampling frequency in Hz rounded up
```

```python
f1 = np.fft.fft(np.array(g1))  # FFT computation

f2 = np.fft.fft(np.array(g2))

f4 = np.conjugate(f2)

x = np.fft.fftfreq(N, d=1 / fs) #Frequency generation for spectral amplitude plot


#Phase difference computation

Gxy = f1 * f4

wg = []

for i in Gxy:

    ans = (np.arctan(np.imag(i)/np.real(i)))

    wg.append(ans)

ns = N/8 #Number per segment window

fx,Cxy = sg.coherence(g1,g2,fs=fs,nperseg=ns,noverlap = 0.1 * ns)


#Spectral, Coherence and Wrapped Phase Plot

plt.figure(1)

plt.subplot(221)

plt.plot(x,np.abs(f2),"ko",label='Geophone 1',ms=2)

plt.plot(x,np.abs(f1),"bo",label='Geophone 2',ms=2)

plt.xlim(5.,fs/2)

plt.title("Spectral Amplitude")

plt.ylabel("Spectral Amplitude")
```

```python
plt.xlabel("Frequency(Hz)")

plt.legend(loc='best')

plt.tight_layout()

plt.grid(True)



plt.subplot(222)

plt.plot(fx,Cxy,'b',label='Segment Length ='+str(int(ns)),ms = 2)

plt.axhline(y= 0.9,color = "k", linestyle = '--')

plt.yscale("linear")

plt.ylabel("Coherence")

plt.xlabel("Frequency(Hz)")

plt.title("Coherence plot")

plt.xlim(5.,fs/2)

plt.ylim(0.,1.)

plt.legend(loc='best')

plt.tight_layout()

plt.grid(True)



plt.subplot(223)

plt.plot(x,wg,"ro", ms = 3)

plt.axhline(y=180,color = "k", linestyle = '--')

plt.axhline(y=-180,color = "k", linestyle = '--')
```

```python
plt.title("Wrapped phase spectrum Power")

plt.xlabel("Frequency(Hz)")

plt.ylabel("Phase angle (deg)")

plt.ylim(-5,5)

plt.xlim(0.,200)

plt.tight_layout()

plt.grid(True)

plt.show()



#Unwrapping Phase differences

data1 = []

for i in range(len(x)):

    data1.append("Frequency of" + " " + str(x[i])+ " " + "and phase difference of " +  "
" + str(wg[i]) + " " + " at an index of " + " " + str(i) + "\n")



easygui.msgbox(data1,"All Frequencies") #Prints suggested frequencies at which
jumps may be unwrapped

stop = True

while stop:

    mk = int(easygui.enterbox("Please enter index position 0 to quit",

                    "Unwrapping Phase differences"))

    if mk == 0:

        stop = False      #Exits while loop
```

```python
    elif mk != 0:

        difference = wg[mk] -wg[mk-1] #Finds differences at that point

        if difference > 0: # If difference is positive

            for y in range(mk, len(wg)):

                wg[y] = wg[y] - np.pi # Unwraps by π for all data values to right hand side


            plt.plot(x, wg, "go", ms=2)  # Plots the graph each time it is unwrapped

            plt.xlabel("Frequency(Hz)")

            plt.ylabel("Unwrapped Phase difference(rads)")

            plt.xlim(0.,fs/2 )

            plt.xticks(np.arange(0,fs/2,20))

            plt.minorticks_on()

            plt.tight_layout()

            plt.grid(True)

            plt.show()

        elif difference < 0: #If difference is positive

            for y in range(mk, len(wg)):

                wg[y] = wg[y] + np.pi # Unwraps by π for all data values to right hand side

            plt.plot(x, wg, "go", ms=2)  # Plots the graph each time it is unwrapped

            plt.xlabel("Frequency(Hz)")

            plt.ylabel("Unwrapped Phase difference(rads)")

            plt.xlim(0.,fs/2 )
```

```python
        plt.xticks(np.arange(0,fs/2,20))

        plt.minorticks_on()

        plt.tight_layout()

        plt.grid(True)

        plt.show()


#Velocity calculation

vel = []

for i in range(int(N/2)):

    ans = x[i]*gd*(2*np.pi/np.abs(wg[i]))

    vel.append(ans)

lf = float(easygui.enterbox("Please enter lower frequency bound",

                "Frequency Range"))

uf = float(easygui.enterbox("Please enter upper frequency bound",

                "Frequency Range"))


f = [] #Frequency list

v = [] #Velocity list

for i in range(len(x)):

    if x[i] >= lf and x[i] <= uf:

        f.append(x[i])

        v.append(vel[i])
```

```python
#Writing data into text file

dp = open("SL8m2kg.txt","w+") #Creates a textfile, + means will create if file doesn't
exist

for i in range(len(f)):

    dp.write(str(f[i])+" "+ str(v[i]) + "\n")   #Writes into columns

dp.close()



#Apparent Dispersion curve plot

plt.figure(2)

plt.plot(f,v,"go",ms = 2)

plt.title("Dispersion Curve")

plt.xlabel("Frequency(Hz)")

plt.ylabel("Velocity(m/s)")

plt.ylim(0.,1100.)

plt.yticks(range(0, 1200, 100))

plt.xlim(lf,uf)

plt.tight_layout()

plt.grid(True)

plt.show()
```